Optical polarimetry of bipolar planetary nebulae

Booth, Paul Anthony

Optical Polarimetry of Bipolar Planetary Nebulae

Paul Anthony Booth B.Sc.

A thesis submitted to the University of Durham
for the degree of Master of Science

Department of Physics

July 2001

ABSTRACT

Chapter 1 gives a brief review of the relevant aspects of stellar evolution leading to the formation of a planetary nebula. Included in this review is a discussion of the most important factors which appear to dictate the shaping and general characteristics of these nebulae.

Chapter 2 follows with a review of polarization theory and its use in the study of planetary nebulae and the interstellar medium. This includes a description of the basic reduction procedures which are used to produce the polarization maps of later chapters. Discussion of the reduction process is accompanied by the analysis and interpretation of linear polarization data from the observation of an extragalactic source.

Chapter 3 presents multicolour polarimetry data for the young bipolar planetary nebula M2-9. Much of the polarization data confirms previously gathered results and shows that extreme levels of polarization occur in the outer regions of the nebula. Polarization structure within the central regions of M2-9, however, appear to contradict a number of previously gathered results and suggest that the central illuminating source of the nebula is extended. The data conclusively proves that the mirror-symmetric condensations have changed position. An estimation of the rotation period of the condensations has been made using calculations which trace their lateral displacement. The result of these calculations agrees well with previously gathered results.

Chapters 4 and 5 present new multicolour polarimetry data for the evolved bipolar planetary nebulae NGC 2440 and NGC 2818. Results provide evidence for the existence of bipolar rotating episodic jets in the evolved Type I bipolar nebulae. The data also shows that both nebulae possess low polarization levels and a lack of clear structure within the polarization pattern. Consequently, the dust distribution of planetary nebulae must become less favourable for the production of radiation scattering with age.

DECLARATION

Work within this thesis deals with the study of bipolar planetary nebulae using the observing and analysis techniques of optical polarimetry. All data presented were recorded by the author using the Durham Imaging Polarimeter during observing time upon the 1.9m telescope at the South African Astronomical Observatory in September/October 1998, May 1999, and February/March 2000. Data reduction, analysis, and interpretation for all data has been carried out by the author. Results for M2-9 have already been published by Scarrott et al. (1993), but fresh analysis was made by the author.

None of the material contained within this thesis has previously been submitted for a degree at the University of Durham or any other university.

The data in this thesis were taken during telescope allocations made to Dr. S. M. Scarrott, Dr. R. D. Wolstencroft, and Mr. P. A. Booth and their permission must be obtained by anyone wishing to publish or use the results beyond this thesis.

CONTENTS

LIST OF FIGURES

LIST OF TABLES

CHAPTER 1

INTRODUCTION TO PROTO-PLANETARY AND PLANETARY NEBULAE

1.1 THE DISCOVERY OF PLANETARY NEBULAE

It was Charles Messier who first observed planetary nebulae (PNe) during the compilation of his famous catalogue of nebulae during the 18th century. Included in this catalogue are the objects known as the 'Dumbell Nebula' designated as Messier 27 (M27) and the 'Ring Nebula' designated as Messier 57 (M57). Due to the limitations of telescopic instrumentation at the time, nebulae were poorly understood. Later it became clear that differences existed between the various categorized objects. Consequently, their intrinsic nature remained the subject of tremendous debate for some time. However, first use of the term 'planetary nebula' was made by William Herschel, who noted that they displayed striking visual resemblance, when viewed through a telescope, to the greenish disc of the outer solar system planet Uranus. The name has been retained solely for historical reasons, as there is no physical connection between PNe and planets. As more PNe were discovered it became clear that most objects possessed similar morphology. This indicated that a common mechanism could exist for their formation and subsequent development.

The 19th century was marked by the discovery of an increasing number of PNe, which by the turn of the century, exceeded 100 objects. During this time, development in the field of astronomical spectroscopy allowed greater understanding of the true nature of PNe. Analyses of nebula spectra led to a clear distinction between PNe and other astronomical sources. Objects such as galaxies were found to exhibit strong continuum spectra with superposed absorption lines, while PNe were found to exhibit strong emission-line spectra. It also became clear at this time that the number ratio of PNe to the estimated total stellar population was very small, of the order of 10^{-5} or less. This created much anxiety amongst the astronomical community about the exact origin of PNe, but was later resolved by defining PNe as objects possessing a very short lifespan.

Further developments in spectroscopy revealed detailed elemental and molecular characteristics of PNe, leading to a greater understanding of the physical processes both inside and outside these objects. It became clear that PNe were composed of ionized material contained inside an expanding gaseous shell. Spectral observation revealed the presence of both emission-line radiation from hot nebulous gas and continuum radiation from the central star. Measurement of the expansion velocities and angular sizes of PNe, however, enabled estimates of their age to be made. Statistical analysis of expansion velocity data led to the inference of dynamical ages of the order of 10^4 years, suggesting that many stars could pass through the PN phase without being detected.

By the 20th century, it had become clear that PNe were integral constituents of galaxies. Evidence to support this claim was gathered from observations of their galactic distribution and kinematical properties. Measurements revealed that the distribution of PNe was largely confined to the galactic plane, with an increasing concentration toward the galactic centre. However, it was later found that some objects inhabited the galactic halo, calling for a revision of stellar evolutionary theory. Supplementary to increasing knowledge of the spatial distribution of PNe, it also became important to gather accurate distance measurements. However, attempts to establish an accurate distance scale were plagued by difficulties. Even today, the distance to any particular PN remains uncertain, presenting further difficulty in the determination of their exact properties. The earliest attempts to estimate PN distance were essentially based upon observed angular dimensions. However, because of the radial expansion of PNe, measured angular sizes included an age dependence as well as a distance dependence. Fortunately, many techniques now exist for PN distance determination. The most favoured of these methods is the use of PNe magnitudes in the Large Magellanic cloud. The distance determination of PNe still remains uncertain, with distances derived by different methods for a particular object varying by a factor of two or more.

During the later years of the 20th century, enormous progress has been made in observational techniques and instrumentation. Theories of PN evolution have been steadily refined as more data has become available. Data obtained with the Infrared Astronomical Satellite (IRAS) and Hubble Space Telescope (HST), in

particular, have led to a significant number of advances in PN research. Many PNe have now been catalogued, currently in excess of 1500 (Acker et al. 1992), and yet thousands more are thought to exist. Use of the HST has allowed unparalleled views of these objects and will undoubtedly reveal many new objects and their features. Many of the difficulties preventing advances in the theoretical aspects of PNe have now been overcome, creating a much clearer understanding of the physics and chemistry which characterize these objects. Increases in computing power have added much to this progress and will surely provide the key to future understanding of these complex astronomical objects.

1.2 THE CLASSIFICATION OF PLANETARY NEBULAE

One of the most striking attributes of (PNe) is the apparently boundless range in morphological diversity. This fact has prompted many attempts to establish some form of scheme with which to classify them. The most common classification schemes are those based upon the visual features of a two-dimensional projection of nebulae upon the plane of the sky. More recent classification schemes, however, have used both physical and chemical characteristics of nebulae, with the aim of modelling the three-dimensional structure of objects.

Although many classification schemes were formulated, those developed during the second half of the 20th century have shown the greatest promise. These have included classification and image catalogues by Evans & Thackeray (1950), Vorontsov-Vel'Yaminov (1961), Perek & Kohoutek (1967), and Hromov & Kohoutek (1968). One of the most promising classification schemes, however, has been developed by Greig (1971). Under the Greig classification, PNe are divided into four main groups. These groups are described as (A) annular, (B) binebulous or bipolar, (C) centric, and (E) egg-shaped. Statistically, data indicates that class B nebulae belonged to the youngest stellar population, while class A and C nebulae are much older and heavy-element deficient. Balick (1989) has also produced a scheme which is based upon the idea of interacting stellar winds (See §1.4 for details). Figure 1.1 shows the basic nebula morphologies and concepts which are involved in nebular shaping.

Aside from morphological analyses, classification schemes began to appear which were based upon the characteristics of elemental abundance and nebular composition. The most popular was that proposed by Peimbert (1978). He realised that PNe could be categorized more easily with the additional constraints provided by chemical characteristics. Like the Greig classification, Peimbert grouped PNe into four basic types. These were described simply as Type I (Helium and Nitrogen rich nebulae), Type II (Intermediate population I nebulae), Type III (High velocity nebulae), and Type IV (Halo population nebulae).

Type I: Helium and Nitrogen rich nebulae

PNe classified as type I appear to form a homogeneous group of objects which are believed to evolve from more massive progenitor stars. Defined in terms of elemental abundances and composition, type I PNe have $n(He)/n(H) \geq 0.125$ or $\log n(N)/n(O) \geq -0.3$. A substantial fraction of type I objects show bipolar structure, with distinctive filamentary sub-structure. It is now apparent that type I nebulae form an extreme subset of Greig's class B nebulae. From the observational standpoint, several facts support this hypothesis and their association with high mass progenitor stars. Study of the kinematics and galactic distribution of PNe reveals that both Greig's class B nebulae and Peimbert's type I nebulae are concentrated towards the galactic centre.

They also show kinematical properties closely linked to those of younger and more massive stars (Acker 1980; Cudworth 1974; Dutra & Maciel 1990; Greig 1972). The hypothesis is also supported by the observations of the central stars of PNe. Gorny et al (1997) showed that the central stars of bipolar PNe generally possess higher values of mass and also show a much wider mass distribution than those of other nebulae. Spectral observations show that type I PNe have strong forbidden lines and possess elements with a broad range of ionization states such as [OI], [NII], [SII], and even up to [NeV]. However, they are generally noted to be oxygen deficient, implying that their excess of nitrogen is of secondary origin from the transmutation of oxygen and not carbon.

Type II: Intermediate population I nebulae

PNe of type II classification are observed to lie within close proximity of the solar neighbourhood and appear to have evolved from stars of intermediate mass between the range $1.2.M_{\odot}$ - 2.4 $M_{\odot}$. Their galactic distribution shows that the vast majority of nebulae lie outside the galactic plane at an average height of 150 pc. Consequently, is has been proposed that type II PNe belong to an intermediate population I. Under the Peimbert classification, type II nebulae are defined as having $n(He)/n(H) < 0.125$, $\log n(N)/n(O) < -0.3$ and $\log n(O)/n(H) > -3.90$. Since their definition, type II nebulae have been sub-divided into classes IIa and IIb by Faundez-Abans & Maciel (1987). Studies revealed that a number of nebulae, known as type IIa possess $\log n(N)/n(H) \geq -4.0$, while a number, known as type IIb possess $\log n(N)/n(H) \leq -4.0$. Accordingly, it was suggested that type IIa nebulae could be associated with the older stellar members of population I, while those of type IIb could be associated with the heavy-element deficient population II found within the galactic disc.

Type III: High velocity nebulae

Nebulae classified as type III have been associated with the stellar objects of population II, indicating that they possess relatively poor heavy-element enrichment and generally originate at very different galactocentric distances from their current positions. The velocity dispersion of type III PNe has been shown to cover a very large range. It is known that the peculiar radial velocities of these objects, measured with respect to the rotational velocity of the galaxy, are generally greater than 60 kms^{-1}. In terms of chemical composition and abundances, the helium and oxygen enrichment is much the same as that of type II PNe. The range of masses of the progenitor stars forming these objects is somewhat constrained and appears to vary from $1M_{\odot}$ - 1.2 $M_{\odot}$

Type IV: Halo population nebulae

Peimbert's final class of PNe are designated as type IV and are observed to belong to the group of stellar objects known as the 'Halo' objects, more technically referred to as extreme population II. Very few objects of this particular class have ever been observed, but those which have been observed have been studied extensively. The fact that very few type IV nebulae have been observed does not mean that they should be neglected, as these types of object have provided essential information in establishing the abundances of heavy-element materials within the interstellar medium. The mass range for type IV objects is very small and appears to fall between the boundaries of $0.8M_{\odot}$ - $1.0M_{\odot}$ It has also become clear that these objects are deficient in oxygen and helium compared with the other types of PNe. However, they do appear to possess an enrichment of carbon.

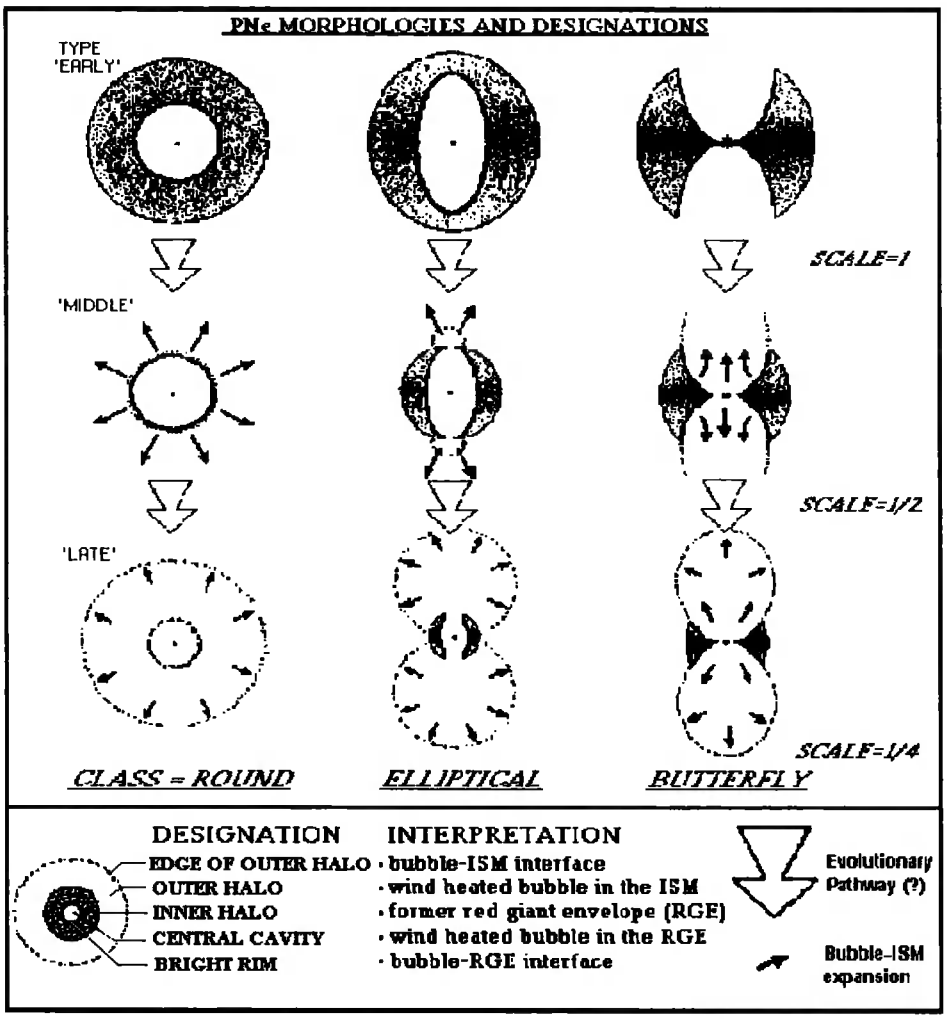

Figure 1.1: Morphological classification and designation of planetary nebulae. Taken from Balick (1989) IAU Symp. 131 (Planetary Nebulae).

1.3 STELLAR DEATH AND THE BIRTH OF PLANETARY NEBULAE

It is now well known that the initial formation of a star within the 'standard theory' of stellar evolution proceeds as a consequence of molecular cloud collapse. The fundamental and overwhelming criterion which governs this development, is that all forces which permeate the cloud structure should be dominated by gravity. Initially, collapse of the cloud shows a gradual development, with an increase in the rate of collapse with time. Eventually a stage is reached when the cloud becomes opaque to its own radiation, at which point the cloud takes on the structure of a 'protostar.' During subsequent development of the cloud, the protostar develops a convective structure. After sufficient time, convective behaviour ceases and a change in structure occurs with the onset of radiative behaviour. Consequently, energy release through the protostellar surface becomes reduced, leading to an increase in the internal energy and central temperature. This continues through the phase known as the 'pre-main sequence', which precedes the point where the star joins the main sequence and begins stable nuclear burning. However, before reaching the main sequence at the 'zero age main sequence', the star begins nuclear fusion reactions in which light elements, not usually encountered in the star's later life, are burnt in order to provide a stabilising effect for the star's emergence as a main sequence object. Although of fundamental importance in the theory of stellar evolution, the phases preceding the main sequence can be regarded as having little or no consequence to the post-main sequence. Although it is known that similarities exist in the appearance of both pre-main sequence and post-main sequence objects, it is unlikely that the phenomena producing these similarities continue throughout the main sequence to the final stages of the post-main sequence.

1.3.1 LIFE AFTER THE STELLAR NURSERY - MAIN SEQUENCE EVOLUTION

It is accepted that stars become main sequence objects when stable equilibrium is reached through the fusion of light elements into heavier elements. This signifies the end of gravitational contraction through the protostellar and pre-main sequence phases, as the star begins an extended period of stability. This is corroborated through observational evidence, which suggests that approximately 90% of all stars exist in this stable state. Upon the main sequence, the energy losses which are incurred by the star must be compensated by the energy generating processes of nuclear fusion reactions. At this stage, the star joins the 'zero age main sequence' (ZAMS) when it becomes fully radiative, possessing a well mixed and homogeneous chemical composition which mirrors that of its parent molecular cloud. Upon reaching the ZAMS, the central temperature of the star, fundamental to the subsequent evolutionary path, is largely dependent upon the initial mass. Once stable upon the main sequence, stars evolve with little movement upon the 'Hertzsprung-Russell' diagram. Consequently, a clear understanding of the internal structure of stars is required to determine their evolutionary paths. As a result, stars have been ascribed to fall within two

loosely defined categories, namely the upper- and lower-main sequence. Alternatively, stars may be described as having low-mass, intermediate-mass, or high-mass. These groupings are based upon such characteristics as the tendency of material within the star to become degenerate as a function of mass, and the particular nuclear fusion reaction sequences found to occur within the central regions as a function of temperature. Originally developed through the collaboration of Elnar Hertzsprung and Henry Norris Russell, the H-R diagram now provides a fundamental tool in the formulation of evolutionary theories and a means of grouping particular stellar types in a systematic way. Its chief representation reveals the fundamental relationship between stellar luminosity and the effective surface temperature of stars. As an alternative means of testing theoretical models, the diagram has since been modified to accommodate spectral classification, thus providing further information on the physical and chemical changes which occur during various stages of stellar evolution. Figure 1.2 shows an example of the H-R diagram. The figure has been taken from Pottasch (1984).

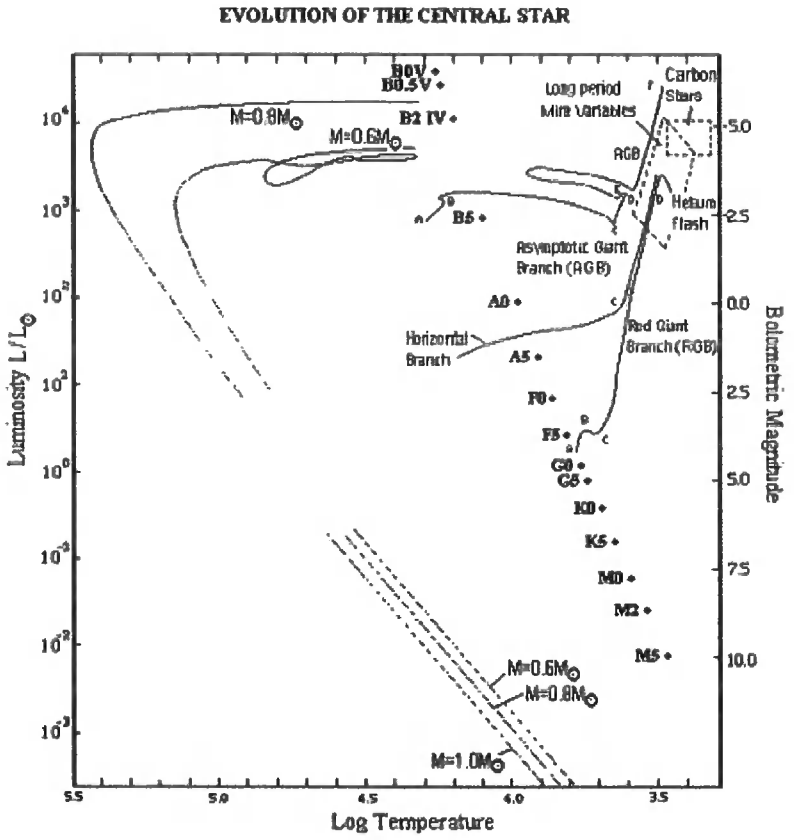

Figure 1.2: H-R diagram showing the evolutionary pathways for main-sequence stars of different mass. The tracks are labelled with letters and descriptions corresponding to critical changes in the stellar interior and the various stages of stellar development. The sequence of points running from M5 to B0 corresponds to the Harvard spectral classification sequence. The line followed by these points shows the position of the main-sequence.

1.3.1.1 LOW MASS STAR EVOLUTION

Lower main sequence or low mass stars are loosely defined as those which possess mass below 2 $M_{\odot}$. After the initial fusion reactions preceding their arrival upon the main sequence, these stars develop a stable structure within the timescale of approximately 10^6 years. Stars are now known to use nuclear fusion or nuclear burning reactions which involve fusing hydrogen into helium through a series of sequences occurring across a number of critical temperature ranges. For low mass stars the fusion of hydrogen into helium occurs through the reaction sequences collectively known as the 'proton-proton chain.' The proton-proton chain reactions include the p-p I, p-p II and the p-p III branches, which occur with increasing values of stellar mass and central temperature. The relatively low temperature dependence of the proton-proton chain implies that energy generation is not contained within the central regions with a high degree of constraint. Low mass stars thus possess radiative cores, although stars possessing higher mass may develop energy transfer mechanisms which depend on convection. The existence of this radiative core has a significant impact upon evolution, as helium remains close to the site in which it was formed. This places an increased abundance of helium at the centre of the star. Eventually, hydrogen becomes depleted in the stellar core, signifying termination upon the main sequence. The timescale of the main sequence is observed to vary most markedly between stars with extremes in physical characteristics, namely stellar mass. Consequently, the timescale of the main sequence shows variation over several orders of magnitude. For a star of mass 0.7 $M_{\odot}$ the duration of the main sequence is approximately 1.5×10^9 years. For a star of mass 1.7 $M_{\odot}$, however, the main sequence lifetime is shortened to approximately 1×10^9 years.

1.3.1.2 INTERMEDIATE AND HIGH MASS STAR EVOLUTION

The main sequence evolution of intermediate and high mass stars with masses exceeding 2.0 $M_{\odot}$ is somewhat different, as the situation regarding the stellar structure is reversed and is also complicated by the creation of additional physical conditions which occur during development upon the main sequence. For higher mass stars the central temperature increases more slowly, but is much higher when the star joins the main sequence. Consequently, a greater fraction of energy generation is produced through nuclear burning reactions which display an increased dependence upon the core temperature. For this reason the predominant series of fusion reactions which occur in higher mass stars, are those of the 'Carbon-Nitrogen-Oxygen (CNO) cycle.' Higher mass stars possess a convective core due to the fact that the increased energy generation requires a energy transfer process which possesses a much greater efficiency than that possessed by radiation.

1.3.2 LIFE AFTER CORE HYDROGEN DEPLETION – THE POST MAIN SEQUENCE

Evolution of a star from the main sequence represents the star's reaction to the depletion of hydrogen fuel within the core. The understanding of this post-main sequence phase is defined in the processes of readjustment which occur within the stellar core and overlying envelope. These processes are believed to occur as a consequence of the creation of additional nuclear burning regions. During this phase, low mass and high mass stars show large differences in development. However, evolution does show a series of commonly encountered characteristics. These characteristics include increasing central density, nuclear burning temperatures, energy generation, and stellar radii.

1.3.2.1 LOW MASS STAR EVOLUTION

In comparison to massive stars, low mass stars evolve very differently after the cessation of hydrogen burning within the stellar core. Because lower mass stars possess little, or no core convection, the consumption of hydrogen fuel results in the growth of a helium core. This is followed by a smooth transition from central hydrogen burning to shell hydrogen burning. Within the lower mass range, the helium core becomes void of nuclear energy sources. Consequently, the core contracts to supply sufficient energy to support the overlying layers. In addition, the large core density means that the electron gas component of the central plasma exists on the border of degeneracy. This has several consequences upon subsequent stellar evolution. Primarily the Schönberg-Chandrasekhar limit of the core becomes irrelevant, as the stellar core becomes degenerate before the limit is reached. As a result, contraction of the core is prevented. For stars of mass 1.0 $M_{\odot}$ - 2.3 $M_{\odot}$, the scenario is somewhat different. In these cases, the growth of the helium core may reach a point which exceeds the limiting mass fraction set by the Schönberg-Chandrasekhar limit. Once exceeded, the core begins to contract in order to provide the necessary temperature and pressure gradient needed to support the gravitational effect of the overlying layers. With the exception of this gravitational energy, no other energy sources exist within the core. Consequently, isothermal conditions become prevalent, with core temperature being solely dependent on the temperature of the surrounding hydrogen burning shell. It follows that the transitory period marking departure from the main sequence varies dramatically with stellar mass, with higher mass stars evolving much more rapidly than lower mass stars.

The events which follow become very complicated, with several readjustment and transition phases occurring during the remainder of the post-main sequence lifetime. Following gravitational contraction of the core, energy is carried away by means of electron conduction. This delays the increase in core temperature which would otherwise provide the suitable conditions for the ignition of helium through the triple-alpha process. A stage is eventually reached, however, when the core becomes sufficiently dense that

an increase in the temperature gradient of the surrounding hydrogen burning shell occurs. Consequently, a rapid increase in nuclear energy generation occurs, which leads to an increase in stellar luminosity and the effective expansion of the stellar envelope. The overall effect of expansion is observed as an increase in the opacity of the star's envelope to escaping radiation. The outcome is therefore a total readjustment in stellar structure, with a gradual transition from radiative energy transfer, to fully convective energy transfer in the outer layers. This is observed as a slight, but gradual movement to the upper right of the H-R diagram. During this readjustment phase, the outer convective layers begin to penetrate deeper and deeper into the interior of the star, eventually exposing a greater proportion of mass to convective motion. At this point, the star begins its evolution along the 'Ascending Giant branch'. As convection penetrates deeper into the star, a stage is encountered where the convective layer extends into a region that has previously become contaminated with the nuclear reaction products of partial hydrogen burning. It is known that the most abundant element in this region is hydrogen, but other elements of greater atomic mass also exist, most notably the isotopes of nitrogen and carbon, N^{14} and C^{13} respectively. The result of partial burning is that processed material is brought to the surface through convective motion. The process by which this occurs is known as the 'First Dredge-up'. During ascent of the giant branch, one further adjustment occurs, namely the interruption of the monotonic increase in its luminosity. This occurs as a consequence of the marriage between the hydrogen burning shell and the outer convective zone. The events which occur during this phase, lead to the formation of a marked discontinuity between the homogeneously mixed outer hydrogen-rich layers and the helium-rich layers below. Consequently, a reduction in stellar luminosity occurs, with a reversal in the direction of the evolutionary track.

As core helium is depleted, shell burning processes become dominant once again. At this point, the stellar core of carbon and oxygen is surrounded by a helium-burning shell and a hydrogen-burning shell. Fusion within the helium shell suppresses energy generation within the hydrogen-burning shell, leading to the cessation of hydrogen fusion processes. However, the consumption of helium within the helium-burning layer allows hydrogen fusion to resume. With no energy source, the helium-burning shell becomes degenerate as it contracts. The temperature increase caused by this contraction initiates 'Triple-α' burning reactions within the helium layer. However, the halt of contraction within the helium-burning shell is not enough to remove degeneracy. Consequently, a thermal runaway reaction occurs known as the 'Helium Flash.' This removes degeneracy within the helium shell, but also causes a large-scale expansion of the stellar envelope. The cycle then repeats in a process collectively known as the 'Thermal Pulses.' The duration of the thermally pulsing period depends upon the mass of the star, with a typical timescale of approximately 10^4 years for massive stars, and 10^5 years for lower mass stars.

Evolution along the AGB is divided into two distinct phases. The first of these phases occurs before the initiation of the thermal pulses and is designated as the 'Early-Asymptotic Giant Branch' (E-AGB). The second phase occurs much later and is characterised by the action of thermal pulsation. This second phase is

known as the 'Thermally Pulsing-Asymptotic Giant Branch' (TP-AGB) and plays an important role in the events leading to the formation of a PN. During evolution along the AGB, the star spends the majority of its lifetime in the E-AGB state and only experiences the TP-AGB for a relatively short period. The total duration of the AGB phase is of the order of 10^6 years, but is dependent upon the mass of the star when it joins the AGB (Iben & Renzini 1983). Towards the later stages of this rapid phase of evolution, stars develop additional pulsational instability due to changes in envelope structure. The onset of these pulsational phenomena marks the initial stages of a prolonged period of substantial mass loss, during what has become known as the 'Mira' phase.

1.3.2.2 INTERMEDIATE AND HIGH MASS STAR EVOLUTION

Unlike low mass stars, the situation involving intermediate and high mass is somewhat different. It is known that these stars have much higher central temperatures than those of lower mass. Consequently, nuclear energy generation occurs through the CNO cycle, which because of its higher temperature dependence compared with that of the p-p chain, leads to the formation of a fully convective core. The presence of a convective core means that the products of nuclear burning become well mixed. Consequently, core hydrogen fusion is relatively steady, but shows a dependency upon stellar mass. Following the depletion of core hydrogen, a phase of hydrogen shell burning begins. Furthermore, the core begins to contract in order to compensate for the deficit in energy production caused by a decrease in hydrogen abundance. During this phase, the central regions remain non-degenerate, since the initial central densities of higher mass stars are low in comparison to those found within low mass stars. As a result, a rapid increase in core heating follows, subsequently causing an ignition of helium fuel. At this point, rapid contraction of the core ceases and the star becomes capable of self support through its newly found energy source. Coincidentally, the outer envelope begins to display a rapid expansion, marking the termination of the main sequence. The entire process signifying the transformation of main sequence stars to red giants occurs very rapidly, as very few stars are observed at this stage of development. For this reason, the H-R diagram contains a portion known as the 'Hertzsprung gap,' which shows that the timescale over which these changes occur is of the order of several thousand years.

After joining the RGB, more massive stars follow a very different evolutionary path. Consequently, nuclear burning reactions continue beyond helium-burning, producing a core of carbon and oxygen. However, during the depletion of core helium, stars of intermediate and high mass begin to undergo pulsational instability. These stars make several crossings of the H-R diagram across a particular zone known as the 'instability strip.' At the point of helium exhaustion, core material is composed of C^{12}, O^{16} and Ne^{20}. The lack of core energy production leads to gravitational contraction and an increase in temperature. This increase in temperature ignites the helium shell surrounding the carbon/oxygen core. With the onset of

nuclear fusion within the helium shell, two shell sources then exist with an overlying hydrogen rich envelope. Following this stage, the convective envelope begins to penetrate into the stellar interior, such that a further episode of chemical enrichment occurs at the stellar surface. This 'Second Dredge-up' process allows further products of the CNO cycle to appear. For stars of intermediate mass between $3M_{\odot}$ - $7M_{\odot}$, it is believed that the carbon-oxygen core eventually becomes degenerate, leading to a similar event to the helium flash in lower mass stars. However, for massive stars, the situation is not so passive. Stars whose core mass never reaches the Chandrasekhar limit of $1.4M_{\odot}$ lose their hydrogen rich envelopes before degeneracy sets in. These stars leave the AGB and evolve towards the blue end of the H-R diagram, passing through to the PN phase experienced by all lower mass stars. However, stars whose core mass exceeds the Chandrasekhar limit experience degeneracy. When a temperature is reached to ignite material of the stellar core, an explosive detonation occurs known as 'carbon deflagration'. Shortly after, the star becomes visible as a supernova.

1.3.2.3 MASS LOSS DURING THE POST MAIN SEQUENCE

The exact rate at which mass is lost from the stellar envelope of RGB and AGB stars is still a matter of some debate. This remains as one of the ongoing problems which prevents a full understanding of the later stages of stellar evolution. Over the years, however, increased quality of observational data has allowed rapid convergence towards a more unified picture. Various models have been proposed to match observation, some of which achieve partial success, whilst others simply lack the required accuracy. The earliest reasonable models provided originality and new direction for generalised theory, but lacked sufficient accuracy to predict the observed rates of mass loss. The model put forth by Renzini (1981) showed that stellar mass loss followed an abrupt increase, from a steady rate, to a highly accelerated rate at the tip of the AGB. Later Baud & Habing (1983) postulated that the mass loss rate displayed a slowly increasing nature without the abrupt demarcation suggested by Renzini. Olofsson et al. (1990) described mass loss as being intermittent, thus providing a possible solution to the observation of multiple detached shells in some PNe. Perhaps the most consistent model to emerge, however, was that produced by Judge & Stencel (1991). Though it is inevitable that research will continue to provide improved theory upon stellar evolution, it will be some time before a clear picture is produced about the phenomenon of mass loss.

It is now known that PNe originate from the outer envelope of their progenitor red giant stars. The idea, first suggested by Shklovskii (1956), stated that the evolution of a typical nebula shell, when traced backwards, would resemble the tenuous atmosphere of the red giant from which it formed. Later Abell & Goldreich (1966) provided further support to this work, through the measurement of PN shell expansion velocities. The concept behind their work was to argue that the escape velocities of RGE material could account for the observed structure and expansion of the PN shells. It followed from further work, that PNe were

representative of a short-lived class of object, providing a transitory bridge between red giants and white dwarf stars. However, with the advancement of observing techniques and the accessibility of other wavebands, it was found that intermediary stages were present between the red giant and PN phase, specifically those encapsulating the AGB and proto-planetary nebula (PPN) phase (Pottasch 1992).

The term 'proto-planetary nebula' has become somewhat loosely defined as a class of objects which include AGB stars and young PNe. Consequently, it was agreed that the term should apply to stars which are in transition from the AGB to becoming a PN. The transitional period at the end of the AGB is believed to be very short and has been estimated to be of the order of 10^4 years (Vassiliadis & Wood 1993, 1994). During this short timescale, the fact that the PN becomes observable in the visible, means that the surface temperature of the central star changes from approximately 5000 K to more than 30000 K. However, it was conjectured that the evolutionary timescale of the central star would not necessarily coincide with the dynamical timescale of the nebula. It thus followed that the central star could evolve much more slowly or much more rapidly than the ejected nebula itself. In the case of slow stellar development, nebular material would disperse before the star's surface temperature could reach a level to produce ionization. Contrarily, if the central star developed rapidly, the nebular material would be illuminated only for a brief period before the star finished all nuclear burning and settled down to become a white dwarf. The difficulties posed by this problem were tackled by Paczynski (1970, 1971), who assumed that central star evolution was dependent upon the mass of the electron degenerate carbon-oxygen core. It followed that stars with low mass cores developed slowly, while those with higher mass cores developed very rapidly. Consequently, only stars possessing core masses within a very narrow mass range between 0.6 $M_\odot$ – 1.2 $M_\odot$ would become observable as PNe.

The fact that the period between the RGB and final PN is very short, implies that many properties of the progenitor star could be observed at more advanced stages of evolution. In particular, it was observed that the extensive circumstellar envelopes of giant stars were also observed in PNe. Many of the spectral features of red giants were thought to remain during the transition to PNe. This was found to be true, with the existence of the 9.7 μm spectral feature of silicate dust (Woolf & Ney 1969; Merrill & Stein 1976). Although commonly observed within the envelopes of oxygen-rich giant stars, a long period of time passed before it was finally discovered in a number of young PNe (Aitken et al. 1979). Surprisingly, observations revealed that most PNe possessed a dual dust component, comprising hot and cold grains (Telesco & Harper 1977; Moseley 1980). Consequently, it was proposed that grain formation could occur episodically. The cool dust component was believed to have originated when grains formed within the envelope of the red giant progenitor, and subsequently survived the various phases of mass loss. The hot dust component, however, originated when newly condensed grains formed after the production of the PN (Kwok 1980). Infrared observations of post-main sequence objects now provide useful information in the study of nebular

dust. These observations are now used as one of the primary means of identifying and classifying PPNe and young PNe.

A somewhat problematic area of study, however, is the observation that most PNe appear to be asymmetric, although the nebulae form from seemingly symmetric progenitor stars. It is known that interactions occur between the nebular envelope and the surrounding ISM, leading to morphological distortions from those normally observed. However, the true nature PN asymmetry seems to stem from a more fundamental level associated with the physics of the nebulae themselves.

1.4 THE EVOLUTIONARY EFFECTS OF STELLAR WIND PROCESSES

Although it became widely known that the progenitors of PNe were stars of the RGB and AGB population, the exact details regarding the transition between the two remained unclear for a long period of time. It is now known that considerable mass loss takes place while the progenitor evolves along the RGB and AGB. In doing so, RGB and AGB stars produce extensive circumstellar envelopes, often becoming invisible at optical wavelengths. Mass loss occurs through the action of radiation pressure upon dust grains which condense within the cool atmosphere of evolved stars. Consequently, dust grains transfer their momentum to the surrounding gas by means of dust-gas collisions, resulting in the eventual ejection of gaseous matter. The rate at which matter is lost is considerable, with values ranging from 10^{-7} - 10^{-4} $M_{\odot}$ yr^{-1}. The velocity with which material is pushed outward, however, is quite low, with typical values of 5 - 25 kms^{-1}. Later stages of evolution are marked by a change in the mass loss process, as matter is lost at a much lower rate, with values ranging from 10^{-9} - 10^{-7} $M_{\odot}$ yr^{-1}. At this point, mass ejection occurs as a consequence of the direct action of radiation pressure upon the gas, with velocities one or two orders of magnitude greater than those of the previous wind. It is now clear, however, that the red giant winds alone are incapability of producing the observed range in PN morphology.

To resolve this problem, many theories have been formulated. Most failed to provide reasonable explanation of the quantitative and qualitative aspects of the observations. It was not until the model of 'interacting stellar winds' was proposed by Kwok et al. (1978), (see also Weaver et al. 1977; Kwok 1982; Kahn 1983; Balick 1987; Balick et al. 1987; Icke et al. 1992; Aller 1993; Kwok 1994; Frank 1994; Frank & Mellema 1994; Mellema & Frank 1995; Dwarkadas et al. 1996) that the process of PN formation from RGB stars was finally realised. Now considered to be the most widely accepted scenario for the formation and evolution of PN, the general hypothesis of the model is that PNe are formed through the interaction of two stellar wind phases. The initial 'slow wind', originating from the RGB and AGB star, acts to produce a massive red giant envelope (RGE) which expands outward into the surrounding interstellar medium (ISM). Later, a second episode of stellar wind mass loss is initiated, marking the beginning of the 'fast wind' which emanates from the post-AGB planetary nebula nucleus (PNN). This second wind occurs at a much higher velocity, although the amount of material which is carried by the fast wind is very small in comparison to the earlier episode of mass loss. Consequently, the fast wind reaches the inner boundary of the slow wind and begins to sweep up material of the remnant RGE in a snowplough effect. Consequently, a high density shell is formed at the interface between the two winds. One of the attractive features of the ISW model is that it assumes no physical process which has not been observed. Furthermore, it offers definite predictions for comparison with observations. In addition to providing details of the transition from red giant to fully ionized PN, the ISW model has also been used to describe various processes which occur during the shaping of PNe.

The ISW model has displayed great success in providing a clear picture for the formation of spherical PNe and now provides a concise account of the many observational characteristics which they possess (Schmidt-Voigt & Koppen 1987; Marten & Schönberner 1991; Mellema 1994, 1995). However, the number of PN which are observed to possess spherical morphology is known to be small. The majority are observed to display a variety of more complex morphologies based upon the elliptical and bipolar forms, described by Balick (1987). Under this scheme, it is suggested that the different forms of PNe may be described by ISW theory, if mechanisms are included for the ejection of the RGE. The general consensus is that elliptical and bipolar nebulae are formed as a result of increased mass loss in the equatorial plane of the star. Subsequent morphology and evolution of PNe is then described by the interaction of equatorial material with the 'fast' stellar wind. However, the exact mechanism behind the causality of differing asphericity within the RGE remains unclear.

Before stellar winds were recognised to be of importance in PN formation, attempts to identify the mechanism for the transition of RGB stars into PNe focussed upon large-scale envelope instabilities. These instabilities were suggested to operate during a very brief phase of the transition. Under the circumstances proposed by the theory, ejection of the RGE was suggested to occur suddenly. However, it was later realised that a sudden envelope ejection could not explain the quantitative aspects of observation. It is now accepted, that mass loss through the action of stellar winds provides the chief governing factor determining the transition process which occurs between the RGB and PNe.

It is now known that mass loss upon the AGB occurs in two distinct phases. First proposed by Renzini (1981), it was suggested that two separate wind processes could occur during evolution upon the AGB and that this could be used to explain the ejection mechanism for the RGE. The first episode of mass loss is identified with the formation of a classical Mira-type variable star. The rate of mass loss which occurs during this phase is relatively moderate and ranges from 10^{-8} – 10^{-6} $M_{\odot}yr^{-1}$. This 'normal wind' features predominantly over the duration of the AGB, but a dramatic change is observed during the late stages of the AGB. When this stage is encountered, it is observed that the rate of mass loss increases dramatically, with typical values in the range 10^{-5} - 10^{-4} $M_{\odot}yr^{-1}$ (Bowen & Willson 1991). The second episode of mass loss, termed the 'superwind' phase, is identified with the formation of an OH/IR star and is signified by a change in the internal structure of the star. The appreciable increase in the rate of mass loss means that the star becomes enshrouded in a thick circumstellar envelope, which because of its high dust content and high density, becomes optically thick. For this reason, extinction in the optical spectrum becomes significant and the object features predominantly in the IR.

Hydrodynamical modelling of the AGB stellar envelope during the transitional period, between the cessation of the 'normal wind' and the onset of the 'superwind', suggests that the superwind phase is triggered by the modal transformation in the pulsation of the star. Theoretical studies of AGB pulsation

point towards a change from overtone pulsation to fundamental pulsation, which occurs through a series of discrete ejections repeated over several pulsation periods (Tuchman et al. 1979; Wood 1974). Observational evidence indicates that Mira-type stars possess overtone pulsations and that OH/IR stars possess fundamental pulsation modes, further strengthening the link between Mira and OH/IR star evolution. However, the pulsation mode of Mira-type variables has not yet been unambiguously confirmed to be that of an overtone mode, as it has been conjectured that they could be fundamental pulsators (Hill & Willson 1979). This has led to further controversy over the exact production mechanism of the superwind. Without doubt, however, the identification of the exact pulsation mode of Miras bears strongly upon the physical nature of the superwind and its understanding. The timescale over which ejection of the RGE occurs, is calculated to be extremely short, and is estimated to be of the order of 10^4 years. The exact duration of the ejection period, however, displays a large dependence on the mass of the progenitor star, being shorter for stars of higher mass. Subsequent evolution of the AGB star after cessation of the superwind phase shows that the mass loss rate decreases and becomes stable once again around 10^{-8} - 10^{-6} $M_{\odot}yr^{-1}$. It also shows that a change in the stellar wind velocity occurs with an increase of a few orders of magnitude.

Evidence now exists to suggest that additional phenomena occur in the formation of PNe. Almost all models of nebula shaping now include the effects of stellar rotation, magnetic fields and interaction with the interstellar medium (ISM). Early modelling of stellar rotation effects upon the ejection of the RGE conjectured that it was possible for a single star to produce the levels of asphericity needed for the formation of the majority of PN morphologies. Although it appears that the distribution of material within many nebulae points towards an association between stellar rotation and mass loss though stellar wind processes, it now seems likely that this is not entirely true. Evidence now suggests that the observed asymmetry of PNe can be explained by the inclusions of supplementary shaping mechanisms.

Recent modelling of the processes shaping bipolar and elliptical PNe by Garcia-Segura et al. (1999) has led to the proposal that both stellar rotation and magnetic fields play an important role in the shaping processes from single stars. Not only do the asymmetries within the stellar wind of the AGB star play a key role, but so too do magnetic field phenomena (Pascoli et al. 1992; Chevalier & Luo 1994). The recent results show that the inclusion of strong magnetic field effects within the existing models of the AGB winds leads to the strong collimation effects which act to produce PNe of predominant bipolar morphology. Inclusion of weaker magnetic field effects have shown the resulting collimation effects lead to the production of PNe with a range of elliptical morphologies.

In addition to its description of the 'macroscopic' structure of PNe, the theory of interacting stellar winds has been employed to describe many of the 'microstructures' which are present within PNe. Some of the most striking microstructures include the 'ansae' and collimated jet-like outflows. Although these phenomena appear to be common in compact PNe, the presence of jets and ansae within larger PNe, such as elliptical, is

less frequently observed. Using ISW theory Frank et al. (1996) proposed that jets and ansae could form inside elliptical PNe through the development of a wind-blown bubble, driven by the interacting stellar wind.

It was recognised that the transitional change in wind character from slow to fast should occur over a period of time, leading to a gradual increase in velocity to a maximum of the order of 10^3 kms^{-1}. During the early proto-planetary nebula (PPN) phase, the wind velocity would be sufficiently low to allow the formation of streams of cool gas. However, the formation of jet and ansae structures is proposed to occur only through the action of the preceding aspherical slow wind. Modelling of the slow wind has shown that an equatorial-polar density contrast would ensue, producing a prolate profile for shocked material at the boundary between the fast and slow wind components. This would then act as a 'refractive' interface to channel streamlined gas into a converging conical flow. The intersection of the gas flows at the tip of the prolate bubble would then collide, producing a further shock which would channel material into the observed jets and ansae. Recent studies, however, have shown that shear-induced instabilities along the cavity walls of the wind blown bubbles, would act to effectively disrupt the convergence of any streamlined gas flows. This would then imply that the frequency of observed knots and jet-like features could not be adequately explained through the application of ISW theory.

During the observational study of PNe, it became apparent that many nebulae displayed multiple-shell structure, prompting a rise in the number of models to explain their origin. Although many morphologies have now been observed in the classification of multiple-shell planetary nebulae (MSPN), their initial classification was far from simple due to lack of understanding. Simplification came when Kaler (1974) developed a scheme which laid down a solid base from which all other development could take place. The scheme described the archetypal MSPN as being one in which an outer shell or halo and an inner shell could be observed. The outer shell forms a regular ring surrounding at least half of the inner shell, and displays a discontinuity in surface brightness at the boundary with the inner shell, producing the appearance of a double shell structure. Given the various morphological and kinematic structure of the shells, the obvious explanation for the production process became that of wind driven mass loss. The models proposed by Kwok et al. (1978) and Renzini (1981) now provide evidence for the majority of structural formations which exist within these objects. However, the more complicated morphologies have been more difficult to explain and have led to the remaining question as to their exact origin. Gurzadyan (1996) proposed that the multiple shells of PNe could be described by the effects of radiation pressure. However, it is now accepted that the ISW model provides a suitable explanation, once the morphology and kinematics of the shells have been shown to be quantitatively consistent with the model predictions. Those nebulae possessing 'co-expanding envelope' structures have been more difficult to explain, since the outer shell does not appear to interact with the inner shell in the same way as displayed by the other MSPNe. One suggestion to explain the lack of interaction between the shells is that an abrupt change may occur in the mass loss rate during the superwind

phase of the slow wind. However, MSPNe containing two or more independently expanding shells cannot be explained with the theory of interacting winds alone, but evidence has shown that these objects may have formed through the interaction of a binary PNN.

1.5 THE EVOLUTIONARY CONSEQUENCES OF STELLAR BINARITY

The physical processes leading to the bipolar appearance of many PNe are now believed to be associated with asymmetric mass ejection from the progenitor star during the AGB and early PPN phases. Theoretical studies have shown that mass loss alone is unable to provide adequate explanation for the exact physical processes which dictate nebula shaping. The most plausible mechanism for the shaping process is that of mass loss which occurs through the interaction of a close binary star system (Morris 1981). The frequency of such binary systems throughout the galaxy indicates that their presence must play a significant role in the formation of PNe. Within the theoretical framework of binary star evolution, PN morphology may be understood by the orbital characteristics of the binary system and by the evolutionary status of the primary star (See Bond & Livio 1990; Morris 1987). The general picture of binary systems which produce PNe, is that of an evolved mass losing primary star and a main sequence dwarf star, both of which exist in the presence of either a detached (non-interactive) or common (interactive) envelope configuration. Formation of a particular type of PN depends upon the exact nature of the binary, since theoretical modelling has suggested that several variations in the evolution of the system may exist (Soker 1997). Under the circumstances encountered in wide binary systems, only minor evolutionary developments occur, although close binary systems show more pronounced effects upon the final appearance of the PN.

The majority of PNe which possess close binary nuclei occur as a result of nebular ejection after common envelope (CE) evolution. Although the accepted model for CE evolution implies that matter outflow from the primary occurs preferentially in the equatorial (orbital) plane, it remains unclear whether the mechanism is capable of producing the required degree of envelope asymmetry observed in many PNe. Theoretical modelling of PN shaping mechanisms therefore requires a greater understanding of nebula formation through single star and binary star evolution. Several models produced in recent years have attempted to explain PN shaping through asymmetric mass loss upon the AGB and post-AGB. Those found to provide the most favourable explanation for stellar wind shaping are based upon non-radial stellar pulsation, stellar rotation, and magnetic field compression. Although very different in approach, the underlying processes involved possess a general commonality. For stellar rotation models, the velocity needed to create asymmetric mass loss is extremely high and could only be achieved by the presence of a binary nucleus which would act to 'spin-up' the more massive primary star. For magnetic field compression models, the need for binarity would again hold relevance in order to produce sufficient dynamo effect from stellar rotation. Models based upon the existence of non-radial pulsation, however, could be explained in several ways, but pulsational excitation could theoretically be induced by the presence of a binary companion in the common envelope of an AGB star.

Work carried out on the influence of binary star interaction upon PNe formation has been done so with relation to systems possessing a highly interactive nature. It is likely, however, that a number of binary

systems show little interaction and contain stellar components of wide separation (Soker 1994). Observations of PNe thought to contain this type of binary system appear to show displacement of the primary from the centre of ejection, suggesting that some tidal interaction occurs from the secondary. Argument still exists as to whether this could be the true mechanism for primary star displacement within PNe. Evidence suggests that the apparent offset of a PNN from its central position could occur as a result of motion of its associated nebula through the ISM. Most PNe are believed to contain close binary nuclei in which mass loss occurs through the effects of gravitational interaction between the primary and secondary stars. Two distinct evolutionary paths exist which correspond to the two classes of non-spherical (i.e. elliptical and bipolar) PNe described by Balick et al. (1987). The first class of PN binary nuclei to be defined are those containing close binary systems which avoid interaction for a large part of their evolution during the CE phase. In general, these binary systems only experience a CE phase after a substantial degree of mass loss. The process of mass loss encountered is due to accretion from the primary by the gravitational interaction of the secondary. Consequently, a preferential ejection of matter occurs in the equatorial plane of the system. The second class of PN binary nuclei defined are those which experience a prolonged CE phase. The close proximity of the stars in these systems implies that the secondary becomes engulfed by the primary's envelope during Roche-lobe overflow (Iben & Livio 1993). Shaping of the ensuing PN depends mainly upon the evolutionary stage of the primary during inclusion of the secondary star within the common envelope, but also upon the orbital characteristics of the system during initiation of the CE phase. If the spiralling-in process occurs whilst the primary is still evolving along the RGB then ejection of the envelope results in a high density contrast and the production of a bipolar-like PN. If the spiralling-in process occurs during development of the primary upon the AGB, however, then a moderate density contrast results, producing an elliptical PN.

In most cases the binary nature of the PNN is not apparent, since the stars are obscured from direct view by the presence of circumstellar gas and dust. A number of PNe, however, show unusual features such as point-symmetric phenomena, jets, and ansae. Explanation for their existence comes from the presence of a binary PNN (See Corradi, Schwarz, & Stanghellini 1993, and Soker & Livio 1994). This acts to perturb the rotational axis of the star whose collimated beam produces excitation of gaseous material. The production mechanism for these structures still remains somewhat unclear, as modelling has shown that problems still remain. Although much evidence has been gathered, the exact role binary nuclei play in PN evolution remains unclear. Undoubtedly, binary systems play a key role in the formation and shaping of PNe, particularly those possessing non-spherical morphology. In recent years, however, observations using IR imaging and adaptive optics programs have captured images of a number of binary systems, providing the possibility to develop an increased understanding of their significance (Roddier et al.1995).

1.6 SUMMARY

The observed characteristics and accepted origins of PNe have been reviewed and summarised in this chapter, with the aim of providing a general picture of their integration into the framework of stellar evolutionary theory. Much remains to be understood about the physical processes which govern the formation and shaping of these objects. However, the advent of new observing methods and new technologies means that many of the theoretical difficulties which have been highlighted, will in future be overcome. Without doubt, mass loss plays a key role in promoting the transition from Red Giant to PN and it is now clear that stars begin to lose mass well before reaching the PN phase. Much work is still required to provide adequate quantitative and qualitative description of the full range of physical processes which act during the short evolutionary period leading to the fully developed PN.

From a polarimetric perspective, the most interesting phase of PN evolution appears to occur between the tip of the AGB and formation of a fully ionized PN. During this stage, the progenitor star is enshrouded by the products of earlier mass loss. Radiative transfer and hydrodynamical theories now account for the great number of morphological forms of PNe and now provide rudimentary models to match their structure. The physics of the processes described by these theories are just coming to light, as new data begins to provide increasing levels of constraint against which more sophisticated models may be developed. It is here that optical polarimetry can be applied as a powerful diagnostic and analytical tool, providing a means of analysing the immediate circumstellar environments of nebulae, thereby revealing information which other observing techniques are unable to do. These particular methods of study allow subtle refinements to be made within the theories of mass loss and interaction of PNe with the ISM.

It is now known that many PNe contain large quantities of dust. Analysis of the spectral energy distribution and internal extinction measure of nebulae allows the properties of this dust to be determined. Polarimetry also provides a prime means of studying dust grains and has already been used successfully to determine their properties and distribution within nebulae and the ISM alike. Relating the study of dust to the environments both in and around PPNe and PNe has led to a greater understanding of the process of nucleosynthesis, grain formation, and enrichment of the ISM. In addition to the study of young, dust rich PNe, more evolved PNe have also been observed. These objects show interesting structural phenomena in the form of jets, ansae, and fast, low ionization emission regions (FLIERS). Optical polarimetry provides an effective means of investigation into the true nature of the light which emanates from these structures and is thus of major importance in the study of PNe. From these studies, a picture may be constructed to determine the mechanisms and geometry under which polarized light is produced. Polarimetry thus provides a means of differentiating the various conditions which prevail in PNe.

The following chapter includes a discussion of polarization phenomena and the mechanisms by which they are produced. A description of the basic reduction and analysis procedure is also included, with additional details of data interpretation.

CHAPTER 2

INTRODUCTION TO POLARIZATION

2.1 INTRODUCTION

The nature of astronomical observation means that every possible wavelength range is exploited. Together with theoretical development, these observations allow an interpretation of the physics that apply to many astronomical objects. One area which has gained success in complementing observational data is that of polarization. The field of polarimetry has undergone much advancement since its initial development and has increased our understanding of many phenomena which occur in the extremes of astronomy. An exceptional observing technique, polarimetry has become appealing for its ability to yield information which other techniques fail to provide. In the early stages of development, however, it became synonymous with the notoriety of providing inaccurate results. However, the introduction of modern electronic detectors and sophisticated computer analysis techniques has turned polarimetry around.

2.1.1 THE USE OF POLARIMETRY IN THE STUDY OF PLANETARY NEBULAE

Since its initial development, polarimetry has shown extensive application. Its use in the study of astronomical objects has led to an increase in knowledge which spans distances ranging over several orders of magnitude. Polarimetric studies range from observation of the solar system planets, out to the most distant radio galaxies. In particular, it has shown great promise in the study of PNe.

Objects having been analysed with polarimetry include those undergoing a transition from red giant to planetary nebula. These objects are generally referred to as 'proto-planetary nebulae' (PPNe), Although these objects possess high surface brightness, they possess small angular dimensions which means that they are often excluded from observational surveys. The majority of objects which are observed are more evolved and thus possess larger angular dimensions. These objects are generally referred to as 'planetary nebulae' (PNe). Most PNe, especially those which are morphologically evolved, possess moderately low levels of polarization, although certain objects show extremely high levels of polarization (See Johnson & Jones 1991; Trammell et al. 1994 for a basic review of the use of polarimetry in the study of AGB and post-AGB objects). Both PPNe and PNe are associated with copious amounts of dust. The formation of this dust is believed to occur within the cool atmosphere of the progenitor star. The association with dust often implies that the central star of young PNe is generally obscured from direct view. Consequently, dust is able to exist freely without the likelihood of destruction through the action of radiation or wind driven shocks. Following subsequent evolution, however, the amount of dust appears to fall as shock phenomena and radiation pressure begin to take effect.

Objects which have received particular interest by the Durham polarimetry group include the maser emission star OH 231.8+4.2, believed to be in the process of becoming a PPN. The selection of PPNe includes IRAS 09371+1212 'Frosty Leo nebula', Roberts 22, and Henize 401. All show high levels of polarization typical of the presence of moderate sized dust grains. Objects of young to intermediate age, the young PNe, include IRAS 07131–0147, Mz3, and M2-9, the latter of which is studied in this thesis. More evolved PNe include NGC2346, NGC2440, NGC2818, IC4406, and J320. Of these, NGC2440 and NGC2818 are discussed later in this thesis. These objects tend to display lower levels of polarized emission typical of dilution by hot emission line gas and lower levels of dust content.

It is clear that these studies provide a great deal of information about the later stages of stellar evolution, for PPNe and PNe alike. It is evident that dust plays a major role in the physical characteristics of these objects and marks each individual nebula with its own characteristic polarimetric signature.

2.2 THE MATHEMATICAL ASPECTS OF POLARIZATION THEORY

The classical representation of light is now well established in the arena of modern science. Like sound, light is classically described as a wave-like phenomenon. However, unlike sound which possesses the attributes of a scalar quantity, light possesses the attributes of a vector quantity. It is this quality which allows transverse light waves to experience many phenomena, including polarization. The nature of light means that its description becomes considerably more complicated than that of sound, requiring the employment of an increased number of parameters. The exact parameters used in this description, however, depend solely upon the theoretical application and the conventions used therein.

It is now known that light is composed of electromagnetic waves and is described by the mathematical equations derived by Maxwell. These equations show that electromagnetic radiation is composed of an oscillating electric and magnetic field, both mutually perpendicular to one another and perpendicular to the direction of propagation.

For a time dependent oscillating field, Maxwell's equations may be written as follows (Bohren & Huffman 1983):

$$\nabla \bullet (\varepsilon E) = 0 \qquad \textbf{(2.1)}$$

$$\nabla \times E = i\omega\mu H \qquad \textbf{(2.2)}$$

$$\nabla \bullet H = 0 \qquad \textbf{(2.3)}$$

$$\nabla \times H = -i\omega\varepsilon E \qquad \textbf{(2.4)}$$

Here $\boldsymbol{E}$ and $\boldsymbol{H}$ represent the electric field strength and magnetic field strength respectively. The constants μ and ε represent the permeability and permittivity of the medium through which the wave is propagating. ω represents the angular frequency of the oscillating wave.

A monochromatic time dependent oscillating wave which satisfies these equations can then be described by:

$$E = \mathrm{Re}\{(A + iB)\exp(ikz - i\omega t)\} = A\cos(kz - \omega t) - B\sin(kz - \omega t) \qquad \textbf{(2.5)}$$

Here $\boldsymbol{A}$ and $\boldsymbol{B}$ represent the amplitude of the electric field vector. Visual analysis of this wave function in a particular plane (e.g. z = 0) shows that the electric field vector describes a curved path which is given by:

$$E_{z=0} = A\cos\omega t + B\sin\omega t \qquad \textbf{(2.6)}$$

This equation has the form of an ellipse and is generally described as the 'vibrational ellipse'. Solution to this equation leads to the various states of polarization. Although elliptical polarization is the most general form, linear and circular polarization form special cases. For linear polarization, the vibrational ellipse simplifies to a straight line, thus leading to zero magnitude for either of the electric field vector amplitudes (i.e. an axis ratio = 0). However, for circular polarization, the magnitude of the electric field vector amplitudes become equal and the axis ratio then becomes unity.

In the natural environment its interpretation becomes more complicated since it then possesses a polychromatic character. In this case light consists of a superposition of many waves, all possessing a quasi-monochromatic character. Each of these waves possess a small range in frequency, with similar amplitude and phase characteristics. With no stable phase relation between the electromagnetic field over the frequency range, light consequently becomes incoherent.

Under the terminology of polarization theory, the chief element of light which quantifies the exact state and nature of the observed polarization is the electric field vector. By convention, the electric field vector is used to describe the magnitude, direction, and state of polarization, with the scalar elements of frequency, amplitude and phase playing only minor roles in the mathematical description. Under conditions in which the electric field vector of each constituent elementary wave is randomly orientated, light is described as being 'unpolarized'. However, if conditions govern that the electric field vector of constituent elementary waves displays a preference for a particular plane, then light is said to be 'plane polarized' or 'linearly polarized.'

Although the concept of polarization may be simple, and its description in terms of certain properties of the vibrational ellipse relatively straightforward, its visualization in terms of ellipsometric parameters is not. In order to understand and visualize the individual components (i.e. scattered, reflected, and absorbed) of a polarized wave train, analysis of the ellipsometric parameters must be simplified. The matter was resolved when Sir George Stokes constructed a set of alternative parameters. Although these parameters are also difficult to visualize (even more so than the ellipsometric parameters), they possess the advantage of describing quantities which are easily measured. All quantities defined by the Stokes parameters are based upon intensities, unlike those defined by ellipsometric parameters. The exact specification of Stokes parameters implies that the determination of properties such as intensity, degree of polarization, and the plane of polarization may be carried out with ease. Definition of the Stokes' Parameters can occur in a number of ways. Use of both real trigonometric wave functions and complex exponential functions allows different aspects of the light wave to be exploited. Following the work of (Van de Hulst 1957; Chandrasekhar 1960; Bohren & Huffman 1983), it is usual to consider a right-handed co-ordinate system in which a monochromatic light beam is travelling in the positive z direction. The complex functions describing the electric field components of the wave are then:

$$E_x = a_x \exp(i\varepsilon_1)\exp(-ikz + i\omega t) \quad \textbf{(2.7)}$$

$$E_y = a_y \exp(i\varepsilon_2)\exp(-ikz + i\omega t) \quad \textbf{(2.8)}$$

Here a_x and a_y are non-negative quantities which represent the amplitudes of the wave components. Both ε_1 and ε_2 are constants which incorporate the phase relations of the wave components. The quantity k represents the wave number and is equal to $2\pi/\lambda$. The quantity λ is the wavelength of the wave. In this definition, the Stokes parameters then become:

$$I = E_x E_x^* + E_y E_y^* \quad \textbf{(2.9)}$$

$$Q = E_x E_x^* - E_y E_y^* \quad \textbf{(2.10)}$$

$$U = E_x E_y + E_y^* E_x^* \quad \textbf{(2.11)}$$

$$V = I(E_x E_y^* - E_y E_x^*) \quad \textbf{(2.12)}$$

Here, ***I*** represents the total intensity received by the detector system, ***Q*** and ***U*** represent the linear polarization state, and ***V*** represents the circular polarization state. The inclusion of an asterisk in the above descriptions denotes the use of the complex conjugate. Substitution of equations 2.7 and 2.8 into these equations thus leads to the following:

$$I = a_x^2 + a_y^2 \quad \textbf{(2.13)}$$

$$Q = a_x^2 - a_y^2 \quad \textbf{(2.14)}$$

$$U = 2a_x a_y \cos(\varepsilon_1 - \varepsilon_2) \quad \textbf{(2.15)}$$

$$V = 2a_x a_y \sin(\varepsilon_1 - \varepsilon_2) \quad \textbf{(2.16)}$$

Here $a_x^2 + a_y^2 = a^2$ and equals the specific intensity of the beam.

In terms of physically measurable quantities, the Stokes parameters simply become the relative differences of intensity with known phase relations:

$$I = I_0 + I_{90} \quad \textbf{(2.18)}$$

$$Q = I_0 - I_{90} \quad \textbf{(2.19)}$$

$$U = I_{45} - I_{135} \tag{2.20}$$

$$V = I_{RC} - I_{LC} \tag{2.21}$$

Here I_{RC} is the intensity from the right-handed component of circularly polarized light, whilst I_{LC} is the intensity of the left-handed component of circularly polarized light.

Since light from astronomical sources is polychromatic, the wave function amplitudes and phase relations then become time dependent so that time averages become necessary. In cases where 100 % polarization exists:

$$I^2 = Q^2 + U^2 + V^2 \tag{2.22}$$

However, this is rarely encountered. In most cases, astronomical objects display little or no levels of polarization. In cases which are unpolarized, this means that $Q = U = V = 0$. However, in the case of partial plane polarization:

$$I^2 \geq Q^2 + U^2 + V^2 \tag{2.23}$$

This then leads on to the concept of polarization possessing both magnitude and direction. The degree of polarization for a source which is linearly polarized, is given by:

$$P(\%) = \sqrt{\frac{(Q^2 + U^2)}{I}} \times 100 \tag{2.24}$$

The degree of polarization which is circularly polarized is given by:

$$P_{CIRC}(\%) = \frac{V}{I} \times 100 \tag{2.25}$$

The direction, or position angle of polarization, which determines the plane in which the electric field vector of the light source is confined, is derived by:

$$Tan2\theta = \frac{U}{Q} \tag{2.26}$$

Here θ describes the angle the polarization vector (i.e. the electric field vector) makes with some reference direction on the sky, usually taken to be North. The angle is measured anti-clockwise from this point, through East.

The four values which describe the Stokes parameters, collectively form the Stokes vector. Any change which appears in the state of polarization following interaction of the incident light beam with some external agent, is also accompanied by a similar change in the Stokes vector. Transformations which occur within the Stokes vector are successfully described using matrix theory. Both R.C.Jones and H.Mueller calculated precise solutions to the problem through the use of different, but complementary methods of matrix manipulation. In most analyses of polarization transformations, the use of Mueller matrices is sufficient to describe all aspects of the incident and transmitted light beams (Mueller 1948). However, certain cases arise in which phase information becomes important. In these cases, the use of Jones matrices provides more meaningful description (Jones 1941). For an introduction to the derivation and application of the Stokes' vector, Mueller matrices, and Jones matrices, the reader is referred to (Hecht 1998; Born & Wolf 1964; Tinbergen 1996). For a more detailed and rigorous description of these topics, accounts may be found in (Huard 1997; Kliger et al. 1990; Shurcliff 1962).

2.3 MEASUREMENT OF POLARIZATION

Determination of the Stokes parameters is based upon the measurement of brightness modulations or intensity ratios, depending on the configuration of the measuring system. In order to do this, polarimeters make use of a phenomenon known as 'Birefringence'. This property is inherent to particular crystals and makes them sensitive to the plane of vibration of the incident radiation. Upon passing through a polarimeter, light passes through a modulator or retarder. This distinguishes between orthogonal vibrations of electromagnetic waves and introduces a phase difference between them, resulting in a net rotation of the plane of polarization. The emergent beam is then separated into its constituent 'ordinary' and 'extraordinary' components by passing through an analysing Wollaston prism.

The first documented use of a polarimeter is by Arago, who in 1811 observed changes in the state of polarization corresponding to the changing phases of the moon (Dougherty & Dollfus 1989). Since this humble beginning, the design and use of the astronomical polarimeter has become much more elaborate, with many designs and applications in use today. One of the classic designs still in use today is that based around the use of the half-wave plate/Wollaston prism combination. Unlike polarimeter designs based upon the rapid modulation of signal through the constant rotation of the retardation plate, the half-wave plate/Wollaston prism design works by exact movement of the retardation plate. This system is adopted in the Durham Imaging Polarimeter and is based upon the concepts first proposed by Pickering (1873) and Ohman (1939).

2.3.1 THE DURHAM IMAGING POLARIMETER

Although relatively simple in its design, the Durham Imaging Polarimeter is a very efficient instrument. Figures 2.1 and 2.2 show the optical layout of the instrument in both its standard configuration and recently modified configuration. It can be seen that modification enables the system to measure both linear and circular polarization. In operation, light beams enters the instrument through a grid mask and are subsequently reduced in width by means of a field lens. Having been reduced, the light then passes through a super-achromatic half-wave plate, and in doing so, experiences a known phase shift between the components parallel and perpendicular to the half-wave plate optical axis. The plane of polarization is then rotated by 2θ degrees, where θ is the position angle of the path of the incident light. After its passage through the half-wave plate, the light beam passes through the Wollaston prism, whereupon it is split into two mutually

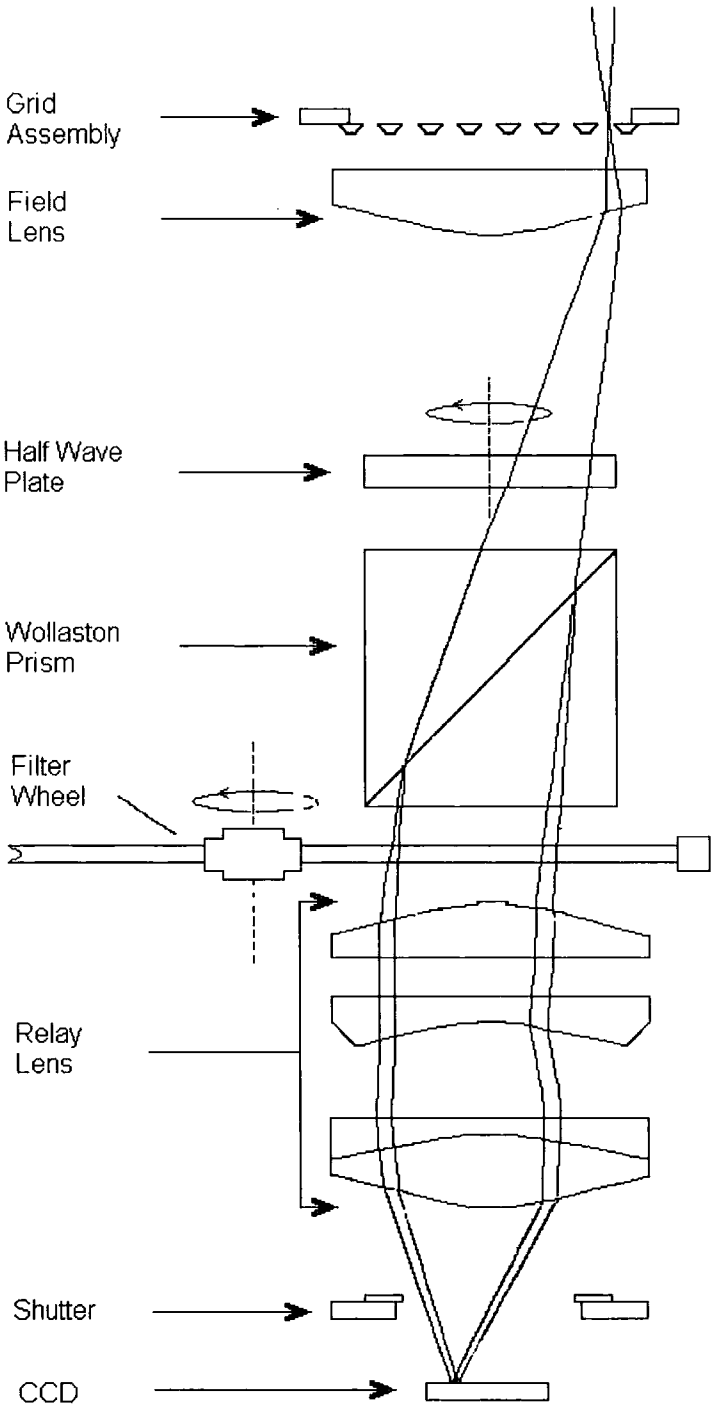

Figure 2.1: Unmodified Imaging Polarimeter for the collection of linearly polarized light only.

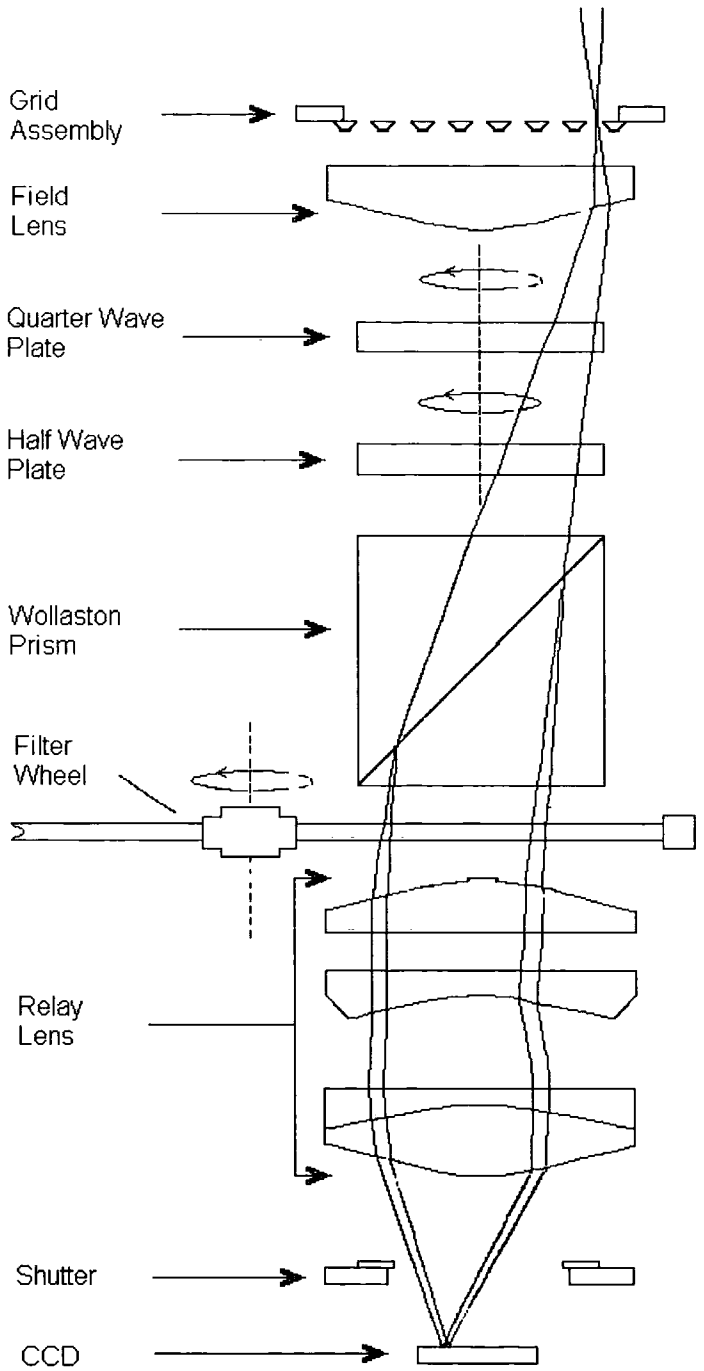

Figure 2.2 Modified Imaging Polarimeter for the collection of linearly and circularly polarized light.

perpendicular polarized beams corresponding to the o and e rays. The two rays then diverge and are subsequently focussed as two images by the relay lens upon the CCD.

Recent modification of the polarimeter has added a further important component to the optical layout. This is the quarter-wave plate. The quarter-wave plate is situated between the field lens and half-wave plate, and assumes only two positions. Unlike the half-wave plate which rotates between 0°, 22.5°, 45°, and 67.5°, the quarter-wave plate only rotates between 0° and 90°. The inclusion of the quarter-wave plate results in a transformation of circularly polarized light into linearly polarized light, which then passes through the half-wave plate before being analysed.

In addition to the primary components of the optical system described above, the polarimeter also incorporates further components to enhance its application. These components include a filter wheel and a grid mask. The filter wheel allows multi-wavelength observations to be gathered, whilst the precisely engineered grid mask accounts for the negligible image overlap. This ensures that alternate strips of the telescope image are blocked from view of the detector, thereby eliminating interference from these parts of the image. All operations of the mobile polarimeter components and CCD detector are controlled by means of computer control through the interface of dedicated control hardware. Full details of the Durham polarimeters' operations can be found in (Scarrott et al. 1983; Scarrott 1991; Stockdale 1996; Warren-Smith 1979), whilst details of the components and their characteristics are given by (Draper 1988).

2.4 POLARIMETRIC OBSERVATIONS

The optical polarimetric results discussed in this thesis are based upon the observations of bipolar PNe belonging to Peimbert's type I PNe. The objects included in the discussion were carefully selected on a number of criteria. Based upon objects contained within the ESO catalogue of PNe, the practical selection criteria include positional observability dependent upon the observing period, sufficient angular dimension giving adequate image resolution, and sufficient surface brightness giving adequate signal-to-noise. Other criteria used, however, were selected with the objective of providing an evolutionary link between objects in terms of the polarimetric aspects of observations. These include central star properties, angular size and expansion velocities of the surrounding nebula material, and abundance and excitation state of the elemental products contained within the nebular material. The total number of bipolar PNe included in this thesis is only three, namely M2-9, NGC 2440, and NGC2818. However, the total sample of potential sources fitting the selection criteria, numbered 10 objects. Although this would have obviously provided a greater sample for the arguments of this thesis, time constraint and observability issues prevented data collection for these additional sources.

All polarimetric data gathered upon the bipolar PNe included in this thesis were collected using the Durham Imaging Polarimeter in conjunction with the 1.9m SAAO telescope in South Africa. However, previous data pertaining to M2-9 have been gathered using the 3.9m Anglo-Australian telescope (AAT) in Siding Springs, Australia. These data are re-analysed and compared to the most recently gathered data. Full observational details are given in the results chapters.

2.5 REDUCTION, ANALYSIS, AND INTERPRETATION OF POLARIZATION DATA

Reduction of data gathered with the Durham Imaging Polarimeter has been previously described in detail elsewhere (Draper 1988; Warren-Smith 1979). However, a brief summary describing the rudiments of the process will be covered here to provide a general picture of the overall data collection, reduction, and analysis process.

Initially, processing of the raw CCD frames involves correct frame orientation. This is usually done by means of a comparison with electronic sky survey data. CCD frames are then corrected for large- and small-scale structural changes across the detector. Correction involves the use of flatfield frames gathered during the same observing programme. Both sky and dome flatfields possess corresponding wavelength profiles to the object frames, thus allowing accurate removal of spurious effects. Corrected object frames are then aligned between the left- and right-hand polarimeter channels and are subsequently corrected for any polarized sky signal through the process of sky subtraction. Finally, the frames are calibrated to eliminate any systematic errors produced by the polarimeter and changes which occur in sky transparency.

Polarization data are then extracted from the calibrated object frames and subsequently checked for quality and consistency. However, several systematic errors can occur which can not be corrected through the use of automated error checking. These include inefficient flatfield correction, inadequate frame normalization, and the manifestation of extraneous scattered light. Of particular note are image normalization and extraneous light sources. The occurrence of image normalization errors arise, in part, from the large dynamical data range possessed by certain astronomical objects. Errors of this type also occur through inadequate frame overlap, where frames are collected after changes in the position of the telescope. Calibration of these images can be particularly difficult to rectify. However, the calibration of images which display extraneous light source effects is much more simplified. In principle, extraneous light can be removed through careful sky subtraction, however, it often becomes difficult and the process generally becomes more complicated.

In order to describe the analysis and interpretation of linear polarization data, attention is drawn to work previously undertaken on the extragalactic object NGC5253. Although this object bears no relevance to the objects upon which this thesis is based, it merely serves to provide a brief introduction to the interpretation of polarimetric data.

As seen in figure 2.3, most polarimetric image maps consist of a greyscale or contour map with superposed polarization vectors. This is particularly useful as it allows a direct comparison between the pattern of polarization and distinct morphological features of the object. In this case, the object is a starburst galaxy.

As with other objects of this type, the magnitude of polarization is fairly low, with levels typically around a few percent. Different types of object, however, may show increased levels of polarization which can be accounted for in terms of the scattering particles. The patterns of polarization vary considerably between objects of different type, but show many similarities for those of the same type. Distinct differences do, however, exist between objects of the similar type. These differences can be attributed to object evolution, differing physical conditions leading to the production of different polarization mechanisms, changes in chemical composition of scattering particles, and geometrical effects.

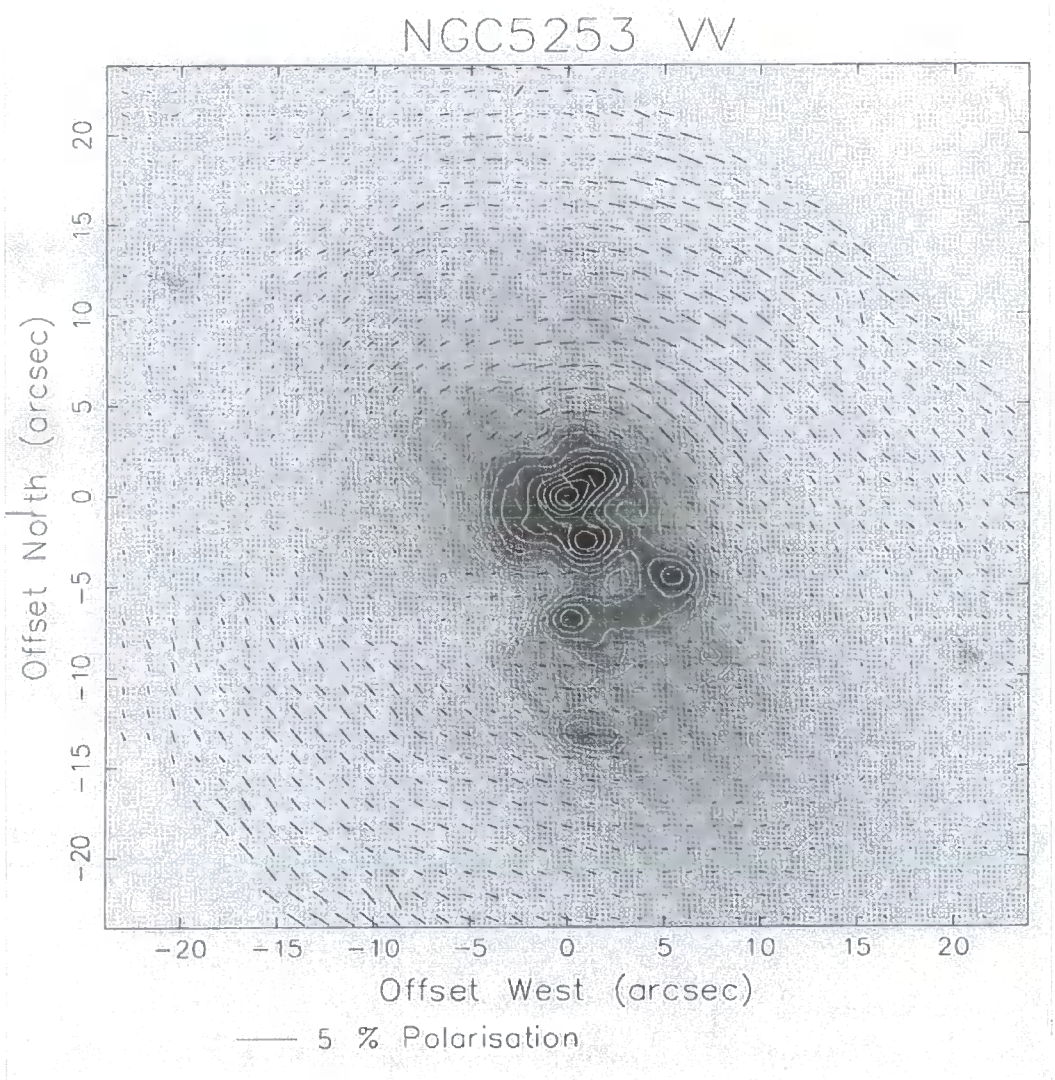

Figure 2.3: Broadband V total intensity greyscale image with superposed intensity contours. The image also includes an overlay of polarization data which has been integrated into square bins of size 5 pixels. These have been spaced at regular intervals of 3 pixels to produce data smoothing.

Within certain objects, the polarization levels and patterns follow a non-uniform distribution with subtle changes across the extent of the source. In others, the patterns are more uniform and display regular structure. Consequently, many polarization patterns arise from known physical and geometrical conditions. In order to gather significant information about objects, observing programmes usually involve the collection of multi-wavelength measurements. This not only allows a discussion of the intrinsic properties of the object, but also provides information about the intervening medium.

In this case, the object was recorded using a broadband V and narrowband Hα filter. It can be seen that the object possesses an irregular and rather amorphous structure in ground-based observations, but possesses intricate filamentary structure at the higher resolutions afforded by HST observations. This implies that only large-scale structures are sampled with adequate precision. Analysis of the large-scale V-band polarization map of figure 2.3 shows the subtlety encompassed in the polarization pattern. The lack of high levels of polarization, however, does not detract from the point that significant amounts of information exist within the image. Careful analysis shows that polarization magnitude is highest close to the minor axis, but decreases with increasing offset along the major axis of the object. Essentially, the subtle change shows that the polarization occurs predominantly within an opening angle of ~ 45° centred upon the galactic centre. Together with the fact that significant star formation is known to have occurred during the evolution of the galaxy, the polarization cone can be used to explain the presence of a galactic 'superwind'. Such conjecture requires meticulous attention and significant knowledge of the physical conditions which could exist in such an object. Analysis of the galaxy nucleus using smaller integration bins allows smaller structural details to be discussed. In essence, the use of broadband V and narrowband Hα allows polarization structure to be measured for continuum and emission line features. However, for true continuum measurements, a passband free of emission-line features would have to be employed. Figure 2.4 shows both broadband V and Hα polarization maps. The general patterns of polarization in the north, north-east, and north-west, are indicative of centro-symmetry. These patterns are prevalent within objects which contain 'reflection nebulae'. Centro-symmetric polarization patterns are produced through dust scattering processes, which under suitable physical and geometric conditions, result in high levels of polarization. However, the levels and patterns of polarization may also be affected by other processes. For example, depolarization and dilution of scattered radiation may occur as a result of multiple scattering events or conflicting polarization mechanisms. In the latter case, dilution occurs when the conflicting polarization mechanism rotates the plane of polarization through 90° to that produced by scattering. The process of dichroic or differential extinction is one such process. In many cases, the centro-symmetric polarization pattern deviates from that which is characterized by simple reflection nebulae. Such deviations appear as an increasing ellipticity towards the centre of the object. The presence of an elliptical polarization pattern often implies that the illuminating source, usually found at the centre of a centro-symmetric pattern, is extended rather than point source. This is indicative of a dust disc or torus, which surrounds the central illuminator.

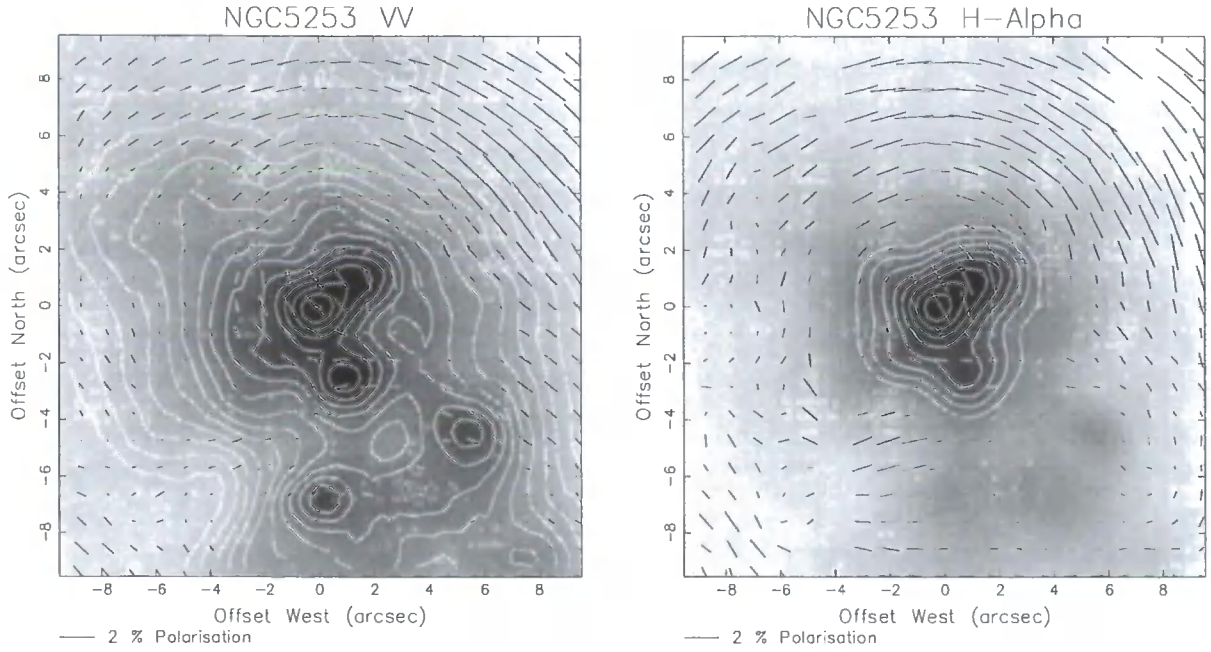

Figure 2.4: Broadband V total intensity greyscale image with superposed contours and polarization data. This is accompanied by an Hα total intensity greyscale image with superposed contours and polarization data. All polarization data has been integrated into square bins of size 3 pixels. These data bins are spaced at intervals of 2 pixels to provide data smoothing at a higher resolution.

Inspection of both Hα and V-waveband images shows that the pattern of polarization immediately south of the galaxy nucleus becomes very complex, with features indicative of intricate structure. A number of 'null points' are observed in this region. These are explained by the presence of conflicting polarization mechanisms. Consequently, the appearance of the null point vectors indicates that both scattering and dichroic extinction processes are present within the same region. These mechanisms act to produce polarization vectors which lie parallel and perpendicular to the scattering plane, thereby cancelling out. The general result is then little or no polarization. Although the southern regions of the galaxy core display patchy obscuration, the knot-like structures, which represent the condensations of previous star formation activity, do not act as individual illuminators to produce their own centro-symmetric polarization pattern. Consequently, such results would suggest that the knot-like structures were foreground to the patchy obscuration. This demonstrates that polarimetry can be utilized as an extremely useful tool in describing the three-dimensional structure of objects. The study of polarimetric data provides additional means of probing the inner structures of astronomical objects, along with IR and radio observation.

A look at the distribution of polarized light by means of a contour map can often display features which are not always apparent in vector maps. Figure 2.5 shows a polarized intensity contour map superposed upon a regular greyscale intensity map. Inspection of the image reveals a complex distribution of brightness structure within the region of the nucleus. Close examination of the contours, however, reveals a large-scale bipolar structure which becomes more apparent along the minor axis towards the outer boundaries of the galaxy. Naturally the polarized light distribution represents some combination of the way in which dust is dispersed throughout the galaxy, but also represents the nature of asymmetric illumination. Polarization observed in NGC5253 is consistent with dust scattering processes. Knowledge of the object type, however, would suggest that it was metal deficient and therefore depleted in elements needed for the formation of dust. Such a suggestion would imply that star formation within the nucleus of the galaxy had processed material and enriched the surroundings with significant levels of dust.

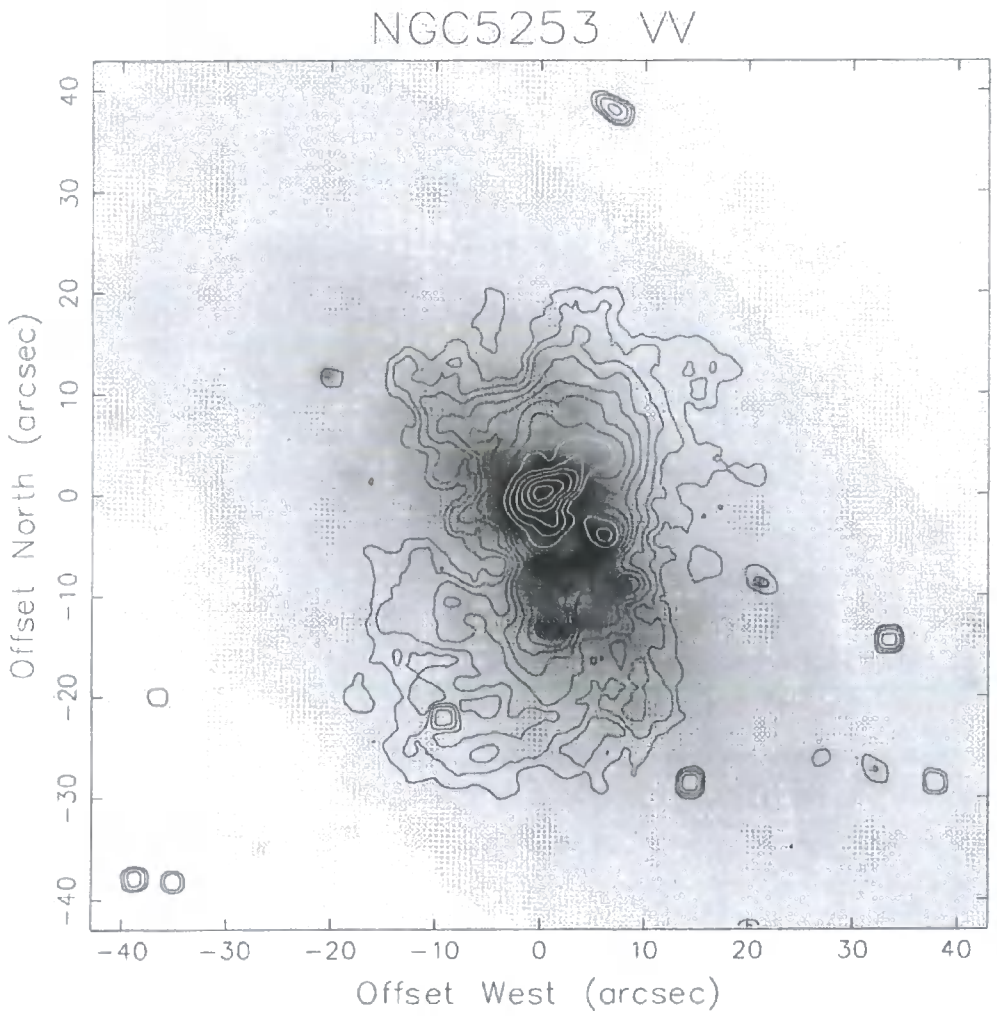

Figure 2.5: Broadband V total intensity image with superposed polarized intensity contours.

2.6 PRODUCTION OF POLARIZATION

Polarization arises in many of the astrophysical processes involving the generation and transfer of radiation. An important factor in its production is the presence of magnetic fields. These interact indirectly with radiation through electron or dust grains which subsequently affect radiative emission. The role of magnetic fields essentially provides the large-scale ordering of emission or scattering that is necessary for the production of polarization.

The predominant source of polarization observed in the objects described in this thesis is that of scattering. A brief description of the process involved will be given in the next sub-section. Further polarization mechanisms may also exist in these objects. The majority of polarization mechanisms lead to the production of linearly polarized light. A number of mechanisms, however, sometimes lead to the production of circularly, even elliptically polarized light. The mechanisms which produce polarized light have been discussed elsewhere (See Berry 1985; Gledhill 1987; Martin 1989; Alton 1996), but are included here for clarity. Of the whole range of mechanisms encountered in astrophysical objects, only the most common are described here.

2.6.1 PROCESSES LEADING TO THE PRODUCTION OF POLARIZATION

It is now known that the ISM is largely responsible for the partial plane polarization of starlight. In general, it is observed that objects which display reddening, usually display some degree of polarization. It appears that the effects of reddening are well correlated with those of interstellar polarization. The accepted model accounting for this correlation employs the effects of dichroic extinction. This involves the preferential extinction of radiation through the action of non-spherical dust grains which have become partially aligned by their interaction with the galactic magnetic field. First hypothesized by Davis & Greenstein (1951), it is now widely regarded that dust grains align themselves through paramagnetic relaxation resulting from the interaction between the grain's dipole moment and the ambient magnetic field. For a region of interstellar space, containing both gas and dust, the presence of a magnetic field can induce internal magnetization in the dust grains. Generally the galactic magnetic field is involved, although smaller scale fields, such as those within particular nebulae, can also cause the same effect. This internal magnetization consequently leads to a magnetically influenced torque, thus inducing a net rotation of the grains. Figure 2.6 shows the way in linear polarization is produced through the process of dichroic extinction.

In the original analysis, Davis & Greenstein assumed that grain rotation is produced by random impulsive torques, each resulting from collisional interaction with gas atoms. In order to observe net grain alignment, the time over which paramagnetic relaxation can occur, has to be less than the time over which collisional

interaction occurs. However, this can only occur if the grain temperature is lower than the kinetic temperature of the gas. Under such conditions, the frequency of gas-grain collisions becomes sufficiently low for the grains to align through dissipative magnetic torque.

Work on the mechanism of dust rotation carried out by Purcell (1979) shows that preferential extinction by aligned grains can also occur through the process of 'Suprathermal spin'. Theory suggests that dust grains are able to act as reaction centres for the formation of molecular hydrogen. This scenario occurs within molecular clouds where molecular hydrogen forms upon the catalytic surface of a dust grain, and, in doing so releases binding energy. This energy is then imparted to the dust grain, causing it to rotate. Under these conditions, grains experience a rotation in which their major axes become oriented perpendicular to the direction of the magnetic field. Any radiation whose electric field vector is parallel to the major axis of the grains then experiences preferential scattering. The levels of polarization produced from these processes is generally low, with typical magnitudes ranging from 2% - 5%, depending on the degree of alignment between dust grains.

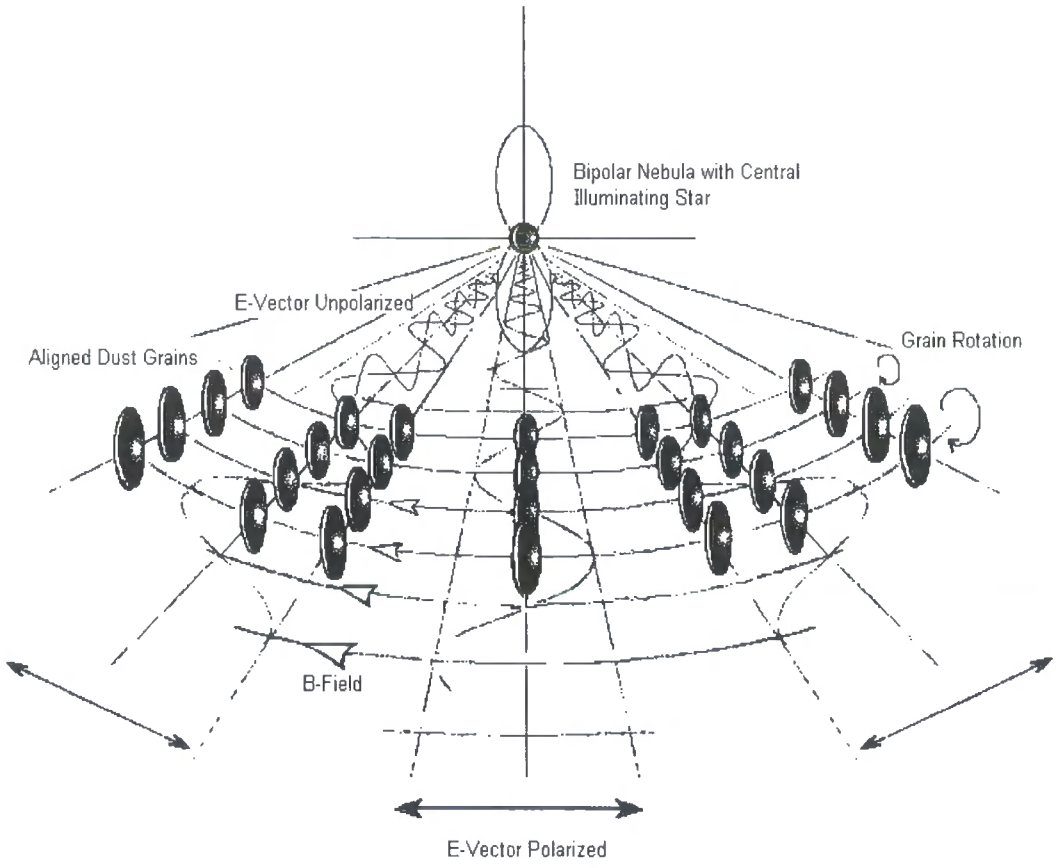

Figure 2.6: Production of linearly polarized light through the effects of magnetic field grain alignment. This mechanism of polarization is known as 'dichroic extinction.'

An important point which has been realized, however, is that dichroic extinction may only occur if certain criteria are fulfilled. The main factors involved in its appearance are that dust grains possess anisotropic optical properties and that they are non-spherical, tending towards an elongation.

Although the degree of polarized light produced from dichroism is low when compared with that from scattering, conditions may exist to enhance these levels. Amendments to dichroic extinction theory suggest that dust grains which incorporate inclusions of ferrous material, can act to concentrate magnetic flux. Increase in magnetic field strength would then induce a greater alignment throughout the population of dust. Such behaviour is known as 'Superparamagnetism'. This becomes apparent as the grain size distribution shifts to encapsulate a larger range. Though observations show general dichroic polarization levels to be low, the phenomenon of superparamagnetism is likely to be present in a large number of cases.

Observations show that systematic variations exist in the way dust reacts to light of differing wavelength. These variations are fully described by the empirical law known as 'Serkowski's law' (Serkowski et al. 1975), which is given by and shown by figure 2.7. (See Martin & Whittet 1990; Whittet et al. 1992; Somerville et al. 1994 for further details).

$$\frac{P_\lambda}{P_{MAX}} = \exp\{-K \ln^2(\frac{\lambda_{MAX}}{\lambda})\} \qquad \textbf{(2.27)}$$

Here P_λ is the polarization level which occurs at a wavelength λ. $\mathbf{P_{max}}$ is the peak level in polarization which occurs at a wavelength of λ_{max}. K is an environmental parameter, originally believed to be constant with a value of 1.15. Further observations of the wavelength dependence of polarization by (Wilking et al. 1982), however, have shown that K is in fact variable, and changes under differing environmental conditions. (Whittet et al. 1992) went on to show that:

$$K = (0.10 \pm 0.05) + (1.66 \pm 0.09)\lambda_{MAX} \qquad \textbf{(2.28)}$$

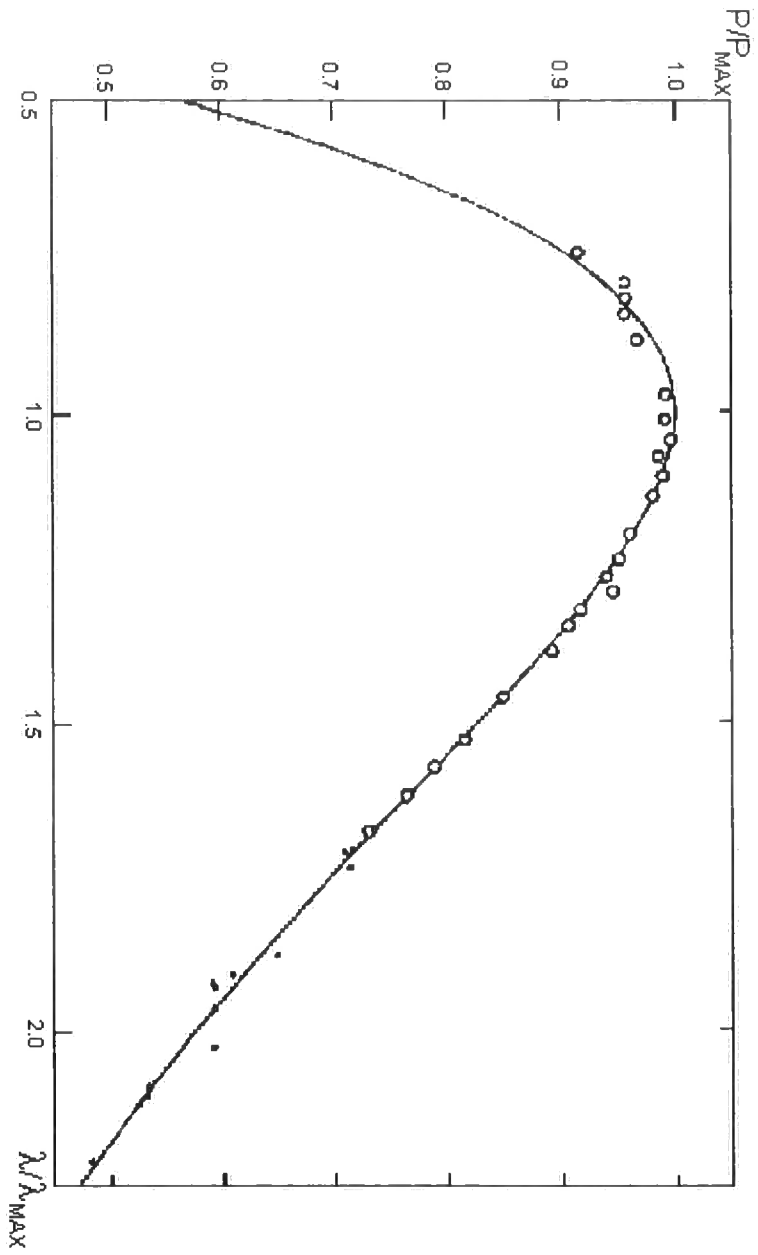

Figure 2.7: The Wavelength Dependence of Interstellar Polarization. Serkowski et al. (1975)

In addition to their obscuring effects, dust grains also betray their presence through the process of scattering. It is known that our galaxy is filled with a diffuse light. This light does not appear to emanate from any particular direction, implying that it is actually scattered. Its origin is from distant luminous sources, but appears diffuse through the effects of dust in the ISM.

Besides scattering leading to the appearance of diffuse galactic light, scattering also occurs in galactic nebulae. A key observational feature of such nebulae is the degree of polarization. Typically, polarization levels are very high, often as much as 20 % - 30 %. In these cases, the size distribution of dust particles tends towards average grain sizes comparable, or greater than the wavelength of the incident radiation. Nevertheless, under circumstances in which the particle sizes are much less than the wavelength of incident radiation, the degree of polarization becomes extremely high, sometimes approaching 100 % with favourable geometry.

Models of scattering are essentially sub-divided into two loosely defined groups, namely those based upon Rayleigh scattering and those based upon Mie scattering. The simplest case is that of Rayleigh scattering, in which the size of the dust grains is smaller than the wavelength of the incident radiation. The function of percentage polarization displayed by this process is dependent upon the scattering angle. It shows a symmetrical distribution and peaks at scattering angles around 90°. The mathematical formalization of this function is given by:

$$P(\%) = \frac{(1-\cos^2\theta)}{(1+\cos^2\theta)} \times 100 \qquad \textbf{(2.28)}$$

Here, θ is the scattering angle and thus describes 'forward scattering' for $\mathbf{0° < \theta < 90°}$ and 'backward scattering' for $\theta > \mathbf{90°}$.

For dust grains possessing sizes comparable to, or greater than the wavelength of incident radiation, the solutions of Maxwells' equations are then applied through Mie scattering. Independently derived by Mie (1908) and Debye (1909), theory applies to smooth, homogeneous spherical grains. Following this work Van de Hulst re-analysed the theory and subsequently created supplementary solutions for infinite cylindrical grains. Further solution to the theory is also presented by Wickramasinghe (1973), Draine (1988), Asano & Yamamoto (1975), and Matsumura & Seki (1991).

A further mechanism also exists in the production of polarization. This particular mechanism is associated with high energy astrophysical phenomena and often involves extreme environmental conditions. Objects which display this phenomenon include cataclysmic variable star systems, certain types of supernovae, and the certain type of active galaxy. The exact processes involved in the production of polarization are

associated with relativistic particles and their interaction with magnetic fields. These magnetic fields are often intrinsic to the object and are usually of small size. In some cases, however, galactic scale magnetic fields may possess sizes on a galactic scale, such as those inherent to galactic jet features of AGN's. Radiation produced under these conditions is known as 'synchrotron radiation'. The levels of polarization observed through synchrotron emission are typically ~ 10 %, but can reach higher values. The mechanism involves the gyration of electrons travelling at near light speed around lines of magnetic flux. As electrons are accelerated, they emit radiation. The electric field vector describing this radiation is parallel to the direction of acceleration. Consequently, the electric vector becomes perpendicular to the direction of the magnetic field, thus producing a radial 'lighthouse' beam of radiation.

2.7 POLARIZATION IN THE ASTRONOMICAL ENVIRONMENT

2.7.1 POLARIZATION IN THE INTERSTELLAR MEDIUM

It has long been known that space is far from being empty. The space between stars and nebulae is filled with the components of both gas and dust. Although it is now clear that dust contributes only a small fraction to the total mass of this interstellar medium ~ 1%, it plays a major role in describing its global characteristics. Particularly startling is the effect of dust upon the distribution of starlight throughout the galaxy. Throughout the history of observational astronomy, studies show that light from distant sources is distributed in a non-uniform manner. Star fields within the galaxy are interspersed by regions containing little or no luminous sources. These 'dark' regions are attributed to obscuration by intervening material. Extensive analyses of stellar statistics show that obscuration occurs predominantly within the plane of the galaxy, following a non-uniform pattern. However, obscuration also occurs on much smaller scales, particularly around stars and galactic nebulae. The general appearance of results suggest that obscuration levels, and hence dust concentrations are particularly high in the galactic plane. Catalogues by Axon & Ellis (1976) demonstrate this increase in dust content, through the analysis of polarization data. They also show that the effects of dust become more apparent with increasing galactocentric distance. This is shown in figure 2.4. Studies have also demonstrated the existence of a much more extensive and diffuse extinguishing phenomenon. The appearance of this extinguishing effect is attributed to a tenuous, but more uniformly distributed dust component. This dust component is manufactured and subsequently ejected into the ISM from the atmospheres of evolved stars. Rigorous studies of interstellar dust reveal that its general distribution follows that of the population I objects in the galactic plane. However, they also show that it exists above and below this plane and extends outward into the galactic halo. Theoretical studies of obscuration (hereafter extinction) show that it may be observed through the action of light absorption or the action of light scattering and, under certain circumstances, both. The predominant mechanism of extinction is determined by its effect upon the wavelength of radiation which it affects. If absorption represents the dominant factor of the extinction process, the efficiency with which radiation is affected is proportional to λ^{-1}. However, if scattering is dominant, then the efficiency with which radiation is affected is proportional to λ^{-4}. Consequently, light photons of shorter wavelength (i.e. towards the blue spectral region) are affected more so than those of longer wavelength (i.e. towards the red spectral region).

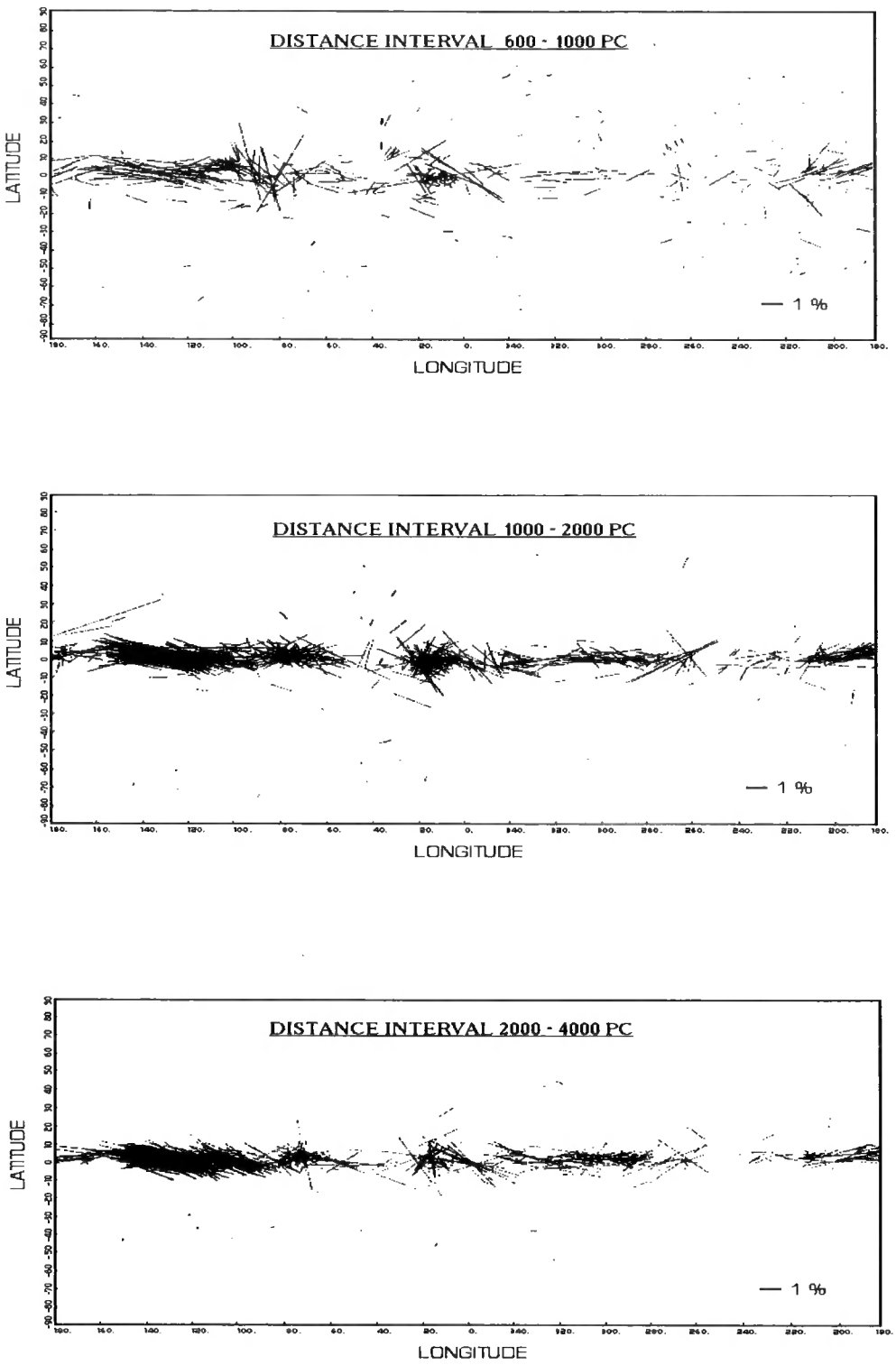

Figure 2.8: Interstellar polarization as a function of distance. Axon & Ellis (1976)

The principal effect of this selective scattering is therefore to create a 'reddened' appearance of the source. However, this would only become apparent with the presence of small scattering centres (i.e. those involved in Rayleigh scattering). Theory suggests that where scattering processes occur, polarization often follows. This polarization can provide many details needed in solving some of the problems still facing the theory of the ISM. Studies of polarization can be used to ascertain the optical properties of interstellar dust and its interaction with the interstellar radiation field. They can also provide information about the distribution of dust, magnetic field environments, and help to describe the way in which dust interacts with these fields. Of particular interest is the study of dust composition. In this study, the use of polarimetry becomes an invaluable tool providing rigorous constraint upon the physical parameters of dust.

Within the ISM, the presence of dust is characterized by reddening, extinction, and the depletion of elements which exist in the gaseous phase. The variety of elements and composition of compounds from which interstellar dust forms, is very limited (Greenberg 1978). Model fitting to observational data shows that the largest fraction of dust consists of carbonaceous compounds and silicate materials (Whittet 1992). At optical and IR wavelengths, extinction caused by these materials is normally observed to be wavelength dependent. However, neutral extinction (i.e. wavelength independent) is also known to exist. Analysis of this neutral extinction shows that large dust grains ~ 1 – 100 μm present negligible effects within the ISM, implying that no substantial populations of such grains exist. Analysis of wavelength dependent extinction, however, is more fruitful. Observations show that extinction in the optical and IR can be explained by the presence of a small selection of grain materials. Grains composed of these materials are found to possess dielectric optical properties and size characteristics of classical grains ~ 0.1 – 0.3 μm. However, measurements of extinction in the UV present difficulties, for which classical grains cannot account. Development of a multi-component grain model (Mathis 1990) has shown that classical grains which contribute to optical/IR extinction, also affect UV extinction. However, difficulties arise in the interpretation of data when the extinction curve is extended to shorter wavelengths. Absorption features in the extinction curve are attributed to the existence of small grain populations. Here, graphite seems to provide adequate description of data, which would explain the depletion of carbon throughout the ISM. However, a further component is now known to exist, accounting for the increase in extinction towards the FUV. This component is associated with the very small grains (VSG's) which possess grain sizes below 0.01 μm. In addition to the contribution from VSG's, molecular compounds may also play a role in the effects of the ISM. Observations show that hydrogenated organic compounds; namely polycyclic aromatic hydrocarbons (PAH's), are readily produced within the cool atmospheres of evolved stars (e.g. Omont 1986, Tielens 1993). Injection of these compounds into the ISM has been used to explain the 'unidentified IR bands'. However, the total contribution of PAH's to interstellar dust is likely to be small (Greenberg et al.1993). In general, interstellar dust is found to possess very similar composition to that which is formed and processed in the outer atmospheres of evolved RGB and AGB stars. Consequently it is believed that an evolutionary link must exist between the two. Analysis

of AGB stars and subsequent stages of stellar evolution therefore enable important theoretical predictions to be made about the ISM.

2.7.2 POLARIZATION IN THE CIRCUMSTELLAR ENVIRONMENT

The fact that most evolved stars pass through a stage of high mass loss, means that circumstellar material becomes significant. The presence of such material not only implies that gas is present, but also astrophysical solids. It is these solids, formed from the condensation of gas phase refractory elements, which lead to the appearance of polarization within circumstellar environments.

The physical conditions which exist within these environments are significantly different from those encountered in the ISM. Typical circumstellar environments are characterized by high particle densities, higher temperature, and higher pressure. Consequently, the observed polarization levels are often different from those observed elsewhere. Additionally, conditions which lead to a change in the state of polarization may exist, causing a transformation from linearly polarized light to circularly, even elliptically polarized light. Although this is also apparent in the ISM, the higher particle densities found in circumstellar shells usually lead to a higher incidence of other forms of polarized light (Coyne et al. 1988). In many cases, the predominant form of polarized light will be a linear state. However, it is most probable that the levels of linearly polarized light become diminished as a result of additional polarization processes. This is particularly true of nebulae that possess central stars with circumstellar envelopes (e.g. PPNe). In these cases, polarization levels observed within the circumstellar regions become much lower than those found within surrounding nebulous material. This is often explained by the presence of high levels of extinction. However, similar results are reproduced by the process of multiple scattering.

Multiple scattering is associated with an increase in dust density. Consequently, higher levels of dust naturally lead to a higher degree of multiple scattering and increased levels of depolarization of single scattering events. Although multiple scattering can produce a depolarization of singly scattered light, the chief mechanism for its diminution is that of extinction. When related to the pattern of polarization, multiple scattering produces no contribution to the radially propagating radiation field of the illuminating star. Thus, multiple scattering does not contribute to the centro-symmetric polarization pattern observed in the optically thin regions of nebulae possessing central illuminating sources.

One further consequence of multiple scattering is that of increased surface brightness. Nebulae which display multiple scattering processes are also known to display increased levels of surface brightness, since its effect is much higher upon surface brightness than it is upon polarization. This is explained when singly scattered light generally suffers extinction after the first scattering. Although light is scattered multiple times

before leaving the nebula the effects of extinction are alleviated. This then leads to the observed brightness increase.

2.7.3 POLARIZATION IN THE NEBULAR ENVIRONMENT

Polarization levels found within these nebular environments vary enormously, but generally tend towards higher degrees of magnitude. In such cases the probability of light being absorbed and subsequently re-emitted in a different direction is fairly high. However, in the case of dichroic extinction, a substantial population of dust particles must first exist. This dust must also possess significant levels of large-scale alignment and also possess anisotropic optical properties. Consequently, the probability of such criteria being fulfilled become much less.

Typical nebular environments include those of reflection nebulae, young bipolar ouflows, planetary nebulae, and HII emission regions. All display a range of polarization but possess a high degree of commonality in the pattern of polarization. Typically, reflection nebulae display the highest levels of polarization, as suggested by their dust content. The colours of these nebulae are generally blue, indicative of scattering by small dust grains (Rayleigh scattering). It is these Rayleigh scatterers which produce the high levels of polarization, typically between 30 % - 60 %, although higher levels are sometimes encountered. Dust found within reflection nebulae is often associated with the clouds from which stars form. Most objects are found to be open clusters of young stars. The fact that small grains exist suggests that grains had little time to condense and grow, before the ionizing radiation of nearby stars led to their destruction, and radiation pressure blew them away. Here favourable geometries exist which increase the probability of scattering. On the other hand, HII regions display much lower levels of polarization. This is explained by the dilution of scattered radiation by stellar continuum radiation and intrinsic emission in the nebular gas. Although the presence of dust is likely, its geometry and distribution are unfavourable for the enhancement of scattering. In this case most of the dust will have been photodestroyed.

Within young bipolar nebulae and PNe, the levels of polarization are smaller than those from reflection nebulae, but higher than those from HII regions. Both young bipolar nebulae and planetary nebulae possess similar attributes and often display very similar physical phenomena. Consequently, the degree and pattern of polarization found within these objects also display similarity. Although planetary nebulae display a great range in morphology, a large proportion fall into the category of bipolar nebulae. These objects bear striking resemblance to the young bipolar outflows, although subtle differences do exist. In general these objects display polarization levels upward of 3 %, to almost 100 %. The lowest levels encountered are those associated with the high excitation nebulae which are characterized by high intrinsic emission. PNe often show shock phenomena which act to destroy dust. Furthermore, the high levels of UV flux which exist in

more evolved nebulae also act to reduce the distribution of nebular dust (Stasinksa & Szczerba 1999; Lenzuni et al. 1989; Pottasch et al 1984). Further account of the processes which act to destroy dust may be found in Furton & Witt (1992), Dinerstein et al. (1995), and Corradi & Schwarz (1995). The pattern of polarization generally reproduce those of simple reflection nebulae for both young bipolar outflows and bipolar planetary nebulae, but often show deviation from the typically centro-symmetric polarization pattern.

CHAPTER 3

M2-9

3.1 INTRODUCTION

M2-9 (PK 10 + 18°.2), sometimes known as the 'Butterfly Nebula', was first discovered and classified as a PN by Minkowski (1947). It has become the archetypal bipolar PN and has been used in many theoretical studies to address the possible link between bipolarity and stellar binarity. At optical wavelengths M2-9 is much like other bipolar PNe, with the exception of a number of peculiar features. Like other nebulae of this type, M2-9 displays a pair of diametrically opposed lobes extending from a bright, centrally condensed core. Observations also reveal the presence of an optically thick circumstellar disc or torus, aligned perpendicular to the bipolar lobes (Aspin, McLean & Smith 1988). The most intriguing feature of M2-9, however, is a series of knot-like structures within the walls of the nebular lobes. The special significance of these knots is that they appear to have undergone mass motion within the lobe walls and display a rotational motion over a period of the order of decades. Aside from these observations, M2-9 is believed to be in the early stages of development as a PN, placing it on the borderline between PPN and young PN (Walsh 1981). Observations also suggest that M2-9 shows similarities with symbiotic stars and that its nucleus shares many characteristics with very close mass-transfer binary systems (Livio 1982).

3.2 PREVIOUS STUDIES OF M2-9

Situated in the southern skies at a position RA 17h 05m 37.6s, Dec. –10° 08′ 32″ (2000.0), M2-9 has received considerable attention having been the subject of study to monitor changes in its morphology. The high resolution archival HST images of M2-9 which are reproduced in figure 3.1 and figure 3.2 show three prominent components of the nebula. The centre of the nebula is characterized by a 'non-stellar' condensation from which two symmetric lobes or 'wings' extend. The nebular lobes represent the second component of M2-9. Oriented in a north-south direction almost face-on, the lobes are inclined to the plane of the sky by 11° - 15°, with the northern lobe inclined away from the observer (Goodrich 1991; Schwarz et al. 1997). The lobes of the inner nebula extend some 20 arcseconds (0.06 pc ~ 12800 AU at a distance of 640 pc) above and below the central condensation, although deep sky images show two faint arcs which extend beyond the inner lobes and increase the size of the nebula to 1 arcminute (0.19 pc ~ 38400 AU at a distance of 640 pc) above and below the equatorial plane. These outer arcs form the third component of the nebula and contain a number of condensations which are suggestive of ansae. Nebular structure appears complex, with the existence of several bubbles and knot-like structures. All condensations within the nebula possess unusual mirror symmetry, except for the outer condensations which possess point-symmetry. The central core of the nebula is approximately 4 arcseconds in diameter, with a non-stellar appearance.

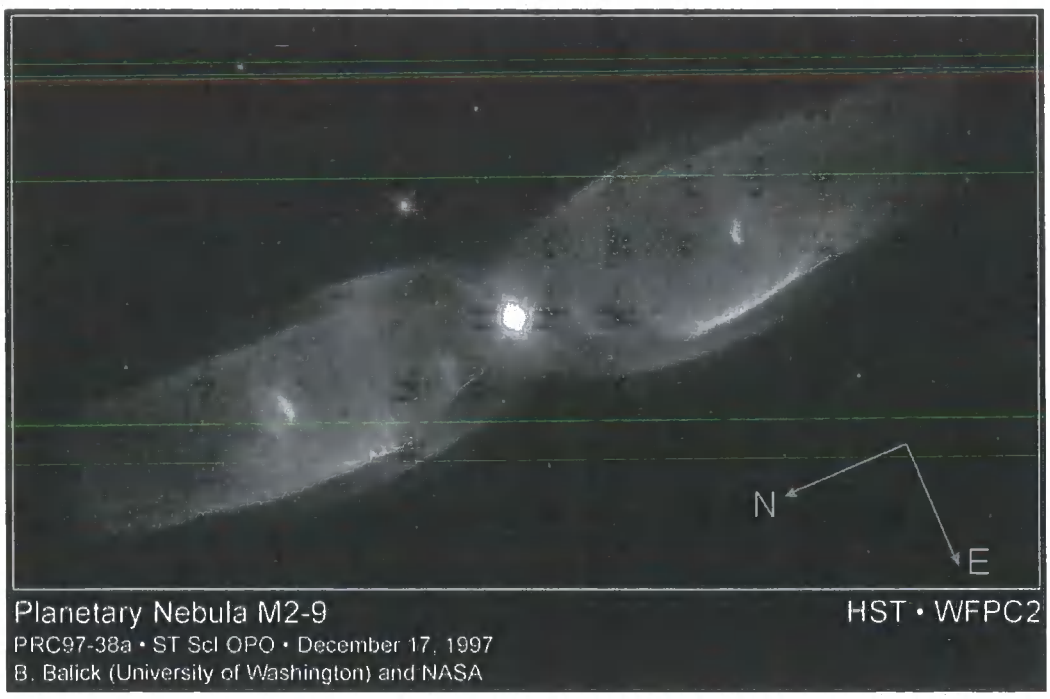

Figure 3.1: Archival HST image of M2-9.

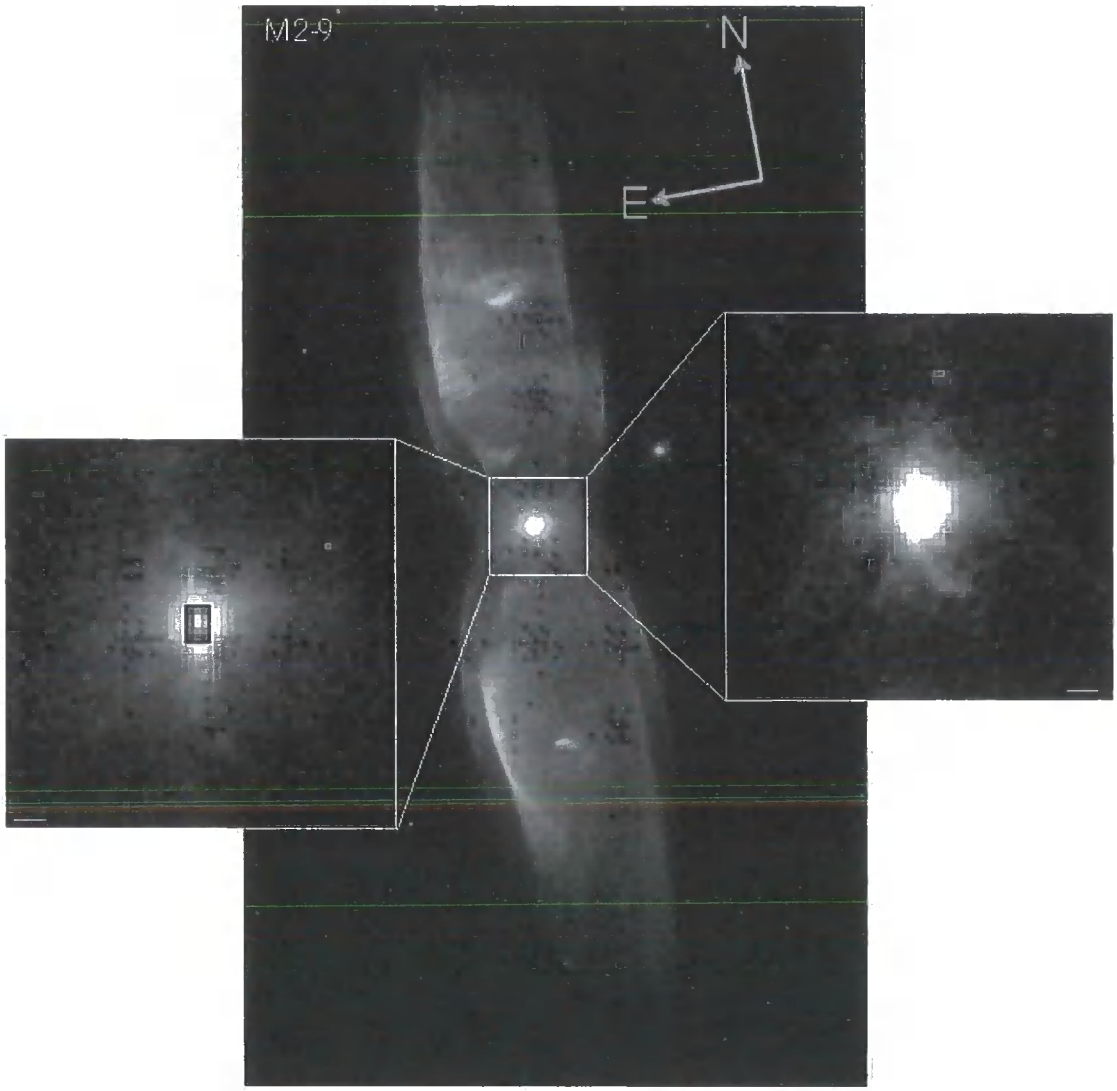

Figure 3.2: Archival HST image of M2-9 showing high resolution details of the nebular core.

Observations of the core of M2-9 show that the central star is partially obscured from direct view. This is due to the presence of an optically thick circumstellar disc. The asymmetry of this disc appears to provide an obvious collimation of the stellar wind from the central star, leading to a pronounced bipolar morphology of the associated nebula. A reduction in the intensity of nebulosity occurs close to the core, which results in an obvious narrow waist. The total extinction which occurs in the core has been determined to be A_v=5.35 ± 0.30 (Calvet & Cohen 1978), which was later confirmed by Swings & Andrillat (1979). Measurements taken across the inner lobes of the nebula show that extinction is reduced, implying that the central regions of the nebula possess the highest concentration of dust and gas. The central source has a temperature of the order of 10^4 K, with a spectral class having been determined by the use of radio flux measurements. Calvet & Cohen (1978) suggest that the central star has a spectral classification of B1 and a luminosity class V (Main Sequence). Swings & Andrillat (1979), however, argue that the star is likely to be of type O due to the size and nature of the nebula. It is generally accepted that the nucleus of M2-9 is unique among PNe. Several features in the emission-line spectrum, such as the presence of iron, chromium, and nickel, suggest that the nucleus resembles a symbiotic star (Lutz et al. 1989). Values for the integrated magnitude of the nebular core agree considerably well. Unfortunately, information regarding the wavebands in which data were collected wasn't included in all cases. Allen & Swings (1972) find a value of magnitude 13, while Shao & Liller (1968) find a value of magnitude 14.7. Using the International Ultraviolet Explorer (IUE), Feibelman (1984) shows that the V band magnitude is 13.7, although this value includes a small contribution from the nebular wings. Table 3.1 shows various magnitude measurements which have been gathered since the discovery of the nebula.

MAGNITUDE MEASUREMENT	OBSERVER	YEAR
14.7	Shao & Liller	1960
13.0	Allen & Swings	1972
13.7	Feibelman	1984
15.65	Phillips	2000

Table 3.1: Magnitude measurements for M2-9

At a distance of 640 pc, Schwarz et al. (1997) determined that the bolometric luminosity of M2-9 was lower than that for a typical AGB star. Schwarz et al. suggested that the luminosity of a main sequence B5 star at 640 pc should be L=550 $L_\odot$. However, the presence of [OIII] line emission in the nebular spectrum indicates that a further energy source must exist within the core of M2-9. The most likely explanation for the observed features of M2-9 is that the central source is a binary. The hot component of the binary system ionises the nebular gas to produce the high excitation emission, while the cooler component provides a

fraction of the luminosity. The interaction of this binary would also explain the highly collimated morphology of the nebula.

The distance of M2-9 has been reviewed a number of times and has undergone much revision due to the uncertainty of PN distance measurement. A number of distance values from previously published literature are listed in table 3.2.

DISTANCE MEASUREMENT (Kpc)	OBSERVER	YEAR
3.45	Cahn & Kaler	1971
1.0	Allen & Swings	1972
5.3	Barker	1978
1.0	Calvet & Cohen	1978
3.291	Maciel & Pottasch	1980
0.050	Kohoutek & Surdej	1980
0.640	Schwarz et al.	1997

Table 3.2: Distance measurements for M2-9

Spectroscopic study shows that M2-9 is an emission-line object, with the presence of many discrete spectral features and an underlying continuum. Its spectrum is dominated by strong recombination lines of the hydrogen Balmer series. Both permitted and forbidden emission line features occur, showing a range of ionization states. Strong spectral features include [OI], [OIII], and [HeI], while weaker features include [SIII], SiII, [NI], [NII], [FeII], and [FeIII]. The continuum is very weak and is weaker than that observed in other PNe. Using spectral features sensitive to temperature and density, the electron temperature and density of various nebular regions were calculated. Measurement by Allen & Swings (1972) using the lines of [Fe II] produced core electron temperature values ranging from 9000 K to 18000 K. Further studies using the [O III] lines have produced an electron temperature of the order of 10^4 K throughout the nebula. Studies of the electron density, however, have produced very different results for the various nebular components. High densities have been found within the nebular core, with values exceeding 10^6 cm^{-3}. Applying a temperature of 10^4 K, Allen & Swings found an electron density of 10^7 cm^{-3}. Because of the higher core density, collisional de-excitation becomes apparent, and this is exemplified by weaker [N II] line strength in the nebular core. [N II], however, is stronger in the nebular wings, which suggests that lower electron density is prevalent. Furthermore, [O II] line studies revealed extreme line strengths within the nebular lobes. Consequently, the electron density could be determined to be lower than 10^4 cm^{-3}.

It has been revealed that M2-9 possesses excess emission throughout the near-infrared (NIR). More IR radiation is being released by the nebula than is normally observed from free-free and bound-free electronic energy transitions, suggesting that an additional IR energy source exists. Evidence reveals that IR emission is largely concentrated within the nebular core. Measurements taken by Allen & Swings (1972) show that more than 90% of 2μm flux originates from a region only 3 arcseconds in diameter, corresponding to an actual size of 0.009 pc at the most recently proposed distance of 640 pc. This is confirmed by the analysis of IR colour indices V – K (2.2μm) ≈ 6, H (1.6μm) - K ≈ 2.3, and K – L (3.5μm) ≈ 2.7. Swings & Andrillat (1979) showed that M2-9 occupies a position on the colour-colour diagram (H – K against K – L) which is situated amongst the region characterized by B[e] emission-line stars. Excess emission beyond 1.5μm has now been fitted with a blackbody spectrum possessing an effective temperature of 830 K (Aspin, McLean & Smith 1988.) This is interpreted as UV radiation which has been absorbed and subsequently emitted at longer wavelengths by a dust component surrounding the central source. A cooler dust component radiating at 450 K has also been postulated in accordance with measurements by Cohen & Barlow (1974). IR morphological studies by Aspin, McLean & Smith (1988) show that significant changes occur in the appearance of M2-9 when observed at progressively longer wavelength. Observations taken in the J, H, and K wavebands of the NIR spectral range show a trend toward greater emission and reduced morphological structure. Towards longer wavelength the nebular condensations fade into the main body of nebulosity, while the central condensation increases in size and emission. Consequently, the IR structure of M2-9 becomes amorphous. Spectroscopic results suggest that increased reddening occurs at longer wavelengths and imply that greater extinction occurs towards the north. The (J - K) and (H - K) images display complex structure over the inner regions of the nebula and show a peak in emission both east and west of the core. The bipolar lobes themselves display little difference in structure, although the walls of the lobes show increased amounts of reddening. The total extent of emission about the core is approximately 20 arcseconds in the east-west direction. Hora & Latter (1994) show that the nebular lobes have a double-shell structure. The inner shell is dominated by emission from the recombination of free electrons with ionized hydrogen, while the outer shell is dominated by emission from molecular hydrogen. Results suggest that emission occurs predominantly through radiative excitation. Although wind generated shocks are observed within M2-9 (Icke et al. 1989,) emission from H_2 does not follow these structures. However, emission appears to trace out a region of photodissociation which is marked by the separation of hydrogen recombination and UV excited molecular emission.

IRAS observations of M2-9 classify the object as a point source, with the designation IRAS 17028–1004. Included in several of the general IRAS catalogues and those more specific to PNe, M2-9 possesses significant IR emission (Hora et al. 1999; Zuckerman & Dyck 1986; Thronson et al. 1988; Iyengar 1986; Zhang & Kwok 1990). Observable in the 12μm, 25μm, 60μm, and 100μm flux bands, M2-9 shows peak emission in the FIR, at about 60μm. Together with NIR observations, this suggests that M2-9 possesses both hot and cool dust components. Adopting the methods used by Van der Veen & Habing (1988), the IRAS

colours reveal that M2-9 resides in region IV of the colour-colour diagram ([12μm] – [25μm] against [25μm] –[60μm]). Use of the methods employed by Walker & Cohen (1988) and Walker et al. (1989) appear to suggest that M2-9 belongs to group of 'blue' PNe and contains substantial amounts of dust.

The UV spectrum of M2-9 is mostly characterized by low-ionization emission lines, although a number of high-ionization lines exist for nitrogen. No forbidden lines exist in the UV, but there is a weak underlying continuum. The UV spectrum of M2-9 displays a marked difference to the UV spectra of B[e] stars despite showing remarkable similarity with these objects in the IR. Although the UV continuum appears relatively weak when compared with the IR continuum, it displays an increase in flux distribution at shorter wavelengths, implying that a hot stellar component could be present within the nebular core. Emission from particular elemental constituents, such as carbon and oxygen, show significantly reduced levels in the gas phase compared with hydrogen and nitrogen. The apparent lack of abundant carbon and oxygen is also confirmed by the weakness of the [CIII] line at 190.9 nm, normally the strongest emission line in PNe, and also by the total absence of [CIV] at 154.9 nm. This is consistent with optical data which also show that carbon abundance is very low. The lack of carbon in the gaseous phase suggests that it is probably locked up in dust or other astrophysical solids such as. Polycyclic Aromatic Hydrocarbons (PAH's). This is also true of the oxygen abundance, suggesting that gaseous phase oxygen has been locked up in the formation of silicate dust grains.

Radio observations of the core by Purton, Feldman & Marsh (1975) show that the radio flux at 10 GHz is very low. Together with measurements of the corrected Hβ flux and [OIII] emission line measurements of the electron density, the size of the core must be very compact. Their measurements constrain the size of the dense gas core to a value of ~ 0.1 arcseconds. The mean flux density measured at 10 GHz was found to be 45 ± 7 mJy with appropriate weight being applied to the relevant measurements. Milne & Aller (1974) gathered radio data at 5 GHz and found a mean flux density of 35 ± 8 mJy, which implies that the nebula is optically thin over the frequency range 5 – 10 GHz. Purton et al. (1982) suggested a three-component model to explain the observed radio data. The model describes M2-9 as being composed of (i) a core, (ii) a 'halo', and (iii) a confusing source. Data show that the core becomes significant at frequencies greater than 10 GHz. Marsh et al. (1976) suggest that the confusing source is situated 9 arcseconds east and 26 arcseconds south of the core, and is of comparable flux density to the halo. Measurements collected by Kwok et al. (1985) using the Very Large Array (VLA) radio interferometer, show that the radio morphology at 20 cm bares striking resemblance to the optical morphology, although the extended wings are clearly distinguished from the central core. Observations at 6 cm, 2 cm, and 1.3 cm wavelengths show that the size of the core decreases monotonically with wavelength, suggesting that the core becomes optically thick towards higher frequency. Observations by Kwok et al. (1985) also suggest that mass-loss processes are still active within the core of the nebula. This is corroborated by the measurements of the core Hα profile which shows extreme levels of line broadening (Carsenty & Solf 1983; Balick 1989). Although observations by Balick

(1989) show that the core Hα line presents a base width of ~11000 kms^{-1}, calculations by Kwok et al. (1985) use the earlier value of 1600 kms^{-1}. Adopting the procedures used by White & Becker (1982), the mass loss rate was determined to be 3.3×10^{-5} $M_{\odot}$ yr^{-1} for an assumed distance of 1 Kpc. Although the value for the stellar wind velocity is consistent with the values for other PNe (Perinotto 1983), the mass-loss rate is several orders of magnitude higher than is normally encountered.

Radio imaging of the nebular wings shows that the electron densities encountered are somewhat lower than those derived from forbidden lines. Purton et al. (1982) derive a value of 1.5×10^{3} cm^{-3}, while Kwok et al. (1985) derive a value of 6.0×10^{3} cm^{-3}. The discrepancy in value is accounted for by noting that the radio flux is collected from the whole nebula and will thus produce lower density values for smaller filling factors. These observations also imply that higher density condensations exist within the nebular lobes, with angular sizes of ~ 1 arcsecond in diameter. These condensations are hypothesized to exist around the cores of cold neutral gas. This would imply that the edges exposed to the strong radiation field would display spectral signatures from ionised elements, while the edges pointing away from the radiation field would remain neutral.

Mapping of molecular gas throughout the nebula shows that M2-9 is detectable in both H_2 and CO emission. Observations of ^{12}CO (J=2-1) emission by Bachiller et al. (1990) reveal a dual peaked profile around the central core. This suggested that an expanding ring of gas is present around the central star. Measurements show that the ring has a diameter ≤ 10 arcseconds corresponding to a radial distance of 1.5×10^{12} km at a distance of 1 Kpc. The measured expansion velocity is 7 kms^{-1}, which is relatively low when compared with the expansion velocities of circumstellar envelopes of AGB stars. At a distance of 1 Kpc, the measured expansion velocity and angular dimension of the molecular envelope produces a kinematical age < 3500 yr. However, the actual expansion velocity of M2-9 could be significantly greater than the value determined, due to the effects of projection. This would then imply a much smaller kinematical age. Observations of ^{12}CO (J=1-0) by Bachiller et al. (1988) and Zweigle et al. (1997) also confirm previous molecular line data, but suggest that the kinematical age of the molecular envelope is only 2100 yr for a distance of 1 Kpc. Their data also suggest a molecular gas mass of the order of 10^{-3} $M_{\odot}$, indicating that the mass of ionised and molecular material could be comparable. These observations also show that molecular material possesses a clumpy density distribution. The clumpiness of such gas provides evidence that the envelopes of AGB- and Post-AGB stars are also clumpy, and that this is retained throughout the mass-loss process. It is presumed that the young age of the molecular envelope provides an explanation as to why CO has not been fully dissociated through the action of the UV radiation field. Measurement of the expansion velocity of the inner lobes by Schmidt & Cohen (1981) reveals that the nebula is ~ 5000 yr old.

Polarimetric studies of M2-9 have revealed many details concerning nebular structure and geometry, and have shown that the nebula contains substantial amounts of dust. Early polarimetric work carried out by

King et al. (1981) show that the nebula possesses high levels of polarization, with levels reaching almost 30 % between 4 – 10 arcseconds north and south of the nebular core. Results also showed that the nebular condensations possessed increased levels of polarization, although the increase in polarization relative to the surrounding levels is insignificant. Furthermore, it was observed that the polarization pattern within a number of the nebular condensations showed odd results. To account for this, King et al. used the theoretical models developed by Gold (1952) and Harwit (1970) to suggest that additional polarization mechanisms existed inside the condensations. Aspin & McLean (1984) presented polarimetric results across the entire optical spectrum. Their results corroborated many of the conclusions proposed by King et al. However, Aspin & McLean showed that the orientation of polarization within the nebular condensations was the same. Hα polarization data collected by Scarrott et al. (1993) revealed that the nebular lobes of M2-9 contain both scattered radiation and intrinsic emission radiation. Results also showed that polarization was produced by the scattering of radiation from an inclined circumstellar disc and the walls of the nebular lobes. It was concluded that the lobes were hollow cavities which had been excavated by the action of stellar wind processes. This was later confirmed with spectroscopic analyses by Phillip & Cuesta (1999). IR polarimetry by Lacasse (1982) shows that significant polarization occurs in the IR K-band at 2.2 μm, with values reaching ~20 %. Like the results of optical polarimetry, IR polarimetry revealed that the polarization levels within the nebular core were very low, with values of ~2 %. This indicated that scattered emission was significantly reduced within the central regions of M2-9, as a consequence of increased particle densities.

First discovered by Kohoutek & Surdej (1980), the outer regions of M2-9 possess a high degree of collimation, and are marked by pair of faint loops which end in unusual double ansae. Unlike the mirror-symmetric brightness distribution of the inner nebula, the outer loops of M2-9 possess 'point-symmetry.' Schwarz et al. (1997) showed that both ansae of the outer nebula display redshifted spectra. The expected Doppler pattern would normally display both redshifted and blueshifted components. To explain this unusual result, Schwarz et al. proposed that the ansae must contain dust which scatters light from the nebular core. It is assumed that the ansae are moving outward from the inner nebula, but possess different redshift velocities because of projection effects (Solf 2000). The presence of dust within the outer ansae was confirmed by Schwarz et al. (1997) using polarimetry. Results show that the outer extremities of M2-9 are highly polarized, with polarization levels exceeding 60 %.

The expansion velocity of the outer lobes has been found to be 164 km s^{-1}, while the expansion velocity of the inner lobes is 23 km s^{-1} Schwarz et al. (1997). This would imply that shocked gas should be present. However, shock-excitation of gas appears to be absent within the outer lobes. Schwarz et al. (1997) suggest that the surrounding interstellar medium (ISM) must be extremely tenuous. Consequently, interactions between the ISM and the outer lobes of M2-9 must be too small to produce significant emission along the line of sight. The presence of shocks within the outer ansae would lead to lower levels of polarization through the destruction of scattering grains.

Morphological studies of M2-9 have revealed the presence of a series of knot-like condensations which reside within the walls of the nebular lobes. It is now established that these structures exhibit almost perfect lateral motion within the lobes, following a regular cycle of the order of several decades. Following the observations by Van den Bergh (1974) it was discovered that the nebula had undergone considerable change since the observations by Minkowski. It was revealed that the nebular condensations had traversed the face of M2-9 and that changes had also occurred in nebular brightness and structure. To explain these observations, Van den Bergh proposed that material within the nebular lobes is illuminated by the modulation of UV radiation from the central star. The cyclic illumination of nebular gas is then provided by the presence of obscuration from dust clouds surrounding the central star. Although acceptable, the simple illumination model proposed by Van den Bergh was later rejected because it could not account for the mirror-symmetry of the nebular condensations.

Observations by Kohoutek & Surdej (1980) during the period 1977-1978 show that the nebular condensations originally located in the west, completely traversed the face of the lobes, thereby appearing in the east. Following this discovery, it was suggested that the lateral motions of the condensations could be explained in terms of solid body rotation. Adopting a nebular distance of 1 Kpc, it was found that the angular velocity of the condensations became extremely large, with values of the order of 10^3 km s^{-1}. To account for this, revision was made to the distance of M2-9, placing it within the local neighbourhood at a distance of only 50 pc. Consequently, the proposal was ruled out on the basis of both unaccountable extinction measurements and inconsistent Doppler shifts.

Goodrich (1991) and Trammell et al. (1995) showed that the nebular lobes possess a series of bands, which are believed to contain high density material. The bands are illuminated by UV radiation from the central source, thereby causing the material to fluoresce. This would explain the motion of the condensations about the equatorial plane. The appearance of high density structures along the bipolar axis suggests that periodic mass ejection could provide a possible solution. Balick (1989) suggested that M2-9 has recently experienced such a mass-loss event. The precessing fan of radiation described in the model developed by Goodrich, however, does not account for the mirror-symmetry of the nebular condensations. Instead, a point-symmetric geometry will be seen. To resolve this problem, a matching UV illuminating beam would be required, possessing the same characteristics. However, this would seem unlikely and suggests that the process by which the symmetry of the condensations is produced, is much more complicated than previously believed.

Recent analysis by Doyle et al. (2000) suggests that the nebular condensations have formed as result of a 'jet-splash' process. The basic concept of this model involves the interaction of a high velocity 'non-radiative' collimating jet, with the walls of the nebular lobes. Estimation of the jet velocity is modelled upon

the amount of broadening which is apparent in the circumstellar Hα line. Balick (1989) found that the wings of the Hα line exhibit velocities close to 11000 km s^{-1}, indicating the presence of an extremely high speed outflow at the centre of M2-9. Density gradients produced during mass loss upon the AGB and the presence of a binary nucleus would act to distort the outflow of the central source and thus provide a means of explaining the unusual mirror-symmetry of the lobe condensations. Model calculations suggest that a period of 50-100 yr could account for the observed changes in nebular morphology.

3.3 POLARIMETRIC OBSERVATIONS

3.3.1 OBSERVATIONAL DETAILS

The sets of polarimetric data discussed in this chapter were gathered during two separate observing runs. The first observations were carried out during September and October 1998 using the 1.9m South African Astronomical Observatory (SAAO) telescope in Sutherland, South Africa. Data collection was taken at the telescope's Cassegrain focus, which has focal ratio of f/18. During the observing run, data was collected through both R and Hα filters. Both R-band and Hα filters were used for the collection of linear polarization data. The characteristics of filters used in the collection of data with the Durham Imaging Polarimeter are included in table 3.3. A review of the characteristics of filters commonly used in astronomical observations is also included in table 3.4.

FILTER	λ_{MAX} (nm)	λ_{MEAN} (nm)	FWHM (nm)
Broadband V	525	545	130
R	595	663	157
Hα	656	661	70

Table 3.3: Characteristics of filters used with the Durham Imaging Polarimeter

FILTER	$\lambda_{CENTRAL}$ (nm)	BANDWIDTH (nm)
R	700	220
I	900	240
J	1250	280
H	1600	280
K	2200	480
L	3500	700

Table 3.4: Characteristics of other filters commonly used in Astronomical Observation

The instrument detector used in data collection was a SiTe (Tektronix) CCD measuring 512×512 pixels. The pixel dimensions are 27μm×27μm, which give adequate spatial resolution for this type of object. The detector is thinned to allow greater quantum efficiency over the shorter wavelength range. For the particular telescope/instrument/detector combination, the final image scale of the sky was 0.5 arcseconds per pixel. At the most recent quoted distance of 640 pc (Schwarz et al. 1997), the image scale corresponds to a true scale

of ~ 0.0015 pc per pixel. During the entire observing run seeing conditions remained relatively constant, varying between 2.0 and 2.5 arcseconds. A number of images, however, displayed worse seeing due to increased zenith distance of the object. Seeing disc diameters were determined using the full width half maximum (FWHM) measures of field star images.

Due to the favourable orientation of M2-9 upon the plane of the sky, broadband V, R, and Hα data were collected at one telescope position only, since the object could be fitted and aligned between successive plates of the grid mask. 32 CCD frames of the object were taken with the polarimeter configured to collect linearly polarized light. 16 frames were collected for the R-band dataset and 16 frames for the Hα dataset. These were supplemented with suitable sky and dome flatfields. Due to the nature of the nebula, a large dynamical intensity range was observed in the data. Consequently, a range of exposure levels was taken. For the R filter, integration times varied between 30 seconds, capturing only the central core of the nebula, up to 120 seconds to account for the low surface brightness of the faint outer nebulosity contained in the arcs and ansae. For the Hα filter, integration times were increased to account for the decrease in throughput of the smaller passband. Consequently, exposures ranged from 60 seconds for the nuclear region, up to 300 seconds for the outer nebular regions.

Previous Hα data gathered upon the 3.9m Anglo-Australian Telescope (AAT) has been compared with recently gathered data, but displays a larger image scale of 0.31 arcseconds per pixel. No data resampling was conducted, however, as a direct comparison could be made with the published data. No significant differences were observed between the 1991 and 1998 data, although a full discussion will be made later in this chapter.

Data collected during the second observing run were obtained during May and June 1999. Measurements were taken upon the 1.9m SAAO telescope at the Cassegrain focus. Instrument and detector characteristics remained the same as those of the previous observing run. Only linear polarization data were gathered, using broadband V and R-waveband filters. A total of 32 CCD frames were made. 12 of these frames form the R-band dataset, while the remainder form the V-band dataset. A number of frames are affected by shifts in telescope focus and unfavourable weather conditions. The majority of image frames, however, possess good signal-to-noise and have provided ample data for reduction. Integration times for the R filter were 30 seconds for the nebular core and 300 seconds for the fainter nebular regions. Integration times for the V filter were also 300 seconds, although a number of the frames required 600 second exposures because of telescope focus problems and ridge cloud.

3.4 RESULTS

3.4.1 IMAGE DETAILS

To aid in the discussion of polarimetric findings for M2-9, a number of pictorial representations are included within the text. Figures 3.3 through 3.17 represent broadband V, R and Hα data for M2-9. All images are oriented with north at the top and east to the left. Each image is centred upon the peak nuclear intensity, and includes a pair of axis labels with an arcsecond scale by which image features may be clearly highlighted. Unless otherwise stated, the greyscale and contour maps represent images of total intensity, with regions of highest intensity being indicated by darker coloration. A number of images show the fraction of polarized intensity within the object. These images are accompanied by corresponding isophotal contours. Like the total intensity contours, the polarized intensity contours are plotted logarithmically so as to encapsulate the large intensity range of the nebula. Polarization data are plotted with suitable intensity cuts or signal-to-noise cuts to eliminate randomly orientated and spurious results. Polarization vectors were calculated by the binning of data. Depending upon the size and magnification of the image, data were integrated into square bins which were moved by suitable amounts to either smooth data or check its consistency. Ideal representation of data came from the use of bin sizes and step sizes set to either 5 pixels moved on by 3 pixels, or 3 pixels moved on by 2 pixels. However, a check was made upon the continuity of the data by placing it in independent bins. It appears that the data display good continuity after independent checks, implying that smoothed data could be used alone in the discussion.

The nature of the Hα interference filter produced a number of ghost image artefacts in the image plane of the instrument. Suitable image cropping and intensity cuts meant that the artefacts could be eliminated. However, a number of problems were removed through the application of corrective measures. The most prominent of these problems were those of normalization and image misalignment. Both normalization and misalignment problems have largely been removed from the final data, although the effects are still observable within the images of polarized intensity. Artefacts observed during data reduction included the effects of electromagnetic cascades produced as a result of cosmic ray interactions with molecules in the upper atmosphere. The effects of electromagnetic cascades were removed by the use of flagging software. High levels of noise were also found in a number of images due to unfavourable atmospheric conditions. Data images affected by cloud cover were not used in the data reduction, but were discarded, since the number of affected images was very small.

3.4.2 THE EFFECTS OF INTERSTELLAR POLARIZATION

M2-9 is positioned at Galactic co-ordinates (l=10°, b=+18°.1). Though its galactic latitude is quite large and its most recently quoted distance of 640 pc reasonably small, it still suffers from the extinction effects of the ISM. A look at the graphical representation in §2 of linear polarization data made available by Axon & Ellis (1976) suggests that influence from the ISM would account for levels of ISP approximately 3 – 4 % in magnitude, at a position angle around 60° – 70°. Measurements previously gathered by Scarrott et al. (1993) assume that the polarization level of the nebular core (3.9 % ± 0.25 % at position angle 77° ± 1.9° in Hα) is solely due to ISP.

It was found that ISP in Hα measured 3.3 % ± 0.3 % at a position angle of 81.6° ± 2.2°. The result confirms that the polarization results for M2-9 are strongly affected by the effects of the ISM. The newly gathered measurements in broadband V and R-waveband provide ISP results of a similar magnitude to the ISP level determined in Hα. The value of ISP for broadband V data was found to be 2.8 % ± 0.3 % at a position angle of 78.7° ± 3.3°. The magnitude of ISP for R-band data was found to be 2.8 % ± 0.2 % at a position angle of 75.9° ± 1.5°. Results were gathered through the use of aperture polarimetry upon the nebular core, surrounding field stars, and the northern bow-shock ansa. Selected field stars were chosen to meet several criteria. These criteria were based upon radial distance from the nebula and grid edges, angular size and intensity, and the presence of pixel saturation. Various aperture sizes were used in the analysis, ranging from 10 pixels (corresponding to ~ 0.03 pc at a distance of 640 pc) to 6 pixels (corresponding to ~ 0.019 pc at 640 pc). The measurements showed a large range in both polarization magnitude and position angle for the field stars. Light from these stars travels different distances before reaching the observer and will therefore suffer different degrees of extinction. Consequently, only polarization measurements from the nebular core and nebular ansae have been used to determine the value of ISP for the three filters. Data from analysis of the nebular core is shown in tables 3.5, 3.6, and 3.7, with measurements taken at a variety of aperture sizes. These tables show the results of aperture polarimetry for broadband V, R, and Hα respectively. Polarization levels found within the nebular condensation N3 and the surrounding field stars were considerably different from polarization measured in the nebular core, with values differing more than 5 % in some cases. Although a number of the field stars displayed erroneous results, the majority of stars show similar results. The polarization level found within the foreground star and the nebular knot N3 were higher than those from the nebular core, which suggests that ISP is differential across the face of M2-9. The fact that the authors results do not coincide with those of Scarrott et al. (1993) reveals the difficulty in obtaining precise values for ISP.

Aperture Size (Pixels)	Pixel Coordinates	Polarization (%)	Polarization Error ± (%)	Position Angle (°)	Position Angle Error ± (°)	Waveband
10	233.083, 254.796	3.833	0.290	71.031	3.562	VV
10	233.083, 257.275	2.862	0.277	74.630	4.387	VV
10	233.083, 259.754	2.546	0.783	79.587	5.033	VV
10	236.459, 259.754	2.828	3.288	80.274	2.695	VV
10	236.459, 257.275	2.839	1.754	78.622	2.911	VV
10	236.459, 254.796	3.034	1.608	79.834	2.616	VV
10	240.431, 254.796	2.203	3.463	89.185	4.097	VV
10	240.431, 257.275	2.147	5.307	78.196	3.559	VV
10	240.431, 259.754	2.750	2.421	72.171	3.008	VV
8	233.083, 254.796	4.210	0.496	65.143	3.374	VV
8	233.083, 257.275	2.818	0.381	68.151	3.870	VV
8	233.083, 259.754	2.178	0.415	77.789	5.453	VV
8	236.459, 259.754	2.726	0.233	81.550	2.450	VV
8	236.459, 257.275	2.638	0.249	79.993	2.706	VV
8	236.459, 254.796	2.928	0.249	81.085	2.437	VV
8	240.431, 254.796	1.754	0.381	94.005	6.222	VV
8	240.431, 257.275	1.808	0.280	73.620	4.440	VV
8	240.431, 259.754	2.770	0.327	67.220	3.382	VV

6	233.083, 254.796	4.912	0.476	59.371	2.773	VV
6	233.083, 257.275	3.104	0.316	62.746	2.918	VV
6	233.083, 259.754	1.999	0.389	77.373	5.579	VV
6	236.459, 259.754	2.616	0.217	82.916	2.377	VV
6	236.459, 257.275	2.233	0.200	81.810	2.570	VV
6	236.459, 254.796	3.027	0.242	82.709	2.294	VV
6	240.431, 254.796	1.641	0.506	113.052	8.831	VV
6	240.431, 257.275	1.466	0.342	62.911	6.676	VV
6	240.431, 259.754	3.037	0.444	60.557	4.185	VV

Table 3.5: V-band aperture polarimetry results for the measurement of ISP. These results have been determined from the analysis of the nebular core only.

Aperture Size (Pixels)	Pixel Coordinates	Polarization (%)	Polarization Error ± (%)	Position Angle (°)	Position Angle Error ± (°)	Waveband
10	221.612, 243.59	3.470	0.14880	76.212	1.480	R
10	221.612, 245.781	2.895	0.27135	76.875	1.232	R
10	221.612, 248.062	2.658	0.69610	101.740	19.797	R
10	224.293, 248.062	2.738	0.25980	77.509	1.820	R
10	224.293, 245.781	2.875	0.31400	78.718	2.400	R
10	224.293, 243.599	3.060	0.29742	77.460	2.182	R
10	226.875, 243.599	2.673	2.00001	71.171	8.372	R

10	226.875, 245.781	2.656	0.77997	60.835	3.514	R
8	221.612, 243.59	3.582	0.134	71.448	1.075	R
8	221.612, 245.781	2.768	0.133	73.410	1.376	R
8	221.612, 248.062	2.586	0.133	77.579	1.472	R
8	224.293, 248.062	2.582	0.150	77.393	1.660	R
8	224.293, 245.781	2.760	0.148	76.670	1.539	R
8	224.293, 243.599	2.956	0.149	77.146	1.443	R
8	226.875, 243.599	2.566	0.151	82.107	1.684	R
8	226.875, 245.781	2.503	0.150	76.508	1.715	R
6	221.612, 243.59	3.847	0.136	71.090	1.010	R
6	221.612, 245.781	2.839	0.134	72.462	1.348	R
6	221.612, 248.062	2.625	0.133	77.575	1.454	R
6	224.293, 248.062	2.466	0.150	77.367	1.746	R
6	224.293, 245.781	2.442	0.149	77.001	1.744	R
6	224.293, 243.599	2.924	0.149	78.171	1.461	R
6	226.875, 243.599	2.674	0.152	84.021	1.629	R
6	226.875, 245.781	2.468	0.150	77.057	1.745	R

Table 3.6: R-band aperture polarimetry results for the measurement of ISP. These results have been determined from the analysis of the nebular core only.

Aperture Size (Pixels)	Pixel Coordinates	Polarization (%)	Polarization Error ± (%)	Position Angle (°)	Position Angle Error ± (°)	Waveband
10	221.688, 246.057	3.214	0.253	79.780	2.251	Hα
10	221.688, 194.523	3.059	0.240	79.756	2.244	Hα
10	221.688, 229.233	3.670	0.244	84.505	1.901	Hα
10	224.269, 306.513	3.484	0.229	83.677	1.883	Hα
10	224.269, 320.955	2.586	0.234	79.519	2.596	Hα
10	224.269, 175.363	2.944	0.235	81.802	2.285	Hα
10	226.707, 166.427	2.168	0.179	110.772	2.371	Hα
10	226.707, 287.065	1.483	0.178	105.404	3.443	Hα
10	226.707, 301.307	1.516	0.179	109.044	3.387	Hα
8	221.688, 246.057	3.657	0.269	82.353	2.106	Hα
8	221.688, 194.523	3.361	0.241	81.287	2.053	Hα
8	221.688, 229.233	4.219	0.253	88.339	1.720	Hα
8	224.269, 306.513	4.288	0.220	86.634	1.471	Hα
8	224.269, 320.955	2.994	0.222	84.965	2.123	Hα
8	224.269, 175.363	3.735	0.229	82.323	1.754	Hα
8	226.707, 166.427	2.488	0.181	114.341	2.085	Hα
8	226.707, 287.065	2.024	1.179	118.773	2.527	Hα
8	226.707, 301.307	1.967	0.180	115.505	2.624	Hα

6	221.688, 246.057	4.199	0.303	82.659	2.063	Hα
6	221.688, 194.523	3.658	0.255	83.643	1.994	Hα
6	221.688, 229.233	4.662	0.267	93.222	1.642	Hα
6	224.269, 306.513	5.192	0.219	90.119	1.205	Hα
6	224.269, 320.955	3.739	0.207	86.432	1.584	Hα
6	224.269, 175.363	4.811	0.229	82.271	1.364	Hα
6	226.707, 166.427	5.343	0.250	76.421	1.338	Hα
6	226.707, 287.065	3.953	0.227	80.369	1.641	Hα
6	226.707, 301.307	5.384	0.240	85.827	1.277	Hα

Table 3.7: Hα aperture polarimetry results for the measurement of ISP. These results have been determined from the analysis of the nebular core only.

3.4.3 INTENSITY IMAGES – V BAND

Analysis of the broadband V image of M2-9 shown in figure 3.3 (p84) reveals the prominent bipolar structure of the object and explains the 'butterfly' appearance. Both the central core and inner nebular wings possess high levels of surface brightness above the noise level which is governed by the signal of the sky. Isophotal contours show two sources within the region of the equatorial plane. The source which is offset west by ~ 6 arcseconds from the plot centre is a foreground star. The other source, however, marks the location of the nebular condensation which obscures the central star. The intensity contours of the nebular core appear slightly elongated in the east-west plane. This provides evidence for the existence of a circumstellar disc around the central star of M2-9. Both greyscale and isophotal data clearly show the north and south lobe condensations which possess the unusual characteristic of 'mirror-symmetry'. Using the designations first used by Kohoutek & Surdej (1980), the V-band total intensity data includes labels for the nebular condensations. Table 3.8 shows the positions of the nebular condensations for broadband V data. No comparison has been made with the results gathered by Kohoutek & Surdej (1980) or Scarrott et al. (1993) as positional data appears to have been collected in Hα only. A further feature of figure 3.3 is the contrast in the intensity gradient between the planes parallel and perpendicular to the equatorial plane. A readily

discernible increase in intensity gradient is observed normal to the polar symmetry axis. This occurs at the lateral extremities of the bipolar outflow and is indicative of limb-brightening due to an increase in the mass and density of material within those regions of the nebula.

Condensation Designation	Offset North (arcseconds) 1999	Offset West (arcseconds) 1999
N1	4.250	-0.902
N2	9.340	-2.542
N3	12.387	0.191
S1	-3.100	-0.937
S2	-10.004	-3.600
S3	-11.756	-1.630

Table 3.8: V-band positional data for the nebular condensations of M2-9

3.4.4 INTENSITY IMAGES – R BAND

Figure 3.8 (p94) shows a significant degree of similarity with the broadband V image, although subtle differences in structure appear in the inner nebular condensations and nebular core when compared with V-band data. The intensity isophotes of the nebular core in figure 3.8 reveal no evidence for the existence of an elongated central source. The east-west angular extent of the central condensation has a diameter of ~ 7 arcseconds in both V-band and R-band data. However, the R-band intensity contours show a greater extension of the nebular core to the immediate north and south. For this reason the nebular condensations N1 and S1 remain poorly defined when compared with V-band results. Although the southern condensation S1 is more clearly visible than its northern counterpart, it remains unresolved from the nebular core. Table 3.9 shows the positions of the nebular condensations for R-waveband data. Once again, comparison has not been made with previous results. The degree of limb-brightening observed in figure 3.8 appears lower than is present in the V-band data. This is clearly seen from the intensity gradient at the edges of the nebular lobes. However, isophotal contours and greyscale intensity data clearly reveal the bubble-like feature in the southern lobe. Like the V-band image, the R-band image shows little indication of a wind-blown bubble in the northern lobe. This is explained by the region of enhanced emission which crosses the northern lobe between ~ 6 – 9 arcseconds above the equatorial plane. A similar region of emission exists within the southern lobe, although it appears less well defined. This band of emission crosses the southern lobe between ~ 4 – 7 arcseconds below the equatorial plane.

Condensation Designation	Offset north (arcseconds) 1999	Offset West (arcseconds) 1999
N1	4.060	-0.750
N2	9.871	-2.121
N3	12.207	0.341
S1	-3.940	-1.161
S2	-10.013	-3.893
S3	-11.857	-1.690

Table 3.9: R-band positional data for the nebular condensations of M2-9.

3.4.5 INTENSITY IMAGES – Hα

Inspection of figure 3.13 (p104) reveals that the Hα image of M2-9 is very similar to both V-band and R-band images. The Hα image of the nebular core appears slightly smaller than in the other two wavebands, with a measured diameter of ~6 arcseconds. Because the difference in angular size between the different wavebands is smaller than the size of the recorded seeing disc, the difference is insignificant. The bubble-like structure of the southern lobe which features in V-band data, also features strongly in Hα. The bands of enhanced emission also feature in the Hα image, but appear at 4 – 8 arcseconds north and 3 – 7 arcseconds south of the equatorial plane. It is observed in the northern lobe that these bands of emission encircle the collimated outflow of the central source. The intensity isophotes are clearly distorted and appear to curve downward, particularly at the western edge of the lobe.

The structure of the nebular condensations in Hα appears very similar to V-band and R-band results, although differences do occur. The southern nebular condensation S1 features more strongly in Hα, but remains indistinct from the nebular core. The northern condensation N1, however, remains poorly defined due to the effects of increased obscuration. The obscuration can be observed by its effect upon the shape of the isophotal contours to the west of N1. The maxima of the lobe condensations N2 and S2 appear well defined, which enables their positions to be accurately compared with those determined by Kohoutek & Surdej (1980) and Scarrott et al. (1993). Isophotal data also shows that the condensations N2, N3, S2, and S3 feature strongly and display differences in brightness structure to the other wavebands.

Comparison of positional data collected in 1986 and 1992 by Scarrott et al. (1993) with data collected in 1977 by Kohoutek & Surdej (1980) shows that very subtle differences occur in the offset locations of the intensity maxima of the nebular condensations. However, Scarrott et al. concluded that the nebular condensations have not moved from the positions measured by Kohoutek & Surdej. Furthermore, Scarrott et al. suggested that the regular rotation of the nebular condensations about the major axis of M2-9 is a fallacy.

Measured by Scarrott et al. (1993), the positions of the nebular condensations have changed very little since the first observations of this kind by Kohoutek & Surdej (1980). The position of the central maxima of the nebular condensations is again reviewed in the current study with comparative discussion against previous results. Table 3.10 and table 3.11 shows the results of the analysis for the Hα data, together with a comparison of results by Scarrott et al. (SSW) and Kohoutek & Surdej (KS) respectively.

Condensation Designation	Offset North (arcseconds) 1999	Offset West (arcseconds) 1999	Offset North (arcseconds) 1992 (SSW)	Offset West (arcseconds) 1992 (SSW)	Offset North (arcseconds) 1986 (SSW)	Offset West (arcseconds 1986 (SSW)
N1	3.480	-0.760	4.03	-2.36	-	-
N2	9.480	-2.330	10.00	-3.88	9.5	-2.5
N3	12.480	0.670	14.31	0.14	13.5	0.16
S1	-3.520	-1.152	-4.17	-2.50	-	-
S2	-10.020	-3.830	-11.25	-4.44	-11.1	-4.0
S3	-11.910	-1.830	-13.62	-0.83	-	-

Table 3.10: Comparison of Hα positional data measured by Scarrott et al. (1993) and Hα gathered by the author.

Condensation Designation	Offset North (arcseconds) 1999	Offset West (arcseconds) 1999	Offset North (arcseconds) 1978 (KS)	Offset West (arcseconds) 1978 (KS)	Offset North (arcseconds) 1952 (KS)	Offset West (arcseconds) 1952 (KS)
N1	3.480	-0.760	3.65	-2.32	4.34	2.27
N2	9.480	-2.330	8.40	-2.58	8.64	3.58
N3	12.480	0.670	14.02	-0.45	14.14	1.04
S1	-3.520	-1.152	-4.44	-1.97	-4.16	2.32
S2	-10.020	-3.830	-10.63	-2.96	-11.08	4.38
S3	-11.910	-1.830	-13.21	0.31	-13.88	1.32

Table 3.11: Comparison of Hα positional data measured by Kohoutek & Surdej (1980) and Hα gathered by the author.

Comparison of present positional data with that from 1986, reveals that the nebular condensations N1, N2, S1, and S2 show little change in their location. However, comparison of present data with that gathered in both 1986 and 1992, shows that in 1992 the nebular condensations were offset east of the measured positions in 1986 and 1999. Consequently, it is proposed that the nebular condensations moved from the back of the lobes until they displayed similar offsets at the front of the lobes. However, depending upon the

direction of rotation about the major axis of M2-9, positional data could suggest that the nebular condensations have moved from the front to the back of the lobes

Following the rotational motion and corresponding lateral displacement of the nebular condensations, simple calculations reveal that the projected displacement is ~0.22 arcseconds per year. The period of full rotation then corresponds to 70 – 80 yr. This agrees particularly well with the result of revised calculations by Goodrich (See Scarrott et al. 1993), who suggests that the displacement of nebular condensations may be fitted with a rotational period of 65 – 75 yr.

3.5 POLARIZATION RESULTS

3.5.1 V-BAND, ISP UNCORRECTED

Broadband V linear polarization data for M2-9 are shown in figures 3.4 through 3.7. The maps of figures 3.4 and 3.5 present data which are uncorrected for the effects of ISP. Each map shows two adjacent images which contain both spatial and polarization information. The first of these images incorporates a greyscale intensity image with superposed intensity contours. The second image provides the corresponding polarization data and intensity contours for the image field. The field size has been suitably scaled so as to encapsulate all regions of the nebula for which data with ample signal-to-noise had been collected. Although the outer lobes of the nebula appear in the V-band data, only the inner lobes and the nebular core are featured in the pictorial data representations. The intensity contours are logarithmically spaced at intervals of 0.3 magnitudes and the polarization vectors have been placed in square bins of size 5 pixels (2.5 arcseconds) which are spaced at intervals of 3 pixels (1.5 arcseconds). For the most recently quoted distance to M2-9 of 640 pc, one arcsecond upon the image corresponds to a true distance of some 0.003 pc or ~640 AU in the plane of the sky. This would then imply that the total size of the nebula is ~0.4 pc or ~76800 AU.

Both figures show several interesting features in the pattern of polarization. These features include enhanced regions of polarization and the weak signature of centro-symmetric scattering. Indication of centro-symmetric scattering is clearly noted within the region close to the nebular core, out to a radial distance of ± 8 arcseconds. Beyond 8 arcseconds, the indication of centro-symmetry becomes less distinct. Clearly apparent is the distortion upon the polarization vector pattern from that which is expected from a simple reflection nebula. The elliptical distortion of polarization vectors has been interpreted as the result of a spatially extended east-west illuminating source (King et al. 1981; Aspin & McLean (1984). However, Scarrott et al. (1993) later highlighted that ellipticity of the centro-symmetric pattern could be explained by the effects of the ISM. The position of the central illuminating source, however, agrees well with the location identifying the centre of the distorted centro-symmetric polarization pattern.

General examination of the polarization map of figure 3.4 shows that levels of polarization reach over 30%, implying that substantial amounts of dust exist within M2-9. The high levels of observed polarized intensity also indicate that favourable geometric conditions prevail. Inspection of the radial distribution of polarization vectors along the major axis of the nebula within figure 3.4 shows that polarization levels within the region ± 2 arcseconds of the central intensity maximum are low. Because of the high particle densities observed within the circumstellar region of the nebula, the low levels of polarization can be explained by the effects of multiple scattering processes Moving outward, the levels of polarization begin to

increase, reaching a maximum of ~21% between ± 4 - 9 arcseconds from the equatorial plane. Uncertainties in the levels of polarization and position angle within these enhanced bands are ~0.2 – 0.5 % and 0.2 – 0.9 degrees. Beyond ± 9 arcseconds, the levels of polarization begin to decrease and become essentially flat with a magnitude of ~10%. Uncertainty in the measured levels of polarization and the position angle are 0.2 – 0.4 % and 0.6 – 1.4 degrees.

Along the bipolar lobe walls, the levels of polarization increase. Here polarization levels reach ~40 % between + 4 and + 9 arcseconds north, while the levels reach ~31 % between - 4 and - 9 arcseconds south. At radial distances beyond 6 arcseconds north, isophotal data shows that obscuration from the circumstellar disc is reduced. Consequently, the difference in polarization between the northern and southern lobes is attributed to the geometrical effects of nebula inclination. Results would suggest that the southern lobe is inclined towards the observer. Furthermore, polarization within the lobe walls appears different between the eastern and western halves of the nebula. It is observed that polarization levels are lower in the eastern half of the bipolar lobes, with levels showing a decrease of ~ 20 % in the south and ~11 % in the north. This is explained by the high degree of intrinsic emission within the nebular condensations. Greyscale data clearly show that this emission is greatest in the southern lobe, which accounts for the larger decrease in polarization in the south.

Figure 3.5 shows V-band polarized intensity data before the removal of ISP. Differences between polarized intensity and total intensity data are immediately apparent. Like the total intensity image, however, the polarized intensity image shows an open-ended appearance, strengthening the proposal that the bipolar lobes have been blown out at the ends. It can be seen that the image of polarized intensity does not show the east-west asymmetry which is shown in the total intensity image. Instead, polarized emission is largely confined to a pair of bands between ± 4 – 10 arcseconds. Emission is strongest at the eastern and western edges of the bands, presumably due to higher concentrations of scattering particles. Polarized emission also coincides with the bow-shock ansae at ± 14 arcseconds from the equatorial plane. This would suggest that the ansae may be polarized. However, it is observed that the regions of polarized intensity do not coincide with the total intensity maxima of the other nebular condensations. This indicates that the nebular condensations N1, N2, S1, and S2 are unpolarized. The bands of polarized emission coincide almost perfectly with the bands of both enhanced optical emission and enhanced Br γ emission identified by Hora & Latter (1994). Following the work of Goodrich (1991) and Trammell et al. (1995) it is reasonable to assume that enhanced optical, IR, and polarized emission highlights the presence of enhanced concentrations of gas and dust within the discrete bands. Observation that the high density bands encircle the collimated outflow of the central star, suggests that episodic mass loss may have occurred within M2-9.

The outer lobes and ansae of M2-9 are not included in the greyscale, contour, or polarization images because of the low levels of surface brightness which they possess. However, aperture polarimetry

measurements have been taken for both the northern and southern ansae. Results of the analysis using various sized apertures are shown in tables 3.12 and 3.13 for the northern and southern ansa respectively. Results show that polarization levels are extremely high, with levels exceeding 40 % within certain portions of the ansae. Within the northern ansa, average polarization levels range between ~36 % - 44 %, while in the southern ansa, average polarization levels range from ~36 % to 43 %. Uncertainties in the measurements of polarization and the position angle are of the order of 4 - 6 % and 2 - 4 degrees. Clearly the high levels of polarization indicate that substantial amounts of dust reside within the outer lobes and that this dust is optically thin. The small difference in polarization between the ansae of the outer nebular lobes indicates that the outer lobes are inclined only slightly to the plane of the sky.

Aperture Size (Pixels)	Pixel Coordinates	Polarization (%)	Polarization Error ± (%)	Position Angle (°)	Position Angle Error ± (°)	Waveband
10	243.992, 356.260	39.143	4.602	93.158	3.246	VV
10	243.992, 358.045	38.497	4.558	93.391	3.273	VV
10	243.992, 359.830	37.241	5.200	92.986	3.868	VV
10	242.205, 359.830	39.285	4.798	93.116	3.371	VV
10	242.205, 358.045	39.707	4.118	93.690	2.860	VV
10	242.205, 356.260	37.952	4.039	93.586	2.945	VV
10	240.616, 356.260	37.162	4.051	94.119	3.020	VV
10	240.616, 358.045	39.400	4.190	94.037	2.935	VV
10	240.616, 359.037	40.280	4.473	93.955	3.060	VV
10	240.616, 359.830	39.983	4.874	94.276	3.360	VV
8	243.992, 356.260	37.666	4.245	94.772	3.120	VV
8	243.992, 358.045	37.729	4.156	94.782	3.049	VV

8	243.992, 359.830	35.529	4.828	94.458	3.776	VV
8	242.205, 359.830	38.986	4.471	94.020	3.167	VV
8	242.205, 358.045	41.924	3.688	95.047	2.416	VV
8	242.205, 356.260	40.945	3.742	93.453	2.515	VV
8	240.616, 356.260	41.655	3.788	93.834	2.499	VV
8	240.616, 358.045	44.025	3.827	94.356	2.378	VV
8	240.616, 359.037	43.490	4.164	94.000	2.622	VV
8	240.616, 359.830	40.966	4.651	93.538	3.124	VV
6	243.992, 356.260	35.290	4.115	97.236	3.241	VV
6	243.992, 358.045	35.489	3.921	98.062	3.070	VV
6	243.992, 359.830	35.052	4.747	95.872	3.766	VV
6	242.205, 359.830	38.278	4.309	96.680	3.113	VV
6	242.205, 358.045	42.762	3.524	95.011	2.260	VV
6	242.205, 356.260	43.324	3.582	93.582	2.265	VV
6	240.616, 356.260	48.562	3.721	92.250	2.076	VV
6	240.616, 358.045	47.088	3.709	93.432	2.141	VV
6	240.616, 359.037	45.714	4.081	93.945	2.433	VV
6	240.616, 359.830	42.240	4.633	93.994	3.011	VV

Table 3.12: V-band aperture polarimetry for the northern ansa of the outer lobes.

Aperture Size (Pixels)	Pixel Coordinates	Polarization (%)	Polarization Error ± (%)	Position Angle (°)	Position Angle Error ± (°)	Waveband
10	233.958, 156.391	37.340	3.920	90.714	2.908	VV
10	233.958, 157.780	38.825	3.374	89.385	2.401	VV
10	233.958, 159.565	40.659	3.210	88.863	2.174	VV
10	235.051, 159.565	40.698	3.486	88.618	2.358	VV
10	235.051, 157.780	39.525	3.764	88.839	2.627	VV
10	235.051, 156.391	37.119	4.490	89.598	3.352	VV
10	235.845, 156.391	36.681	5.247	88.744	3.967	VV
10	235.845, 157.780	39.844	4.275	88.140	2.959	VV
10	235.845, 158.771	40.632	4.012	88.411	2.719	VV
10	235.845, 159.565	40.910	3.918	88.924	2.635	VV
8	233.958, 156.391	37.587	3.736	89.865	2.752	VV
8	233.958, 157.780	40.996	3.020	89.397	2.027	VV
8	233.958, 159.565	43.090	2.811	88.112	1.787	VV
8	235.051, 159.565	43.120	3.1690	87.838	2.014	VV
8	235.051, 157.780	41.444	3.509	88.632	2.238	VV
8	235.051, 156.391	37.773	4.403	89.447	3.226	VV
8	235.845, 156.391	35.553	5.437	88.515	4.249	VV
8	235.845, 157.780	40.675	4.174	88.159	2.825	VV

8	235.845, 158.771	42.835	3.852	87.348	2.465	VV
8	235.845, 159.565	43.751	3.784	88.114	2.367	VV
6	233.958, 156.391	38.266	4.009	88.719	2.897	VV
6	233.958, 157.780	43.944	2.826	88.604	1.759	VV
6	233.958, 159.565	45.193	2.613	88.218	1.1578	VV
6	235.051, 159.565	44.178	3.105	88.108	1.922	VV
6	235.051, 157.780	42.757	3.404	88.002	2.183	VV
6	235.051, 156.391	36.901	4.827	88.795	3.626	VV
6	235.845, 156.391	35.973	5.829	88.525	4.498	VV
6	235.845, 157.780	40.810	4.306	87.466	2.904	VV
6	235.845, 158.771	42.247	3.873	87.239	2.516	VV
6	235.845, 159.565	43.328	3.727	87.761	2.356	VV

Table 3.13: V-band aperture polarimetry for the southern ansa of the outer lobes.

3.5.2 V-BAND, ISP CORRECTED

Figures 3.6 and 3.7 show V-band linear polarization data which has been corrected for the effects of ISP. Figure 3.6 shows total intensity greyscale data and corresponding intensity isophotes, together with an adjacent polarization image. Interestingly, the elliptical pattern of polarization is still present about the nebular core, implying that ellipticity is caused by the presence of a circumstellar disc rather than ISP. Although ISP has been shown to exist across the face of M2-9, its effect is therefore to reduce the signal of intrinsic polarization of the nebula.

Figure 3.7 shows V-band linear polarized intensity data for M2-9. The figure incorporates total intensity and contour data, with an adjacent polarized intensity and contour map which is corrected for ISP. Both images

incorporate greyscale and contour information. Like the total intensity image, the polarized intensity image shows an open-ended appearance to the lobes. The polarized intensity image also shows that the lobes possess limb-brightening. Comparison of the images of polarized intensity before and after ISP removal shows that little change occurs in the structure of polarized emission. The appearance of the bow-shock ansae N3 and S3 within figure 3.7 would indicate that the ansae are polarized. As explained previously in the discussion of ISP determination, the magnitude of polarization across the face of M2-9 appears to be differential, with measured ISP levels being lower in the nebular centre than across other areas of the nebula. This accounts for the polarized appearance of N3 in particular.

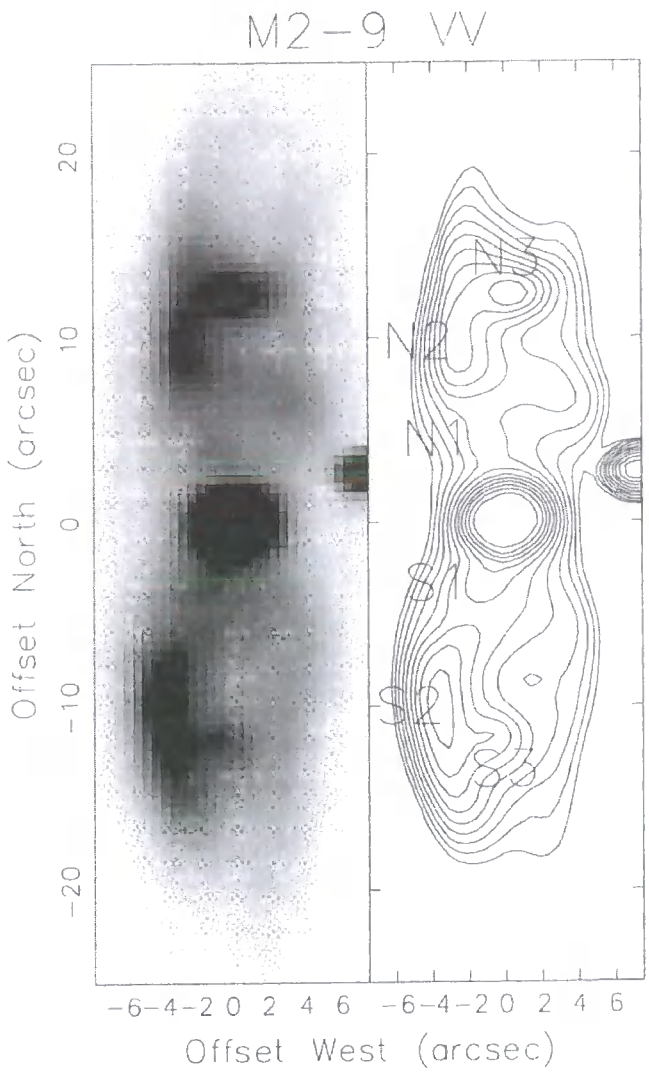

Figure 3.3: Broadband V total intensity image with adjacent intensity contours. Also included are the nebular condensation designations first used by Kohoutek & Surdej (1980)

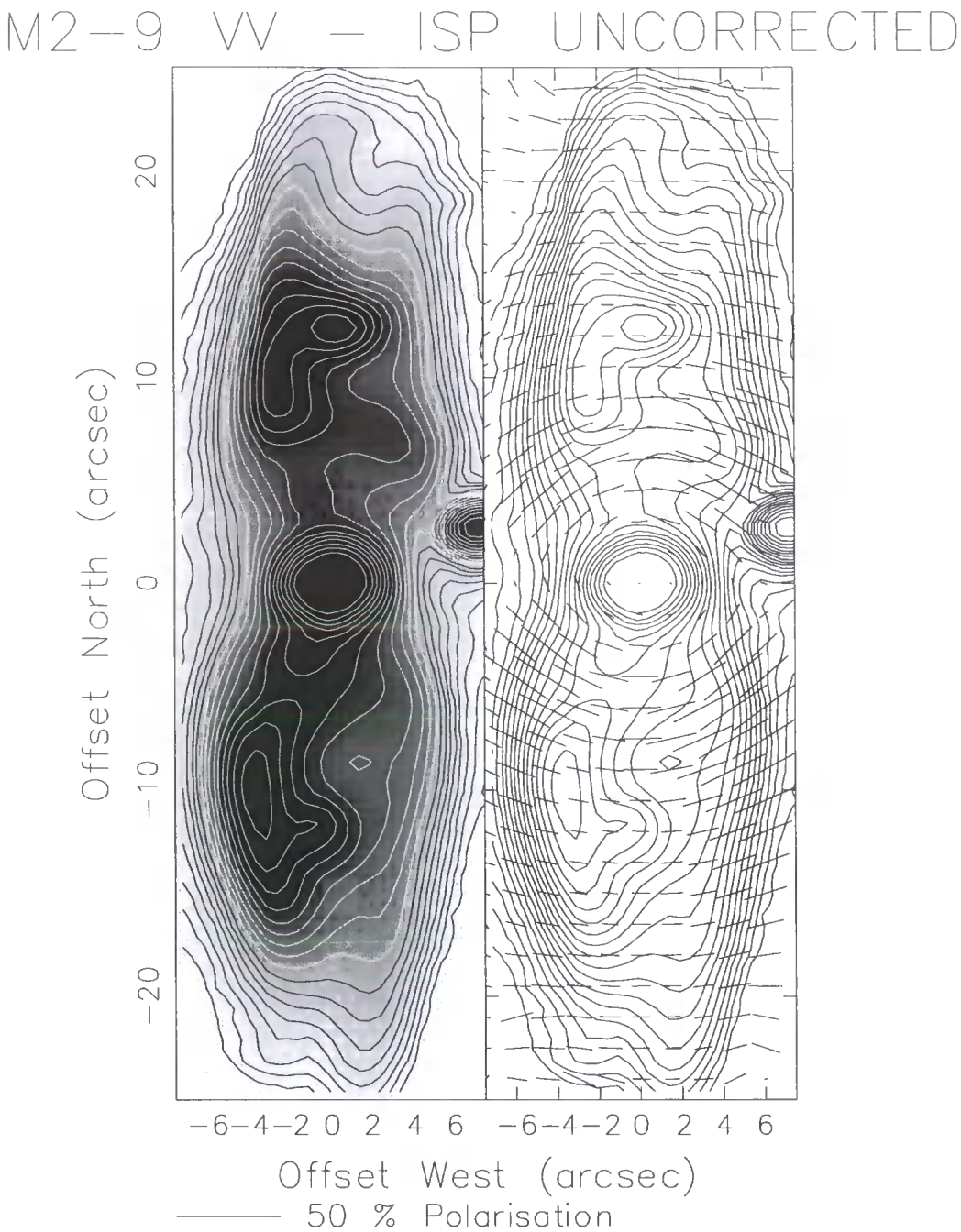

Figure 3.4: Broadband V total intensity greyscale image with superposed contour data, and polarization image with superposed contours. Polarization data are uncorrected for ISP.

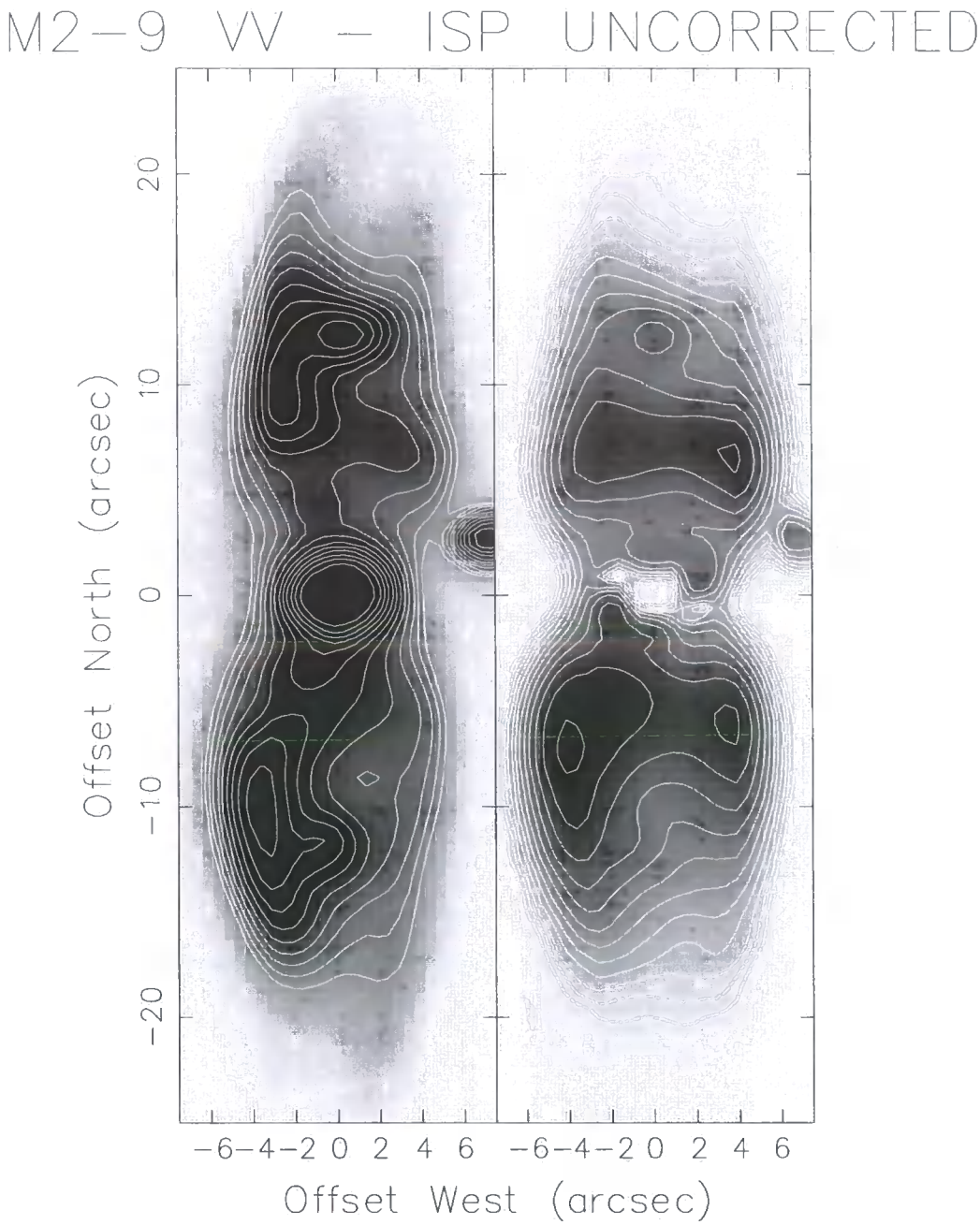

Figure 3.5: Broadband V total intensity greyscale image with superposed contour data, and polarized intensity image with superposed polarized intensity contours. Polarization data are uncorrected for ISP.

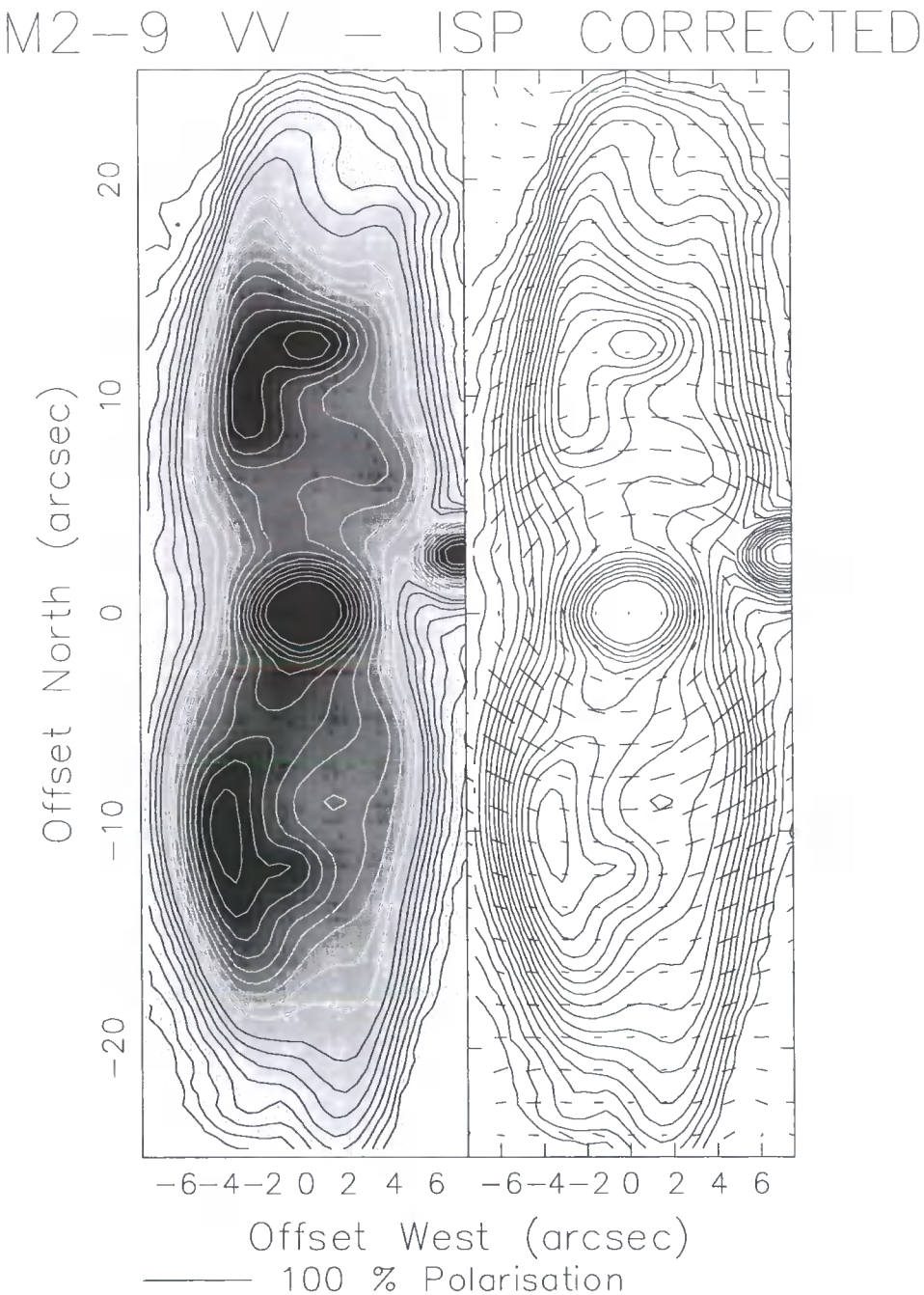

Figure 3.6: Broadband V total intensity greyscale image with superposed contour data, and a map of polarization vectors. Polarization data are corrected for ISP.

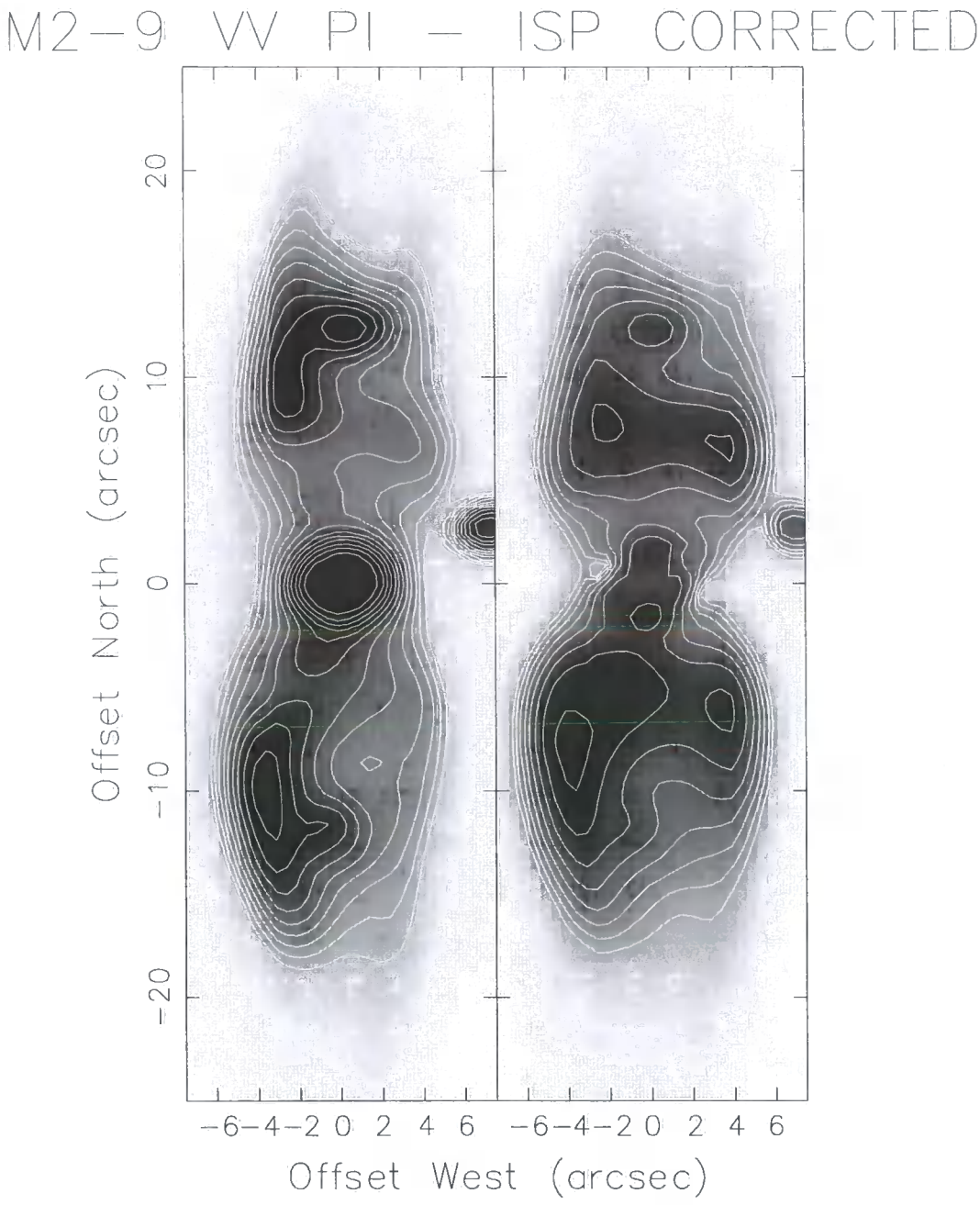

Figure 3.7: Broadband V total intensity greyscale image with superposed contour data, and polarized intensity image with superposed polarized intensity contours. Polarization data are corrected for ISP.

3.5.3 R-BAND, ISP UNCORRECTED

R-band linear polarization data for M2-9 is shown in figures 3.9 through 3.12. The images of figure 3.9 and figure 3.10 present data which are uncorrected for the effects of ISP. All images incorporate both greyscale and polarization data, each with superposed contour data. The field size of both R-band and V-band polarization maps is identical. Consequently, each arcsecond corresponds to a true distance of ~0.003 pc. The intensity contours are logarithmically spaced at intervals of 0.3 magnitudes and the polarization vectors have again been placed in square bins of size 5 pixels (2.5 arcseconds) which are spaced at intervals of 3 pixels (1.5 arcseconds).

Like V-band polarization data, the R-band data within figure 3.9 present several interesting features. Although these polarization structures appear identical to those featured in the V-band, differences are observable. The most prominent of these differences occurs within the region ± 2 arcseconds about the nebular core. R-band data shows a higher level of polarization across the nebular core. This could imply that the level of ISP is higher in the R-band or that intrinsic polarization is higher. Inspection of the radial distribution of polarization vectors along the major axis of the nebula shows that the transition from low to high polarization is more gradual. Outside the inner region of the nebula, the polarization level reaches a maximum of ~19 % between ± 4 - 9 arcseconds from the equatorial plane. Uncertainties in the magnitude of polarization and position angle are of the order of 0.2 % and 0.2 – 0.4 degrees respectively. R-band data also shows an increase in polarization along the walls of the nebular lobes. However, the observed levels of polarization are lower than those found in the V-band data, ranging from ~20 % up to 35 % within the southern lobe, and ~16 % up to 27 % in the northern lobe. Again it is observed that the high levels of polarization occur between ± 4 - 9 arcseconds from the equatorial plane.

The overall pattern of polarization across the inner lobes and nebular core implies that an extended illuminating source exists along the east-west symmetry axis of M2-9. Polarization vectors also suggest that the bipolar lobes are wind-blown bubbles. This is confirmed by limb-brightening of isophotal contours along the walls of the nebular lobes. Together with increased levels of polarization, the steep intensity gradients tracing the lobe boundaries indicate that the walls contain a larger fraction of gas and dust than the lobe interiors.

Figure 3.10 shows R-band polarized intensity data before the removal of ISP. Like the V-band image, R-band polarized intensity differs markedly from the total intensity data. Polarized emission is observed between 4 – 10 arcseconds north and 4 – 9 arcseconds south of the nebular equator. Maxima in polarized emission appear along the eastern and western edges of the nebula. Outside the bands of enhanced polarized intensity, emission also features within the ansa N3. Compared with the V-band polarized intensity image, R-band polarized intensity data shows very poor definition of the bow-shock ansae N3 and S3. Tables 3.14

and 3.15 provide aperture polarimetry data which has been carried out upon the outer ansae of the R-band data.

Aperture Size (Pixels)	Pixel Coordinates	Polarization (%)	Polarization Error ± (%)	Position Angle (°)	Position Angle Error ± (°)	Waveband
10	230.024, 343.963	38.986	3.421	87.891	2.424	R
10	230.024, 345.847	40.427	3.427	86.995	2.340	R
10	230.024, 347.731	34.484	3.861	89.291	3.116	R
10	231.911, 347.731	34.757	3.526	90.613	2.822	R
10	231.911, 345.847	40.688	3.118	88.652	2.110	R
10	231.911, 345.963	41.773	3.163	88.618	2.080	R
10	234.095, 345.963	39.640	3.375	87.049	2.349	R
10	234.095, 345.847	36.565	3.288	90.700	2.494	R
10	234.095, 347.037	34.276	3.418	90.560	2.776	R
10	234.095, 347.731	30.546	3.561	90.5817	3.265	R
8	230.024, 343.963	38.567	3.349	87.795	2.400	R
8	230.024, 345.847	42.860	3.276	87.795	2.096	R
8	230.024, 347.731	38.147	3.843	89.217	2.786	R
8	231.911, 347.731	36.375	3.405	91.608	2.597	R
8	231.911, 345.847	46.634	3.064	87.751	1.788	R
8	231.911, 345.963	43.572	3.113	89.063	1.956	R

8	234.095, 345.963	44.651	3.429	89.253	2.098	R
8	234.095, 345.847	44.765	3.298	90.560	2.012	R
8	234.095, 347.037	38.976	3.370	90.630	2.388	R
8	234.095, 347.731	30.460	3.491	89.959	3.209	R
6	230.024, 343.963	33.768	3.258	88.908	2.688	R
6	230.024, 345.847	42.212	3.389	89.885	2.204	R
6	230.024, 347.731	41.566	4.015	89.641	2.655	R
6	231.911, 347.731	37.784	3.555	87.567	2.604	R
6	231.911, 345.847	50.789	3.214	89.730	1.706	R
6	231.911, 345.963	43.348	3.286	84.121	2.076	R
6	234.095, 345.963	51.926	3.647	91.915	1.889	R
6	234.095, 345.847	56.028	3.555	91.000	1.690	R
6	234.095, 347.037	46.602	3.589	89.967	2.095	R
6	234.095, 347.731	36.419	3.819	89.151	2.909	R

Table 3.14: R-band aperture polarimetry for the northern ansa of the outer lobes.

Aperture Size (Pixels)	Pixel Coordinates	Polarization (%)	Polarization Error ± (%)	Position Angle (°)	Position Angle Error ± (°)	Waveband
10	215.018, 146.112	25.925	10.314	86.399	11.210	R
10	215.018, 147.798	30.630	9.502	83.699	8.686	R
10	215.018, 149.682	29.458	9.654	91.520	9.191	R

10	216.905, 149.682	32.620	5.982	90.448	5.119	R
10	217.004, 147.798	33.050	5.778	88.402	4.877	R
10	216.905, 146.112	26.213	6.358	91.850	6.832	R
10	218.792, 146.112	42.236	3.324	88.544	2.161	R
10	218.891, 147.798	42.329	2.996	89.506	1.943	R
10	218.891, 148.889	43.698	2.950	90.507	1.847	R
10	218.891, 149.682	43.042	2.981	90.960	1.898	R
8	215.018, 146.112	34.700	10.183	92.165	8.165	R
8	215.018, 147.798	32.234	8.773	89.085	7.602	R
8	215.018, 149.682	29.030	8.968	90.499	8.669	R
8	216.905, 149.682	33.787	2.886	86.742	2.380	R
8	217.004, 147.798	36.440	2.784	90.848	2.119	R
8	216.905, 146.112	35.989	3.128	90.169	2.413	R
8	218.792, 146.112	42.563	3.136	90.532	2.021	R
8	218.891, 147.798	41.858	2.774	91.797	1.820	R
8	218.891, 148.889	42.272	2.771	91.669	1.799	R
8	218.891, 149.682	43.008	2.918	91.377	1.860	R
6	215.018, 146.112	46.690	8.545	95.969	4.979	R
6	215.018, 147.798	32.318	6.059	97.908	5.256	R
6	215.018, 149.682	26.527	8.986	88.039	9.538	R

6	216.905, 149.682	33.243	3.066	85.731	2.572	R
6	217.004, 147.798	37.734	2.392	89.475	1.755	R
6	216.905, 146.112	40.942	3.282	92.715	2.206	R
6	218.792, 146.112	42.395	3.211	94.667	2.078	R
6	218.891, 147.798	41.408	2.692	94.0306	1.787	R
6	218.891, 148.889	40.997	2.765	93.455	1.856	R
6	218.891, 149.682	43.984	3.094	93.590	1.924	R

Table 3.15: R-band aperture polarimetry for the southern ansa of the outer lobes.

3.5.4 R-BAND, ISP CORRECTED

Figures 3.11 and 3.12 show R-band linear polarization data which has been corrected for ISP The value used for the level of ISP was 2.8 at a position angle of 76 degrees. Figure 3.11 shows a total intensity greyscale and contour image with an adjacent polarization map. The intensity contours are logarithmically spaced at intervals of 0.3 magnitudes, while the polarization vectors are integrated into square data bins of size 5 pixels which are spaced at 3 pixel intervals.

Analysis of the data shown in figure 3.11 has revealed that negligible change occurs in the pattern of polarization after the removal of ISP. However, it is observed that the magnitude of polarization throughout the nebula is lower than that presented in the data which is uncorrected.

Figure 3.12 shows R-band linear polarized intensity data for M2-9. The figure incorporates total intensity and contour data, with an adjacent polarized intensity and contour map which is corrected for ISP. Comparison of the images of polarized intensity before and after ISP removal shows that little change occurs in the structure of polarized emission. The only discernible change in polarized emission appears in the southern lobe of the nebula. It is observed that the band of enhanced polarized intensity within this lobe shows greater definition, such that maximum emission appears to form a shell structure. This has been shown to be true, as observations by Trammell et al. (1995) revealed the presence of a high density shells

surrounding the lobes of the nebula. The polarimetric observations presented here, show that radiation scattering from these shell structures occurs at their inner edge.

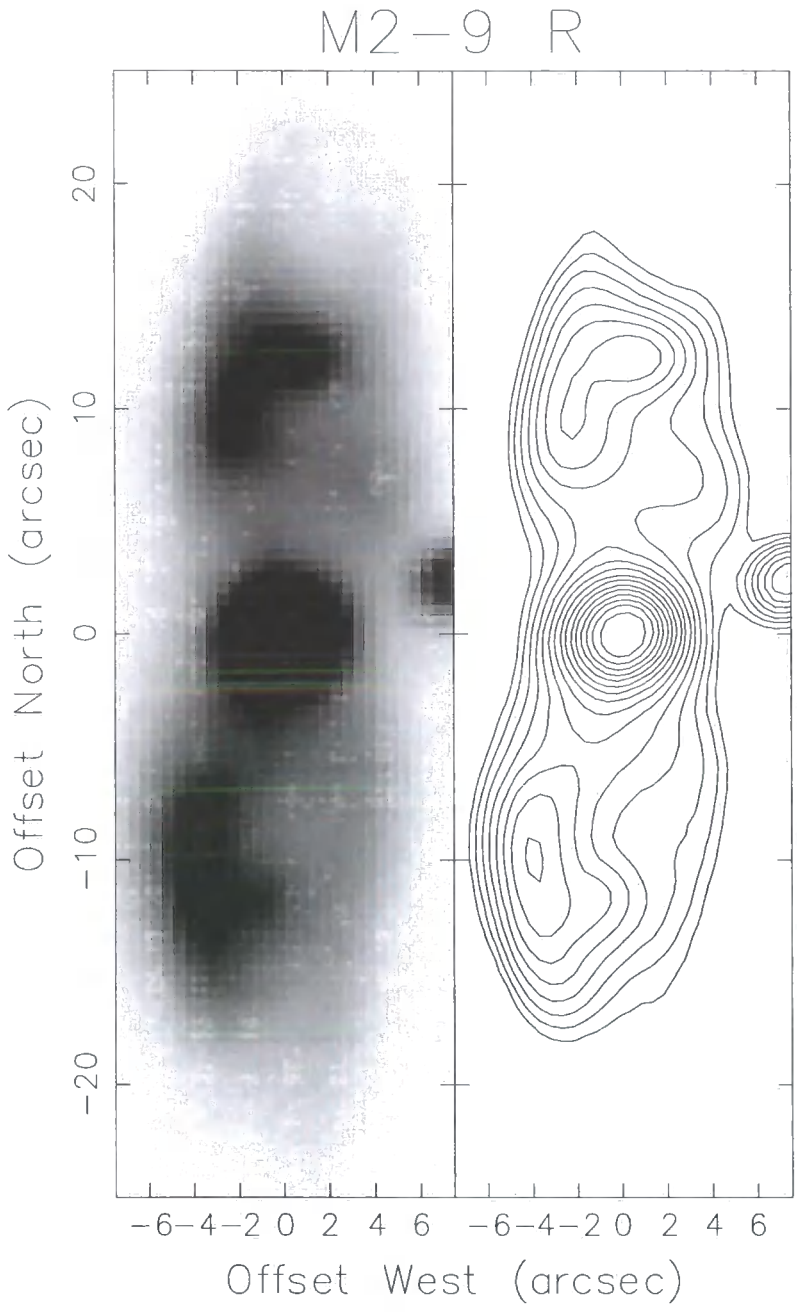

Figure 3.8: R-band total intensity image with adjacent intensity contour data.

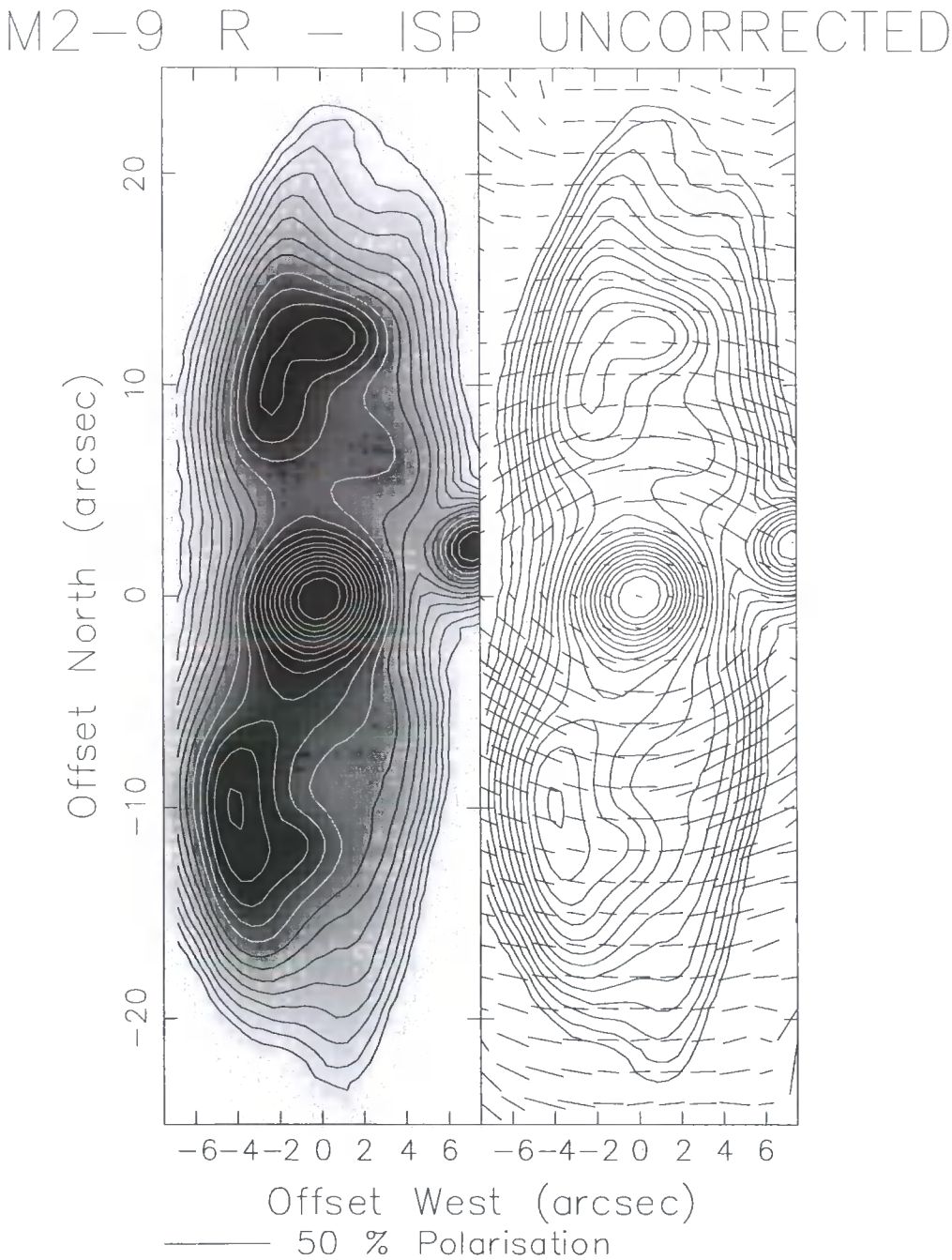

Figure 3.9: R-band total intensity image with superposed contour data, and polarization image with superposed contour data. Polarization data are uncorrected for ISP.

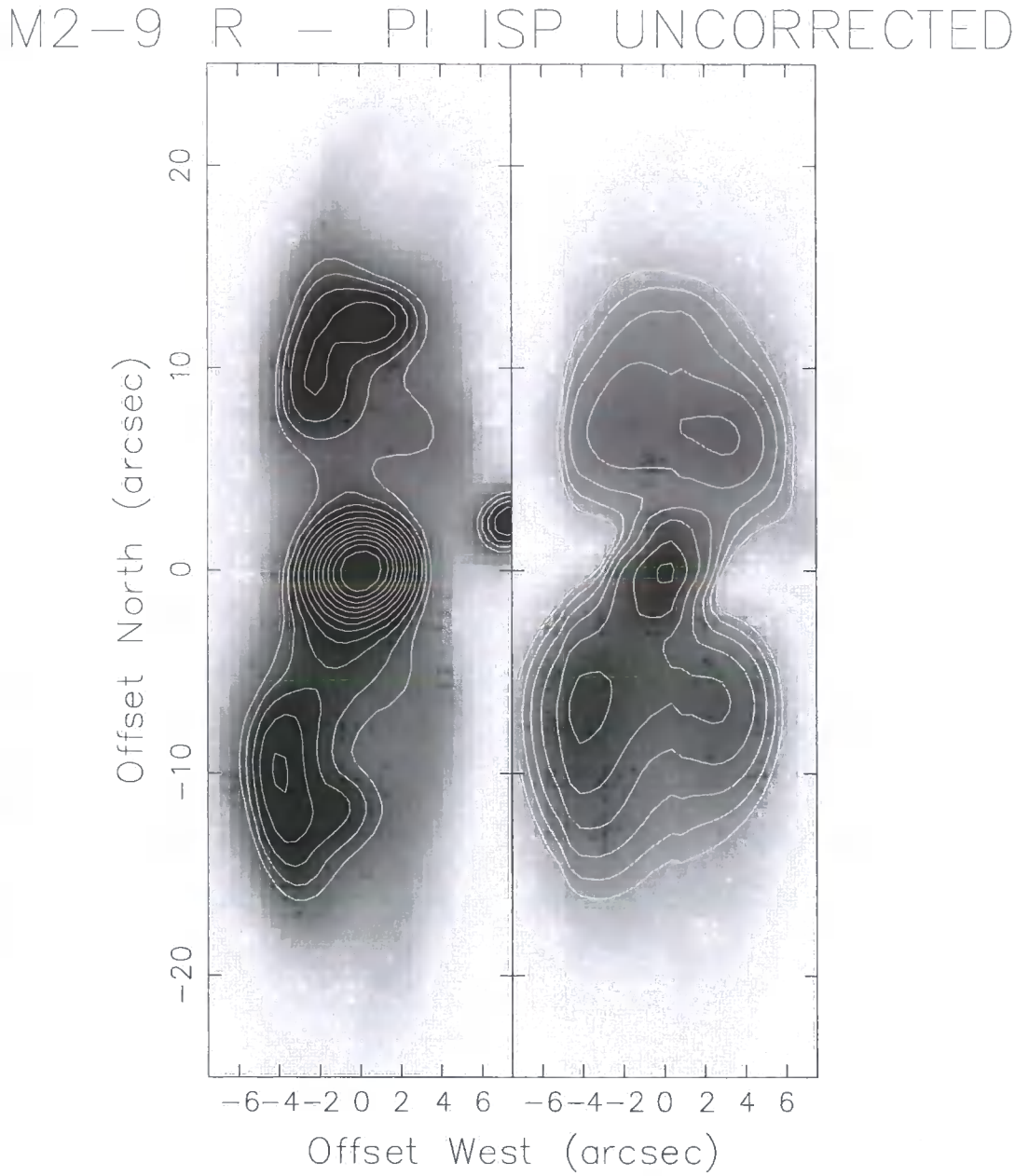

Figure 3.10: R-band total intensity image with superposed contour data, and polarized intensity image with superposed polarized intensity contours. Polarization data are uncorrected for ISP.

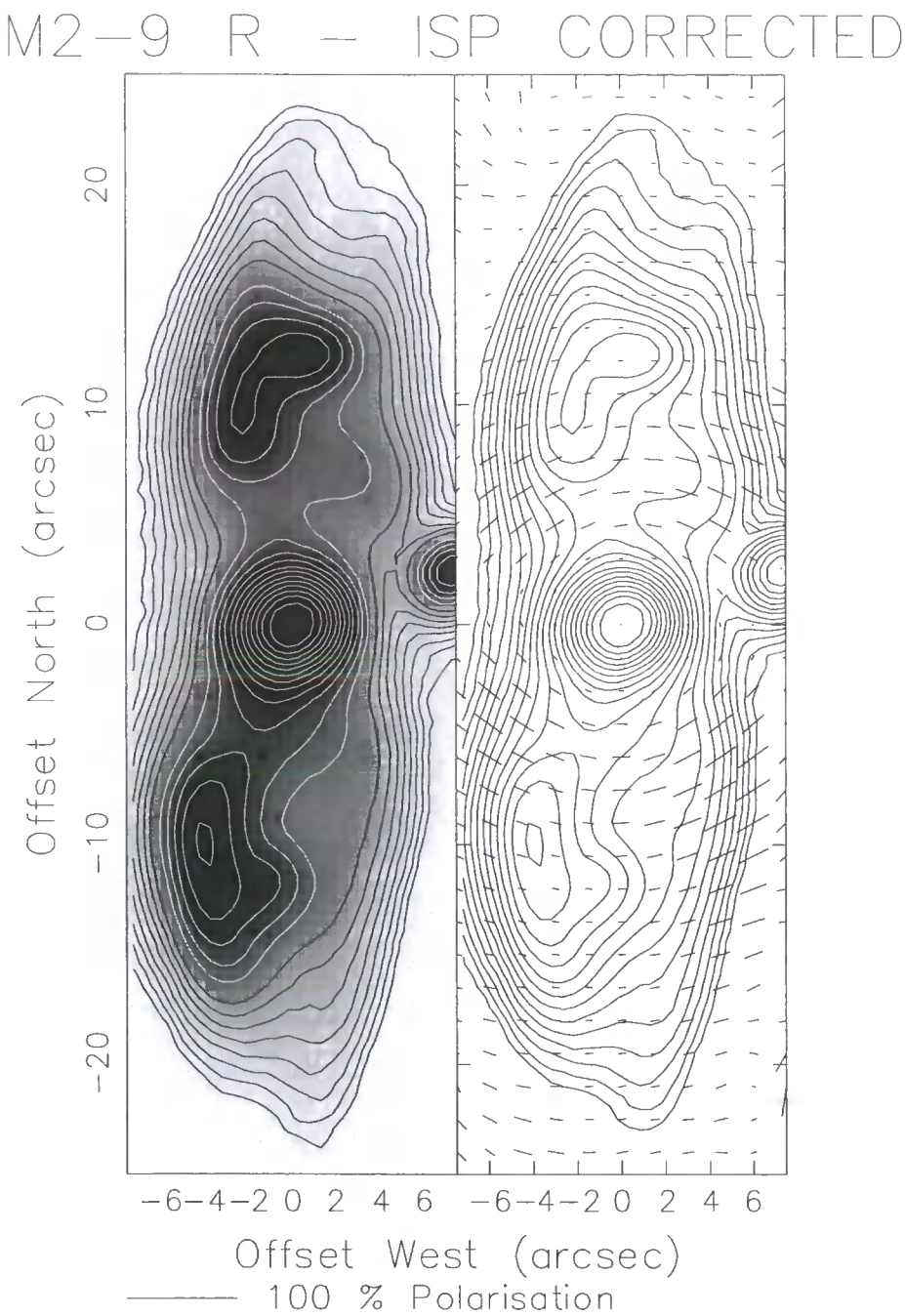

Figure 3.11: R-band total intensity image with superposed contour data, and polarization image with superposed contour data. Polarization data are corrected for ISP.

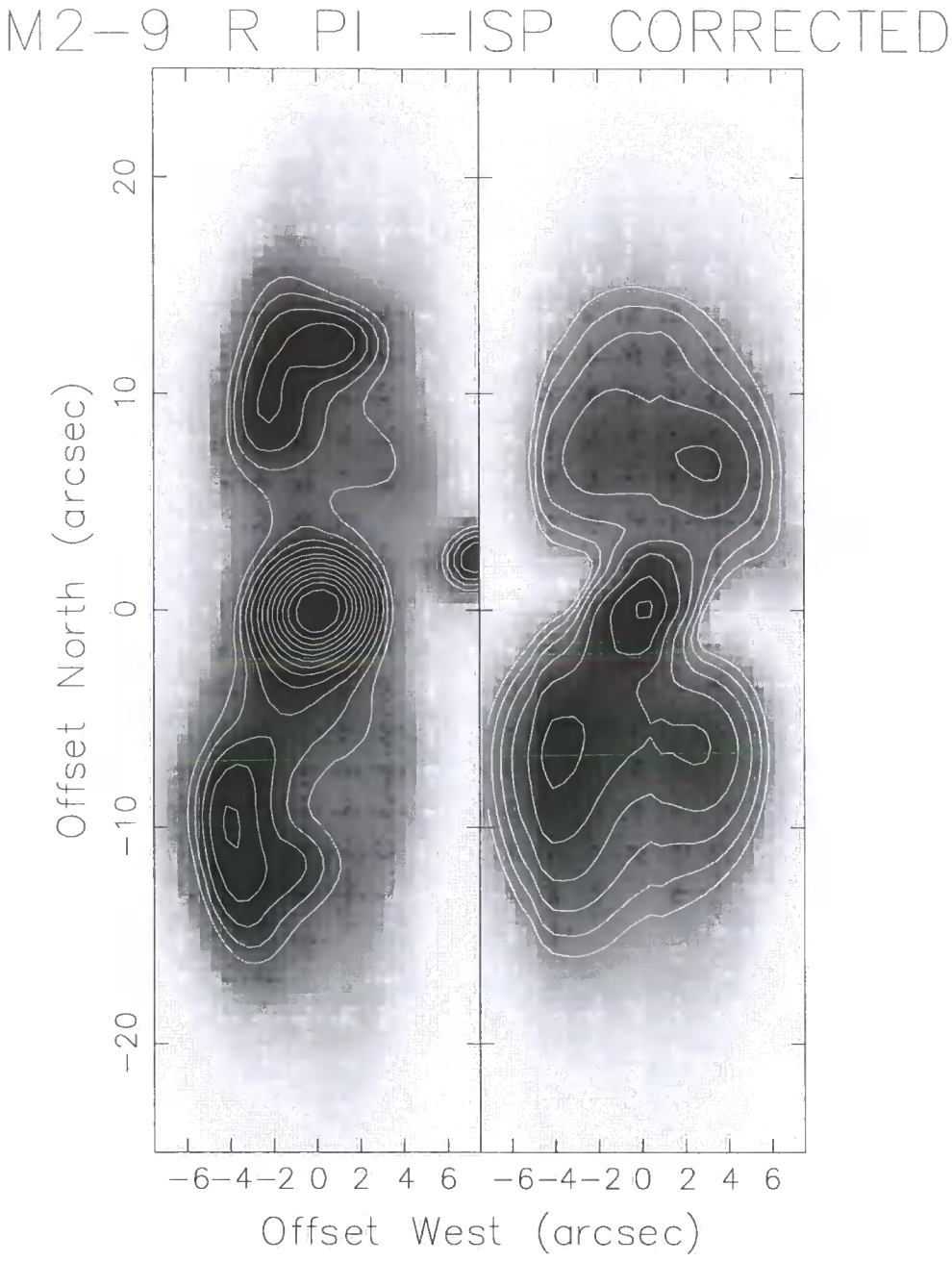

Figure 3.12: R-band total intensity image with superposed contour data, and polarized intensity image with superposed polarized intensity contours. Polarization data are corrected for ISP.

3.5.5 Hα, ISP UNCORRECTED

Figures 3.14 through 3.17 present Hα linear polarization data for M2-9. Data contained in figure 3.14 and figure 3.15 are uncorrected for ISP. The image format for Hα data is exactly the same as that for both V-band and R-band data. Intensity contour data included within the images are logarithmically spaced at intervals of 0.3 magnitudes. Polarization vectors are contained in square integration bins of size 5 pixels and are spaced at intervals of 3 pixels, as for broadband V and R-waveband data.

Inspection of figure 3.14 shows that the pattern and magnitude of polarization in Hα is very similar to that of the V-band and R-band. The radial distribution of polarization vectors along the major axis of the nebula also show a similar character to that presented in the other wavebands. Within the inner nebula, scattering is highest between ± 4 - 9 arcseconds. Polarization which arises through scattering in these bands shows that greatest magnitude in the south, with values ranging from ~23 % to 40 %. In the northern lobe, however, the magnitude of polarization ranges from ~19 % to 31 %. High levels of polarization in Hα indicate that copious amounts of scattering of emission-line radiation from the nebular core occurs, and can even be observed in the outer regions of the M2-9.

Figure 3.15 shows Hα polarized intensity data which are uncorrected for ISP. The similarity in morphology of polarized emission in Hα, R-band, and V-band data shows that Hα emission originates from the same region as continuum emission. Results also suggest that continuum and emission-line radiation experiences similar scattering geometry. In addition, the Hα polarized intensity maxima of the nebular condensations N1, N2, S1, and S2 do not coincide with the maxima of the Hα total intensity image, strengthening the suggestion that the nebular condensations are intrinsically unpolarized.

Aperture polarimetry measurements of the outer lobes and ansae of M2-9 have been taken in Hα. Results of the analysis using various sized apertures are shown in tables 3.16 and 3.17 for the northern and southern ansa respectively. Results show that the overall magnitude of polarization is higher than that for continuum observations. This would suggest that emission-line radiation from both the nebular core and the inner nebular lobes, is scattered in the outer regions of M2-9. Hα observations reveal that polarization levels exceed 50 % in certain portions of the outer lobes. The highest levels of polarization occur within the northern ansa, with average values of ~45 % up to 55 % at a position angle around 90 degrees. In the southern ansa, average polarization ranges between ~45 % and 50 % at similar position angles as those observed in the north.

Aperture Size (Pixels)	Pixel Coordinates	Polarization (%)	Polarization Error ± (%)	Position Angle (°)	Position Angle Error ± (°)	Waveband
10	265.802, 348.317	42.124	1.506	92.746	0.982	Hα
10	265.802, 350.300	40.509	1.506	92.411	1.024	Hα
10	265.802, 352.283	40.904	1.700	91.318	1.144	Hα
10	267.192, 352.283	47.067	1.689	90.340	0.975	Hα
10	267.192, 350.300	47.492	1.499	91.358	0.857	Hα
10	267.192, 348.317	44.277	1.459	92.555	0.901	Hα
10	268.979, 348.317	42.170	1.474	92.302	0.960	Hα
10	268.979, 350.300	50.622	1.563	91.337	0.833	Hα
10	268.979, 351.292	53.690	1.659	88.672	0.828	Hα
10	268.979, 352.283	51.807	1.770	89.675	0.919	Hα
8	265.802, 348.317	45.909	1.561	88.037	0.927	Hα
8	265.802, 350.300	47.647	1.616	88.442	0.921	Hα
8	265.802, 352.283	47.013	1.843	88.928	1.066	Hα
8	267.192, 352.283	52.107	1.778	90.056	0.917	Hα
8	267.192, 350.300	51.694	1.541	88.015	0.802	Hα
8	267.192, 348.317	48.192	1.508	88.732	0.849	Hα
8	268.979, 348.317	47.691	1.545	88.667	0.879	Hα
8	268.979, 350.300	53.222	1.602	88.833	0.807	Hα

8	268.979, 351.292	54.019	1.704	89.117	0.844	Hα
8	268.979, 352.283	53.223	1.851	90.061	0.932	Hα
6	265.802, 348.317	49.041	1.757	88.020	0.970	Hα
6	265.802, 350.300	56.986	1.907	89.794	0.889	Hα
6	265.802, 352.283	53.175	2.229	87.492	1.124	Hα
6	267.192, 352.283	57.465	2.067	90.112	0.955	Hα
6	267.192, 350.300	57.525	1.733	89.066	0.799	Hα
6	267.192, 348.317	50.511	1.667	89.914	0.890	Hα
6	268.979, 348.317	49.629	1.734	88.128	0.945	Hα
6	268.979, 350.300	52.026	1.738	89.439	0.898	Hα
6	268.979, 351.292	51.899	1.840	90.592	0.953	Hα
6	268.979, 352.283	53.0382	2.051	91.610	1.037	Hα

Table 3.16: Hα aperture polarimetry for the northern ansa of the outer lobes.

Aperture Size (Pixels)	Pixel Coordinates	Polarization (%)	Polarization Error ± (%)	Position Angle (°)	Position Angle Error ± (°)	Waveband
10	249.653, 152.231	46.640	1.090	90.254	0.636	Hα
10	251.838, 152.231	47.877	0.978	90.021	0.555	Hα
10	254.420, 152.231	45.554	1.014	90.096	0.607	Hα
10	249.653, 150.842	46.817	1.058	90.483	0.615	Hα

10	251.838, 150.842	46.487	0.958	89.804	0.561	Hα
10	254.420, 150.842	45.144	1.007	89.411	0.609	Hα
10	254.420, 149.057	43.270	1.079	88.695	0.683	Hα
10	251.838, 149.057	46.556	1.004	89.945	0.587	Hα
10	250.646, 149.057	45.957	1.035	89.972	0.613	Hα
10	249.653, 149.057	44.838	1.095	90.513	0.667	Hα
8	249.653, 152.231	48.319	1.139	89.977	0.639	Hα
8	251.838, 152.231	49.917	0.983	89.498	0.532	Hα
8	254.420, 152.231	47.538	1.064	90.047	0.608	Hα
8	249.653, 150.842	48.813	1.058	90.003	0.587	Hα
8	251.838, 150.842	50.613	0.942	89.524	0.502	Hα
8	254.420, 150.842	48.035	1.027	88.918	0.580	Hα
8	254.420, 149.057	45.291	1.115	88.215	0.672	Hα
8	251.838, 149.057	48.163	0.983	88.843	0.553	Hα
8	250.646, 149.057	47.500	1.022	89.189	0.584	Hα
8	249.653, 149.057	46.764	1.108	90.611	0.644	Hα
6	249.653, 152.231	48.669	1.305	90.817	0.726	Hα
6	251.838, 152.231	50.547	1.062	89.099	0.567	Hα
6	254.420, 152.231	50.376	1.204	88.787	0.645	Hα
6	249.653, 150.842	50.693	1.151	90.171	0.612	Hα

6	251.838, 150.842	52.687	0.984	88.887	0.501	Hα
6	254.420, 150.842	52.253	1.155	89.498	0.594	Hα
6	254.420, 149.057	46.818	1.246	89.187	0.724	Hα
6	251.838, 149.057	50.277	1.043	87.770	0.560	Hα
6	250.646, 149.057	48.563	1.102	88.476	0.615	Hα
6	249.653, 149.057	47.922	1.232	89.960	0.698	Hα

Table 3.17: Hα aperture polarimetry for the southern ansa of the outer lobes.

3.5.6 Hα, ISP CORRECTED

Figures 3.16 and 3.17 show Hα linear polarization data which has been corrected for ISP. Both figures incorporate greyscale and polarization information with axis labels and a suitable arcsecond scale. Figure 3.16 shows a total intensity image and superposed contour data, with an adjacent polarization map and overlaid total intensity contours. The intensity contours are logarithmically spaced at intervals of 0.3 magnitudes, while the polarization vectors are integrated inside square bins of size 5 pixels (2.5 arcseconds) which are spaced at 3 pixels (1.5 arcseconds).

Inspection of figure 3.16 reveals that the pattern of polarization is slightly more circular after the removal of ISP. This would indicate that ISP not only affects the levels of polarization within M2-9, but also the pattern of polarization. The tendency of the vector pattern towards increasing centro-symmetry suggests that the central illuminator could be a single point source object. However, the pattern of polarization is still elliptical, even after ISP removal. This suggests that the central illuminating object is extended.

All polarization features included in the discussion of ISP uncorrected Hα data are also observed in the ISP corrected data. However, the levels of polarization throughout the entire nebula are lower in the ISP uncorrected data. The highest magnitude of polarization within the inner nebula is observed between ± 4 – 9 arcseconds In the southern lobe, polarization levels range from ~21 % to 38 %, while in the northern lobe polarization ranges from ~19 % to 31 %. Uncertainties in the measurement of polarization and position angle are of the order of 0.2 – 1.8 % and 0.2 – 2.0 degrees.

Figure 3.17 shows Hα polarized intensity data after the removal of ISP. Comparison of the images of polarized intensity before and after data correction shows little difference in the level and distribution of polarized emission within the bands ± 4 – 10 arcseconds about the east-west symmetry axis. However, it is observed that a definite change occurs in the bow-shock ansae N3 and S3. Results show that polarized intensity is dramatically reduced in the ansae after the removal of ISP. This indicates that the ansae are intrinsically unpolarized. This is consistent with the idea that the nebular condensations are simply observed by their intrinsic emission by radiation excitation.

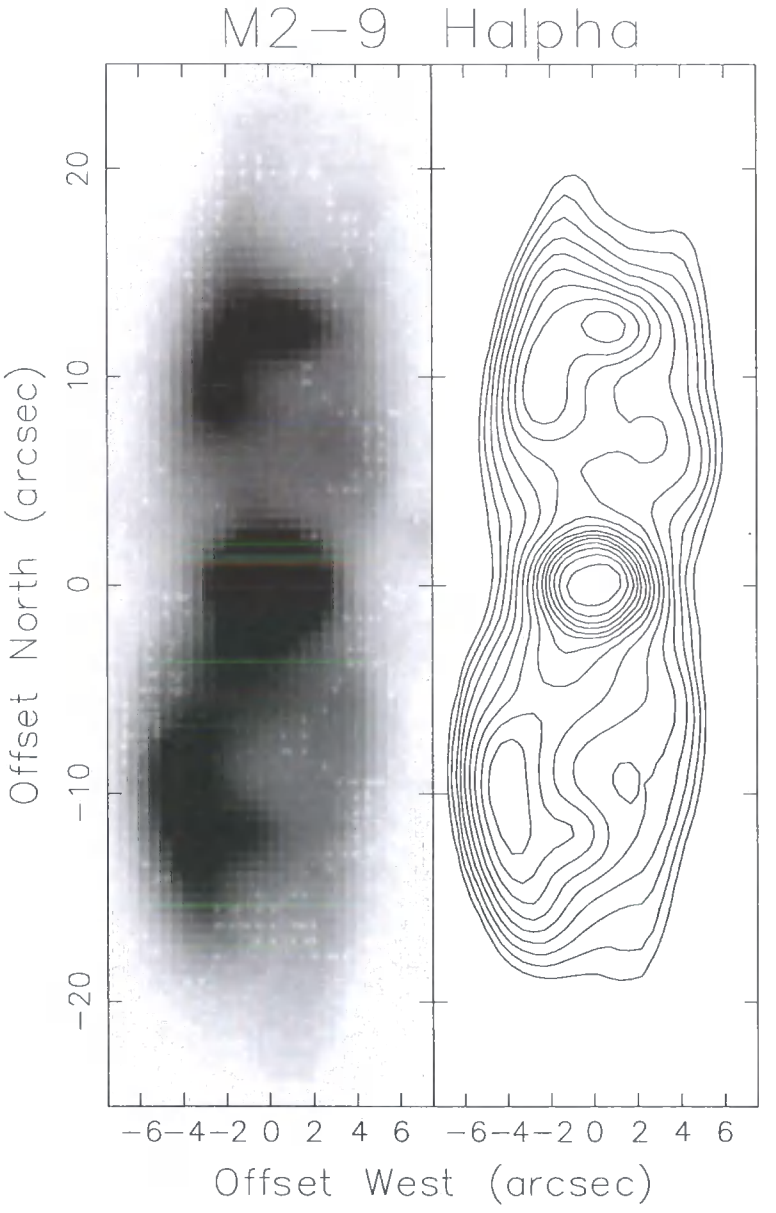

Figure 3.13: Hα total intensity image with adjacent intensity contour data.

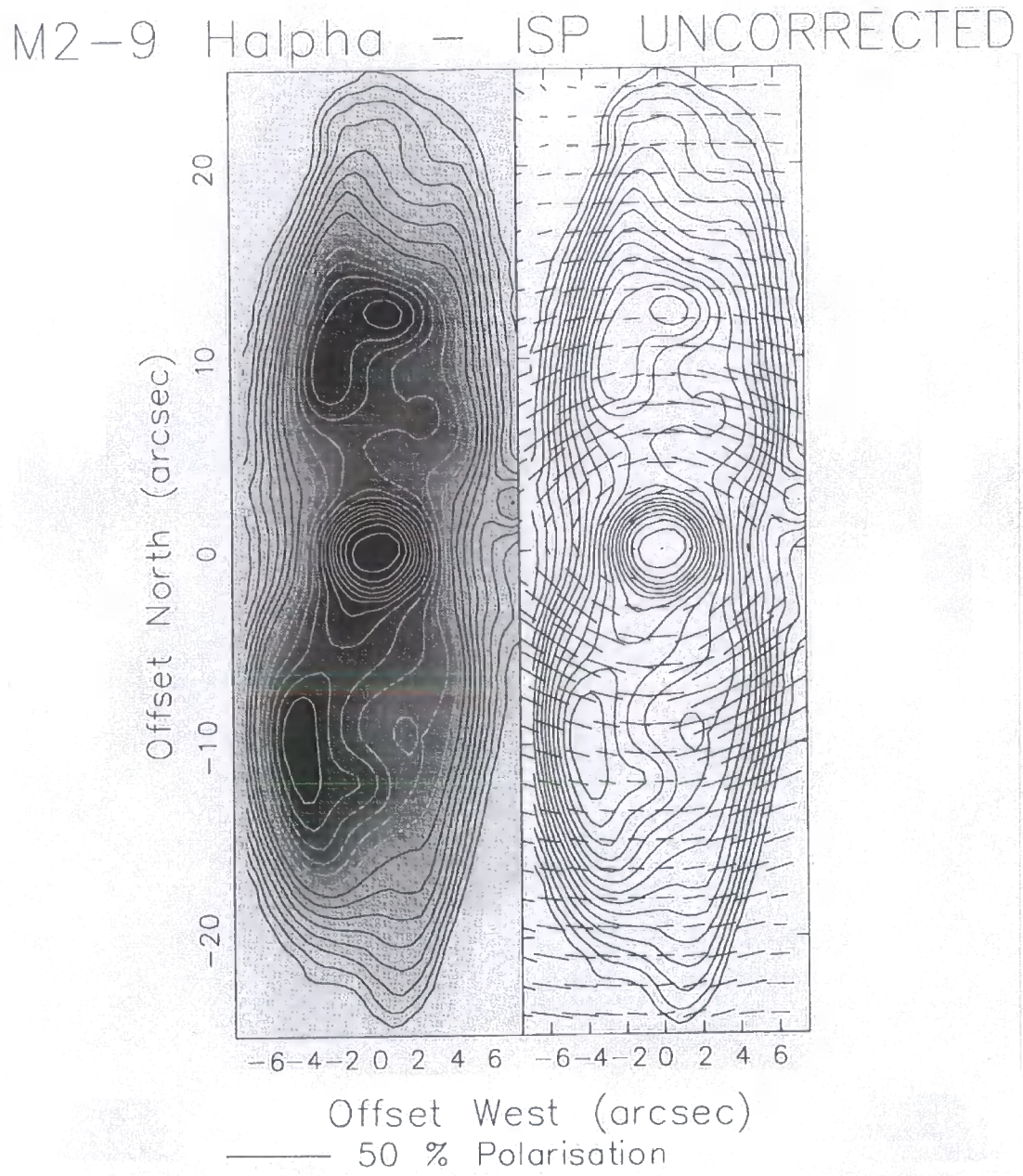

Figure 3.14: Hα total intensity image with superposed intensity contour data, and polarization image with superposed contour data. Polarization data are uncorrected for ISP.

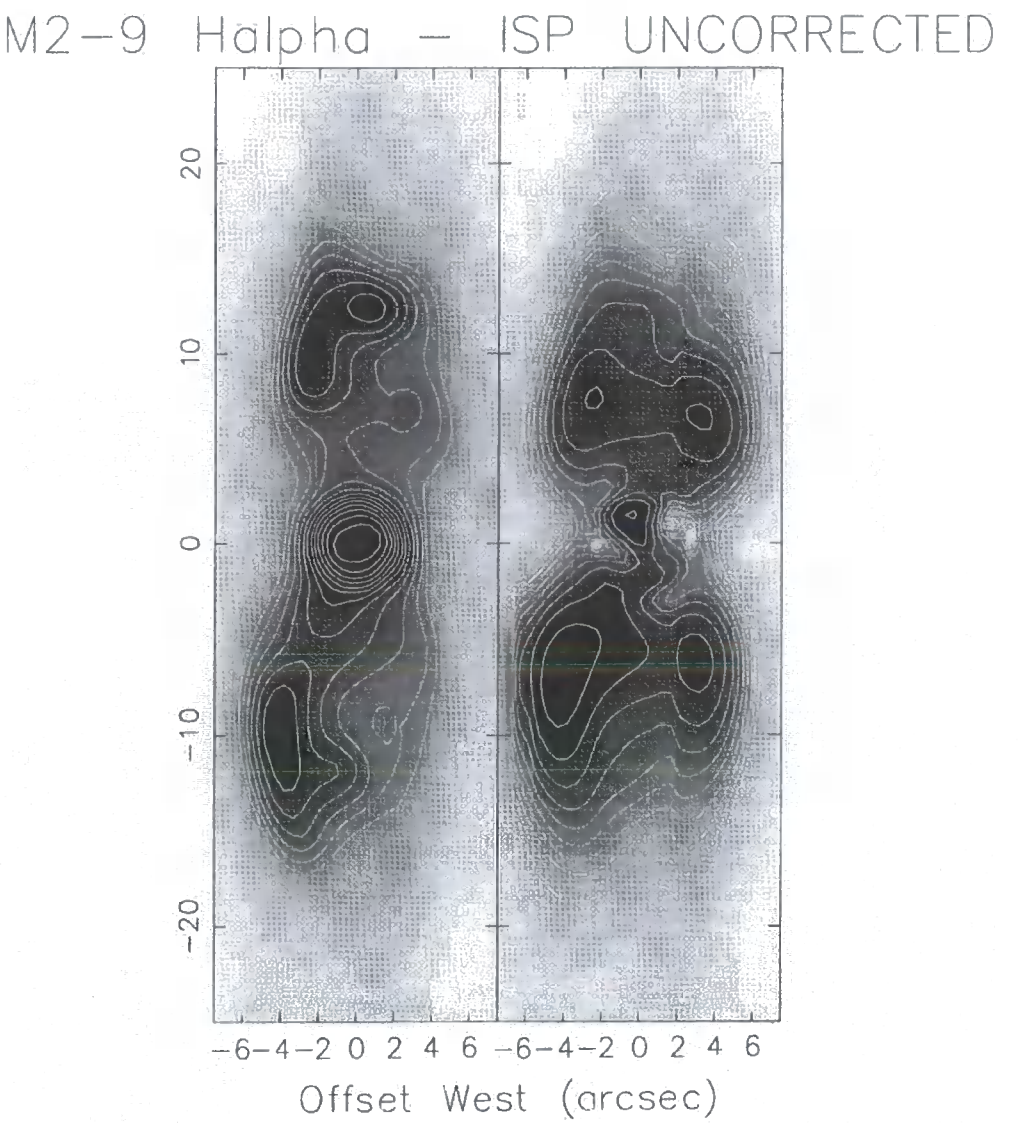

Figure 3.15: Hα total intensity image with superposed intensity contour data, and polarized intensity image with superposed polarized intensity contour data. Polarization data are uncorrected for ISP.

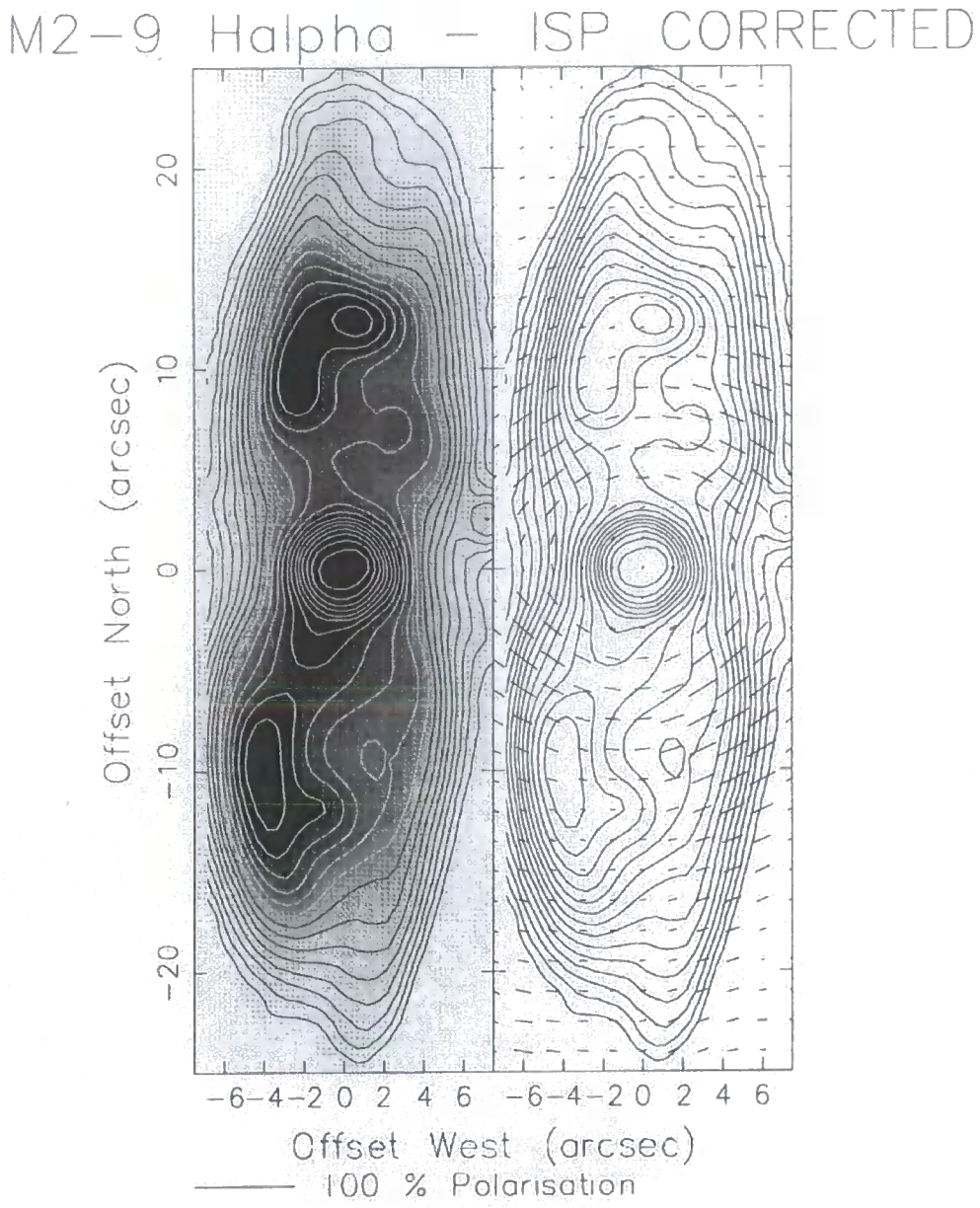

Figure 3.16: Hα total intensity image with superposed intensity contour data, and polarization image with superposed contour data. Polarization data are corrected for ISP.

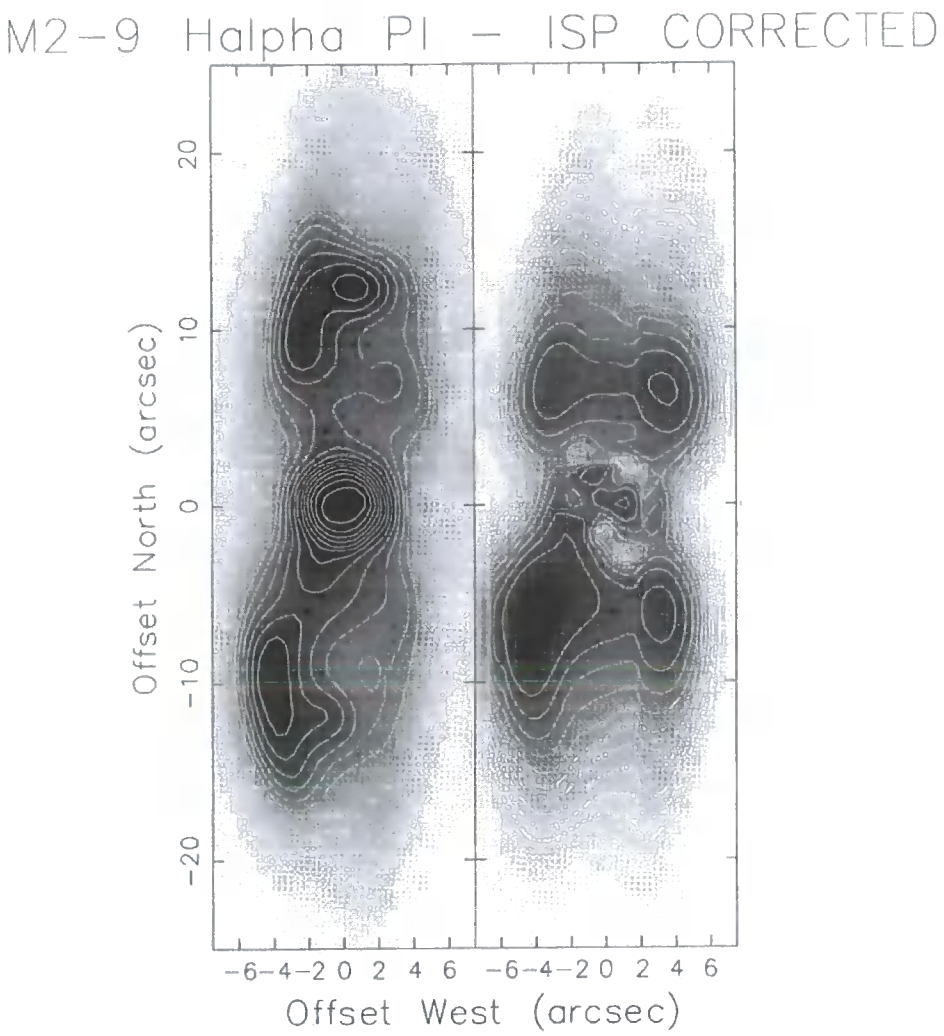

Figure 3.17: Hα total intensity image with superposed intensity contour data, and polarized intensity image with superposed polarized intensity contour data. Polarization data are corrected for ISP.

3.6 DISCUSSION

3.6.1 GENERAL RESULTS

The data presented in this chapter agree well with many of the results previously gathered by other observers. However, a number of results exist which disagree with the conclusions of others and are subsequently discussed here. Although the early polarization results collected by King et al. (1981) show striking similarity with more recent results, including those presented in this thesis, one particular feature appears debatable. Data comparison shows a discrepancy in the polarization pattern of the condensation S1. The author's results show no signs of unusual orientation within the general structure of polarization of this area. This agrees with the result produced by Scarrott et al. (1993) and suggests that the radial orientation of polarization vectors seen in the results of King et al. are probably spurious artefacts of the detection and reduction process. Furthermore, the explanation used by King et al. to account for the unusual polarization pattern, seems somewhat ad hoc and does not account for the other nebular condensations.

3.6.2 PRESENCE OF A CIRCUMSTELLAR DISC

Several features exist in the general morphology of M2-9 which suggest that the nebula possesses a circumstellar disc. Most prominent of these features is the asymmetric nature of nebular morphology. Such bipolar appearance requires a high degree of collimation and asymmetric mass distribution within the central regions of the nebula. An obvious cause for this collimation is the presence of a dense circumstellar disc or torus. Similarly, the narrow waist of M2-9 suggests that obscuration is also present, implying that asymmetric mass distribution must be prevalent. Together with the IR morphology studies carried out by Aspin et al. (1988), polarimetric observations confirm the existence of a circumstellar disc. Polarization data presented here provides confirmation for this. Although the existence of a disc may be insinuated from total intensity isophotal data, evidence appears in the polarized intensity data. Clearly, the difference in morphology of the northern and southern lobes is explained by a tilted disc of obscuring material which overlies the northern lobe. The levels and pattern of polarization found within 2 arcseconds of the equatorial plane clearly reveal that obscuration is present. Furthermore, low levels of polarization within the most central regions of the nebula indicates that intrinsic emission must be high and that multiple scattering is probably occurring due to the high particle densities which are encountered.

Evidence for a circumstellar disc is presented in the form of an elliptical polarization pattern which is reproduced in V-band, R-band, and Hα data. The elliptical polarization pattern is observed across the equatorial regions of the nebula and is still present after the removal of ISP. Consequently, this provides

evidence for the presence of an obscuring disc. This proposal appears to be inconsistent with the results or interpretations produced by Scarrott et al. (1993). Similar disagreement occurs in the observation of discrete bands of high polarization between 4 – 10 arcseconds north and south of the equatorial plane. Scarrott et al. conclude that these bands are formed as a consequence of scattering from the edges of the circumstellar disc. Although scattering from the edges of the disc cannot be ruled out, it is unlikely that strong scattering could occur in this way at such large radial distances. This argument is corroborated by previous measurements upon the inclination of the nebula. Unless the dimensions of the circumstellar disc are extreme, scattering would only occur close to the nebular core. Using the measured range of values for the nebular tilt of 11 – 15 degrees, it is simple to demonstrate that substantial absorption and scattering would occur at radial distances of 2 – 3 arcseconds north and south of the core. The bands of high polarization correspond with rings of high density material and will be discussed in due course.

3.6.3 THE INNER LOBES

The significant levels of polarization which exist within the inner lobes of M2-9 indicate that copious amounts of dust are present. Although this produces a large amount of scattered radiation, the most significant component of nebular emission seems to be intrinsic emission from hot gas. Comparison of total intensity isophotal information from the present data with data gathered by previous observers, shows that slight changes have occurred within the interior of the nebular lobes. These changes, which are described later, occur within the condensations of the nebular lobes. Close examination of polarization levels presented in both northern and southern lobes indicates that M2-9 is inclined with respect to the plane of the sky. Observations show that polarization is greatest in the southern lobe, indicating that the southern lobe is inclined towards us. This follows from the theory of Mie scattering, which suggests that peak polarization occurs for scattering angles ≥ 90 degrees.

Polarization data also imply that the central source provides much of the illumination of scattering centres throughout the nebula, although diffuse emission may also be scattered to some extent. Clearly, the polarization pattern provides details of the structure of the inner nebular lobes. The higher levels of polarization which follow the boundaries of the lobes suggests that the concentration of dust grains within those regions is higher. This follows from the model of interacting stellar winds which is described earlier in this thesis. Consequently, gas and dust present in the slow wind, is compressed to form the dense walls of the lobes. Material within the interior of the lobes then becomes rarefied, resulting in a reduction in scattered emission. It is noted that the high levels of polarization in the lobe walls are much more extensive in the western half of the nebula. This is explained by the presence of the nebular condensations in the eastern half of the nebula. Clearly, the condensations are observed by their intrinsic emission rather than scattered light

from the central source. Consequently, the levels of polarization across the region of the most prominent condensations, is diminished due to dilution from radiative emission.

Examination of total intensity along the major axis of the inner lobes shows that bands of enhanced emission exist between 4 – 10 arcseconds north and south of the equatorial plane. These bands correspond exactly with the enhanced levels of polarization and polarized intensity, and also feature in both HST images and IR images. Although a proportion of polarized intensity appears to coincide with the position of a number of the nebular condensations, the condensations are essentially unpolarized. Goodrich (1991) and Trammell et al. (1995) suggest that these regions are associated with density enhancements which encircle the collimated outflow of the nebula. Following this proposal, these regions are assumed to contain considerable amounts of dust, leading to the increased probability of radiation scattering and an increase in the fraction of polarized emission. Contrary to the suggestion by Carsenty & Solf (1983) that dust is entrained within the low density gas of the bipolar lobe interiors, the presence of dust within the lobe walls provides more definitive explanation for the inherently high level of polarization. To account for the presence of these highly polarized regions, it is assumed that episodic mass-loss has taken place during the evolution of the nebula. This would also explain the very different properties of the dust grains and morphological features of the outer lobes of M2-9.

3.6.4 THE OUTER LOBES

First discovered by Kohoutek & Surdej (1980), the outer regions of M2-9 contain a pair of faint, point-symmetric loops which end in unusual double ansae. These outer lobe structures possess very unusual properties, totally unlike those of the inner bipolar lobes. Spectroscopic measurements by Schwarz et al. (1997) show that contrary to observations of nebular outflows which follow non-zero inclination with respect to the plane of the sky, the outer parts of the bipolar outflow show only redshifted spectra. Their measurements show that the inclination of the outer lobes structures is the same as that of the inner lobes structures within the levels of uncertainty. Consequently, Schwarz et al. suggested that the loops and outer ansae contain outflowing dust which scatters light from the central illuminating source, leading to the appearance of redshifted velocity components only.

The V-band, R-band and Hα polarization datasets presented within this thesis show that the outer ansae are highly polarized, confirming the dusty nature of the outer nebular loops. The levels and pattern of polarization largely agree with results measured by Schwarz et al. (1997). Because polarization levels exceed ~ 50 %, it is suggested that Rayleigh scattering exists in some form (See Code & Whitney 1995). The presence of dust in the outer lobes of M2-9 also indicates that episodic mass ejection may have occurred and that small dust grains may have survived by their entrainment in the collimated outflow of the fast stellar wind.

3.6.5 LOBE WALLS AND THE NEBULAR CONDENSATIONS

As discussed in previous sections, the levels of polarization within M2-9 are high. It is observed that polarization possesses a large range in value across the extent of the nebula. However, it is clear that the highest levels of polarization are present at the extremities of M2-9. Regions of highest polarization include the ansae of the outer lobes and the walls of the inner lobes. It is particularly interesting to note that polarization within the lobe walls is greatest along the western edge of the nebula. This is explained by the presence of the condensations to the east. Because the condensations feature strongly in intrinsic emission, they act to dilute and lower the amount of scattering which occurs within their vicinity. Thus, polarization levels appear slightly lower within the eastern walls of the nebular lobes.

The most interesting features of M2-9 are the nebular condensations which possess unusual mirror-symmetry. The symmetry and apparent motion of the condensations has been the subject of much debate. However, explanation of their origin and exact characteristics has never been completely explained. Having measured and compared the positions of the intensity maxima of the condensations with previous results, it is clear that definite change has occurred. Recent high resolution measurements gathered by Doyle et al. (2000) also show that the condensations have moved, although it appears that the period of rotation is likely to be very long. The presumption made by Scarrott et al. (1993) that little positional change of the condensations indicates that they had not moved, may not be entirely true. Results gathered by Scarrott et al. indicate that the condensations have remained along the eastern edge of M2-9 for some time. This appears to be largely true, but their proposals make no account of the events which could have occurred between the discussed periods of observation. Within the context of their results, it could be suggested that emission from the condensations first took place at the back of the nebular lobes. Following these observations the condensations moved further east, before moving to front of the nebula in a westerly direction. This would then explain why the condensations appeared stationary for such a long period of time. Analysis of positional data from 1952 through to 1999 has revealed that the nebular condensations N1, S1, N2, and S2 have experienced a lateral displacement. This displacement corresponds to a rotational motion which follows a regular period. Simple calculations carried out upon the positional data of the nebular knots have produced a value for the rotational period of 70 –80 yr. This corresponds particularly well with the rotational period of 65 –75 yr determined by Goodrich (See Scarrott et al. 1993).

Positional data presented within this thesis supports the proposal that the condensations N3 and S3 are ansae which lie upon the major axis of the nebula. However, the data also reveals that the ansae follow a lateral displacement indicative of precessional motion. Consequently, it could be suggested that the bow-shock ansae are formed through the action of a precessional beam of ionizing radiation. This has been shown to occur in the bipolar PN known as M1-16. However, the presence of mirror-symmetry within the other nebular condensations contradicts this proposal. In order to resolve the problems associated with the

mechanism of production and complicated motion of the all the nebular knots, much work still remains to be done. The ansae are believed to have formed through the shock-refraction and focussing of the stellar wind along the lobe walls. This process is commonly observed within pre-main sequence cometary and bipolar nebulae (Canto & Rodriguez 1980; Gething et al. 1982; Scarrott & Warren-Smith 1988), and may also be commonly present within post-main sequence nebulae (cf. OH 231.8 +4.2). The PPN which surrounds the star OH 231.8 +4.2 contains shocked emission-line features along the major axis of the nebulae (Cohen et al. 1985; Reipurth 1987). These features, known as Herbig-Haro (HH) objects, may possess similar properties to the inner and outer ansae of M2-9.

Although polarization and polarized intensity results presented within this thesis, suggest that density enhancements exist within discrete bands above and below the equatorial plane, results do not indicate that the condensations of the inner nebula contain dust. Consequently, the proposal of density enhancements within the nebular condensations by Kohoutek & Surdej (1980) and Goodrich (1991) contradict the results presented within this thesis and those presented by Scarrott et al. (1993). Since the nebular condensations arise from the recombination of ionized gas, they must be excited by some form of illuminating beam. However, the mirror-symmetry of the condensations indicates that the illuminating beam becomes distorted inside the volume of the circumstellar envelope (CSE) of the central star. The most likely explanation for this distortion is the presence of a stellar companion within the CSE. This binary companion could then explain the unusual spectral signature of M2-9 (Allen & Swings 1972).

3.7 CONCLUSIONS

M2-9 appears as a young, highly collimated bipolar PN which presents two diametrically opposed lobes either side of the nebular core. The central source of M2-9 is obscured from direct view by the presence of a circumstellar disc. The presence of such a disc has been confirmed with IR imaging and polarimetric observation. These observations show that substantial reddening and absorption occur within the central regions of M2-9, with reduced levels of scattering and lower levels of polarization. This may be explained by the presence of multiple scattering events within the dense circumstellar envelope of the nebula.

The V-band, R-band, and Hα data presented within this chapter conform with the previously accepted proposal of Scarrott et al. (1993) that M2-9 is observed through the combination of emission-line and scattered light. Data presented here also suggests that the nebular lobes exist as hollow wind-blown cavities. The edges of these lobes appear to have been swept up, thereby creating a high density shell structure containing both gas and dust.

Confirmation is given to the previously measured values of polarization within the nebular lobes. No change is apparent in the levels of polarization within the nebular condensations. Although the author's results appear to suggest that the inner nebula ansae N3 and S3 are polarized, this is due to the incomplete removal of ISP from the polarization data. The measurements of polarized intensity do show that the other nebular condensations N1, S2, S1, and S2 are intrinsically unpolarized, because the intensity maxima of the knots in total intensity and polarized intensity do no coincide. Polarimetry results also show that the ansae of the outer loops of M2-9 are highly polarized, with polarization levels exceeding 50 % within certain regions of the ansae. This indicates that substantial amounts of dust exist in the outer extremities of M2-9 and that there is favourable scattering geometry. The difference in polarization levels between the northern and southern ansa suggests that the outer nebula is inclined very slightly and probably possesses a similar inclination to the inner nebula.

Most interestingly, it has been determined that the mirror-symmetric condensations of the inner nebula do possess a rotational motion. This is also true of the bow-shock ansae N3 and S3, although these nebular knots display motion which is indicative of precession. The point symmetry of the ansae strengthen this proposal and suggest that a precessional beam of illuminating radiation exists within the nebular core. For the nebular condensations N1, N2, S1 and S2, however, the complex mirror-symmetry cannot be explained so simply. The problem associated with the method of production of these nebular knots will require further studies. Measurements taken by the author, suggest that the condensations rotate inside the nebular walls with a period of 70 – 80 yr. This is in good agreement with the result determined by Goodrich (See Scarrott et al. 1993).

CHAPTER 4

NGC 2440

4.1 INTRODUCTION

NGC 2440 (PK 234+2°.1) was discovered by Herschel in 1790. It is one of the most unusual objects of its type, having been described by Minkowski (1964) as an object so complicated it defies description. Many studies of NGC 2440 have been undertaken, the majority of which being spectroscopic in nature. At optical wavelengths, observations show that NGC 2440 possesses a pair of opposing lobes of large opening angle. Closer examination shows a second pair of lobes to be present. This second pair of lobes displays a different position angle to that of the larger, outer lobes, and widely different opening angle suggestive of a varying degree of collimation. The central star is extremely faint and displays one of the highest surface temperatures of any planetary nebula nuclei (PNNi).

4.2 PREVIOUS STUDIES

The planetary nebula NGC 2440 has received extensive attention in the past because of its unusual features. Situated in the southern skies at a position RA 07h 41m 55.4s, Dec. -18° 12′ 33″ (2000.0), the nebula is

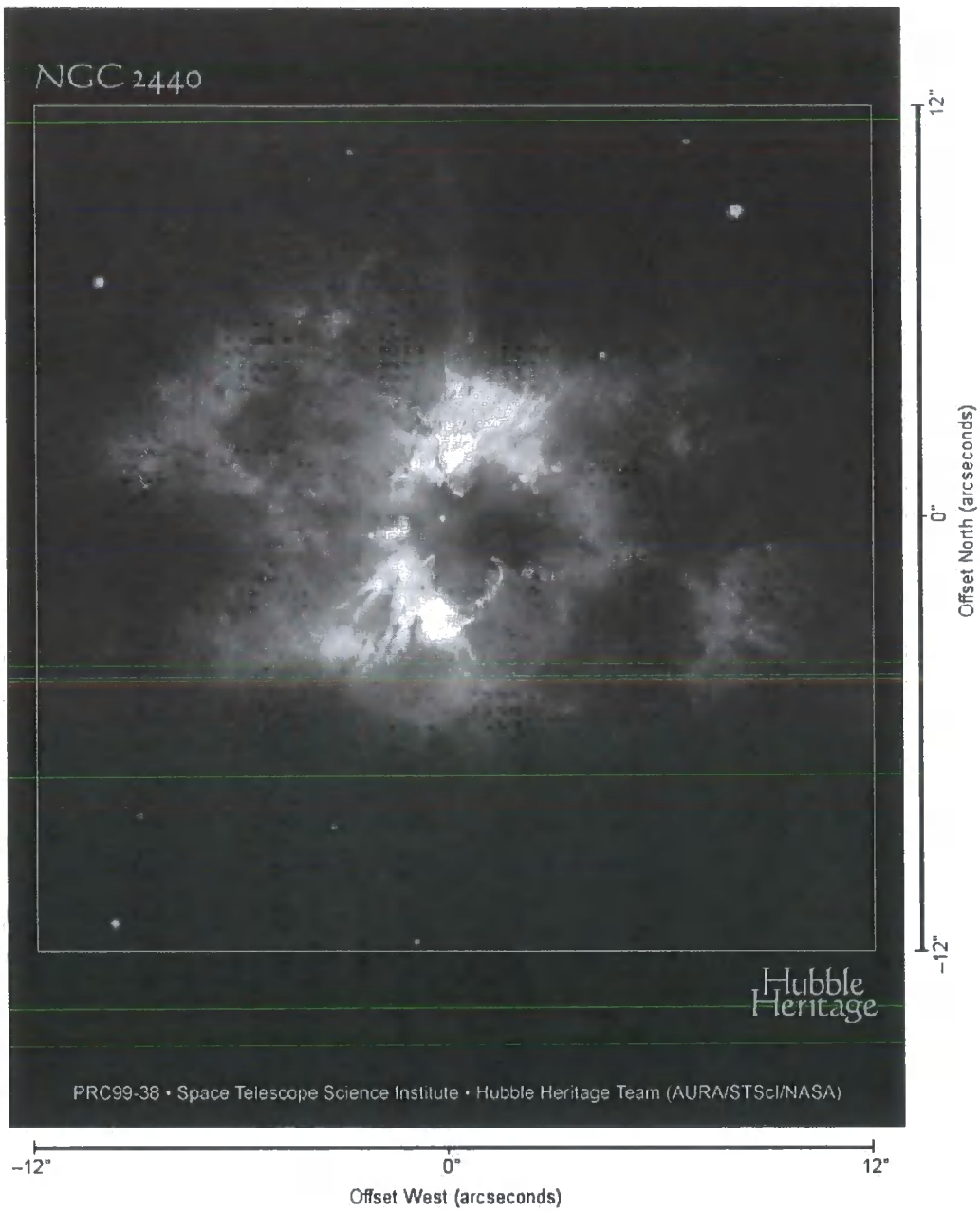

Figure 4.1: Archival HST image of NGC 2440

easily observed as a result of its high surface brightness. Classified as a Type I PN after the studies of Peimbert & Torres-Peimbert (1983), the nebula and central star have evolved from a massive progenitor.

NGC 2440 has always been considered as a bipolar PN. However, analysis of the archival HST image shown in figure 4.1 shows that its morphology is far from that of a common bipolar PN, but more like that of the quadrupolar PNe (Manchado et al. 1996). Though its general appearance is characterized by a large pair of diametrically opposed lobes, closer scrutiny of its image shows that it contains additional bipolar structures. These structures are further supplemented by a complex filamentary appearance which extends throughout the nebula (See Phillips et al. 1980; Terzian et al. 1974). Early observations by Curtis in 1918 reveal a prominent feature coincident with the central region of the nebula. This feature is indicative of a pair of condensations and is separated by 7 arcseconds corresponding to ~ 0.04 pc for an assumed nebular distance of 1.1 Kpc (Hajian & Terzian 1996). Evidence now exists which suggests that these condensations are part of a toroidal structure surrounding the central star. Velocity field measurements gathered from the observations of radio recombination lines show that the central toroid has become distorted and now possesses a non-circular shape (Vasquez et al. 1999). Moving outward from the nebular centre, optical imaging shows that NGC 2440 contains a number of unusual morphological features. Originally classified as a bipolar PN, NGC 2440 displays features indicative of a 'poly-polar' morphology. Two pairs of bipolar lobes are observed, whose symmetry axes have been rotated with respect to one another, and whose dimensions display considerable difference. The apparent offset of the axis of symmetry of each bipolar lobe indicates the presence of some mechanism leading to the precession or rotation of the collimating beam. The apparent difference in size of the two lobe systems, however, indicates a possible episodic character in the ejection of mass. Early analyses of the outer lobes show that the main axes of symmetry are tilted in the plane of the sky by ~ 60 degrees (Kaler & Aller 1974). They also imply that the inner, smaller lobes are expanding much faster than the outer lobes, yet, more recent observations suggest a nebular inclination of ~ 50 degrees (Lopez et al. 1998).

The largest and presumably oldest pair of lobes (labelled A in figure 4.2 on p133) are observed out to a radial distance of 38 arcseconds from the assumed position of the central source, giving the nebula a total extent of ~ 76 arcseconds corresponding to ~ 0.41 pc. The lobes appear to lie almost perpendicular to the central condensations, and follow an east-west projection. The major axis of the lobes lies at an angle of 85 degrees[1] and appears to be inclined by ~ 40 degrees with respect to the plane of the sky. An interesting, yet unexplained feature is observed to extend from the northern region of the eastern outer lobe, and appears in the form of a faint wedge of nebulosity. Kinematical analyses show that the northern spur possesses a high radial velocity with respect to the systemic velocity of the nebula, possibly suggesting an origin from some high velocity outflow. Its full interpretation, however, remains somewhat uncertain.

[1] Note: Position angles quoted are measured from north and increase towards the east.

The second and brighter pair of bipolar lobes is almost certainly younger than the outer lobes. Here the second pair of lobes is labelled B in figure 4.2. The total extent of the lobes is 50 arcseconds corresponding to ~ 0.27 pc for the adopted nebular distance. The major axis of the second pair of lobes lies at an angle of 35 degrees and appears to lie on or very close to the plane of the sky. A conspicuous component of the 35 degree lobes is a bright knot at the apex of each lobe. Evidence exists to suggest that the knots are actually ansae which have formed through the refraction and collimation of an outflow perpendicular to the line of sight.

Close scrutiny of the HST image also shows tentative indications of a further pair of bipolar lobes. These are extremely small and faint with respect to the other lobe features, and possibly define the most recent nebular outflow. The extent of this third lobe system (labelled C in figure 4.2) is somewhat uncertain, as there is no discernible limb-brightening which would identify the lobe boundaries. A reasonable estimation of the radial extent would be 23 arcseconds corresponding to a true size of ~ 0.12 pc. The major axis of this lobe system lies at an angle of 60 degrees and appears to be on or close to the plane of the sky. Because the 35 degree lobes and the 60 degree lobes both lie on or near to the plane of the sky, this presents a difficulty in explaining the exact process by which the whole set of bipolar lobes was formed. The most probable mechanism by which rotation of the ejection axis takes place is suspected to be due to the effects of an interacting binary star system at the core of the nebula, which is able to constrain the mass ejection to a precessional cone (Vasquez et al. 1999).

Images show that the surface brightnesses of the two outer lobes are different. It is clear that the eastern lobe is optically brighter than its western counterpart. This is attributed to the inclination of the outer lobes to the line of sight, such that the eastern lobe is tilted towards the observer. The validity of this assumption is strengthened by kinematical analysis. The position-velocity diagrams of Vázquez et al. (1999) indeed show that the western lobe is receding and the eastern lobe is approaching. In many bipolar PNe it is also apparent that brightness differences between the inner regions of the lobes result from the effects of increased levels of extinction caused by the presence of an inclined circumstellar disc. Rodriguez et al (1985) proposed that extinction across NGC 2440 is uniform. However, the ratio images of radio continuum to Hα taken by Vasquez et al. (1999) show that extinction is present within the inner nebula and decreases outward, differing up to ~ 0.4 magnitudes between the central regions and the farthest zones along the 60 degree axis. This suggests that higher extinction traces the most dense and dusty environment of the toroidal structure.

Early observations of the inner nebula of NGC 2440 resulted in a non-detection of the central star. To explain this, it was proposed that emission from the star is simply overwhelmed by nebular continuum emission. Additionally, increased levels of extinction within the central nebula could play an important role in non-detection of the central illuminating source. Using the argument that the faintness of the central star displayed by certain planetary nebula nuclei, necessitates the fact that they are extremely hot (Pottasch

1981), it was surmised that the central star of NGC 2440 must follow suit. The apparent visual magnitude of m_v ~19.5 estimated by Curtis was later employed by Pottasch, who derived a value for the star's effective temperature of 5×10^5 K. This was later disputed by Kohoutek & Martin (1981), who derived an effective surface temperature of only 10^5 K. In order to resolve the controversy, measurements were taken to maximize the contrast of the star against the nebular background. Atherton et al. (1986) determined a Zanstra temperature of 3.5×10^5 K from a visual magnitude of m_v ~ 18.9, but their data displayed contradiction to the theories of stellar evolution. Table 4.1 shows various magnitude measurements which have been gathered since the discovery of the nebula.

MAGNITUDE MEASUREMENT	OBSERVER	YEAR
19.5	Curtis	1918
18.9	Atherton et al.	1986
17.84	Heap	1987
18.8	Gathier & Pottasch	1988
14.2	Shaw & Kaler	1989
17.6	Heap & Hintzen	1990
17.49	Ciardullo	1999
17.63	Wolff et al.	2000

Table 4.1: Magnitude measurements for NGC 2440

Later observations gathered by Heap (1987) using the IUE showed that the temperature had been previously overestimated by a considerable degree. Using the Zanstra method for a variety of nebular emission lines, Heap determined a temperature ranging from 1.9×10^5 K to 2.1×10^5 K, which was found to be in agreement with that determined using the energy-balance method. More recent data (Heap & Hintzen 1990; Hyung &Aller 1998) appear to provide greater constraint upon the exact value of the star's temperature. The temperature derived from each observing program was 2.0×10^5 K and 1.8×10^5 K, respectively implying that the central star is brighter than was originally suspected. Certain properties of NGC 2440, however, would point to a binary star system for the central source.

Aside from morphological studies and detection programs of the central star, the majority of studies on NGC 2440 have been spectroscopic. The most prominent feature of these studies is that NGC 2440 displays an overabundance of helium and nitrogen, which has classified it as a Type I PN (Peimbert & Torres-Peimbert 1977). Similarly, NGC 2440 appears as a high excitation nebula and therefore presents a diverse range of chemical elements, all of which show a large range of ionization states (Aller et al. 1968.) Study of the products of the CNO and more advanced thermonuclear processes, however, provides particular interest

to the study of polarimetry. Spectroscopy indicates that a number of the gas-phase refractory elements, particularly the heavier elements of Magnesium, Silicon, Calcium, and Iron, show high levels of depletion, suggesting a likely participation of these elements in the formation of dust. Additionally, it appears that carbon is depleted with respect to oxygen, as measurements show that C/O <1 (Condal 1982; Hyung & Aller 1998; Peimbert et al 1995: Shields et al 1981; Kingsburgh & Barlow 1994; Kwitter & Henry 1996). Spectroscopic studies have also been used in the determination of the distance to NGC 2440. As is usual for PNe, the distance determination for NGC 2440 is very uncertain. Distance measurements show striking variation, ranging from 500 pc, out to 2.2 Kpc. Table 4.2 shows a list of distance measurements which have been collected by various authors.

DISTANCE MEASUREMENT (KPC)	OBSERVER	YEAR
2.2	Gathier, Pottasch & Pel	1986
0.5	Bassgen, Diesch & Grewing	1995
1.57	Zhang	1995
1.1	Hajian & Terzian	1996

Table 4.2: Distance estimates for NGC 2440

An apparent feature of the spectra, is the presence of emission-line features associated with the transitions of molecular hydrogen (H_2). These commonly occur within PN, but often possess different excitation mechanisms. H_2 emission within PN arises either as a result of radiative excitation by absorption of UV radiation inside the volume of a photodissociation region (PDR), or by collisional excitation which is driven by shockwave phenomena (See Black & van Dishoeck 1987 and Sternberg & Dalgarno 1989). The exact mechanism by which H_2 is excited depends upon the strength of certain vibrational and rotational lines in the ground electronic state of the molecule. For the case of NGC 2440, molecular imaging shows that H_2 is exceptionally prominent within the region tracing the central torus (Reay et al. 1988). The outer lobes of the nebula, however, display no signature from H_2 at all. Instead, a partially circular halo is observed, which appears in the form of a series of arcuate filaments north and south of the general H_2 emitting region. The apparent offset nature of the arcuate structures with respect to the nebular core, is attributed to the effects of nebular geometry and the line of sight. Also visible is a faint H_2 bar, which appears to connect the filamentary arcs. The linear emission passes through the nebular centre and is oriented roughly north-south in the equatorial plane of the larger bipolar lobes. In most evolved butterfly-type nebulae, H_2 emission occurs predominantly at the lobe boundaries. This observation is expected for nebulae possessing wind-blown bubbles. NGC 2440, however, possesses H_2 emission characteristics which contradict normal observation. Most of the molecular hydrogen is found at the centre of the nebula and is closely associated

with the HII region. For H_2 to survive through all stages of nebular development, substantial amounts of molecular material must have been processed and ejected by the progenitor star. Early observations of molecular emission suggest that shock excitation played a predominant role, thus resulting in low values for the mass of molecular gas (Isaacman 1984). More recent observations, including those by Latter et al. (1995) and Kastner et al. (1996) show that molecular gas excitation occurs through the admixture of radiation and shock processes.

Near-infrared (NIR) photometry by Cohen & Barlow (1974) reveals that NGC 2440 possesses a moderate IR excess, with NIR colour indices H – K = 0.4, and K – L = 1.8. These observations are also supplemented by mid-infrared (MIR) measurements[2] at 10μm and 18μm. Together, the measurements reveal increasing levels of excess emission towards longer wavelength. This strongly suggests that dust is present throughout the nebular volume. Continuum emission within the nebula appears moderately low when compared with line emission, and displays a decreasing trend towards longer wavelength. Emission within a number of the lobe features again shows a predominance of line emission, but one particular feature shows an increase in continuum emission. This would imply an increase in the levels of dust and/or change in the size distribution of inherent dust grains. The presence of neutral oxygen in the spectra of several of the condensation structures would also suggest that the condensations are relatively cool and dense compared to the surrounding gas.

IRAS observations of NGC 2440 classify the nebula as a point source, with a designation IRAS 07396-1805. Observable under each of the IRAS flux bands, the object features reduced emission compared with that from M2-9. This is naturally explained by the difference in the dynamical age of the two objects. As the nebula ages, the filling factor of material decreases, thus reducing the measurable levels of emission. With the cooling of nebular dust, the FIR emission of NGC 2440 is expected to show an increase when compared with younger PNe, such as M2-9. However, this is not observed, suggesting that increased dynamical age and angular size leads to a reduction in the density of dust, and hence emission. Peak emission occurs in the FIR at 60μm, strengthening the argument that the largest fraction of dust is moderately warm. When compared with the dust component of other PNe (cf. M2-9), the dust component of NGC 2440 is relatively cool. All other flux bands show smaller amounts of emission, suggesting that absorption of trapped Lyα photons is weaker, or that the dust population has changed during the life of the nebula.

Adopting the methods used by Van der Veen & Habing (1988), the IRAS colours reveal that NGC 2440 resides in region V of the colour-colour diagram ([12μm] – [25μm] against [25μm] –[60μm]). Use of the methods employed by Walker & Cohen (1988) and Walker et al. (1989) appear to suggest that NGC 2440 belongs to group of 'red' PNe. Blackbody fitting to the IR data suggests that the temperature of nebular dust

[2] Note: The Infrared wavebands display the following passbands: NIR=1-5 μm, MIR=5-30 μm and FIR=30-200 μm

is around 150 K, which is particularly cool when compared to the dust component of younger PNe such as M2-9. The young PNe are observed to possess dust temperatures between ~ 400 – 900 K.

The most interesting and perplexing feature of NGC 2440, however, is the presence of multiple bipolar outflows, each possessing differences in both position angle and degree of collimation. Rotation of the axes of these lobe systems suggests that the agent of collimation is likely to have experienced considerable transformation since the origin of the ionized nebula. It is apparent that the central torus of NGC 2440 has played a significant role in shaping the various lobe structures, due to its distorted shape and broken structure. However, it is difficult to envisage how the torus helped to shape these features, considering that the nebular lobe systems are not perpendicular to the plane of the torus. Clearly, the nature of the multiple bipolar outflows suggests some sort of precessional and episodic effect upon the collimating agent. It is now accepted that interaction between close binary stars can provide the necessary conditions to produce collimated outflows inside PNe. Although the central star of NGC 2440 appears as a single object, it is possible that an unseen binary companion exists, that is similar to that observed in the system NGC 2346.

Recent study into the phenomenon of bipolar rotating episodic jets (BRETs) shows considerable promise in describing the appearance and inherent structure of the multiple outflows of NGC 2440 (Lopez et al. 1995; Lopez 1997, 2000). Numerical simulations carried out by Cliffe et al. (1995) indicate that the basic features of NGC 2440, including the point-symmetric shock excited knots, may be reproduced through the action of BRETs.

4.3 POLARIMETRIC OBSERVATIONS

4.3.1 OBSERVATIONAL DETAILS

Polarimetric data discussed in this chapter was gathered during an observing run which was carried out during February and March 2000. Observations were gathered upon the 1.9m SAAO telescope at the Cassegrain focus, with a focal ratio of f/18. Over the period of the observing run, data were collected using the modified Durham Imaging Polarimeter, with broadband V and R-waveband filters. Both filters were employed for the collection of linear polarization data, but only the broadband V filter was used to collect circular polarization data. The telescope/instrument/detector combination remained the same as that for the observations of M2-9 (See §3 for further details). The seeing conditions were gathered from field star observations. FWHM measures of the stellar angular dimensions were found to range between 2.0 arcseconds and 3.0 arcseconds during the course of observations.

Data were collected at three separate telescope positions in order to sample the entire extent of the nebula. It should be noted, however, that coverage of the nebula in the V-waveband is incomplete. This is explained by the fact that the telescope was incorrectly positioned during several of the exposures. The effect is observed as a series of dark strips traversing the nebular image, in which no data were obtained. Fortunately, the positions of these invalid strips fall across regions of the nebula which are free of significant polarimetric features, with the exception of one of the nebular condensations. 48 CCD frames of the object were gathered using the broadband V filter, and 48 frames using the R filter. No account was made for the large dynamical intensity range of the object, which implied that image saturation could become problematic. However, both the inner nebula and fainter surrounding nebulosity of the lobes were observed without problem. Integration times for the V filter observations measured 30 seconds, whilst for the R filter they measured 25 seconds, because of the higher filter throughput. In order for correct calibration of the image frames, a series of flatfield frames of the twilight sky were taken. Corresponding exactly to the particular passband characteristics of the image frames, the flatfield frames enabled a global correction to be made across the image. Dome flatfields were not taken, however, due to time constraints during the course of the observing run.

4.4 RESULTS

4.4.1 IMAGE DETAILS

The following discussion of results includes several pictorial representations of NGC 2440 data. Figures 4.2 through 4.9 display broadband V continuum data, whilst figures 4.10 through 4.17 display R-waveband data. It should be noted that all images and polarization maps are oriented with north at the top and east to the left, in accordance with the usual convention employed by other authors. Images are centred upon the region midway between the two central condensations where the star is known to reside. All images include a scale in arcseconds and axis labels specifying offset distances from the plot centre. Unless otherwise stated, all greyscale and contour images represent the total intensity of the nebula, with the highest intensity displayed by black. All contours are displayed logarithmically and spaced at 0.3 magnitudes, so as to encapsulate the entire dynamical intensity range of the object. Polarization measurements are plotted with suitable intensity cuts so as to eliminate unwanted noise from the image. The ordered appearance of polarization vectors is explained by the integration of polarization data into data bins. Image overlays are shown with bin sizes of 5×5 pixels moved on 3×3 pixels. The effect of smaller step size is to average and therefore smooth data as a consequence of data bin overlap. Integration of polarization data was also carried out with 7×7 pixel bins moved on 5×5 pixels, and 3×3 pixel bins moved on 2×2 pixels. A check upon the consistency of data was also carried out using 5×5 bin integration moved on 5×5 pixels. Unless otherwise stated, only the 5×5 bins moved on 3×3 pixels are used in the data images. Here, orientation of the polarization vectors represents the preferential direction of the electric field of scattered light, and vector length represents the magnitude of polarization.

A number of images also show polarized intensity data. These are again plotted with black pixels representing the highest levels of emission, with contours being plotted logarithmically. No axis labels or scales are applied to these images, as they represent greyscale information and thus have different scale transformations to those displaying polarization results.

It should be noted that a number of the images contain data which are affected by reduction problems. These problems occur during different stages of the reduction process and often carry through to the final stages. A number of methods were used to eliminate these problems, but were not always successful. Nevertheless, the existence of this problematic data has little effect upon the overall data set which is included in this thesis. Where present, the artefacts are clearly noted and subsequently discussed in relation to the results.

4.4.2 THE EFFECTS OF INTERSTELLAR POLARIZATION

Having been discussed in §2, the effects upon starlight from interstellar dust are of considerable importance. Although the polarization from interstellar dust grains provides essential information about the ISM and galactic magnetic field, its existence presents difficulties in measuring polarization intrinsic to astronomical objects which lie close to, or in, the galactic plane. In this respect, Type I PNe become prime examples for the study of ISP effects.

The Galactic co-ordinates (l=234°, b=+2°.1) of NGC 2440 imply that measured levels of polarization include a contribution from the ISP and that discernible extinction occurs across its extent. Levels of polarization may reach up to 3 % per magnitude of visual extinction when the light path is perpendicular to the galactic magnetic field (Scarrott et al. 1993). At an assumed distance of 1.1 Kpc, the line of sight to NGC 2440 is expected to suffer from ISP levels between 0.3 % – 0.5 %, at position angles around 100° - 120° (Axon & Ellis 1976). The effects of ISP usually produce a reduction and distortion in the intrinsic polarization of the object, but are often suspected by the presence of polarization in field stars.

Although the data of Axon & Ellis point towards a contribution of ISP to the NGC 2440 data, a check was made to confirm the result. Since the image field of NGC 2440 is observed to contain substantial numbers of stars, it was decided that a series of aperture polarimetry measurements should be carried out using a variety of aperture sizes. Stars that were chosen occupied regions far removed from nebular emission and from grid edges. Consequently, aperture polarimetry data were found to be unaffected by diffuse light from and sources of noise from the nebular lobes and grid edges. Results show no significant levels of ISP, assuming that the chosen stars were intrinsically unpolarized.

A further attempt to determine whether ISP is present was made by means of aperture polarimetry upon the inner condensations of the nebula. These areas show the greatest levels of polarized intensity and therefore provide ideal areas in which to find ISP. Surprisingly, in contradiction with field star analyses, the inner regions of the nebula show consistent results that ISP is indeed present. Once again, ISP measurements reveal a dependence upon wavelength, apparently showing a decrease in the R-waveband data (i.e. towards longer wavelength.) Use of a fixed diameter aperture of 10 pixels (5 arcseconds) for each measurement produced a V-band result of 0.74 ± 0.20 % at a position angle of 141.6 ± 7.6 degrees. R-waveband data, on the other hand, produced a result of 0.63 ± 0.40 % at a position angle of 151.9 ± 20.0 degrees. The author's results therefore disagree with those produced by Axon & Ellis, but highlight the difficulty in analysing the graphical plots produced by Axon & Ellis. Tables 4.2 and 4.3 shows the aperture polarimetry data within the central bipolar condensations. This was used in the determination of ISP level.

Aperture Size (Pixels)	Star Number	Position	Polarization (%)	Polarization Error ± (%)	Position Angle (°)	Position Angle Error ± (°)	Waveband
10	1	203.945, 279.386	0.607	0.164	142.753	7.723	VV
10	2	226.201, 276.912	0.805	0.149	133.170	5.312	VV
10	3	222.904, 267.842	0.811	0.135	138.673	4.782	VV
10	4	212.188, 250.526	0.843	0.126	154.486	4.287	VV
10	5	234.444, 252.175	0.561	0.126	128.612	6.451	VV
10	6	218.782, 241.455	0.419	0.164	136.882	11.233	VV
10	7	232.795, 235.683	0.761	0.132	126.885	4.983	VV
10	8	256.699, 235.683	0.881	0.292	153.916	9.501	VV
10	9	256.699, 217.542	0.861	0.336	139.611	11.177	VV
10	10	259.172, 245.578	0.897	0.335	160.827	10.710	VV

Table 4.2: V-band aperture polarimetry results for the measurement of ISP. These results have been determined from the analysis of the nebular core only.

Aperture Size (arcseconds)	Star Number	Position	Polarization (%)	Polarization Error ± (%)	Position Angle (°)	Position Angle Error ± (°)	Waveband
10	1	224.224, 243.969	0.548	0.465	154.05	24.30	R
10	2	223.132, 243.870	0.544	0.256	153.01	13.51	R
10	3	222.337, 242.578	0.716	0.206	139.02	8.25	R
10	4	222.734, 241.187	0.581	0.272	152.36	13.43	R

10	5	223.727, 240.194	0.575	0.474	153.56	23.68	R
10	6	225.416, 239.598	0.578	0.613	155.24	30.37	R
10	7	226.210, 241.088	0.576	0.657	156.56	32.78	R
10	8	225.813, 242.677	0.506	0.646	156.57	32.15	R
10	9	226.409, 250.724	0.534	0.246	150.68	13.91	R
10	10	225.614, 251.817	1.163	0.147	148.26	7.91	R

Table 4.3: R-band aperture polarimetry results for the measurement of ISP. These results have been determined from the analysis of the nebular core only.

4.4.3 INTENSITY IMAGES: V-BAND

Comparison of published emission-line images with the broadband V image of figure 4.2 clearly indicates that emission-line processes play a dominant role in the optical morphology of NGC 2440. It appears that the bipolar lobes feature very strongly in the light of emission lines. However, it is seen that nebular continuum emission also plays an important role, especially in the inner regions of the nebula where continuum radiation appears most intense.

Examination of the total intensity isophotes verifies the existence of the prominent condensations of the inner nebula. Intensity maxima also feature along the 35 degree axis, corresponding to ansae at the apices of the second pair of bipolar lobes. These are accompanied by a further pair of condensations which lie at a smaller radial distance from the nebular core than the ansae. These condensations are especially prominent in the emission from elements in high ionization states, thus indicating their exposure to a large radiation field. Similarly, the shock excitation of mass ejection(s) could also contribute to their enhancement. It is apparent that mass ejection may still be active within NGC 2440, as it had been observed, albeit tentatively, that one further set of bipolar condensations is present within the nebula. These are associated with an apparent bipolar outflow inclined at 60 degrees.

4.4.4 INTENSITY IMAGES: R-BAND

Although the R-waveband image is largely identical to the V-waveband image, differences are observed in the internal structure of the nebula. Unlike the V-band image, the R-band image provides full coverage of the nebula, although a number of problems are still inherent in the data. These problems appear as a pair of structures formed through the alignment of isophotal contours in the North-South plane ±9 arcseconds east and west of the plot centre. This is due to incomplete normalization between image frames, resulting from minimal overlap between adjoining sections of data.

It is observed that the R-band data provides increased levels of definition of the filamentary nature of the internal structure of NGC 2440. A number of the nebular condensation and filaments, however, feature very weakly in the image, suggesting that they possess higher levels of excitation and/or different geometry. The full extent of the western condensation of the 60 degree outflow is clearly visible in the R-band image, in addition to the northern spur feature which is present at ~25 arcseconds north and 0 arcseconds west.

4.5 POLARIZATION RESULTS

4.5.1 V-BAND, ISP UNCORRECTED

V-waveband linear polarization data for NGC 2440 are shown in figures 4.3 to 4.8. Each map shows two adjacent images like those in §3. The first of these images incorporates spatial information in the form of isophotal contours. The second image, however, provides complementary polarization data for the image field. For the most recently quoted distance to NGC 2440 of 1.1 Kpc, one arcsecond upon the image corresponds to a true distance of 0.005 pc in the plane of the sky. This would then imply that the total size of the visible nebula is ~ 0.3 pc or 66000 AU in the east-west plane.

The figures show increasing levels of spatial resolution encapsulating the entire nebula, down to the nebular core. The polarization data is suitably integrated to account for this and is presented with various intensity cuts to reveal the most important features. The images presented in this sub-section are uncorrected for the effects of ISP. Nevertheless, several interesting features are observed. Areas encapsulated by the outer bipolar lobes are neglected in the polarization images, as the polarization vectors appear to be randomly orientated with varying magnitude due to the reduction in signal-to-noise. The most interesting features, however, occur within the bipolar outflows orientated at 35 degrees and 60 degrees. At first glance, the nebular image in figure 4.3 presents a rather uniform and featureless nature to the polarization pattern. Closer inspection reveals structural changes in the nebular core and the 35 degree ansae.

Generally, the levels of polarization are small and uniformly orientated, implying that the distribution of dust has become increasingly uniform and that its density distribution has decreased. The lower levels of polarization are also explained by the high excitation nature of the nebula. Figure 4.3 shows that the levels of polarization range from 0.7 - 1.3 % within the interior of the 35 degree lobes, at position angles between 100 - 153 degrees. Uncertainties within the levels of polarization and position angle throughout the nebula are of the order of 0.1 – 0.3 % and 3 - 7 degrees.

The most prominent feature of the polarization maps is the presence of ellipticity in the pattern of polarization vectors about the region coincident with the inner nebular condensations. Once again, the magnitude of polarization in this region appears fairly low and uniform, following the general trend of vectors at larger radial distances. Closer inspection reveals a decrease in polarization level in close proximity of the plot centre and also at a radial distance of ~10 arcseconds south-east along the position angle ~137 degrees. Unfortunately, coverage of the nebula at a corresponding distance to the north-west is incomplete, thus preventing visual inspection of the nature of polarization within this area. Although this area is largely obscured, it is tentatively observed that the polarization vectors show an increase in

magnitude. This is revealed to the south-east beyond 10 arcseconds, as the polarization levels show a relatively large increase. The presence of ellipticity in the pattern of polarization could indicate that NGC 2440 possesses an underlying centro-symmetric polarization structure, thus providing information upon the location of the central illuminating source. It is known that ellipticity in the pattern of polarization can occur through the action of the ISM. This would then conform with the proposal of a contribution from ISP to the levels of polarization of NGC 2440, primarily on the basis of the uniformity of the observed polarization vectors. It is also known that the presence of an extended central source, in the form of a circumstellar disc or torus, may also lead to an elliptical distortion of centro-symmetric scattering patterns. Attention is drawn to the fact that the central torus of NGC 2440 appears to be inclined along a position angle of ~165 degrees, as determined from the connection of the intensity maxima of the inner nebular condensations. Analysis of the pattern of polarization vectors suggests that the circumstellar torus possesses an equatorial dimension in excess of 20 arcseconds. Examination of the isophotal contours, however, implies that the central torus possesses an equatorial extent of ~17 arcseconds, although the true angular scale may be more. Full discussion of this is provided in the sub-section upon ISP corrected polarization data.

The second feature of the polarization images of figures 4.3, is the slight increase in the levels of polarization within the vicinity of the northern ansa of the 35 degree bipolar outflow. Uncorrected V-band polarized intensity data shows that both ansae are polarized, with the northern ansa presenting the highest levels of polarized intensity between the two regions. Figure 4.7 shows uncorrected polarized intensity data only in the nebular core.

Figure 4.4 shows a high resolution contour image with an adjacent polarization map for the central core of NGC 2440. The high resolution afforded by this image implies that greater constraint may be placed upon the levels and orientation of polarization. The levels of polarization encountered within the inner nebula appear to range from 0.1 - 1.7 %. Uncertainties in these measurements are of the order of 0.1 – 0.3 % and 4 - 8 degrees. It is observed that the polarization pattern in the south-eastern quadrant of the image follows a smooth elliptical formation. The pattern in the north-western quadrant, however, does not follow such a smooth profile. Instead, it appears that the vector pattern becomes warped and also begins to turn over at a smaller radial distance from the plot centre. The reason behind this effect is presumably differences in the geometric exposure of scattering centres beyond the circumstellar torus. If this is true, it is likely that the nebular core contains several illuminating sources, other than the central star. In providing clarification of this proposal, complete removal of ISP must be achieved. ISP corrected images are discussed later in this chapter. Interestingly, a sharp decrease in the magnitude of polarization is observed at the location believed to mark the position of the central star. This would suggest that the central star occupies a region which possesses high levels of intrinsic emission.

4.5.2 V-BAND, ISP CORRECTED

Figures 4.5, 4.6, and 4.8 show V-band polarization data which has been corrected for ISP effects. Although the intrinsic polarization levels of NGC 2440 are similar in magnitude to the levels of ISP, a significant difference in the patterns of polarization is observed. Polarization data in all images are integrated in bins 2.5 arcseconds square. Fortunately, the average seeing for the data used in the reduction is below this limit, implying that the data, although slightly smoothed, are accurate. It was found that integration of data into 1.5 arcsecond square bins resulted in unreliable data, as the bin size fell below the limit of atmospheric seeing. Inspection of the ISP corrected polarization map shows several features in pattern of polarization. These features include several regions of enhanced polarization, a near centro-symmetric polarization pattern, and the suggestion of an outflow.

It is seen in figure 4.5 that the most prominent of these features is the enhanced levels of polarization which appear ~7 arcseconds both north-west and south-east of the plot centre, at a position angle of 135 degrees. This position angle marks the inclination axis of the circumstellar torus and therefore shows that scattering occurs at its edges. Enhancement of polarization continues outward to a radial distance of ~ 14 arcseconds north-west and south-east of the nebula centre. The pattern of polarization within these regions appears to resemble that of centro-symmetry. The centro-symmetric pattern, however, does not encircle the entire region of the inner nebula, but appears to form a discontinuity at ~ 45 degrees above and below that central symmetry axis of 135 degrees. Within the nebular core, at radial distances less than 7 arcseconds, polarization appears to trace out the form of a heart shape. At the centre of this unusual pattern, the polarization vectors are observed to follow a position of ~ 40 degrees, about which they appear aligned. Additionally, the magnitude of polarization appears slightly higher than is present in the immediate vicinity. Inspection along this position angle shows several localized areas of increased polarization. Moving outward along the line to the north-east, it is observed that a slight enhancement occurs between 2 arcseconds and 5 arcseconds. Here, polarization levels reach approximately 0.4 %, oriented at right angles to the 40 degree axis, suggesting the presence of scattering processes. Beyond this region, polarization levels once again revert to lower values, but show an increase once more from ~ 8 arcseconds. It appears that these polarization vectors coincide with the train of nebular condensations along the 35 degree bipolar outflow. Analysis of polarized intensity covering the whole nebula, reveals that the nebular condensations along the symmetry axis of the 35 degree lobes, show enhanced levels to those of the surrounding areas. Interestingly, the vector pattern changes dramatically in the south-west, where the polarization vectors run parallel along the position angle 40 degrees, out to a radial distance of ~ 4 arcseconds. These observations provide evidence for the existence of a possible outflow in this region. Further debate of this observation will be provided in the sub-section on discussion.

The final major feature of figure 4.5 is the increase in form of the centro-symmetric scattering pattern. It appears that the pattern becomes prominent from ~ 7 arcseconds, in coincidence with the increased polarization. The centro-symmetric structure, however, is poorly defined in the inner regions of the nebula and interior of the bipolar lobes. A look at figure 4.6 shows the nebular core at higher spatial resolution. The general axis of centro-symmetry in this case is around the position angle 135 degrees, almost perpendicular to the outflow of polarization vectors mentioned previously. At first glance, the polarization pattern would indicate illumination of scattering centres from the central star only, but closer scrutiny of the vectors suggests that several points of illumination exist in addition to the central star. Most points of illumination seem to lie within close proximity to the central star, forming along the inner walls of the circumstellar torus. Other points, however, appear to lie on the outside of the southern condensation, suggesting that scattering of emission-line gas may be occurring. Although the polarization may, at first, appear relatively simple to explain, closer examination shows that a very complex set of processes exist within the core of NGC 2440. It is possible that the complexity of the vector patterns is associated with the complex filamentary nature of nebular gas.

The higher resolution of figure 4.6 shows features not apparent in the larger scale representations of data. Throughout the space of the inner nebula, polarization levels appear to range from 0.1 % to 1.9 %, with uncertainties ranging from 0.1 – 0.3 % and 4 - 8 degrees. Nevertheless, a number of areas in figure 4.9 show little or no polarization, resulting from the existence of competing polarization mechanisms. The majority of these 'null' vectors appear to lie along the axis of the 40 degree outflow mentioned earlier. The presence of these null vectors highlights the possible coexistence of both scattering processes and alignment processes. These processes do not necessarily occur in the same regions of gas and dust, but can occur through the action of projection effects along the line of sight, as demonstrated by the effects of the ISM. It becomes obvious that the process of dust alignment takes on a predominant role in determining the pattern of polarization towards the south-west. The north-east, however, shows a reversal in the nature of polarization, as scattering and alignment reveal their presence. The inner sector of the flow between 2 arcseconds and 5 arcseconds appears to be dominated by scattering, but this appears to change from 7 arcseconds to ~ 12 arcseconds, where alignment processes begin to feature more strongly.

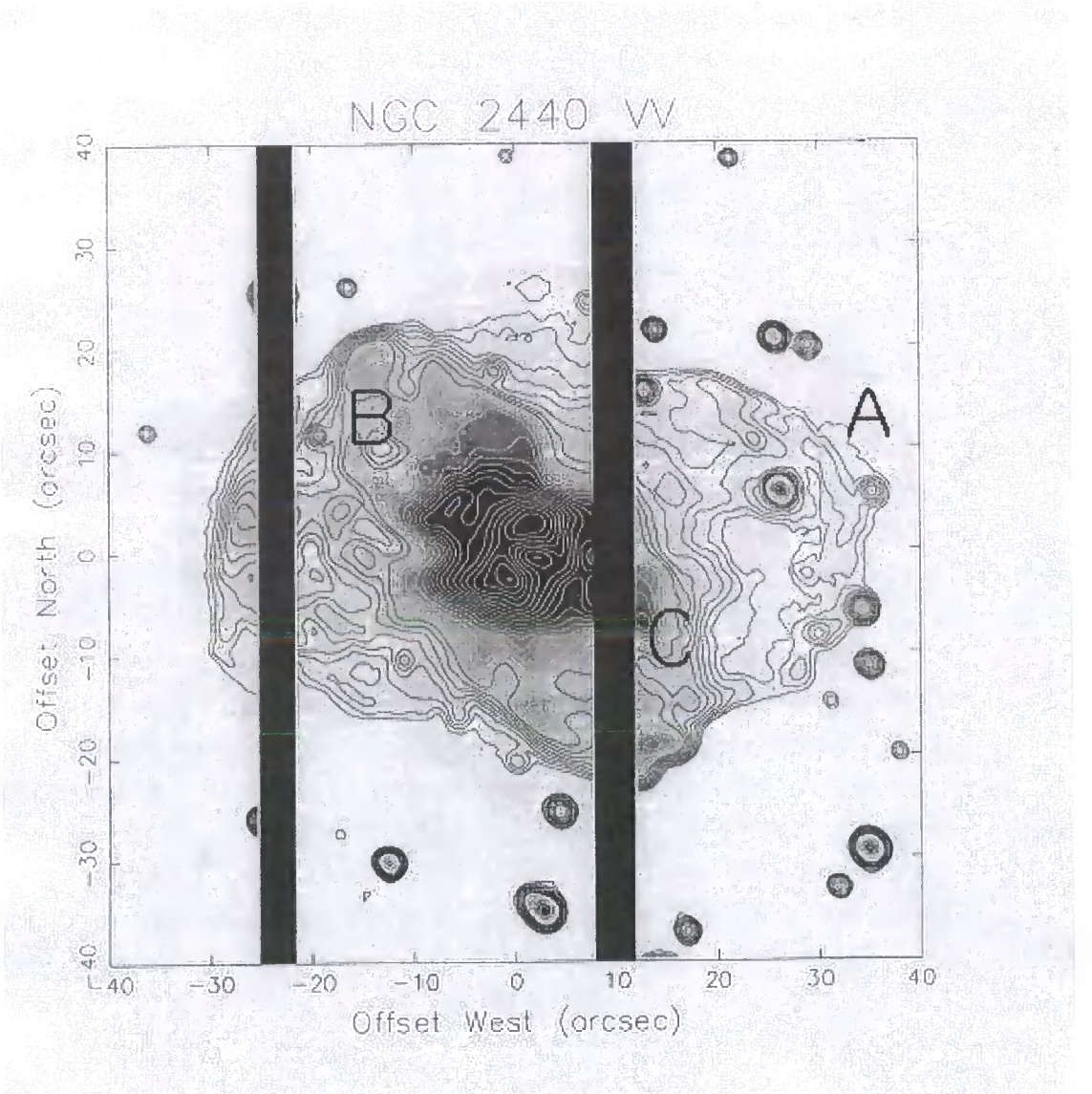

Figure 4.2: Broadband V total intensity image with superimposed isophotal contours

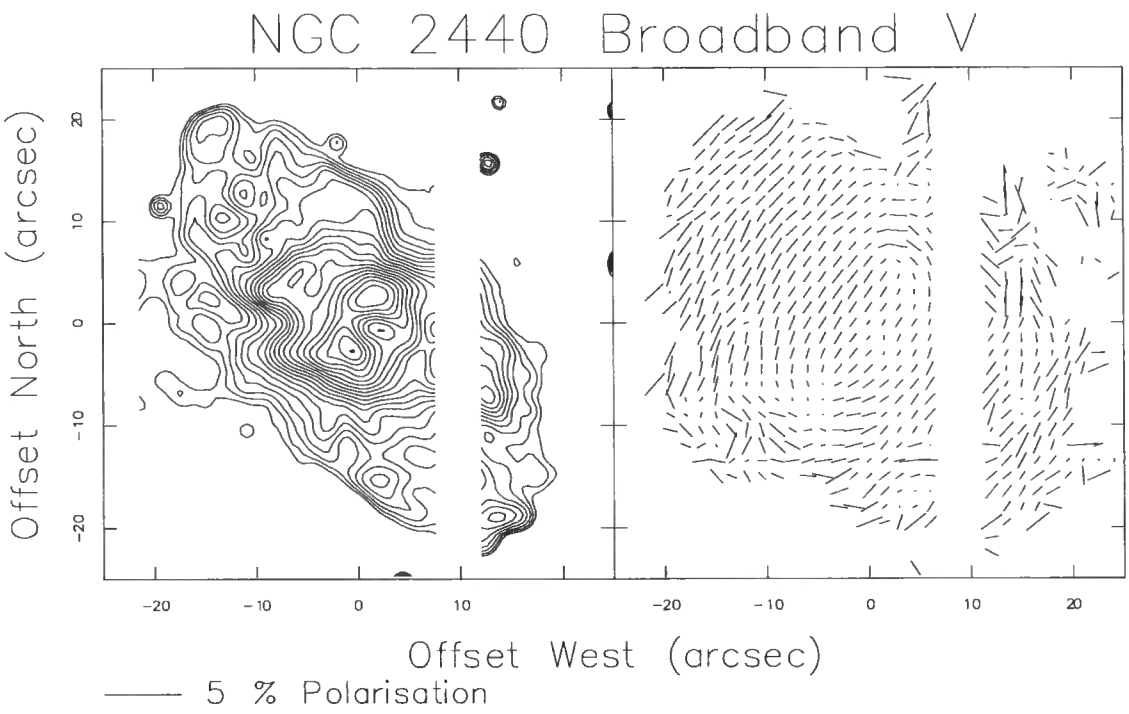

Figure 4.3: Broadband V polarization image (low resolution) showing both contour data and polarization data which are uncorrected for ISP

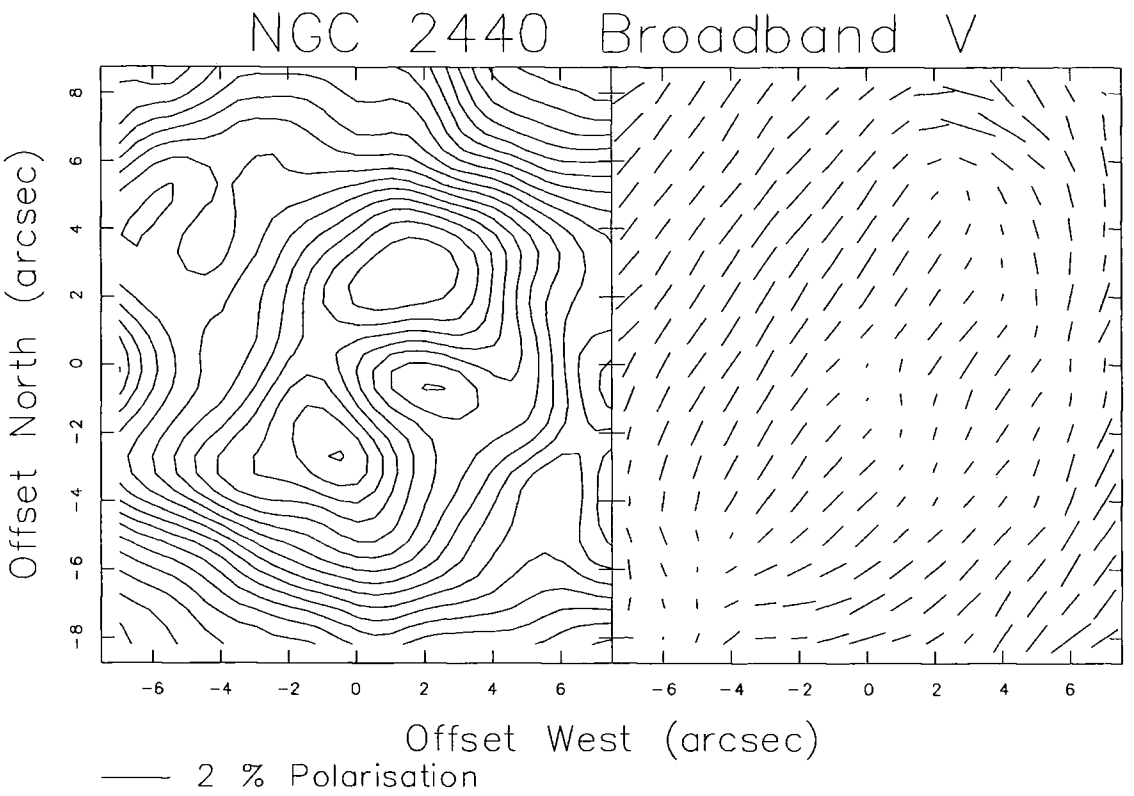

Figure 4.4: Broadband V polarization image (high resolution) showing both contour data and polarization data which are uncorrected for ISP

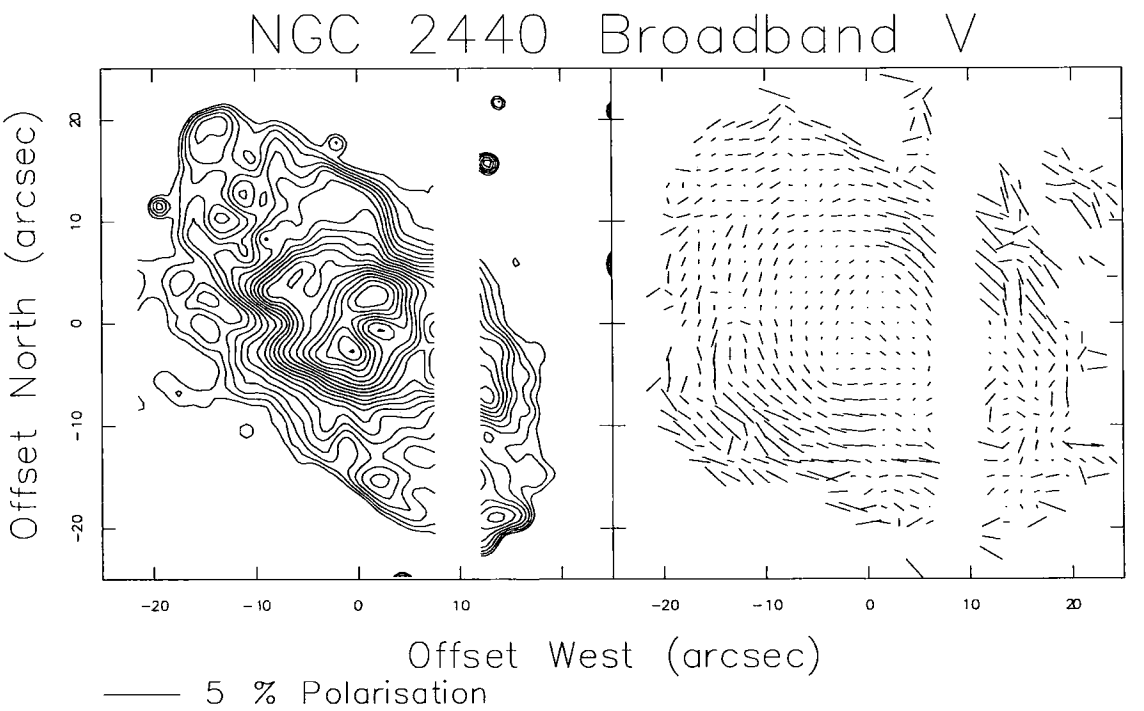

Figure 4.5: Broadband V polarization image (low resolution) showing both contour data and polarization data which are corrected for ISP

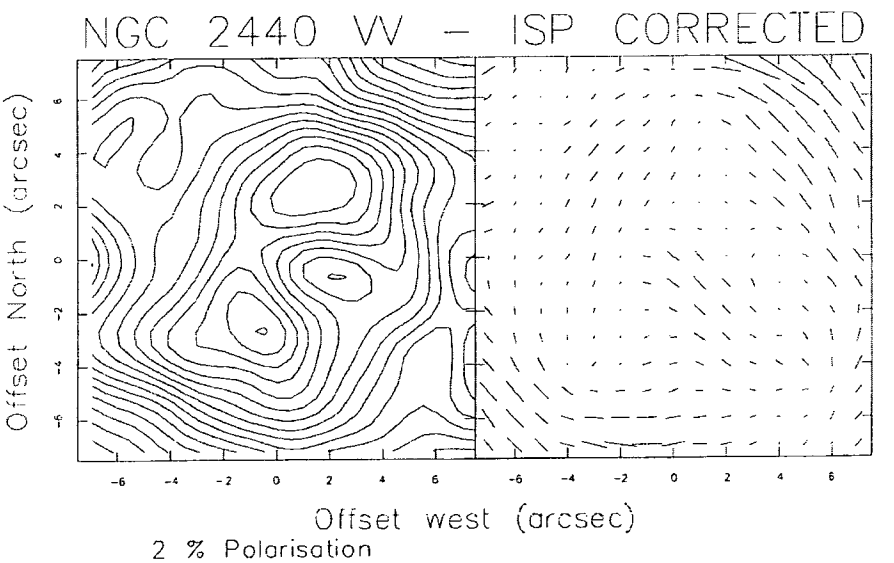

Figure 4.6: Broadband V polarization image (high resolution) showing both contour data and polarization data which are corrected for ISP.

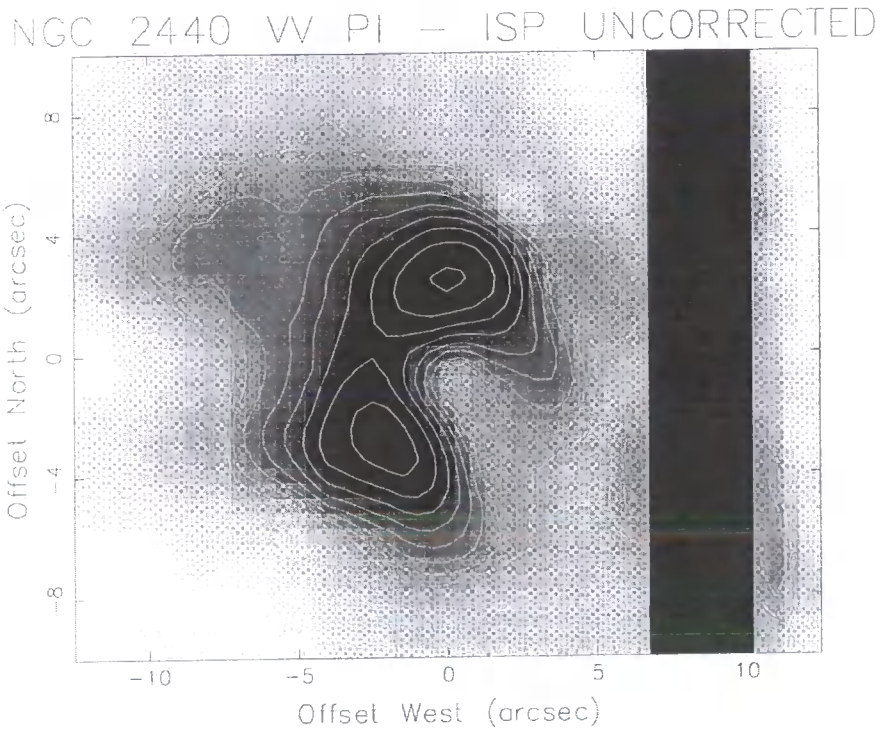

Figure 4.7: Broadband V polarization image showing the polarized intensity of the central regions of NGC 2440. Data are uncorrected for ISP

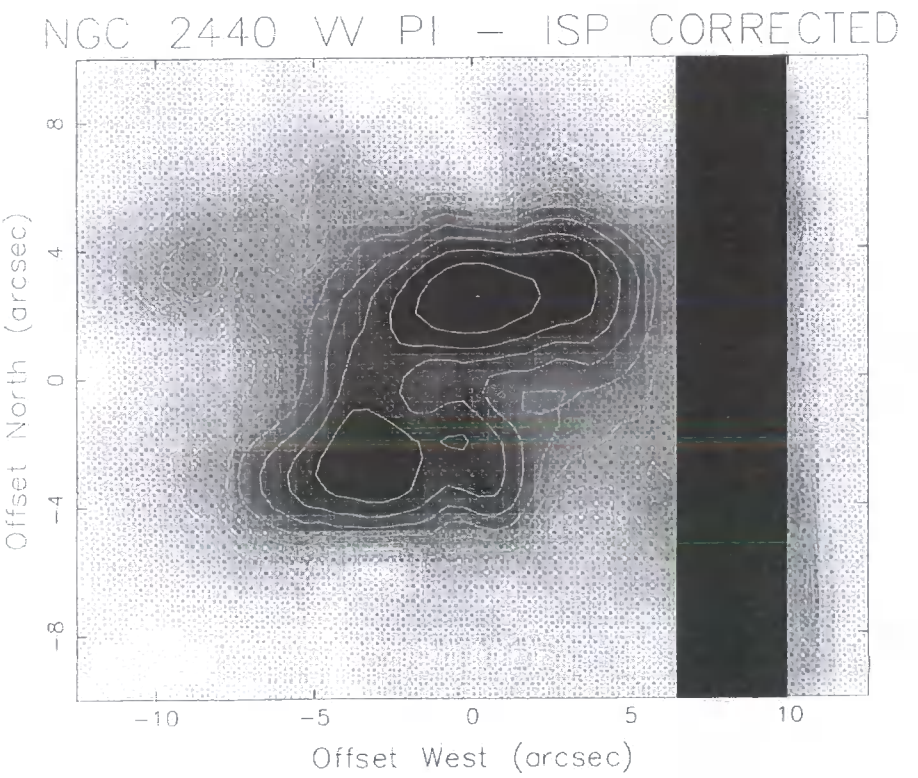

Figure 4.8: Broadband V polarization image showing the polarized intensity of the central regions of NGC 2440. Data are corrected for ISP

4.5.3 R-BAND, ISP UNCORRECTED

Figures 4.10 to 4.15 show spatial and polarization data for R-waveband measurements. Examination of figure 4.10 shows that the apparent uniformity of V-band data is reproduced. Yet closer scrutiny of the polarization image, shows that changes in the polarization pattern exist. Regions identifying the outer lobes have been neglected once again due to decreased signal-to-noise, and suitable intensity cuts applied to the data. It should be noted that irreparable problems occurred during the normalization between image frames. These problems are manifest as a pair of discontinuities in the data extending north-south at offsets of ± 10 arcseconds east and west of the plot centre.

It is apparent that the R-band images show much greater complexity in both intensity and polarization structure, with the manifestation of several features which are not inherent in the V-band data. The most striking of these is the distortion upon the polarization pattern of the nebular core. Unlike the V-band image, which shows a smoothly varying elliptical vector pattern, the R-band image shows a highly disrupted elliptical vector pattern. Consequently, it becomes difficult to make an estimate of the extent of the circumstellar torus from the polarization measurements. Examination of the isophotal contours, however, shows that the position angle of the circumstellar torus is ~165 degrees, as determined form the location of the intensity maxima of the inner bipolar condensations. It appears that the polarization pattern shows a strong tendency to follow this bipolar pattern, although the north-western quadrant of this inner pattern shows an open-ended structure, which seemingly blends into an arc of polarization vectors at a radial distance of ~10 arcseconds and position angle ~153 degrees. Previously unidentified, this polarization pattern appears to coincide with the arcuate filament just beyond the lobes walls of the 35 degree outflow. The apex of this filament appears at a position angle of ~147 degrees. Surprisingly, no corresponding counterpart is observed in the south-eastern quadrant of the nebula. Like the northern spur seen in figure 4.3, the origin of this arcuate structure is at present, unexplainable. However, an increase in polarization is observed in the south-eastern quadrant of the nebula, at a radial distance of 10 arcseconds and position angle ~135 degrees corresponding to the end of the circumstellar torus.

The observed levels of polarization in figure 4.10 range between 0% and 1.8 %, at position angles of 129 - 168 degrees. Uncertainty in the calculated values of polarization is high due to the lower collected signals, with values of the order of 0.2 – 0.4 % and 5 - 10 degrees. Interestingly, the increase in polarization observed within the region of the northerly 35 degree ansa of the V-band data, is not observed in the R-band data. A slight increase is observed, but is a likely result of the reduction in the signal-to-noise. A further analysis and discussion is provided in the sub-section on ISP-corrected polarization data.

4.5.4 R-BAND, ISP CORRECTED

Figures 4.13 to 4.15 show R-band polarization data which has been corrected for ISP. It is observed that the figures show similar features to the corrected V-band data. Differences, however, are apparent in the inner nebula and the interior of the lobes at position angle 35 degrees. Most prominent of these differences, is the decrease in definition and change in geometry of the centro-symmetric polarization pattern. Once again, the orientation of polarization vectors indicates that several illuminating sources exist in the vicinity of the central star. Inspection of the high resolution image of figure 4.14 clearly suggests that illumination occurs from the inner condensations of the nebula, thereby supplementing that from the central star.

Interestingly, the levels of polarization appear stronger in the south-east than in the north-west, suggesting that differences in the geometry of scattering centres exist with respect to the sources of illumination. The differences in peak polarization may then be explained in terms of a tilt upon the circumstellar torus. Mie scattering from dust grains could then explain these observations, since polarization levels would generally possess lower magnitude and would show a peak for scattering angles ≥ 90 degrees. This would then imply that the southern condensation of the inner nebula is tilted towards the observer and the northern condensation tilted away.

Like the corrected V-band data, corrected R-band data also reveals the signature of an outflow, albeit tentatively. Although the polarization pattern of the outflow is less well defined, estimation of the outflow position angle lies in the range 35 – 45 degrees, like that for the V-band data. This provides evidence for the coincidence of the polarization pattern with the actual lobe axis, although no significant outflow signature is observed for the 60 degree lobe system. This would suggest that grain alignment along this position angle is weak and/or suppressed by scattering processes.

Although figure 4.15 is affected by alignment problems, it is reasonable to suggest that no significant change occurs in the structure or level of polarized emission when compared with figure 4.12. Analysis of the ISP corrected polarized intensity data shows that the core and 60 degree lobes are definitely polarized, and also shows that the 35 degree lobes are polarized to a lesser extent.

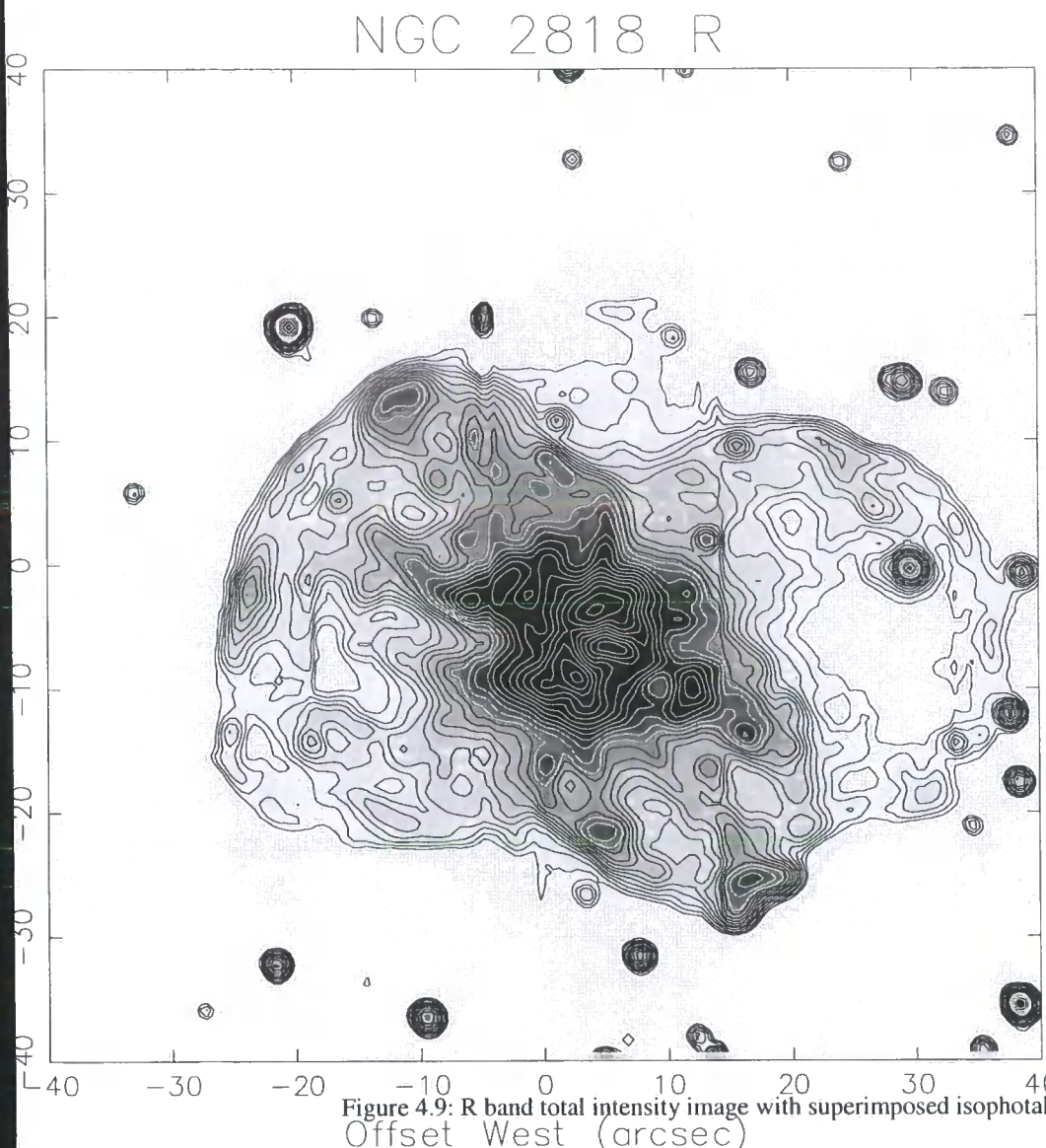

Figure 4.9: R band total intensity image with superimposed isophotal contours

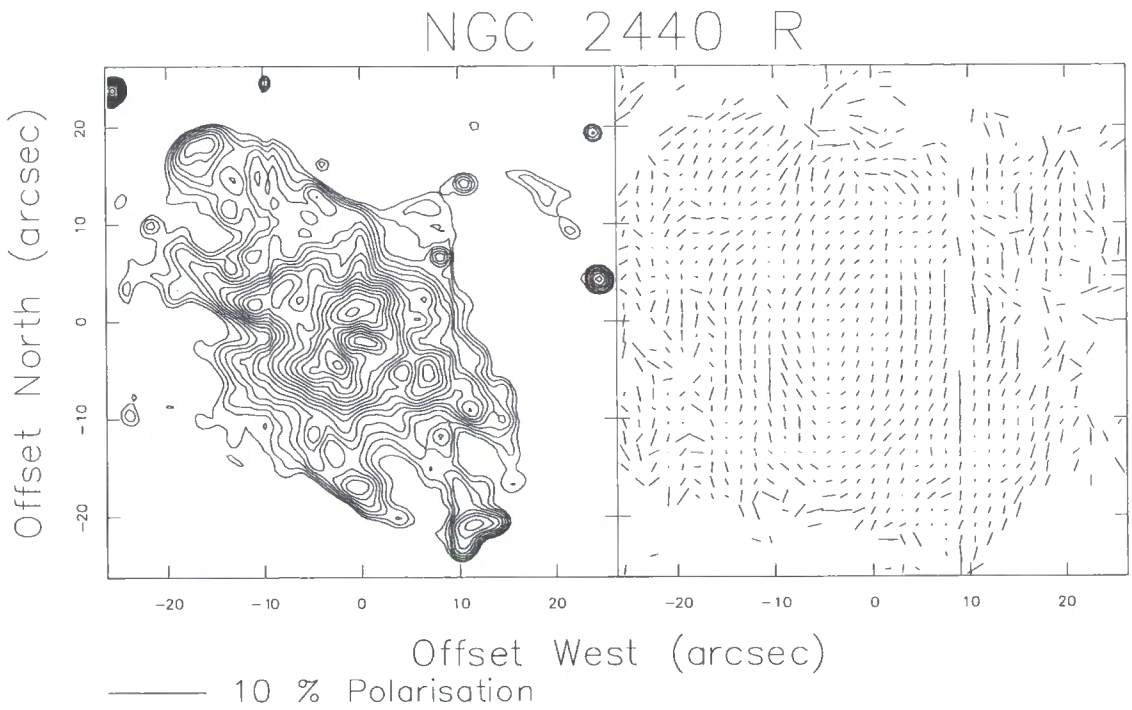

Figure 4.10: R band polarization image (low resolution) showing both contour data and polarization data which are uncorrected for ISP

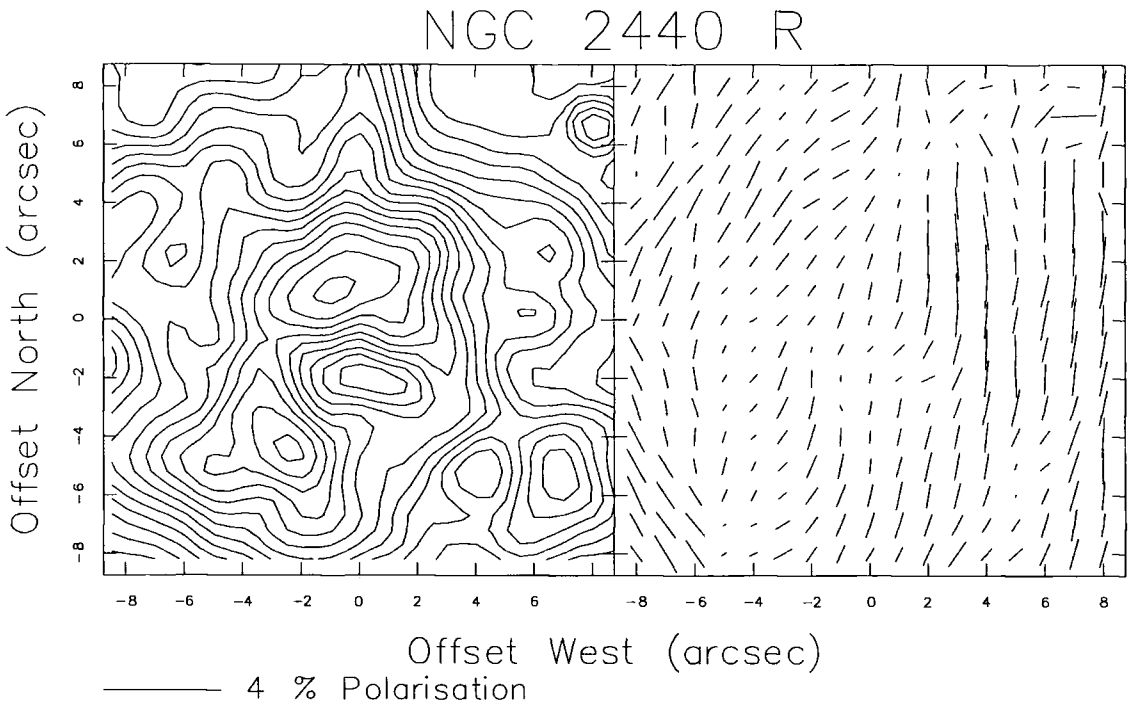

Figure 4.11: R band polarization image (high resolution) showing both contour data and polarization data which are uncorrected for ISP

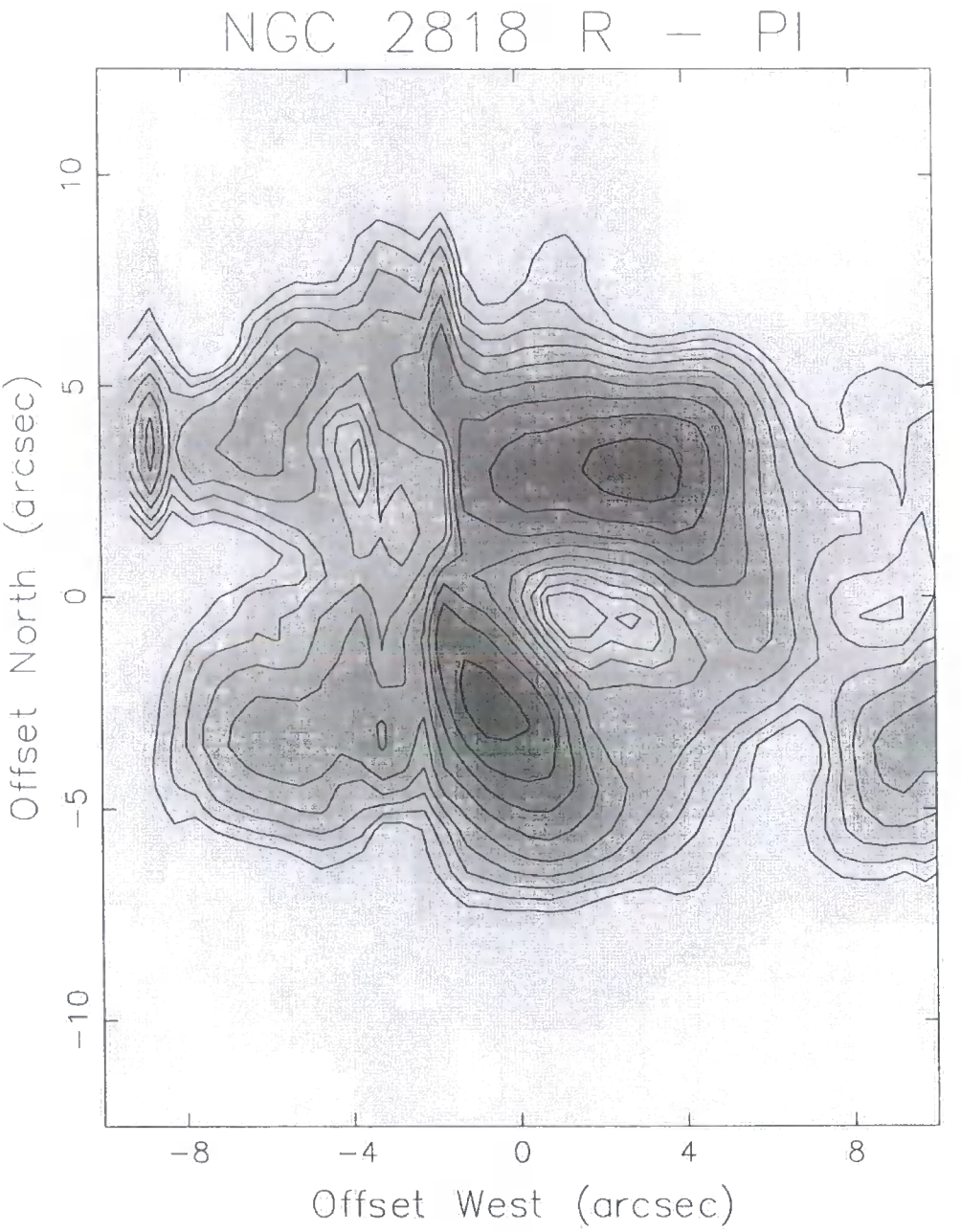

Figure 4.12: R band polarization image showing the polarized intensity of the central regions of NGC 2440. Data are uncorrected for ISP

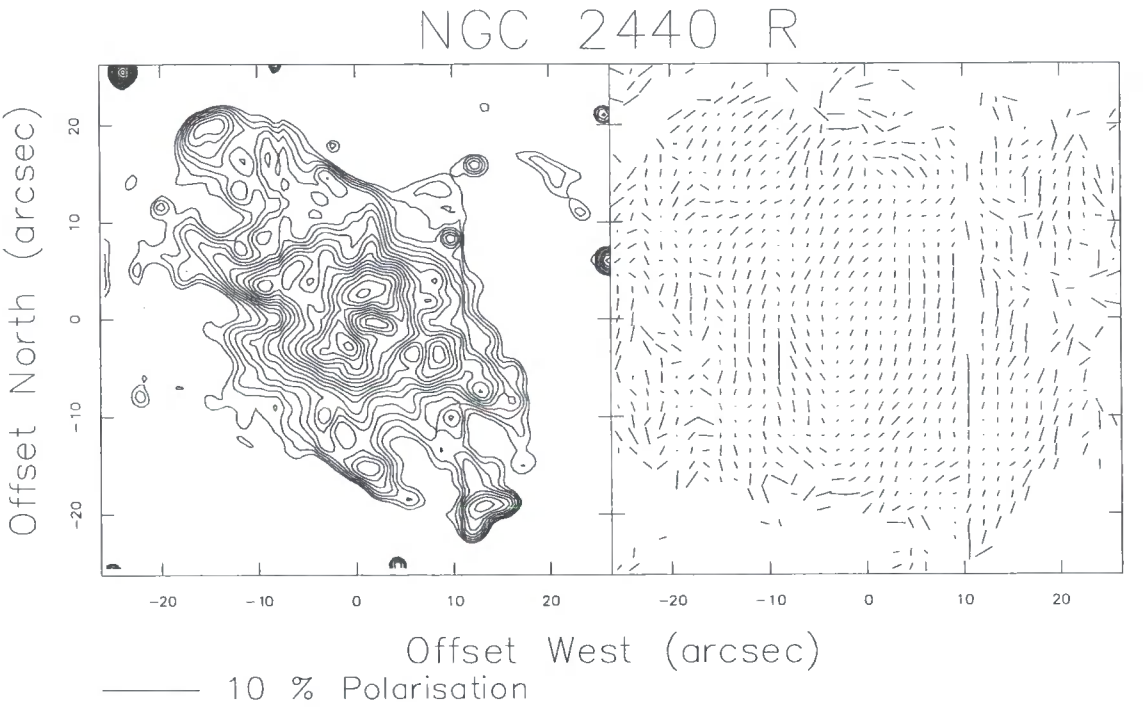

Figure 4.13: R band polarization image (low resolution) showing both contour data and polarization data which are corrected for ISP

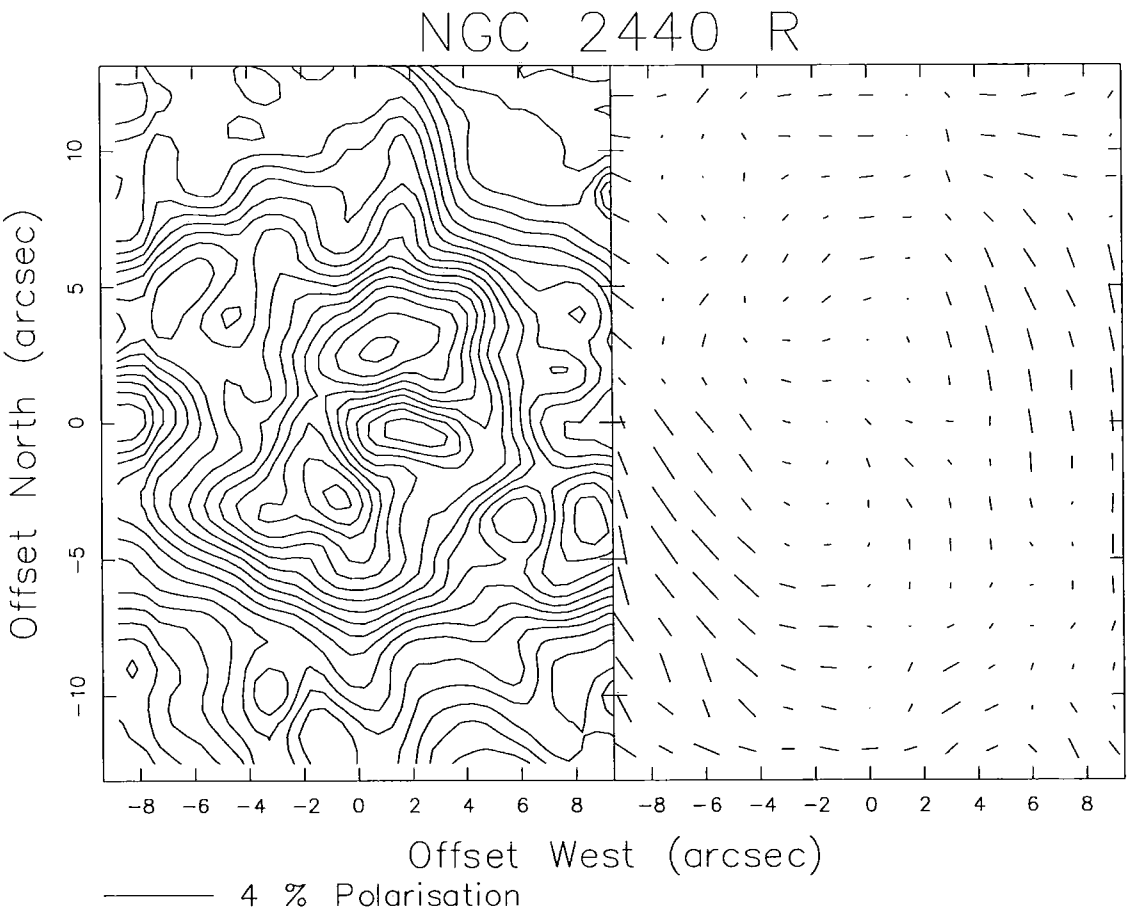

Figure 4.14: Broadband V polarization image (high resolution) showing both contour data and polarization data which are corrected for ISP

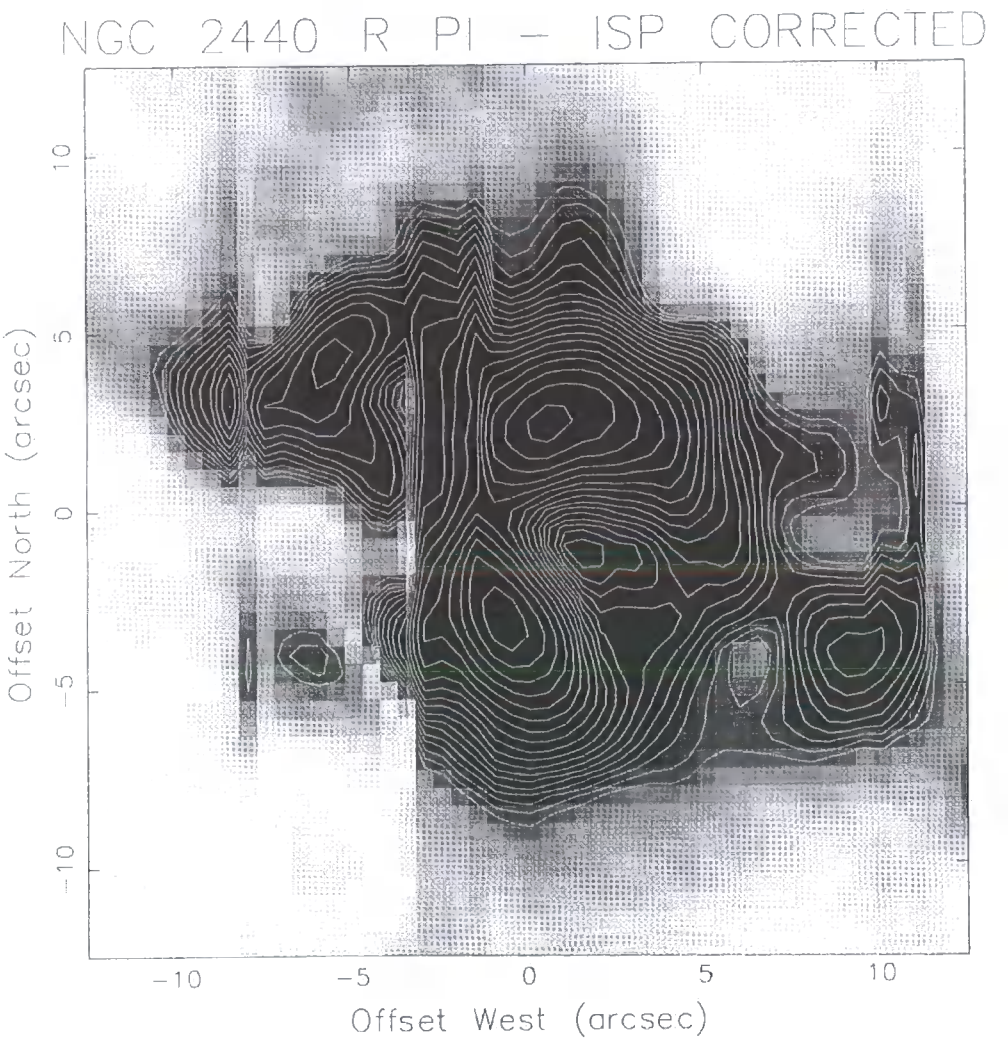

Figure 4.15: R band polarization image showing the polarized intensity of the central regions of NGC 2440. Data are corrected for ISP

4.6 DISCUSSION

4.6.1 CENTRAL TORUS

Within the region marked by the inner condensations, the polarization levels are visibly lower, although this is primarily due to the dilution effects from the overwhelming intrinsic emission of the condensations, it is also possible to argue that a large-scale structure in the form of a circumstellar disc or torus must be present, resulting in an obscuration of scattered light. The observation of higher polarization levels outside the circumstellar torus is attributed to a decrease in the level of intrinsic emission.

Although previous studies have provided details of the kinematical structure of NGC 2440, only recently evidence has appeared to suggest that the nebular core is inclined to the plane of the sky (Vazquez et al. 1999). Polarization data presented in this study strengthens these ideas, providing evidence that the central torus is tilted. Although a figure has not been calculated for the inclination of the circumstellar torus, data suggests that it is inclined with the south-eastern condensation pointing towards the observer and the north-western condensation pointing away. A look at the isophotal data also shows that the south-western edge of the torus suffers a reduction in the levels of emission, presumably due to a reduction in the density of material at that point. The north-eastern edge of the torus, however, appears largely intact. This may suggest that the central torus is inclined with respect to both the 35 degree and 60 degree lobes. Additional observation would be required to confirm this, since present data provide only minimal evidence for such an assumption.

In its present state, the central torus lies off-axis with respect to all three of the bipolar lobe systems. This introduces a large degree of difficulty in associating the torus with the mechanism of collimation and the origin of the bipolar lobes. Currently, orientation of the plane of the torus is almost perpendicular to the bipolar lobe system along the position angle 60 degrees. A similar situation is encountered in the extraordinary PN known as KjPn 8. Steffen & Lopez (1998) determined that the expanding molecular disc of the nebula, originally found by Forveille et al. (1998), is oriented perpendicular to the most recent and highest-velocity bipolar outflow. Evidence also shows that the circumstellar disc of KjPn 8 is oriented far off-axis from the largest bipolar lobes.

Radio recombination line data gathered by Vazquez et al. (1999) include kinematical study of the central torus of NGC 2440. Position-velocity measurements for the inner nebular regions suggest that the western side of the structure is approaching, while the eastern side is receding. This, together with HST optical data gathered by Lopez et al. (1998), molecular H_2 imaging data by Latter & Hora (1997), and optical polarization data presented in this thesis, suggests that the shape of the torus is vastly different from the

original shape. Evidence implies that the torus has suffered from the effects of both stellar wind processes and a large UV radiation field. Detection of the most recent outflow along the position angle 60 degrees, suggests that disruption of the circumstellar torus is ongoing.

4.6.2: BIPOLAR LOBES AT P.A. 35 DEGREES

It is clear that the general level of polarization found within the volume of the 35 degree lobe structures is very low. Explanation of this observation comes from the fact that intrinsic gas emission in the interior of the lobes is high. This emission acts to dilute the amount of scattered light which is present, thereby reducing the true levels. Furthermore, the levels of polarization from scattering processes are affected by the presence of additional polarization mechanisms. Regions appear to exist within the lobes, however, which show increased levels of polarization. The enhancements in polarization appear to occupy very localized areas within the nebula, and may therefore coincide with the densest nebular condensations or filaments. It is known that the interior of each of the lobe systems is comprised of cool, dense filamentary condensations which are immersed in a hot, diffusely ionized gas. Such condensations are therefore likely to harbour substantial amounts of dust, resulting in the appearance of increased polarization.

However, the pattern of enhanced polarization, which appears to partially trace the walls of the nebular lobes is explained with greater difficulty. It is clear that these features exist in the V-band data, but their definition appears weaker, if at all, in the R-band data. Obviously, the results show that increased levels of dust are prevalent within the vicinity of the lobe walls. However, the results show an unexpected polarization pattern for scattering off the inner walls of the lobes. If scattering occurred along the axis of the nebular lobes as expected, the polarization vectors would be aligned perpendicular to the polar axis of the bipolar lobes. Although this is encountered in the low levels of polarization visible in the interior of the lobes, the pattern of peak polarization shows a parallel trend along the lobe walls. This could be attributed to the presence of a reflection nebula just beyond the boundary of the nebula lobes, as is observed in the PN IC 4406 (Scarrott & Scarrott 1995). However, the pattern only appears prominently in the northern part of the nebula, and features very poorly in the south. Although the observations can be explained in terms of geometric effects, the assumption that obscuring material lies between the illuminating sources and reflection nebula seems highly unlikely, since the outer lobes appear to be polarized to some extent. Additionally, R-band data does not reproduce the unusual vector pattern, which strengthens the conclusion that a reflection nebula does not exist outside the boundary of the 35 degree lobes. It seems likely that the polarization pattern is associated with the lobes and that alignment of dust grains has occurred along the flow of gas through the lobe walls. Presumably, disruption in the flow of gas along the southern lobe wall, would cause dust to become randomly oriented with no large-scale ordering, thereby resulting in a randomisation in the ordered polarization pattern observable in the south.

The scattering processes involved in the production of polarization within the interior region of the lobes are most probably caused by the presence of dust grains which have been swept-up with gas, into a dense shell at the inner boundary of the lobe walls. Although this dust may be evenly distributed along the inner face of the lobes, the observed polarization pattern would suggest otherwise. This implies that other processes are acting to distort the true centro-symmetric scattering pattern into the elongated, cone-like patterns which are observed.

4.6.3 THE BIPOLAR LOBES AT P.A. 60 DEGREES

Although the condensations at the apices of the 60 degree outflow feature quite prominently in polarized intensity, it should be noted that the ISP corrected polarized intensity image shows little emission from these structures. Together with ISP corrected polarization results, this would suggest that the condensations are essentially unpolarized and merely observed by intrinsic emission. However, the possibility that an active outflow exists to produce these structures is not to be ruled out entirely. Although the polarization data present insignificant evidence for an outflow, further kinematical observation would provide clear evidence of the true nature of the 60 degree lobes.

4.7 SUMMARY

NGC 2440 is an evolved object, which appears to have largely passed through the transition from AGB star to PN. However, it is evident that mass-ejection is still an active process within the nebula. NGC 2440 is particularly interesting among bipolar PNe, in displaying multiple bipolar outflows. These outflows support the idea that the central star is in fact binary. Explanation of the poly-polar phenomenon, however, appears to extend from the newly developed theory of bipolar rotating episodic jets (BRETs).

The complex and high excitation nature of the NGC 2440 is exemplified by the low levels of polarization, as results suggest that scattering processes play only a minor role in nebular emission, and the complex polarization patterns mirror the filamentary nature of nebular gas. Results also show that the circumstellar torus contains several sources of illumination with respect to the zones of scattering. The levels of polarization suggest that the central torus is inclined with respect to the plane of the sky, such that the SE edge of the torus is tilted toward the observer and the NW edge tilted away. The current orientation of the circumstellar torus presents difficulty in its association with the mechanism of collimation and origin of the nebular lobes.

Evidence exists within the polarization data to suggest the presence of a jet in the bipolar lobes at position angle 35 degrees. This is illustrated by the apparent presence of the competing polarization mechanisms of dust scattering and dust alignment. Although there is no direct evidence in the polarization data to indicate the presence of a jet in the bipolar lobes at position angle 60 degrees, optical imaging reveals the presence of a pair of point-symmetric condensations.

CHAPTER 5

NGC 2818

5.1 INTRODUCTION

NGC 2818 (PK 261 + 8°.1) was first discovered and classified as a PN by Herschel in 1838. It is unique among PNe because of its apparent association with a population I open cluster. Such association has made it possible to develop a greater understanding of the nebula. Further observations are required, however, to derive accurate nebular parameters, since the majority of studies have concentrated solely upon the parent open cluster. In this chapter, optical polarimetry maps of NGC 2818 are presented and discussed within the framework of previous observations using spectroscopy and photometry.

5.2 PREVIOUS STUDIES

NGC 2818 is situated at a position RA 09h 16m 01.7s, Dec. -36° 37′ 49″ (2000.0). Surprisingly, its unique nature received little attention, although it is the only PN believed to reside within a galactic open cluster. Observations carried out by Tifft et al. (1972) show that the nebula lies in close proximity to the open cluster, and shares similar extinction and radial velocity measurements with a number of the cluster members. With galactic co-ordinates l=261°, b=8°.1, the nebula possesses a moderate galactic latitude for

its type. The scale height of NGC 2818 is at least 500 pc above the galactic plane. Analysis of differing morphological types of PNe by Schwarz & Corradi (1995) show that NGC 2818 displays a scale height at the extreme of the range typically shown by bipolar PNe. Such a value for the galactic latitude implies that interstellar reddening is likely to be important. This has since been confirmed through photometric analysis of the open cluster members, and also through polarimetric observation of stars within the galactic plane (Axon & Ellis 1976).

Figure 5.1 shows that NGC 2818 possesses many of the morphological attributes of other nebulae of its type. The core of the nebula is composed of an 'hourglass' figure oriented north-south, and extending 60 arcseconds or more in diameter. The outer nebula is characterized by two bipolar lobes which are seen as series of east-west extending arms. The total extent of the lobes is at least 130 arcseconds in diameter, indicating that the nebula is extremely large. At a recently adopted distance of 2.3 ± 0.2 Kpc (Pedreros 1989), this would imply that NGC 2818 is more evolved than both NGC 2440 and M2-9. A complex filamentary sub-structure is observed within the nebula, although most of this structure remains unresolved. NGC 2818 is classified as a bipolar PN, but its equatorial waist in poorly pronounced, placing it at the boundary between bipolar and elliptical.

The apparent lack of an optically thick circumstellar disc means that the central star is directly observable. Photometric measurements by Kohoutek et al. (1986) yield a value of 18.5 for its visual magnitude, while earlier observations by Tifft et al. yield a visual magnitude of 17.5. The fact that the central star is visibly faint indicates that it possesses a high surface temperature. These measurements have been confirmed, which suggests that the nebular excitation will be high. The spectral class of the star, as determined from fitting to the main-sequence turnoff, is suggested to be around A5. However, the degree of excitation and the size of the nebula would suggest otherwise, pointing to a central star of earlier spectral class.

Spectroscopic studies reveal that NGC 2818 possesses a large variety of elemental constituents, each occupying a range of ionization states. Detailed density and excitation mapping by Phillips & Cuesta (1998) shows that minor axis emission follows a bilobal structure. This is corroborated by observations by Schild (1995) of the molecular hydrogen transition H2 1-0 S(1). Mapping of H_2 shows an inner elliptical ring oriented east-west, extending ~75 arcseconds. The total north-south extent of H_2 is ~50 arcseconds, with a peak in emission forming a detached partial shell to the south. Line ratio measurements of these structures show that the partial shell of the southern regions is excited by shock processes, while the inner ring is excited by radiation from the central star. The western edge of the inner ring appears to coincide with the emission-line feature in the north-western quadrant of the nebula.

Through the analysis of [S II]/Hα and [O III]/Hα line ratio images, Phillips & Cuesta find a shock velocity component $V_s \geq 110$ km s^{-1}, which they believe to be associated with a high velocity wind. However, it is

known that shock velocities above ~ 40 km s^{-1} lead to the dissociation of molecular hydrogen (Pineau des Forêts et al. 2001), which would mean that no trace of H_2 could be found within NGC 2818 at a shock velocity of 110 km s^{-1}. No direct observations have yet been made of such an outflow, but its existence is inferred as being the most probable mechanism for the shaping of the nebula. Modelling by Burton et al. (1992) shows that the observed H_2 flux levels can be attained through the action of J- or C-type shocks. Hα profiles gathered by Banerjee et al. (1990) yield an expansion velocity of ~ 25 km s^{-1}, which is typical of C-type shock velocities.

Direct imaging of selective passbands (e.g. [N II], [S II], [O III], etc.) by Phillips & Cuesta (1998) show that structure is markedly different for differing transitions. It appears that the southern lobe shows greater emission than its northern counterpart, with a broader and more complex structure in the lower ionization states. This is indicative of shock-enhancement of the lower ionization states. Such observations indicate that the lower ionization states of elements are enhanced by shock processes, suggesting that shocks feature more strongly in the southern regions of the nebula.

Catalogued as an IR source, NGC 2818 has been observed by the Infrared Astronomical Satellite (IRAS). Designated as a point source, NGC 2818, also known as IRAS 09140–3625, was observed in all four IRAS data bands; 12 μm, 25 μm, 60 μm, and 100 μm. Analysis of the IRAS colour indices shows that the source occupies a region of the colour-colour diagram marked by evolved PNe. Peak emission occurs in the 100 μm band, unlike typical PNe which radiate most emission around 60 μm. This indicates that the nebula possesses a cool radiative component. Fitting of the data suggests that the measure of emission may be described by the presence of a dust component radiating at ~ 50 K. Adopting the method of analysis used by Van der Veen & Habing (1988), the IRAS colours reveal that NGC 2818 resides in region VIII of the colour-colour diagram. Consensus suggests that this region contains very cool objects of different character. It is possible that NGC 2818 is at the extreme developmental stage of objects such as M2-9 and NGC 2440. Use of the methods employed by Walker & Cohen (1988) and Walker et al. (1989) suggest that NGC 2818 belongs to the group of 'red' PNe, although it remains uncertain whether the nebula originated from an oxygen-rich or carbon-rich star. Elemental abundance measurements show that nebula has a carbon-to-oxygen ratio C/O < 1, indicating that the progenitor was oxygen-rich.

The luminosity of NGC 2818 is low compared with other PNe. It appears that the nebular luminosity lies close to ~110 $L_{\odot}$ which implies that the object is highly evolved, as typical AGB star luminosities lie in the region of 3000 $L_{\odot}$. Spectral analysis shows that significant chemical processing has also occurred, as NGC 2818 shows many abundance ratios at the extreme values determined through theory. Both helium and nitrogen are overabundant suggesting that NGC 2818 belongs to the Type I PNe. Consequently, the mass of the progenitor must have been moderately large (Kwok & Bignell 1984), leading to a rapid evolution of the object.

As with all PNe, determination of an accurate distance is essential in governing their exact physical properties. Early distance determinations for NGC 2818 were fraught with considerable uncertainty and show a wide range in values. The earliest distance determination for NGC 2818 came from Shapley (1930) who proposed an incredibly large distance of 5 Kpc. Later Barkhatova (1950) produced a distance estimate of 1.44 Kpc. More recent measurements, however, show greater success and appear to converge with an uncertainty of ~ 1 Kpc. Although still quite large, the dispersion appears to centre around a value of ~ 2.5 Kpc. (Dufour 1984) obtained a distance of 3.5 Kpc, based upon zero age main-sequence star fitting, suitably adjusted to account for the change in the Hyades distance scale. However, recent estimation by Pedreros (1989), using chemical abundance models for the cluster colour-magnitude diagram reveal a distance of 2.3 ± 0.2 Kpc. This is the most recently adopted distance value and had been used in all literature following its publication. A reasonably comprehensive set of distance estimates from various authors is listed for reference in Table 5.1

DISTANCE MEASUREMENT (KPC)	OBSERVER	YEAR
3.2, 3.5, AND 3.8	Tifft et al.	1972
1.72	Milne & Aller	1975
2.13	Cahn	1976
2.64	Torres-Peimbert & Peimbert	1977
2.26	Maciel & Pottasch	1980
2.02	Daub	1982
3.5	Kohoutek et al.	1986
3.5	Dufour	1984
2.3	Pedreros	1989

Table 5.1: Distance measurements for NGC 2818

With an assumed distance of 2.3 Kpc, analysis of the angular dimensions of the nebula allows an estimation to be made upon its true size. Measurements of 130 arcseconds by 60 arcseconds by Pedreros imply that the nebula is incredibly large, with a true size of 1.44 pc by 0.67 pc. Such a large size indicates that the dynamical age of the nebula is also large. Spectroscopic measurements, although adopting smaller angular dimensions for the nebula, produce values of 5500 yr and 4500 yr for [NII] and [OIII] expansion velocities of 51 km s^{-1} and 53 km s^{-1} respectively. Similarly, imaging programmes produce dynamical ages of 6400 yr for the bilobal nebula structure, and 14000 yr for the nebula lobes.

Use of the statistical distance scale developed by Zhang (1995) produces a larger value than that determined by Pedreros (1989). The statistical distance scale developed by Zhang (1995) uses the correlation between nebular ionized mass, radio continuum surface brightness, and nebular radius. Final distance estimates are then taken as the average of the two distances obtained from each correlation. For NGC 2818, the brightness temperature-radius correlation agrees almost perfectly with the distance measure of Pedreros (1989). However, the ionized mass-radius correlation distance appears to mirror the distance value gathered by Tifft et al. (1972) The average value of 3.05 Kpc is slightly larger than the most widely accepted distance, again introducing a degree of uncertainty into the argument. Consequently, the dynamical age of the nebula appears larger, with values of 17000 yr and 37000 yr using the largest dimensions of the nebular structures. Nevertheless, it is clear that NGC 2818 is in a highly developed stage of its evolution.

5.3 POLARIMETRIC OBSERVATIONS

5.3.1 OBSERVATIONAL DETAILS

Data discussed in this chapter were gathered during an observing run which was carried out in February and March, 2000. All data are original to the Durham Polarimetry group. Measurements were collected upon the 1.9m SAAO telescope at the Cassegrain focus, with a focal ratio of f/18. Broadband V and R waveband imaging of the object enabled a reasonable amount of information to be gathered. Possible follow-up observations taken in B and I wavebands could enable further understanding of the object, and could also reveal important information about the intervening ISM and surrounding open cluster. Both V and R filters were employed in the collection of linear polarization data. The telescope/instrument/detector combination remained the same as that for the observations of M2-9 and NGC 2440 (See §3 for further details). The seeing conditions were again determined from the angular dimensions of field stars, and were found to remain relatively stable during the entirety of the observing run, ranging from 2.5 arcseconds to 3.0 arcseconds FWHM.

Owing to the large extent of the nebula, data was collected at 3 separate telescope positions. Coverage of the nebula is complete, with no occurrence of problematic effects during the data reduction process. 24 CCD frames of the object were gathered using the broadband V filter, and 12 frames using the R filter. No account was made for the large dynamical intensity range of the object, which implied that image saturation could become problematic. However, both the inner nebula and fainter surrounding nebulosity of the lobes were observed without problem. Integration times for the V filter observations measured 240 seconds, whilst for the R filter observations measure 180 seconds, because of the higher filter throughput. In order for correct calibration of the image frames, a series of flatfield frames of the twilight sky were taken. Corresponding exactly to the particular passband characteristics of the image frames, the flatfield frames enabled a global correction to be made across the image. However, no dome flatfields were taken due to time constraints during the course of the observing run.

5.4 RESULTS

5.4.1 IMAGE DETAILS

Throughout this chapter, data is represented in a pictorial format. Figures 5.1 through 5.7 display broadband V continuum data, while figures 5.8 through 5.14 display R-waveband data. All images and polarization maps are oriented with north at the top and east to the left. Images and data are centred about a position between the north and south arcuate filaments corresponding to the origin of the prominent emission-line filament. All graphical presentations include a scale in arcseconds and axis labels specifying offset distances from the plot centre. Unless otherwise stated, all greyscale and contour images represent the total intensity of the nebula, with highest intensity represented by black. All contours are displayed logarithmically, with a spacing of 0.3 magnitudes so as to encapsulate the entire dynamical intensity range of the object. Polarization measurements are plotted with suitable intensity cuts so as to eliminate unwanted noise from the image. The ordered appearance of polarization vectors is explained by the integration of polarization data into data bins. Image overlays are predominantly displayed with bin sizes 5 pixels square moved on 3 pixels. The effect of smaller step size is to average and therefore smooth data as a consequence of data bin overlap. A number of polarization plots, however, are presented with bin sizes of 7 pixels square, moved on by 5 pixels. This meant that data appeared more reliable and did not suffer from the effects of atmospheric seeing. The orientation of polarization vectors represents the preferential direction of the electric field of scattered light, and vector length represents the magnitude of polarization. A number of plots include polarized intensity information through greyscale and contour structure. These images have been found to include a number of irreparable problems, but have been suitably scaled so as to remove the affected areas. Where problems occur in any of the images, they are duly noted and discussed with relevance to the results.

5.4.2 THE EFFECTS OF INTERSTELLAR POLARIZATION

The galactic co-ordinates (l=261°, b=8°.1) and large distance for NGC 2818 implies that the measured levels of polarization should include a contribution from ISP.

A series of aperture polarimetry measurements were taken, using a number of stars in the field of view. Selected stars were chosen to conform with several criteria, based primarily upon radial distance from the nebula and grid edges, angular size and intensity, and the presence of pixel saturation. Interestingly, the aperture polarimetry data suggested that the field stars are unpolarized within the measured errors, assuming that the selected stars are intrinsically unpolarized. This result, however, contradicts the measurements gathered from the inner nebula. Results show an extreme uniformity in the magnitude and direction of

polarization, indicating the presence of a modifying polarization component. Aperture polarimetry carried out on the central bilobal condensation, reveals the presence of ISP. Use of a fixed diameter aperture of 10 pixels (5 arcseconds) for each of the measurements led to the result of 0.62 ± 0.20 % at a position angle of 121.0 ± 7.6 degrees for broadband V data. R-waveband data produced a result of 0.62 ±0.15 % at a position angle of 118.9 ± 10.6 degrees. Data from only the nebular core analysis is shown in tables 5.2 and 5.3. The large uncertainty in the measured contribution of ISP is due to the intrinsically low levels of polarization which are involved. At low signal levels, the levels of background noise become significant and possess comparable magnitude to the measured signal.

Aperture Size (Pixels)	Pixel Coordinates	Polarization (%)	Polarization Error ± (%)	Position Angle (°)	Position Angle Error ± (°)	Waveband
10	247.937, 234.334	0.686	0.268	122.247	11.193	VV
10	253.101, 241.089	0.637	0.135	127.161	6.046	VV
10	259.456, 234.732	0.752	0.023	124.089	0.889	VV
10	265.812, 241.487	0.735	0.124	124.176	4.827	VV
10	258.265, 246.255	0.527	0.072	117.392	3.935	VV
10	249.526, 272.480	0.542	0.214	117.826	11.292	VV
10	242.774, 280.030	0.609	0.186	124.081	8.738	VV
10	254.690, 277.646	0.653	0.073	120.791	3.209	VV
10	258.662, 282.811	0.431	0.269	111.276	17.883	VV

Table 5.2: V-band aperture polarimetry results for the measurement of ISP. These results have been determined from the analysis of the nebular core only.

Aperture Size (Pixels)	Pixel Coordinates	Polarization (%)	Polarization Error ± (%)	Position Angle (°)	Position Angle Error ± (°)	Waveband
10	205.958, 233.321	0.395	0.004	110.109	0.270	R
10	217.278, 238.089	0.524	0.062	121.494	3.395	R
10	215.888, 247.427	0.594	0.187	122.879	8.993	R
10	223.236, 250.407	0.572	0.073	114.387	3.669	R
10	225.421, 239.281	0.560	0.248	126.841	12.707	R
10	232.372, 235.903	0.388	0.247	126.420	18.244	R
10	220.257, 273.056	0.767	0.342	112.370	12.773	R
10	223.435, 282.791	0.515	0.213	113.99	11.862	R
10	214.895, 280.606	0.517	0.110	114.961	6.107	R
10	207.348, 282.990	0.443	0.429	125.598	27.743	R

Table 5.3: R-band aperture polarimetry results for the measurement of ISP. These results have been determined from the analysis of the nebular core only.

5.4.3 INTENSITY IMAGES: V-BAND

A look at the V-waveband image in figure 5.1 immediately shows that continuum radiation plays a dominant role in the central regions of NGC 2818. It is rather amorphous with very little enhancement of the nebular lobes. Analysis of the isophotal contours clearly shows the north-south bilobal appearance, with significant sub-structure in the form of intensity condensations. These condensations are likely to represent clumpy material expanding away from the central star. The image shows that the nebula occupies a large volume of interstellar space, possessing a total extent of ~80 arcseconds in the east-west direction and ~40 arcseconds north-south. This is likely to be a lower limit to the angular dimensions of NGC 2818, as deep sky images show that the east-west projection measures ~130 arcseconds. Like the bipolar condensations observed within the inner nebula of NGC 2440, the bilobal appearance of NGC 2818 at the highest intensity levels, is suggestive of a gas/dust torus. Close examination of the image reveals a difference between the

extended arms. It is observed that the arms marking the western lobe are foreshortened when compared with those in the eastern lobe. This indicates that the nebula is probably inclined to the plane of the sky and that the western lobe is moving away from the observer. A small degree of limb-brightening is observed along the filamentary arms of the nebula in the V-band image, indicating a possible tracer of the lobe walls.

5.4.4 INTENSITY IMAGES: R-BAND

The R-waveband image of figure 5.8 bears striking resemblance to that of the broadband V image. However, it is clear that R-band image reveals much more detailed structure and enhancement of the nebular lobes. A look at the intensity contours confirms the complex sub-structure of NGC 2818, with the appearance of many knot-like features within the north-south bilobal intensity distribution. Greater definition of the extended arms is visible, as enhanced levels of limb-brightening are observed. Also apparent is a series of condensations inside the lobe walls, particularly in the north-eastern arm. This could indicate the possible presence of density enhancements within the lobe walls, caused by instability in the flow of gaseous material.

Although identifiable in the V-band data, the filamentary jet-like emission structure is poorly defined. R-waveband data, however, clearly reveals the structure of this filament and shows that it is composed of several knots along its length. The image also shows a similar, but opposing source of emission about the central nucleus. This filament of emission again consists of a number of knots and presumably forms the complementary component of a bipolar outflow.

5.5 POLARIZATION RESULTS

5.5.1 V-BAND, ISP UNCORRECTED

Polarimetric study of PNe often reveals that most objects show some resemblance to simple reflection nebulae, with the manifestation of a centro-symmetric polarization pattern. It is clear, however, that NGC 2818 does not have this characteristic since its polarization pattern possesses very atypical structure. The polarization maps of figures 5.2 and 5.3, which present no correction for ISP, show several interesting features. These include extreme uniformity in the levels of polarization, almost perfect alignment in the vector pattern across the inner regions of the nebula, and an increasing randomisation of polarization vectors in the outer regions of the nebula. The general lack of structure within the vector pattern means that the location of the central star remains unconfirmed. Analysis of the total intensity contours, however, allows the location to be inferred, thus providing a reference point by which all other nebular features may be compared.

Although it is confirmed that the ISM presents a contribution to the polarization of the object, its effects do not fully mask the signature of a reflection nebula. However, the effects of ISP feature more strongly if its magnitude is comparable to the intrinsic polarization of the object. It can be seen from figure 5.2 that the general level of polarization across the entire face of NGC 2818 is extremely low, with a peak value of ~ 1.0%. Consequently, the levels of polarization from the ISM have significant influence upon the measured polarization of NGC 2818. Polarization levels appear to be of a similar magnitude across the face of the nebula, with vectors being almost perfectly aligned However, a number of regions exist which show clear distortion from this linear pattern, particularly those just west of the nebular centre, and also at ~ 14 arcseconds east and 15 arcseconds south from the nebular centre.

The very low levels of polarization observed in NGC 2818 can be explained simply by the high degree of nebular excitation or by extremely uniform interstellar polarization. Inspection of figure 5.3, marking the north-south bilobal intensity distribution shows that polarization levels vary from ~ 0.2% to 1.0%, following an average position angle of ~ 118 degrees. Uncertainties in the level of polarization are of similar order to the measured levels, with uncertainty in the position angle of 2 - 16 degrees. At the outermost extremity of the nebular wings the signal-to-noise is dramatically reduced. Consequently, the levels of polarization become insignificant and are lost to the noise levels of the sky background polarization. For this reason they are omitted from the polarization images by means of suitably applied intensity cuts.

5.5.2 V-BAND, ISP CORRECTED

With the removal of ISP it is seen that the levels of polarization within the inner nebula are extremely low. Examination of figure 5.5 reveals the difficulty in identifying structure in the polarization pattern. As mentioned previously, the patterns of polarization observed in the inner nebula show reasonable order. Vectors in the outer nebula, however, show increasing tendency towards randomisation. Although incoherent polarization patterns exist across the nebular wings in the V-band data, results also show a degree of order in the walls of the nebular lobes. To account for this observation, concentrations of dust must reside within the material of the walls. Although the trace of polarization along the nebular walls is difficult to decipher in the V-band, it is clearly seen in the R-band image.

Although the general level of polarization is extremely low, attention is drawn to the intrinsic complexity of the vector pattern. Unlike the typical centro-symmetric or elliptical polarization pattern seen in younger PNe, the vector pattern observed in NGC 2818 shows no sign of large-scale centro-symmetric scattering. Examination of figure 5.6 shows the complex nature of the polarization pattern more clearly and reveals that scattering processes occur from very localized regions within the nebular volume. Several regions also exist which show little or no polarization. The lack of polarization in these areas may be explained in several ways and will be discussed later in the chapter.

Levels of polarization found within figure 5.6 range from < 0.1% to 0.8%. Higher values of polarization within the image exist only in spurious and erroneous vectors and should therefore be ignored. A look at figure 5.5 reveals a small region of the nebula which shows relatively strong levels of polarization. This area of enhanced polarization begins at a radial distance of ~ 17 arcseconds and extends outward along an average position angle of 132 degrees to a radial distance of ~ 22 arcseconds. It is clearly observed that the levels of polarization encountered within this region are higher than at any other point within the nebula, with values peaking at ~ 1.6%. Interestingly, the enhanced polarization structure coincides with the extremity of the south-eastern outflow, which opposes the north-western emission-line filament. It is also seen that the intensity gradient appears largest at this point, suggesting an increase in material density and hence dust concentration. Surprisingly, no counterpart polarization pattern is observed, presumably due to a decrease in the intensity gradient at that point. Similarly, the paucity of polarization enhancement in the north-west quadrant of the nebula may be explained by differences in scattering geometry.

Figure 5.7 shows Broadband V polarized intensity within the central regions of NGC 2818 after the removal of ISP. Although the image is affected by erroneous regions of highly polarized emission, the area covering the inner nebula is relatively unaffected. Although the condensations of the bilobal intensity distribution are still polarized after ISP removal, the structure of polarized emission appears more amorphous. The jet-like

filament is also polarized, but the levels of polarization are very low. V-band data therefore provide only tentative evidence for an outflow within the filament.

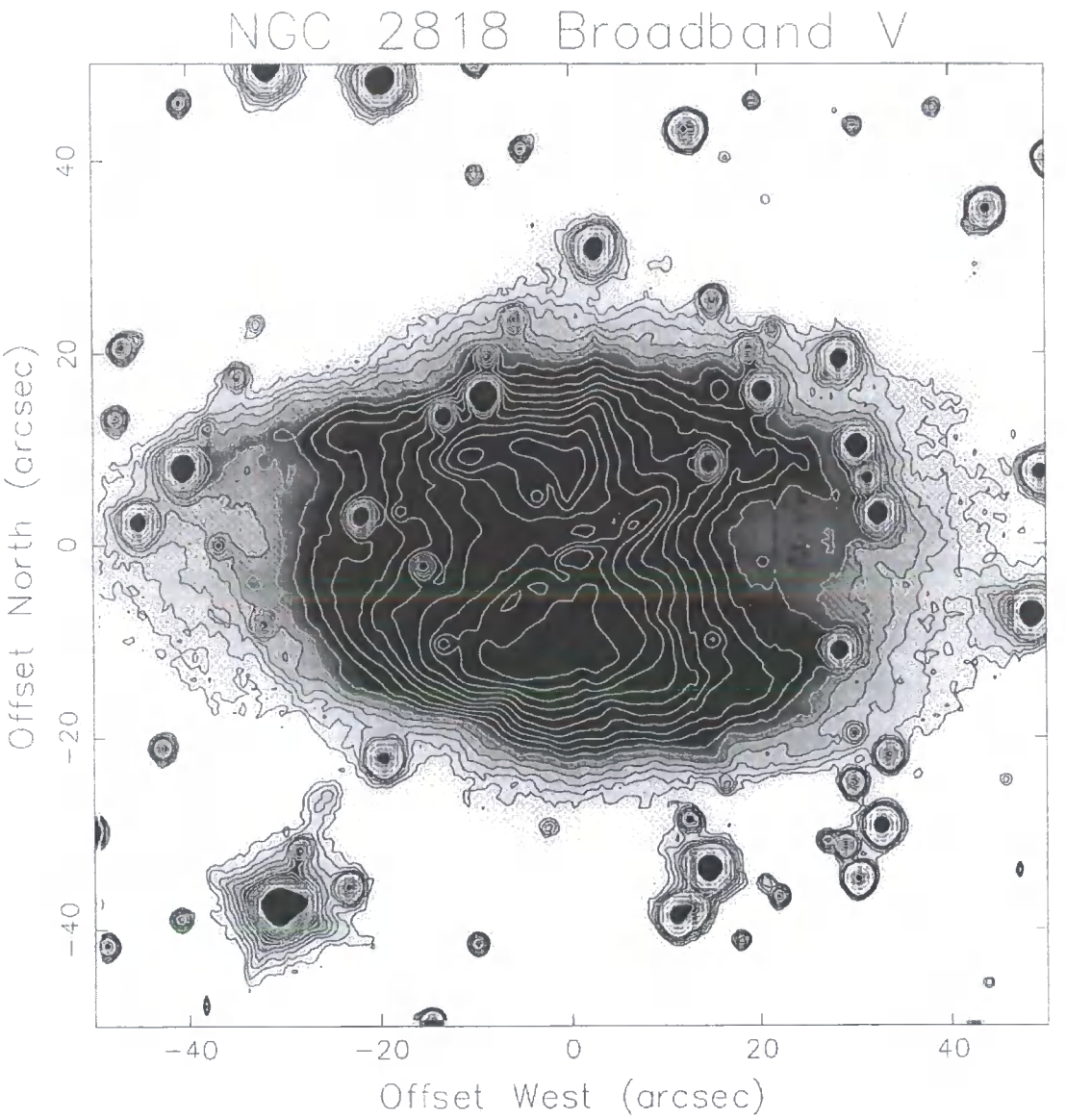

Figure 5.1: Broadband V total intensity image with superimposed isophotal contours

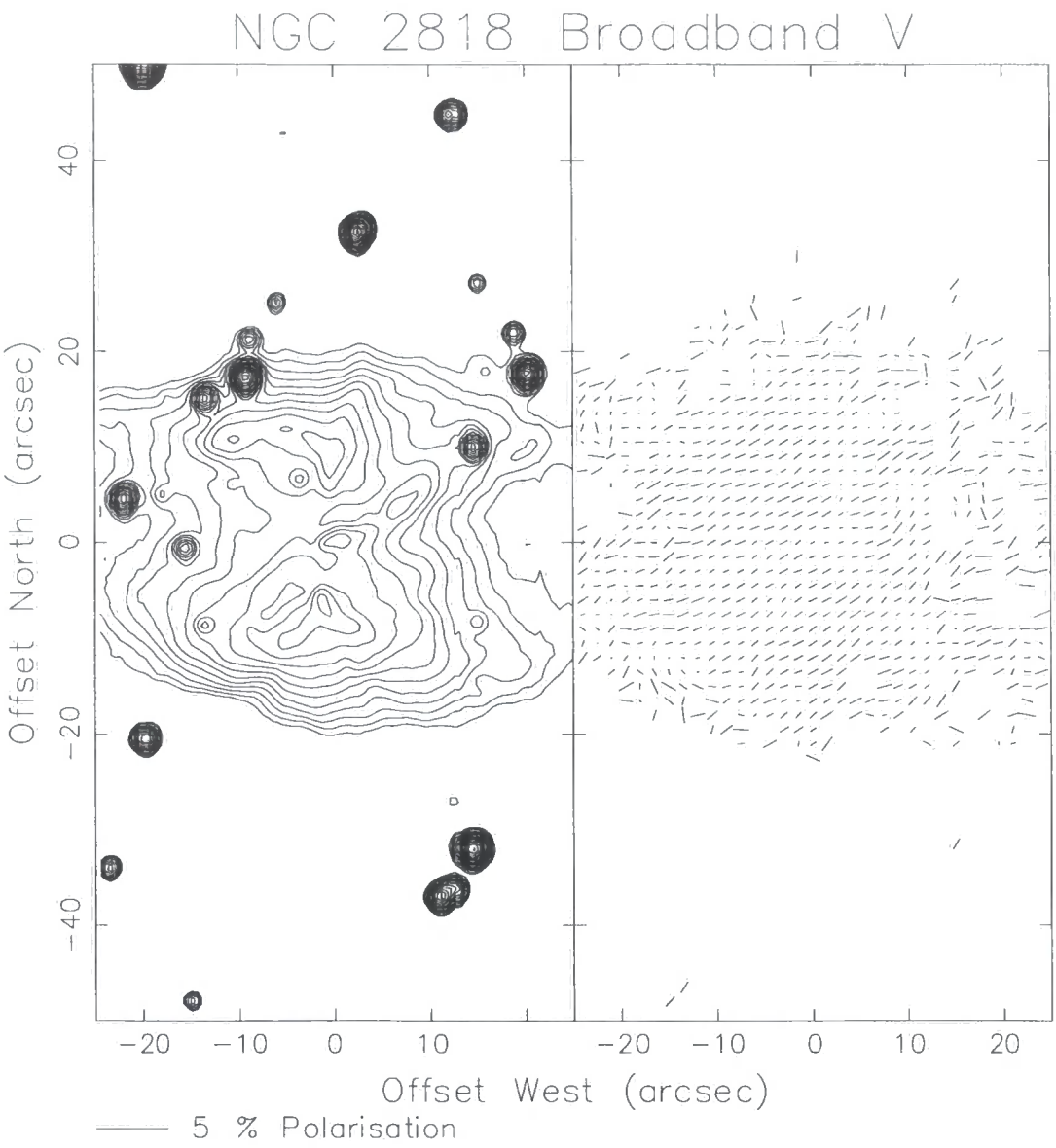

Figure 5.2: Broadband V polarization image (low resolution) showing both intensity and polarization data which are uncorrected for ISP

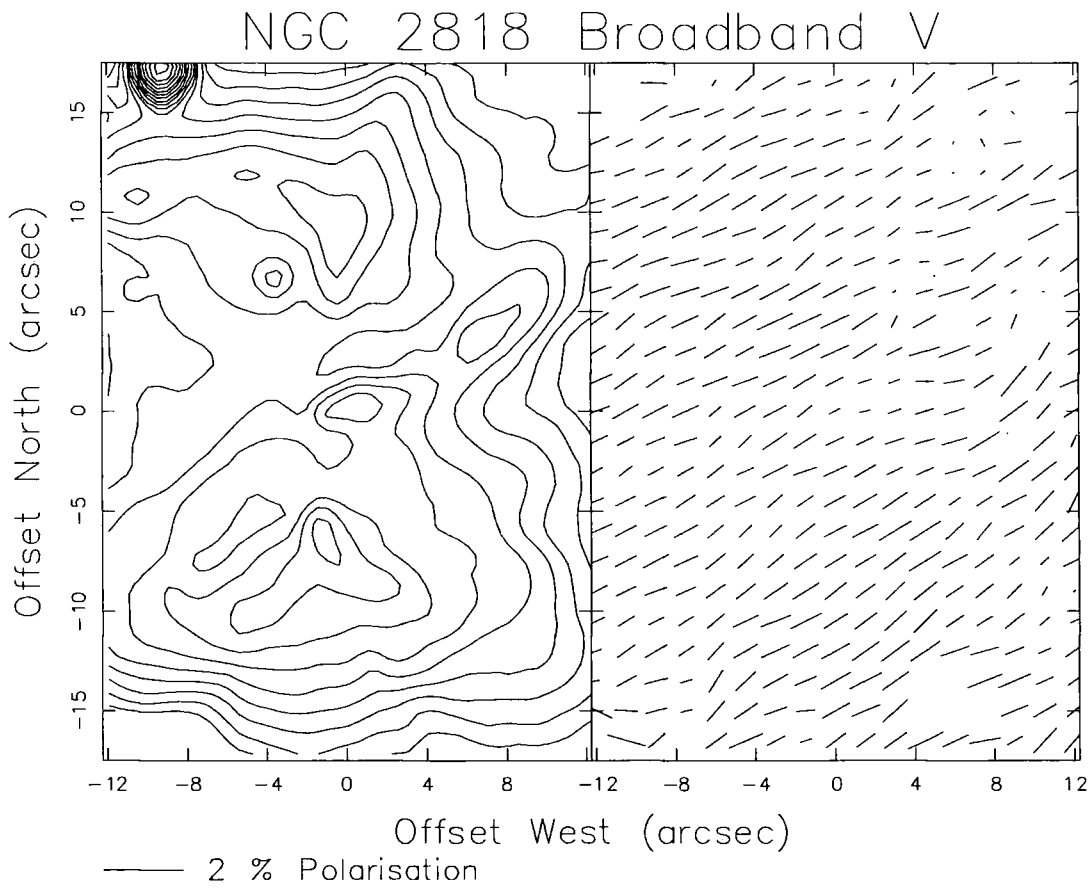

Figure 5.3: Broadband V polarization image (high-resolution) showing both contour data and polarization data which are uncorrected for ISP

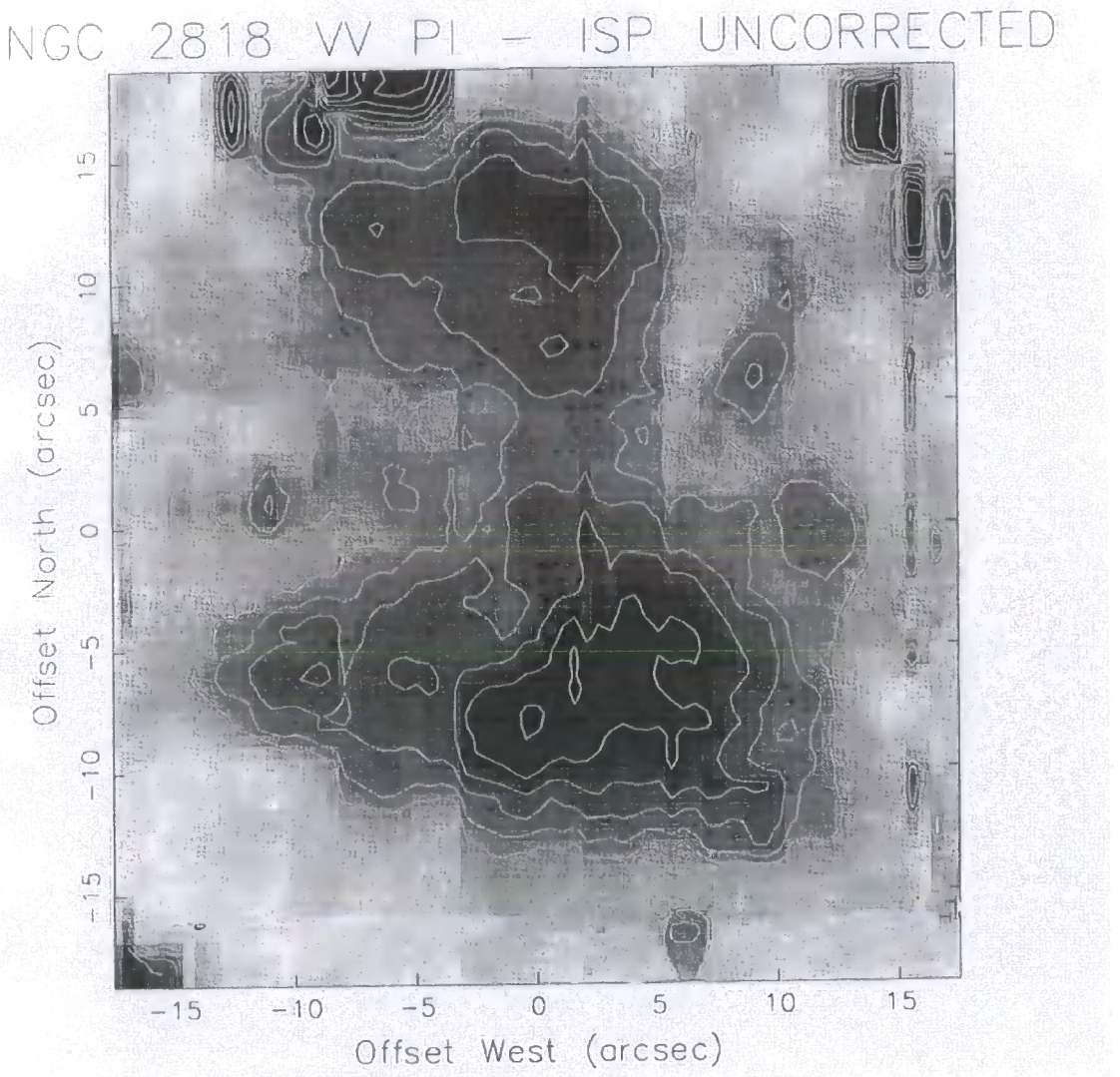

Figure 5.4: Broadband V polarization image showing the polarized intensity of the central regions of NGC 2818. Data are uncorrected for ISP

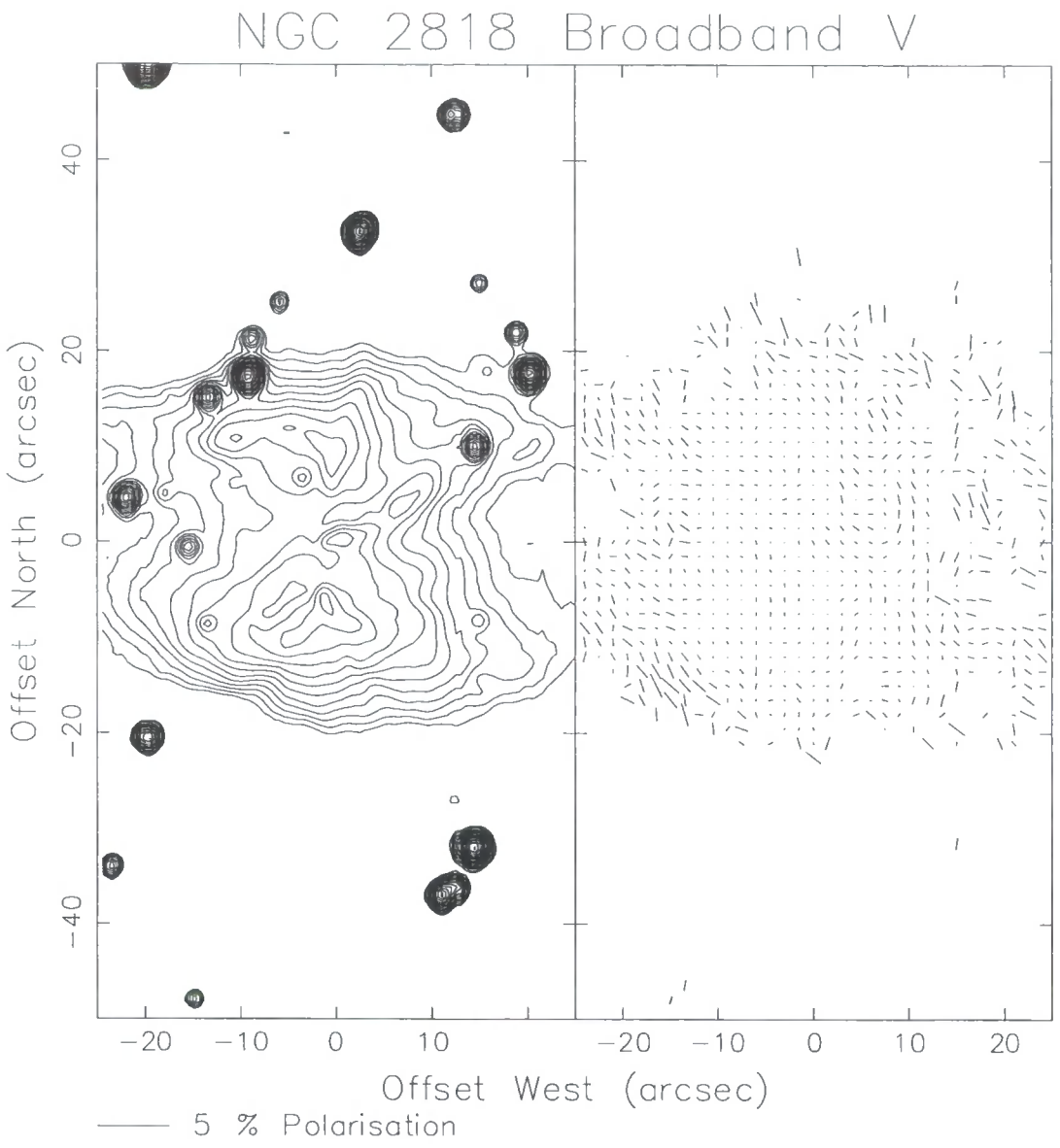

Figure 5.5: Broadband V polarization image (low resolution) showing both contour data and polarization data which are corrected for ISP

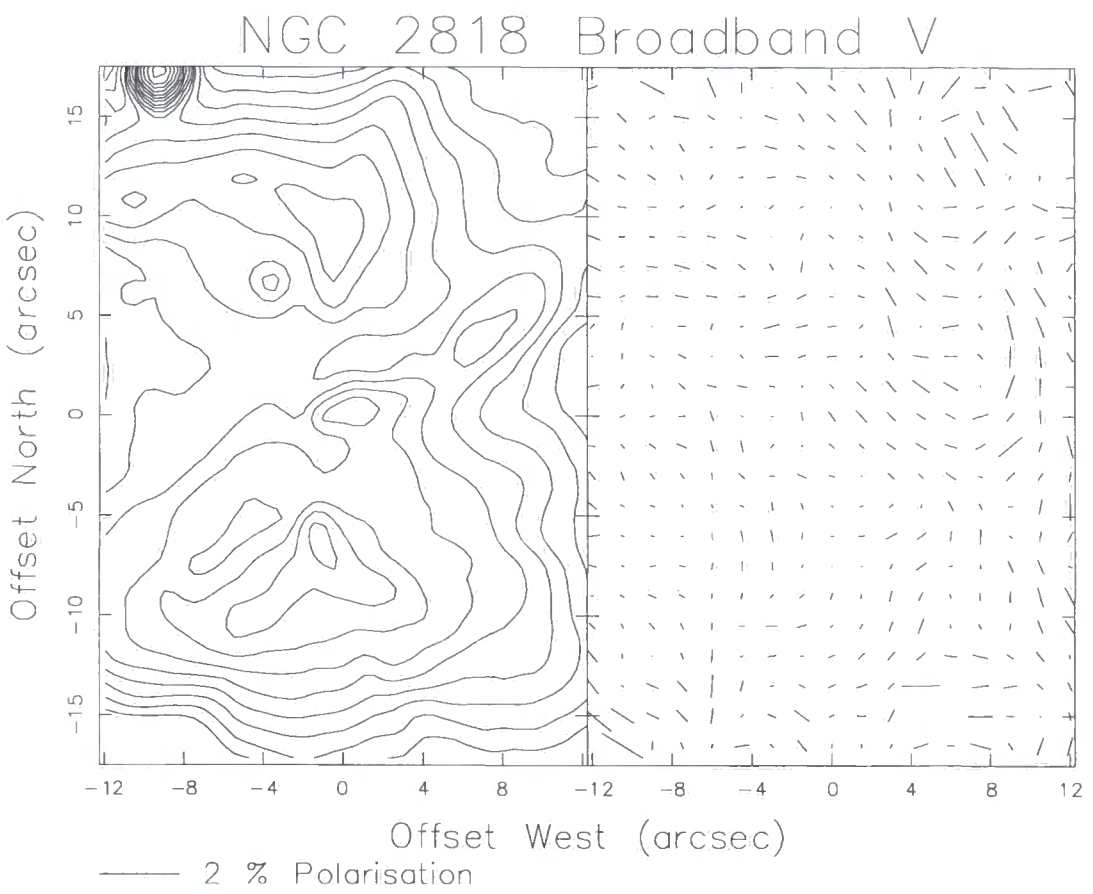

Figure 5.6: Broadband V polarization image (high-resolution) showing both contour data and polarization data which are corrected for ISP

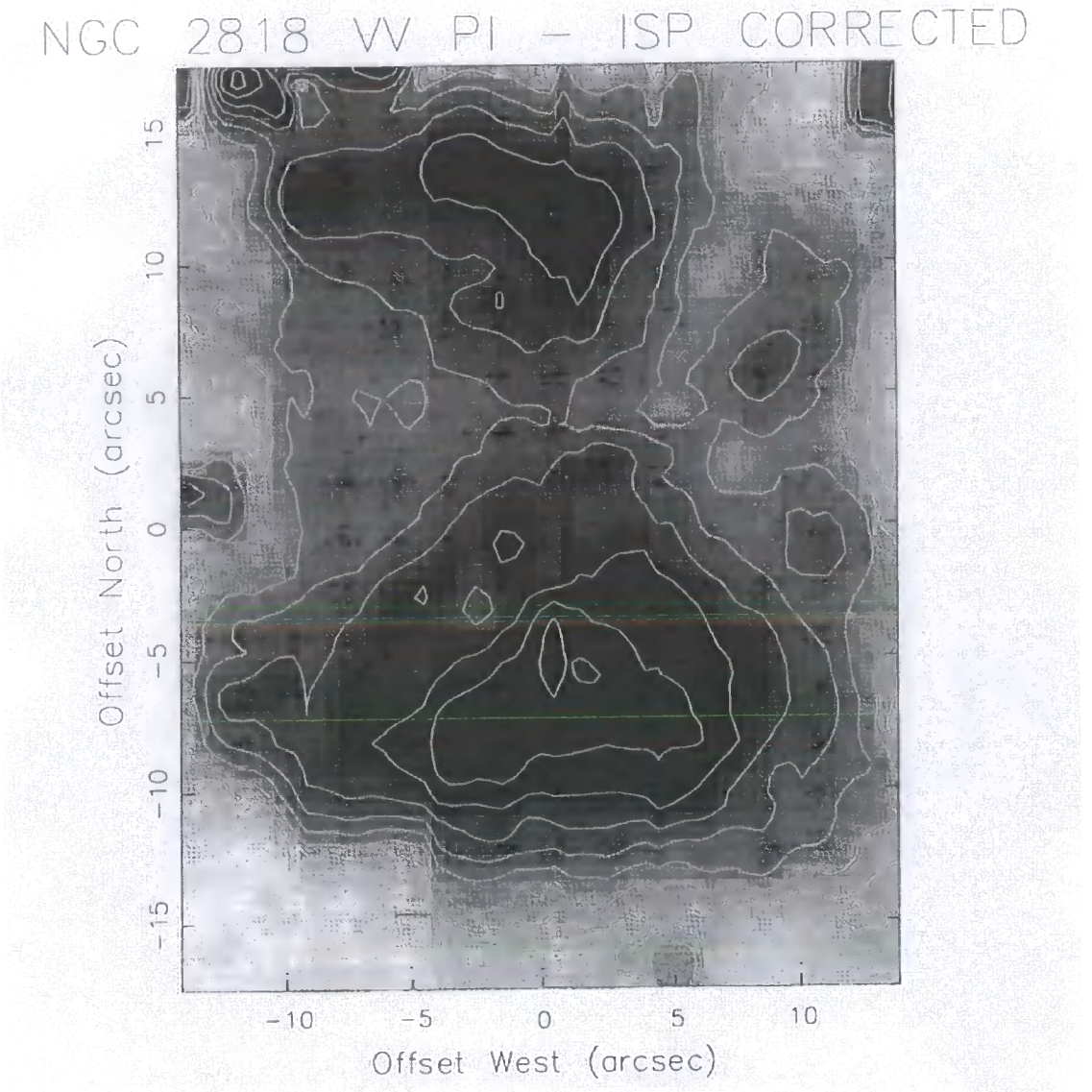

Figure 5.7: Broadband V polarization image showing the polarized intensity of the central regions of NGC 2818. Data are corrected for ISP

5.5.3 R-BAND, ISP UNCORRECTED

Figures 5.9 and 5.10 show R-band intensity and linear polarization data which are uncorrected for the contribution of ISP. In addition to the effects of ISP, R-band data show considerably more detail than the V-band data. Several prominent polarization features are observable within the images of the nebula. These include a number of regions possessing little polarization, the subtle signature of an outflow in the pattern of polarization which is largely coincident with the jet-like emission feature, and polarization which appears to trace the walls of the nebular lobes.

Examination of figure 5.9, which marks the central bilobal intensity distribution, shows that polarization levels are much the same as those encountered in the V-band data, with values ranging from ~ 0.1% to 1.0 % at an average position angle of ~ 123 degrees. Obviously the wavelength dependence of polarization for interstellar grains does little to influence the magnitude of polarization. However, a definite increase occurs in the angle of the plane of polarization. Uncertainties in the polarization data are similar to the measured values of polarization level and 3 - 20 degrees for the position angle. Like V-band data, the R-band data shows no large-scale signs of a centro-symmetric polarization pattern. Figure 5.9 shows that the nebular wings are free of significant polarization. Consequently, intensity cuts were applied to the images in order to remove the majority of randomised polarization vectors. However, it can be seen that relatively strong levels of polarized emission trace the walls of the nebular lobes, particularly the eastern lobe. This is tentatively ascribed to the presence of dust which has been swept up with gas into a dense shell at the inner boundary of the lobes during an earlier epoch of mass loss. This would confirm that wind-driven processes have excavated the nebular lobes and that the interior of the lobes is filled largely with hot, diffuse gas.

A look at the high-resolution image of figure 5.10 shows the presence of several regions across the extent of the inner nebula possessing lower than average levels of polarization. The most natural explanation for this observation would be a variation in the properties of the ISM along the line of sight across the entire extent of the nebula. However, the large distance of NGC 2818 would imply that variation of this kind over such a small angular area is very unlikely. A more realistic answer would be a change in the underlying levels of radiation scattering inherent to the nebula.

The most interesting feature of both figures 5.9 and 5.10 is the change in vector pattern and increase in the level of polarization at ~ 5 arcseconds north-west of the nebular centre, at a position angle of 315 degrees. The details of this polarization structure are most clearly shown by figure 5.10, where it is seen that the polarization vectors follow a conical formation. The levels of polarization inherent to this structure vary between 0.3 % in the outer regions and 1.0 % in the inner regions. Along the boundary of this structure the polarization vectors begin to turn over, particularly in the lower half of the polarization cone. Although the vector pattern largely follows that which is caused by ISP, the conical formation of vectors may tentatively

be ascribed to the presence of an outflow. Further discussion is conducted later, after the sub-section upon ISP corrected data.

5.5.4 R-BAND, ISP CORRECTED

Inspection of figure 5.12 immediately shows the difference between the northern and southern halves of the nebula. R-band data clearly shows that the general level of polarization in the northern regions of NGC 2818 is higher than that in the southern regions. Furthermore, it is observed that higher levels of polarized emission exists within the walls of the nebular wings, particularly in the north-eastern quadrant of the nebula. In the central regions it can be seen that the areas of lowest polarization correspond with the condensations of the bilobal intensity distribution. Although these structures show a degree of polarization, as seen in the images of polarized intensity, the high degree of intrinsic emission from gas means that polarization remains low.

Close inspection of figure 5.12 in the north-western quadrant of NC2818 reveals a very interesting feature in the pattern of polarization. Although the polarization is complicated by the near randomised nature of the vectors, the general structure of polarization in this area is marked by a divergence of vectors about the position angle 307 degrees. Here the polarization pattern turns over on both sides of this position angle, suggesting the presence of a pair of extended illuminating sources. A look at the higher resolution image of figure 5.13 reveals the presence of a pair of null points at ~ 7 arcseconds from the nebular centre at position angles of 127 and 307 degrees. These null vectors coincide with the condensations of the emission-line filament to the north-west and south-east.

Figure 5.14 shows R-band polarized intensity within the central regions of NGC 2818 after correction for the effects of ISP. The image is again affected by spurious regions of high polarized emission, but shows that subtle changes occur after the removal of ISP. In addition to the north-west facing filament, a further filament is observed in a more northerly direction. This filament is also polarized, which suggests that dust must be entrained within its volume The presence of this additional filament strengthens the idea that rotating collimated outflows may have occurred during the evolution of NGC 2818. The question of whether an outflow is still active within the volume of NGC 2818 still remains largely uncertain. However, the fact that different polarization structures are observed within V-band and R-band data suggests that different populations of dust have been ejected during the evolution of the nebula.

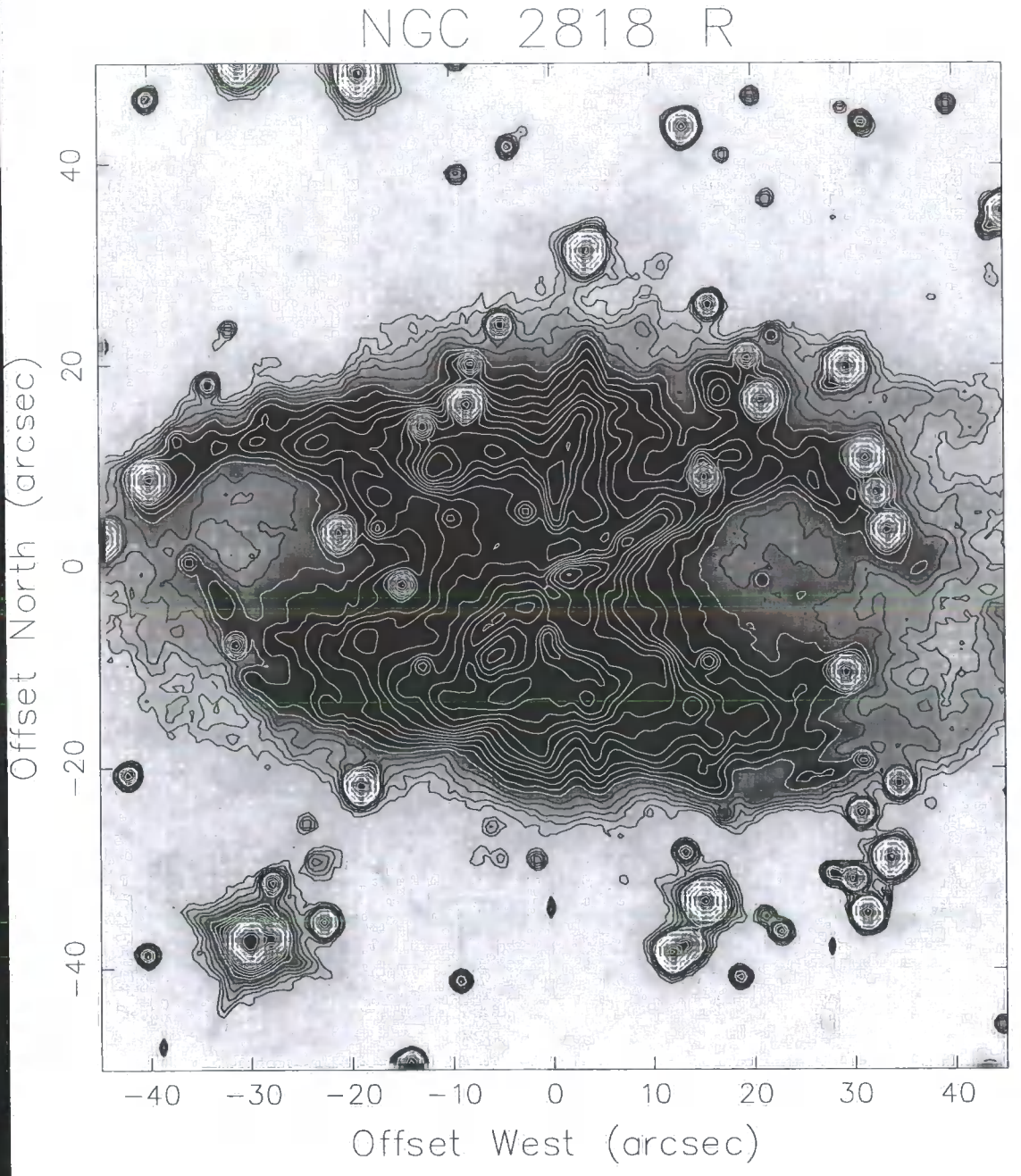

Figure 5.8: R band total intensity image with superimposed isophotal contours

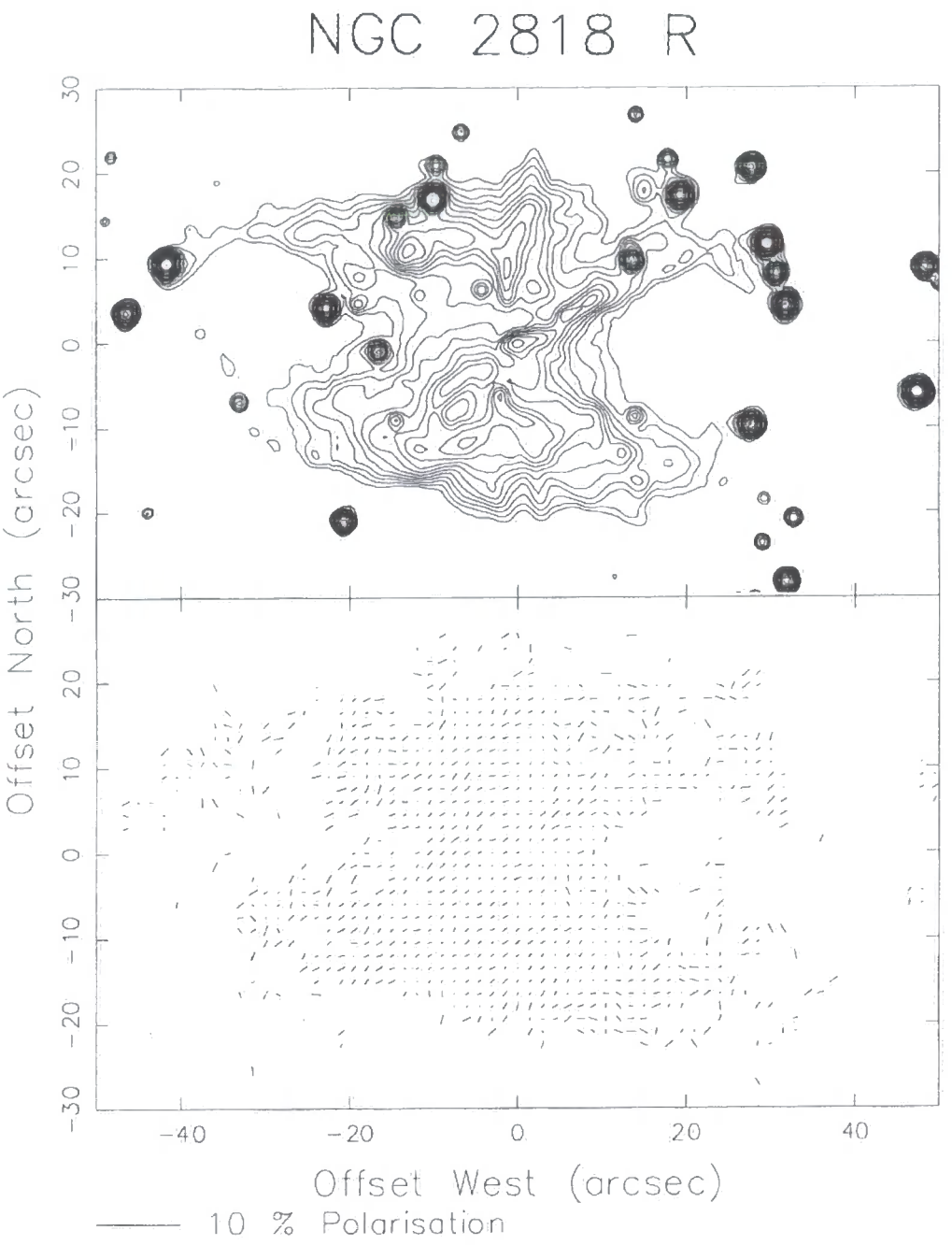

Figure 5.9: R band polarization image (low-resolution) showing both contour data and polarization data which are uncorrected for ISP

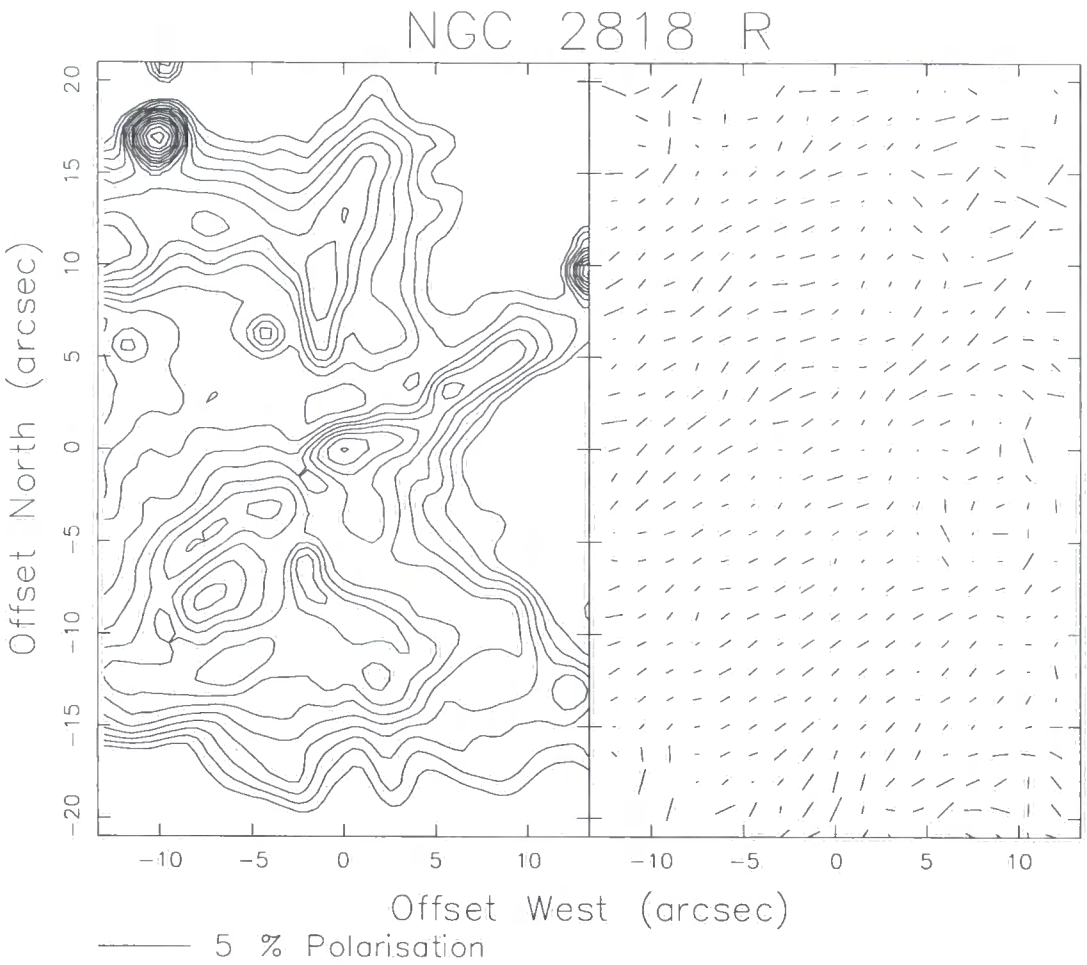

Figure 5.10: R band polarization image (high-resolution) showing both contour data and polarization data which are uncorrected for ISP

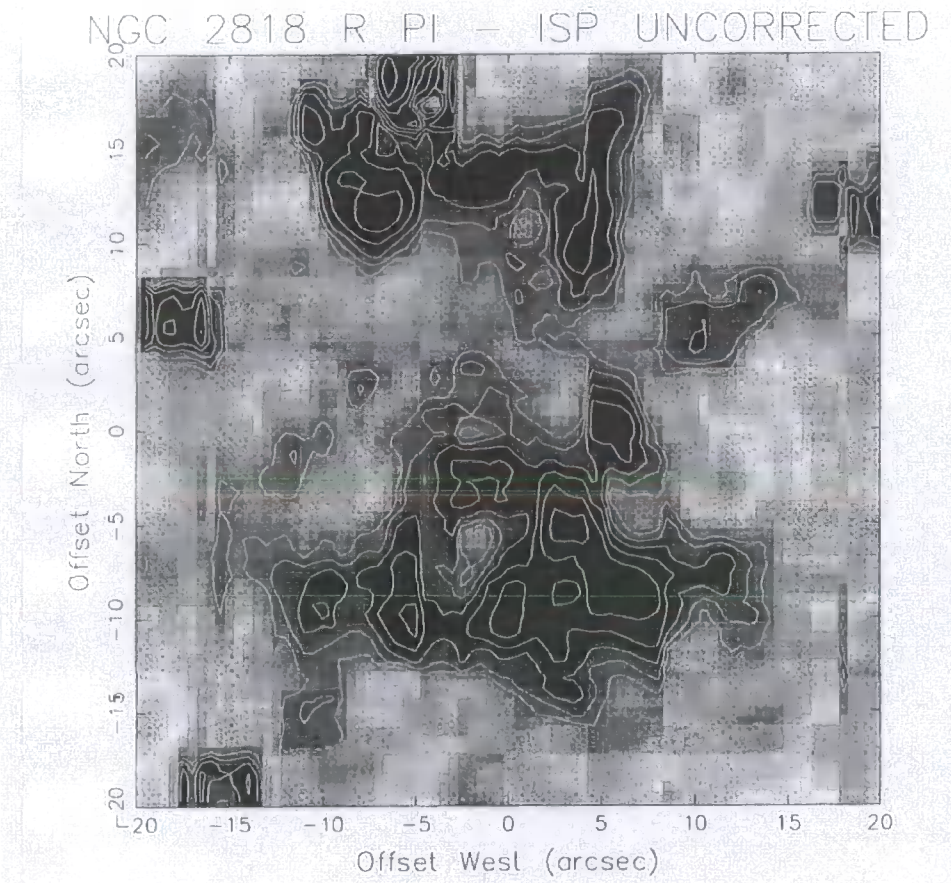

Figure 5.11: R band polarization image showing the polarized intensity of the central regions of NGC 2818. Data are uncorrected for ISP

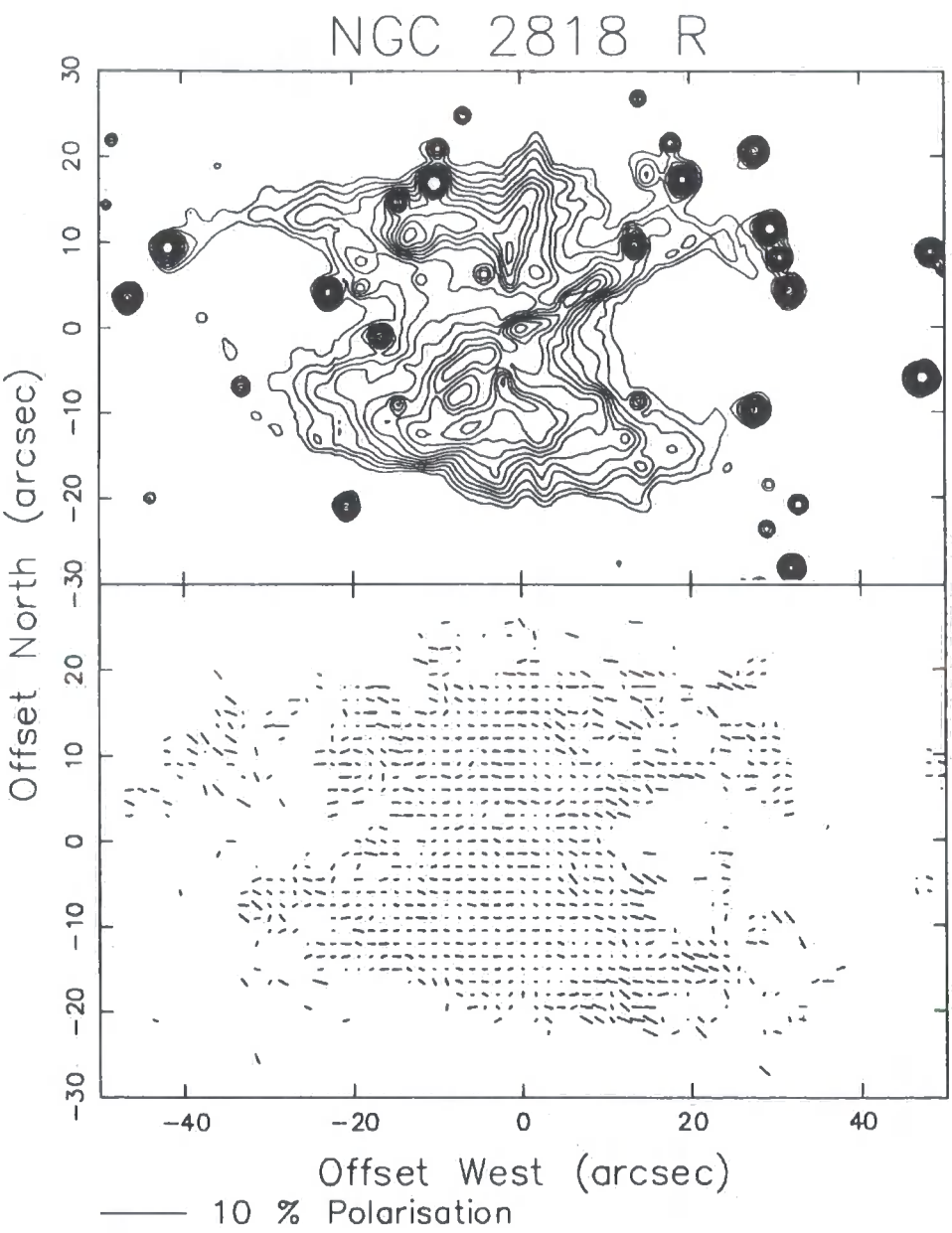

Figure 5.12: R band polarization image (low-resolution) showing both contour data and polarization data which are corrected for ISP

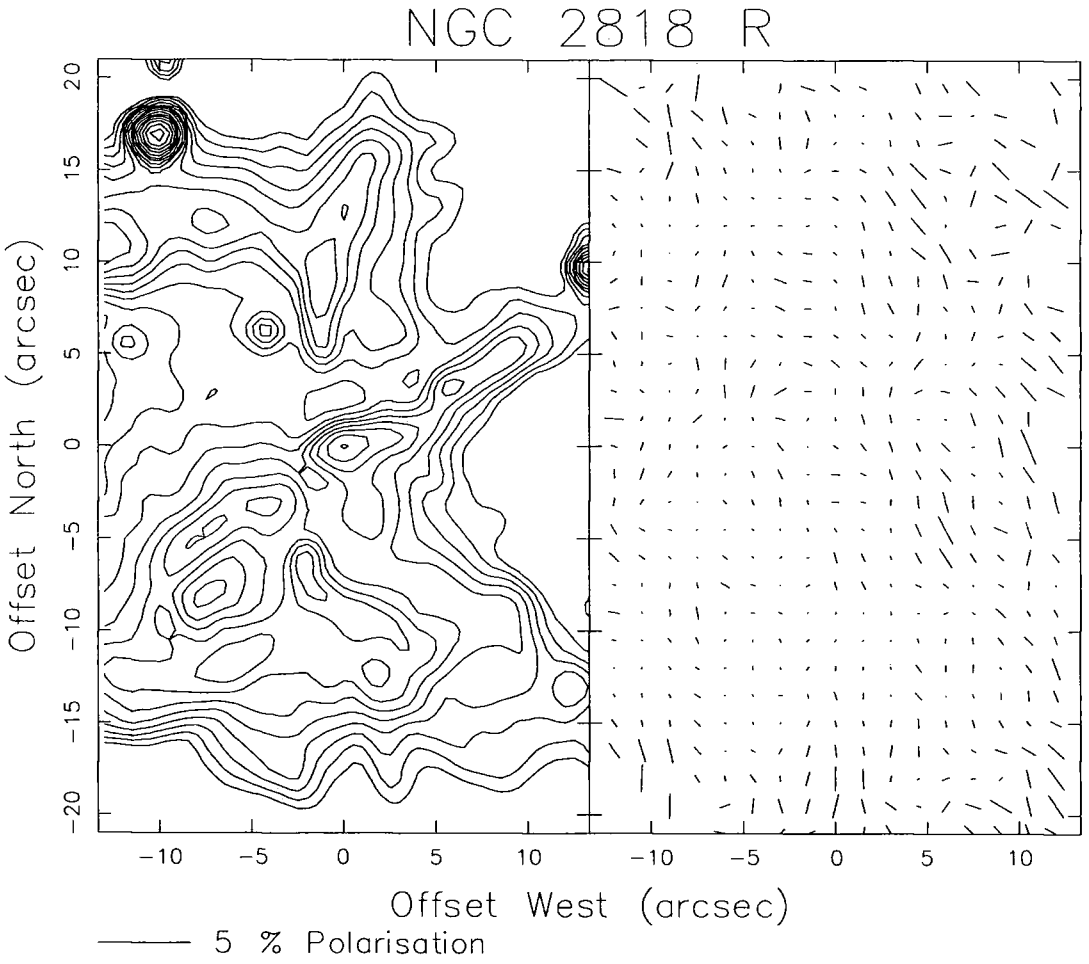

Figure 5.13: R band polarization image (high-resolution) showing both contour data and polarization data which are corrected for ISP

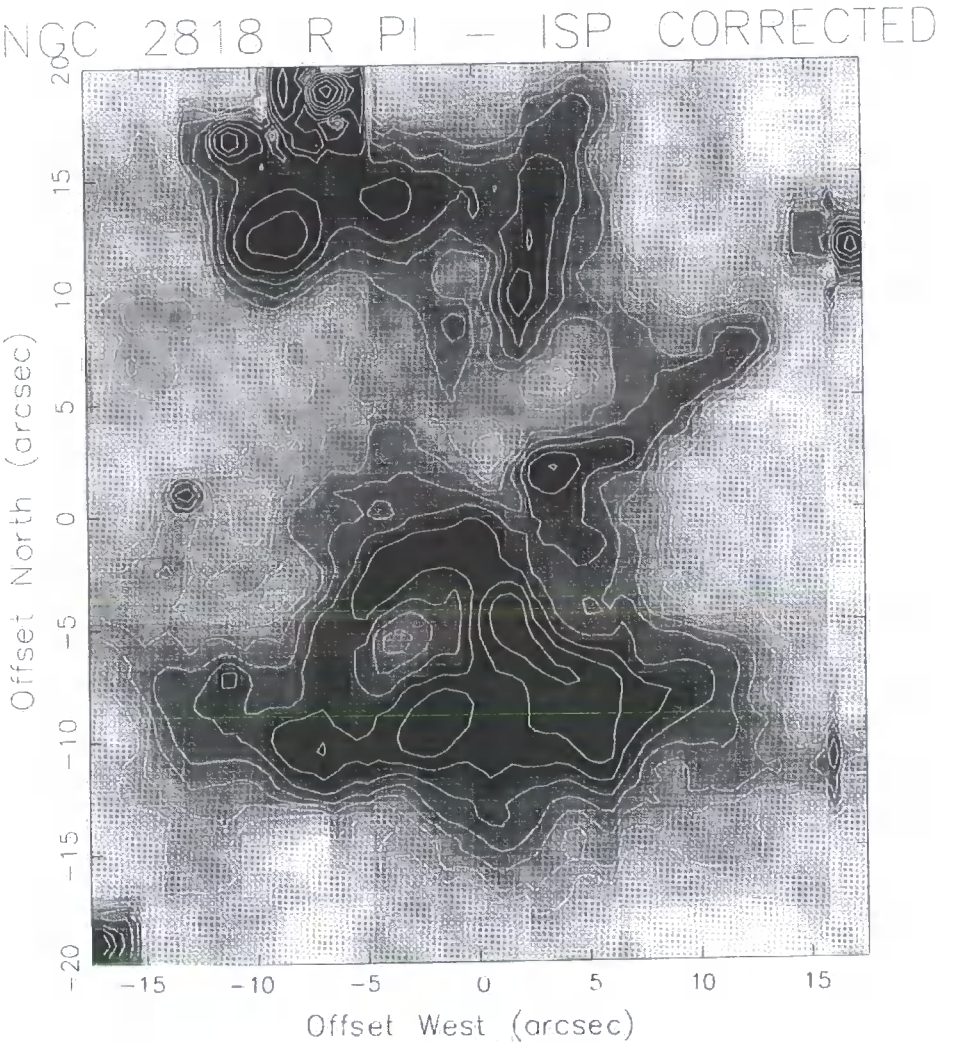

Figure 5.14: R band polarization image showing the polarized intensity of the central regions of NGC 2818. Data are corrected for ISP

5.6 DISCUSSION

5.6.1 INTENSITY DISTRIBUTION AND MORPHOLOGICAL STRUCTURE

Images clearly show that the overall morphology of the nebula is described by an asymmetric, bipolar distribution. The sub-structure of the nebula, however, is very complicated and is characterized by a large number of condensations and filaments. Although it seems plausible to ascribe the north-west to south-east jet-like emission with the effects of a recent bipolar outflow, the morphological appearance of the central bilobal condensation is more difficult to explain without introducing some degree of conjecture. It is clear, however, that the northern condensation of the inner nebula possesses somewhat different structure to that of its southern counterpart.

Evidence suggests that shock-excitation exists in the nebular gas and effects the levels of H_2 emission observed in NGC 2818 (Schild 1995). This is particularly true in the southern condensation, where the levels and extent of radiative emission appear greater. An obvious energy source for shock-excitation would be the presence of a high velocity collimated stellar wind. Together with morphological structure of the nebular wings and the suggestion of a recent jet-like outflow, this would indicate that episodic mass ejection and outflow has occurred during the history of the nebula. Intensity and isophotal data also appears to suggest that rotation of the axis of collimation has occurred. Although the effect is not as prominent as observed in NGC 2440, evidence provides a simple, yet adequate explanation for the morphology of the inner nebula of NGC 2818.

Inspection of polarized intensity data after removal of ISP, shows that scattered emission exists in the central regions of the nebula. Although the levels of polarized intensity are low after ISP correction, the distribution follows a very interesting pattern. Essentially, the regions of highest polarized intensity trace the region of highest total intensity within the central bilobal structure. It is also seen that high levels of polarized intensity exist in the major condensations and filaments of the region, including the jet-like emission feature. However, because the levels of polarization are extremely low and appear almost random in nature, this would imply that considerable emission occurs from nebular gas. Considering that stellar luminosity has decreased during the evolution of the nebula, this indicates that either a large proportion of dust has been destroyed through shock processes, or the spatial density of dust is such that unfavourable scattering geometry now exists.

The nebula is seen through a combination of scattered and intrinsic radiation, although the predominant component appears to be intrinsic emission. Consequently, interpretation of polarization results is complicated, as both scattering geometry and the relative admixture of polarized and unpolarized emission

radiation become important. Furthermore, the dilution effect of intrinsic emission reduces the levels of polarization such that the contribution of polarization from the ISM becomes significant. NGC 2818 appears to represent a highly evolved stage of PN development. Consequently, the nebula is virtually unpolarized and is seen almost entirely by unscattered emission from hot gas. Although this is true, the pattern of polarization contains a small degree of structure, particularly in the region of the inner nebula which shows the greatest levels of polarized intensity. This may be due to a true randomising effect from intrinsic emission, or from an inherent complexity in scattering from a large number of nebular condensations and filaments with different geometry. Because of this, the author is unable to provide adequate explanation of the observed polarization pattern.

It is observed that polarization levels are slightly higher in the northern half of the nebula, suggesting a possible inclination of the northern half of NGC 2818 towards the observer. However, it is possible that the increased levels of polarization are due to an increased concentration of dust. The proposal of increased dust concentration conforms with the observation of a lack of shock-excited H_2 emission in the northern regions of the nebula. Consequently, dust within this region may have survived, giving rise to stronger effects upon radiation. This argument would also explain the lower levels of polarization with the southern half of the nebula, since increased amounts of radiative emission would act to increase the degree of dilution upon scattered radiation. To account for the increase in emission from the southern half of NGC 2818, it is observed that large concentrations of shock-excited H_2 exist. Consequently, atomic gas will also become shock-excited leading to an enhancement in the levels of emission and a decrease in the levels of polarized radiation. Furthermore, considerable amounts of dust are likely to have been destroyed because of the stronger effects of shocks in the southern regions of the nebula.

5.6.2 EVIDENCE FOR A CIRCUMSTELLAR DISC

Comparing NGC 2818 with the morphologically similar PN IC 4406 which Scarrott & Scarrott (1995) studied, it appears that NGC 2818 possesses somewhat different polarization properties. Although the polarization levels of both nebulae are very low when compared with those observed in younger, more dusty PNe, NGC 2818 does not show signs of the simple reflection nebula which is observed at large offset distance from the central bilobal structure of IC 4406. For IC 4406, the centro-symmetric polarization pattern extends across the entire nebular structure, but shows much lower signature within the nebular wings. Polarization levels across the east-west elongation of NGC 2818 appear to be of similar magnitude to those found in IC 4406, but the lack of centro-symmetric scattering along the minor axis of the nebula is surprising. Scarrott & Scarrott (1995) suggest that centro-symmetric polarization exists in IC 4406 as a result of the earlier circumstellar disc or RGE. The lack of centro-symmetric scattering in NGC 2818 would

then imply that any previous circumstellar disc or RGE has been destroyed or has become so tenuous that its effects can no longer be observed.

Because of the age of the nebula, the remnants of a circumstellar disc will be well removed from the central star. Consequently, the central star will provide illumination to all regions of the nebula. As a result, most regions of the nebula will experience high radiation flux thereby reducing the signature of scattered emission. Similarly, regions of zero polarized emission (i.e. the null points) may be explained by conflicting polarization mechanisms. Study of interstellar dust grains under the influence of magnetic field phenomena by Dolginov (1990) reveal that large-scale alignment of simple paramagnetic dust grains takes approximately 10^6 – 10^7 years. Consequently, the presence of dichroic extinction within NGC 2818 seems unlikely for the simple reason that insufficient time has elapsed for the grains to align. The presence of dust alignment may then come from the streaming of gas and dust under the action of a collimating beam.

5.6.3 THE JET-LIKE OUTFLOW

A look at the isophotal data of the jet-like emission-line feature shows that the condensations of the outflow are not perfectly aligned with respect to the nebular core. To explain the unusual positioning of the outflow condensations it is suggested that the central source of the nebula possesses a close binary. Although the central star appears to be a single object, it is possible that the source is a spectroscopic binary (cf. central star of NGC 2346). The proposal of a binary nucleus would also explain the asymmetric structure of the bilobal intensity distribution and the condensations contained within. These condensations imply that bipolar rotating episodic jets may have occurred during earlier development of the nebula, although present polarization data provides no evidence to account for this. However, it can be seen that isophotal data provides some degree of evidence to support such a proposal.

5.7 SUMMARY

NGC 2818 is a highly evolved bipolar PNe which displays very little evidence for present mass ejection. Any outflow present within the nebular volume will carry very little material and its effects will be poorly marked.

The extreme nature of gas excitation dominates emission from the entire nebula and is exemplified by the low levels and randomisation of polarization. Together with the extreme complexity of the polarization pattern, the low level of polarized emission means that description of morphological and polarization structure becomes extremely difficult. Observations show that scattering processes play very little role in radiative emission from the nebula. However, polarization results suggest possible scattering from localised regions of the nebular volume, corresponding to the condensations and filaments of the nebular gas. It is clear that the levels of polarization are also determined by the molecular morphology of NGC 2818. Consequently, the lowest levels of polarized emission are seen in areas of highest molecular enhancement and strongest shock effects. Polarization data present no account of nebular inclination and thus conform with kinematical study of the nebula.

It is proposed that outflow processes have occurred during the development of the NGC 2818. However, polarization results provide little evidence for this, because the polarimetric signature of an outflow remains somewhat uncertain. Difficulties lie in the interpretation as to whether the vector pattern is suggestive of an outflow or is actually part of a randomised region within the overall polarization pattern. Nevertheless, the asymmetric nature of isophotal data and the position of condensations within the inner nebula provide clear evidence for the plausibility of a rotating, episodic outflow.

CHAPTER 6

SUMMARY AND CONCLUSIONS

To end this thesis, the final chapter is used to re-emphasize the main conclusions of the preceding chapters, with additional conclusions being drawn and suggestions of further observations which could be made to extend the work presented here.

Chapter 1 was used to provide a detailed description of the changes which occur inside stars during the various stages of stellar evolution leading to the formation of a PN. This detailed knowledge shows that the PN represents only a brief transitional phase in the overall development of stars. As a result, the lack of sufficient observational data of PNe in the early stages of development still presents a number of difficulties and uncertainties in the formulation of a complete evolutionary picture.

It is now believed that most PPNe and young PNe exhibit small angular dimensions and suffer greatly from the effects of interstellar extinction. Consequently, the number of low and intermediate mass stars which are observed during these stages of evolution is very limited.

During the development of a PN, it is known that stars experience periods of instability and considerable change in internal structure. The most profound changes are known to occur after the cessation of core

hydrogen burning, when mass loss processes become prominent within the outer regions of the star. Although the theoretical foundations of mass loss are somewhat weak, it is clear that mass loss upon the RGB and AGB holds significant importance in the formation and shaping of PNe. As matter is lost from the star, it expands and cools, giving rise to suitable conditions for the condensation of dust grains. This process is believed to induce the development of radiative stellar winds which act to sweep up and compress material into a high density shell surrounding the central star. Together, the effects of stellar outflow and mass loss produce an extreme diversity in the morphology and general properties of PNe. Observations have shown that the characteristics of PNe are considerably more complex than previously assumed.

Formulation of the theory of interacting stellar winds has produced great success in describing the origin of the various morphological types of PNe, although difficulties still remain in explaining the exact nature of the fast and slow winds. Greatest concern appears in explaining the asymmetry of the slow wind which occurs during the AGB. The degree of asymmetry within the distribution of matter of the slow wind is known to be of extreme importance in the development of a PN, governing the morphology of each nebula. To provide an explanation for asymmetric mass loss upon the AGB, theoretical modelling now includes the influence of many factors, such as gas compression by magnetic fields, stellar rotation, stellar pulsation, and stellar binarity. Of the many factors included in these theoretical models, the impact of stellar binarity appears to present the most satisfactory explanation for many PNe features, particularly those observed within bipolar and elliptical nebulae. For the case of bipolar PNe, the presence of a binary nucleus provides convincing evidence for the appearance of the highly collimated aspect of nebular lobes, and also for the precessional motion of point-symmetric structure. A number of PNe also show several pairs of bipolar outflow, suggesting that episodic mass loss has occurred during precessional motion of the stellar outflow. It is evident that these phenomena occur predominantly in bipolar and elliptical PNe, revealing that binary star evolution plays a key role in understanding PN characteristics.

Polarization data presented in chapters 3, 4, and 5 concentrate upon bipolar PNe. All 3 nebulae included in the sample are believed to belong to the group of nebulae known as Type I PNe. With the exception of M2-9, the sample of observed nebulae possess extremely low levels of polarization. Explanation of this fact comes from the observation that these objects are seen through a combination of both intrinsic emission and scattered radiation. Observation of the lower levels of polarization in both NGC 2440 and NGC 2818 also relate to their advanced state of evolution. The nebulae of NGC 2440 and NGC 2818 are now composed almost entirely of gaseous material. The central star of these objects is directly observable and thus provides a large UV flux to the material of the surrounding nebula. Any dust content of the nebula will have been blown out by radiation pressure or destroyed by shock processes and the intense UV radiation. Consequently, the distribution of dust has become sufficiently low that its effects upon radiation are minimal.

With regards to the effects of stellar binarity, all PNe of the data sample display characteristics which would suggest the presence of a binary nucleus. Consequently, the presence of a binary nucleus may be a common feature of the bipolar PNe. Similarly, the appearance of features which are suggestive of episodic mass loss indicate that transient mass loss may occur commonly in PNe. Clear evidence from NGC 2440 and limited evidence from NGC 2818 for the presence of bipolar rotating episodic jets may suggest that precessional outflow is a common phenomenon in PNe, particularly Type I bipolar nebulae.

Together with spectroscopy and photometric study, the use of polarimetry provides additional constraint upon the theoretical models of nebular properties. Consequently, polarimetry remains as a powerful tool in the analysis of PN structure. However, the most important application of polarimetry in the study of PNe, is its use in the determination of dust properties. The effects of dust upon radiation are known to be strongly wavelength dependent. As a result, the use of polarimetric study across a range of wavelengths enables dust characteristics, such as spatial distribution, size distribution, and grain composition to be modelled.

Although the sample of bipolar PNe included in this thesis is small, it is apparent that the magnitude and pattern of polarization within these objects changes as you go from object to object. This is observed as a decrease in the level and structured pattern of polarization with increasing nebular age. This is particularly clear for NGC 2440 and NGC 2818 which possess very similar properties. The only exception in character between the two nebulae appears to be a difference in dynamical age. Consequently, the more evolved nebula, NGC 2818 shows lower levels of polarization and an almost random polarization pattern. In view of the observations, it may be proposed that the levels of scattering are linked to the structure of the inner regions of each nebula. This means that the dust distribution of older PNe becomes sufficiently low that its effects have little importance upon the levels of polarization through radiation scattering. Observations should therefore be made of bipolar PNe spanning a range of dynamical age. These measurements could reveal important knowledge of the changes which occur in the nebular dust distribution with increasing nebular age, and also provide information about the dust of the interstellar medium. Furthermore, the use of polarimetry could provide knowledge of the changes which occur in the high velocity outflows of bipolar PNe and how these changes affect the dust population of each nebula.

The high levels and well structured pattern of polarization observed in M2-9 suggest that the bipolar lobes contain a substantial amount of dust. The extreme levels of polarization observed within the outer ansae may also suggest that the nebula contains two different types of dust which were produced at different times during the evolution of the nebula. Observations show that the circumstellar regions of M2-9 are still dense, producing multiple scattering events which act to reduce the levels of polarization across the nebular core. Evidence for the signature of a circumstellar disc within NGC 2440 and NGC 2818 is less clear. However, the pattern of polarization observed within NGC 2440 shows enough structure to indicate the presence of a circumstellar torus.

It is suggested by the author that further polarimetric studies should be carried out upon the young PN M2-9. These studies should include detailed observations of the nebular core and circumstellar envelope, with the aim of modelling the distribution and composition of dust within those regions. A comparison of these observations and models could then be made against observations of the outer lobes of M2-9. Results from this analysis could then be used to ascertain whether episodic mass loss has occurred during the evolutionary history of the nebula. Comparative analysis of the positions of the nebular condensations of M2-9 has revealed that a definite change has occurred since the last observations in 1993. It is suggested that further observations should be made to monitor the displacement of the condensations, so that accurate determination of the rotation period may be made.

With the recent modification to the Durham Imaging Polarimeter to measure the properties of circularly polarized light, it is suggested that the analysis of PPNe and young PNe may prove useful. It is likely that the youngest objects possess very dense circumstellar envelopes, providing favourable conditions for the formation of circularly polarized radiation. Consequently, the ability to map circular polarization within PNe could provide additional knowledge of the nebular environment between the evolutionary phase at the tip of the AGB and the development of a PPN.

LIST OF ABBREVIATIONS

- AGB Asymptotic Giant Branch
- BRET Bipolar Rotating Episodic Jet
- CE Common Envelope
- CNO Carbon-Nitrogen-Oxygen
- CSE Circumstellar Envelope
- E-AGB Early Asymptotic Giant Branch
- EUV Extreme Ultraviolet
- FIR Far Infrared
- FUV Far Ultraviolet
- FWHM Full Width Half Maximum
- H-R Hertzsprung-Russell
- HST Hubble Space Telescope
- IRAS Infrared Astronomical Observatory
- IUE International Ultraviolet Explorer
- ISM Interstellar Medium
- ISP Interstellar Polarization
- ISW Interacting Stellar Wind
- MIR Mid Infrared
- NIR Near Infrared
- OH/IR Hydroxyl/Infrared
- PAH Polycyclic Aromatic Hydrocarbon
- PN Planetary Nebula
- PNe Planetary Nebulae
- PNN Planetary Nebula Nucleus
- PNNi Planetary Nebula Nuclei
- PPN Proto-planetary Nebula
- PPNe Proto-planetary Nebulae
- P-P Proton-Proton
- RGB Red Giant Branch
- RGE Red Giant Envelope
- TP Thermal Pulse
- TP-AGB Thermally Pulsing Asymptotic Giant Branch
- UV Ultraviolet
- VLA Very Large Array

- VSG Very Small Grains
- ZAMS Zero Age Main Sequence

GLOSSARY

- **Centro-symmetric Scattering:** Radiation scattering which occurs from a single illuminating source. The resulting polarization pattern follows a circular profile. Each polarization vector forms a normal to the radius vector which extends from the illuminating centre to the point of each polarization measurement.

- **Depolarization:** A reduction in the level of polarization or a total removal of polarization from a beam of radiation.

- **Dichroic Extinction:** The property of non-spherical, elongated dust grains which have become aligned by means of a magnetic field. Particles which possess such a structure exhibit varying degrees of absorption and scattering to radiation. This is dependent upon the wavelength of the radiation which is incident upon the dust grain.

- **Geometric Scattering:** Radiation scattering which occurs from particles with sizes greater than the wavelength of the incident radiation.

- **Mie Scattering:** Radiation scattering which occurs from spherical particles with sizes less than or equal to the wavelength of the incident radiation. The intensity of the scattered radiation is proportional to the first power of the frequency of the incident radiation.

- **Mirror-symmetry:** The symmetry of structures which are located at equal distance from the equatorial plane, but appear only on one side of the polar axis of an astronomical object.

- **Point-symmetry:** The symmetry of structures which are located at equal distance from the equatorial plane, but appear on opposite sides of the polar axis of an astronomical object.

- **Polarized Intensity:** The fraction of the total emission from an astronomical object, which is polarized. This is equivalent to the product of the measured intensity and percentage polarization at a point within the object.

- **Rayleigh Scattering:** Radiation scattering which occurs from particles with sizes much less than the wavelength of incident radiation. The intensity of the scattered radiation is proportional to the fourth power of the frequency of the incident radiation.

- **Scattered Radiation Dilution:** The reduction in the degree of scattering caused by the presence of high levels of intrinsic emission, conflicting polarization mechanisms, or multiple scattering events.

BIBLIOGRAPHY

- Abell, G. O., Goldreich, P., 1966, Publ. Astron. Soc. Pac., 78, 232
- Acker, A., 1980, Astron. Astrophys., 89, 33
- Acker, A., Marcout, J., Ochsenbein, F., Stenholm, B., Tylenda, R., Schonn, C., 1992, The Strasbourg-ESO Catalogue of Galactic PNe (Munich: ESO)
- Aitken, D. K., Roche, P. F., Spencer, P. M., Jones, B., 1979, Astrophys. J., 233, 925
- Alton, P., 1996, Ph.D. Thesis, University of Durham
- Allen, D. A., Swings, J. P., 1972, Astrophys. J., 174, 583
- Aller, L. H., 1993, IAU Symp., 155 Planetary Nebulae, ed R Weinberger, A Acker (Dordrecht: Kluwer), p1
- Aller, L. H., Czyzak, S. J., Kaler, J. B., 1968, Astrophys. J., 151, 187
- Asano, S., Yamamoto, G., 1975, Appl. Opt., 14, 29
- Aspin, C., McLean, I. S., 1984, Astron. Astrophys., 134, 333
- Aspin, C., McLean, I. S., Smith, M. G., 1988, Astron. Astrophys., 196, 227
- Atherton, P. D., Pottasch, S. R., Reay, N. K., 1986, Nature, 320, 423
- Axon, D. J., Ellis, R. S., 1976, MNRAS, 177, 499
- Bachiller, R., Martin-Pintado, J., Bujarrabal, V., 1990, Astron. Astrophys., 227, 188
- Bachiller, R., Gomez-Gonzalez, J., Bujarrabal, V., Martin-Pintado, J., 1988, Astron. Astrophys., 196, L5

- Balick, B., 1987, Astron. J., 94,671
- Balick, B., 1989, IAU Symp., 131 Planetary Nebulae, ed S Torres-Peimbert (Dordrecht: Kluwer), 83
- Balick, B., 1989, Astron. J., 97, 476
- Balick, B., Preston, H. L., Icke, V., 1987, Astron. J., 94, 1641
- Banerjee, D. P. K., Anandarao, B. G., Jain, S. K., Mallik, D. C. V., 1990, Astron. Astrophys., 240, 137
- Barker, T., 1978, Astrophys. J., 220, 193
- Barkhatova, K. A., 1950, Astron. Zh. UdSSR, 27, 180
- Bassgen, M., Diesch, C., Grewing, M.,1995, Astron. Astrophys., 297, 828
- Baud, B., Habing, H. J., 1983, Astron. Astrophys., 127, 73
- Berry, D. S., 1985, Ph.D. Thesis, University of Durham
- Black, J. H., van Dishoeck, E. F., 1987, Astrophys. J., 322, 412
- Bohren C. F., Huffman, D. R., 1983, Absorption and Scattering of Light by Small Particles (Wiley: New York)
- Bond, H. E., Livio M., 1990, Astrophys. J., 355, 568
- Born, M., Wolf, E., 1964, Principles of Optics (Pergamon Press: Oxford)
- Bowen, G. H., Willson, L. A., 1991, Astrophys. J., 375, L53
- Bowlzer, S. L., 1997, Ph.D. Thesis, University of Durham
- Burton, M. G., Bulmer, M., Moorhouse, A., Geballe, T. R., Brand, P. W. J. L., 1992, MNRAS, 257, 1
- Cahn, J. H., 1976, Astron. J., 81, 407
- Cahn, J. H., Kaler, J. B., 1971, Astrophys. J. Suppl. Ser., 22, 319
- Calvet, N., Cohen, M., 1978, MNRAS, 182, 687
- Canto, J., Rodriguez, L. F., 1980, Astrophys. J., 226, 455
- Ciardullo, R., Bond, H. E., Sipior, M. S., Fullton, L. K., Zhang, C. Y., Schaefer, K. G., 1999, Astron. J., 118, 488
- Carsenty, U., Solf, J., 1983, IAU Symp.,103 Planetary Nebulae, ed D R Flower (Dordrecht: Reidel), p510
- Chandrasekhar, S., 1960, Radiative Transfer (New York: Dover)
- Chevalier, R. A., Luo, D., 1994, Astrophys. J., 421, 225
- Cliffe, J. A., Frank, A., Livio, M., Jones, T. W., 1995, Astrophys. J., 447, 49
- Code, A. D., Whitney, B. A., 1995, Astrophys. J., 441, 400
- Cohen, M., Barlow, M J., 1974, Astrophys. J., 193, 401
- Cohen, M., Dopita, M. A., Schwarz, H. E., Tielens, A. G. G. M., 1985, Astrophys. J., 297, 702
- Condal, A. R., 1982, Astron. Astrophys., 112, 124
- Corradi, R. L. M., Schwarz, H. E., 1995, Astron. Astrophys., 293, 871

- Corradi, R. L. M., Schwarz, H. E., Stanghellini, L., 1993, IAU Symp.,155 Planetary Nebulae, ed R Weinberger, A Acker, (Dordrecht: Kluwer), p216
- Coyne, G. V., Moffat, A. F. J., Tapia, S., Magahães, A. M., Shulte-Ladbeck, R. E., Wickramasinghe, D. T., 1988, Polarized Radiation of Circumstellar Origin (Arizona University Press)
- Cudworth, K. M., 1974, Astron. J., 79, 1384
- Curtis, H. D., 1918, Publ. Lick Obs., 13, 55
- Daub, C. T., 1982, Astrophys. J., 260, 612
- Davis, L., Greenstein, J. L., 1951, Astrophys. J., 114, 206
- Debye, P., 1909, Ann. Physik., 25, 377
- Dinerstein, H. L., Sneden, C., Uglum, J., 1995, Astrophys. J., 447, 262
- Dolginov, A. Z., IAU Symp., 140 Galactic and Intergalactic Magnetic Fields (Dordrecht: Kluwer), p242
- Dougherty, L. M., Dollfus, A., 1989, Journal British Astron. Assoc., 99, 183
- Doyle, S., Balick, B., Corradi, R. L. M., Schwarz, H. E., 2000, Astron. J., 119, 1339
- Draine, B. T., 1988, Astrophys. J., 333, 848
- Draper, P. W., 1988, Ph.D. Thesis, University of Durham
- Dufour, R. J., 1984, Astrophys. J., 287, 341
- Dutra, C., Maciel, W. J., 1990, Rev. Mexicana. Astron. Astrof., 21, 264
- Dwarkadas, V. V., Chevalier, R. A., Blondin, J. M., 1996, Astrophys. J., 457, 773
- Evans, D. S., Thackeray, A. D., 1950, MNRAS, 110, 429
- Faundez-Abans, M., Maciel, W. J., 1987, Astron. Astrophys., 183, 324
- Feibelman, W. A., 1984, Astrophys. J., 287, 353
- Forveille, T., Huggins, P. J., Bachiller, R., Cox, P., 1998, Astrophys. J., 495, 111
- Frank, A., 1994, Astron. J., 107, 261
- Frank, A., Balick, B., Livio, M., 1996, Astrophys. J., 471, 53
- Frank, A., Mellema, G., 1994a, Astron. Astrophys., 289, 937
- Furton, D. G., Witt, A. N., 1992, Astrophys. J., 386, 587
- Garcia-Segura, G., Langer, N., Rózyczka, M., 1999, Astrophys. J., 517, 767
- Gathier, R., Pottasch, S. R., 1988, Astron. Astrophys., 197, 266
- Gathier, R., Pottasch, S. R., Pel, J. W., 1986, Astron. Astrophys., 157,171
- Gething, M. R., Warren-Smith, R. F., Scarrott, S. M., Bingham, R. G., 1982, MNRAS, 198, 881
- Gledhill, T. M., 1987, Ph.D. Thesis, University of Durham
- Goodrich, R. W., 1991, Astrophys. J., 366, 163
- Gold, T., 1952, Nature, 169, 322
- Gorny, S. K., Stasinska, G., Tylenda, R., 1997, Astron. Astrophys.,318, 256
- Greenberg, J. M., 1978, Cosmic Dust, ed J A M McDonnell (Wiley: New York)

- Greenberg, J. M., Medoza-Gomez, C. X., de Groot, M. S., Breukers, R., 1993, Dust and Chemistry in Astronomy, ed T J Millar, D A Williams (London: IOP Publishing)
- Greig, W. E., 1971, Astron. Astrophys., 10,161
- Greig, W. E., 1972, Astron. Astrophys., 1,70
- Gurzadyan, G. A., 1996, Astron. Astrophys., 311, 997
- Hajian, A. R., Terzian, Y., 1996, Publ. Astron. Soc. Pac., 108, 258
- Harwit, M., 1970, Nature, 226, 61
- Heap, S. R., 1987, Nature, 326, 571
- Heap, S. R., Hintzen, P., 1990, Astrophys. J., 353, 200
- Hecht, E., 1998, Optics (Addison-Wesley)
- Hill, S. J., Willson, L. A., 1979, Astrophys. J., 229, 1029
- Hromov, G. S., Kohoutek, L., 1968, Bull. Astron. Inst. Czech., 19, 1
- Hromov, G. S., Kohoutek, L., 1968, Bull. Astron. Inst. Czech., 19, 81
- Hromov, G. S., Kohoutek, L., 1968, Bull. Astron. Inst. Czech., 19, 90
- Hora, J. L., Latter, W. B., 1994, Astrophys. J., 437, 281
- Hora, J. L., Latter, W. B., Deutsch, L. K., 1999, Astrophys. J. Suppl. Ser., 124, 195
- Huard, S., 1997, Polarization of Light (Wiley: New York)
- Hyung, S., Aller, L. H., 1998, Publ. Astron. Soc. Pac., 110, 466
- Iben, I., Livio, M., 1993, Publ. Astron. Soc. Pac., 105, 1373
- Iben, I., Renzini, A., 1983, Ann. Rev. Astron. Astrophys., 21, 271
- Icke, V., Preston, H. L., Balick, B., 1989, Astron. J., 97, 462
- Icke, V., Balick, B., Frank A., 1992, Astron. Astrophys., 253, 224
- Isaacman, R.,1984, Astron. Astrophys., 130, 151
- Iyengar, K. V. K., 1986, Astron. Astrophys., 158, 89
- Johnson, J. J., Jones, T. J., 1991, Astron. J., 101, 1735
- Jones, R. C., 1941, J. Opt. Soc. Am., 31, 488
- Judge, P. G., Stencel, R. E., 1991, Astrophys. J., 371, 357
- Kahn, F. D., 1983, IAU Symp., 103 Planetary Nebulae, ed D R Flower (Dordrecht: Reidel), p305
- Kaler, J. B., 1974, Astron. J., 79, 594
- Kaler, J. B., Aller, L. H., 1974, Publ. Astron. Soc. Pac., 86, 635
- Kastner, J. H., Weintraub, D. A., Gately, I., Merrill, K. M., Probst, R. G., 1996, Astrophys. J., 462, 777
- King, D. J., Perkins, H. G., Scarrott, S. M., Taylor, K. N. R., 1981, MNRAS, 196, 45
- Kingsburgh, R. L., Barlow, M. J., 1994, MNRAS, 271, 257
- Kliger, D. S., Lewis, J. W., Randall, C. E., 1990, Polarized Light in Optics and Spectroscopy (Academic Press, San Diego)

- Kohoutek, L., Martin, W., 1983, IAU Symp., 103 Planetary Nebulae, ed D R Flower (Dordrecht: Reidel), p534
- Kohoutek, L., Roth-Höppner, M. L., Laustsen, S., 1986, Astron. Astrophys., 162, 232
- Kohoutek, L., Surdej, J., 1980, Astron. Astrophys., 85, 161
- Kwitter, K. B., Henry, R. B. C., 1996, Astrophys. J., 473, 309
- Kwok, S., 1980, Astrophys. J., 258, 280
- Kwok, S., 1982, Astrophys. J., 258, 280
- Kwok, S., 1994, Publ. Astron. Soc. Pac., 106, 344
- Kwok, S., Bignell, C., 1984, Astrophys. J., 276, 544
- Kwok, S., Purton, C. R., Fitzgerald, P. M., 1978, Astrophys. J., 219, 125
- Kwok, S., Purton, C. R., Matthews, H. E., Spoelstra, T. A. T., 1985, Astron. Astrophys., 144, 321
- Lacasse, M. G., 1982, Astrophys. Lett., 23, 61
- Latter, W. B., Hora, J. L., 1997, IAU Symp., 180 Planetary Nebulae, ed H J Habing, H J G L M Lamers (Dordrecht: Kluwer)
- Latter, W. B., Kelly, D. M., Hora, J. L., Deutsch, L. K., 1995, Astrophys. J. Suppl. Ser., 100, 159
- Lenzuni, P., Natta, A., Panagia, N., 1989, Astrophys. J., 345, 306
- Livio, M., 1982, Astron. Astrophys., 105, 37
- López, J. A., 1997, IAU Symp., 180 Planetary Nebulae, ed H J Habing, H J G L M Lamers (Dordrecht: Kluwer), 197
- López, J. A., 2000, Rev. Mexicana. Astron. Astrof., 9, 201
- López, J. A., Meaburn, A., Bryce, M., Holloway, A. J., 1998, Astrophys. J., 493, 803
- López, J. A., Vasquez, R., Rodríguez, L. F., 1995, Astrophys. J., 455, L63
- Lutz, J. H., Kaler, J. B., Shaw, R. A., Schwarz, H. E., Aspin, C., 1989, Publ. Astron. Soc. Pac., 101, 966
- Maciel, W. J., Pottasch, S. R., 1980, Astron. Astrophys., 88, 1
- Manchado, A., Stanghellini, L., Guerrero, M. A., 1996, Astrophys. J., 466, L95
- Marsh, K. A., Purton, C. R., Feldman, P. A., 1976, Astron. Astrophys., 49, 211
- Marten, H., Schönberner, D., 1991, Astron. Astrophys., 248, 590
- Martin, P., 1989, IAU Symp., 135 Interstellar Dust, ed L J Allamandola, A G G M Tielens (Dordrecht: Kluwer), p55
- Martin, P. G., Whittet, D. C. B., 1990, Astrophys. J., 357, 113
- Mathis, J. S., 1990, Ann. Rev. Astron. Astrophys., 28, 37
- Matsumura, M., Seki, M., 1991, Astrophys. & Space Sci., 176, 283
- Mellema, G., 1994, Astron. Astrophys., 290, 915
- Mellema, G., Frank, A., 1995, MNRAS, 273, 401
- Merrill, K. M., Stein, W. A., 1976, Publ. Astron. Soc. Pac., 88, 874
- Mie, G., 1908, Ann. Physik., 25, 377

- Milne, D. K., Aller, L. H., 1975, Astron. Astrophys., 38, 183
- Minkowski, R., 1947, Publ. Astron. Soc. Pac., 59, 257
- Minkowski, R., 1964, Publ. Astron. Soc. Pac., 76, 197
- Morris, M., 1981, Astrophys. J., 249, 572
- Morris, M., 1987, Publ. Astron. Soc. Pac., 99, 1115
- Moseley, H., 1980, Astrophys. J., 238, 892
- Mueller, H., 1948, J. Opt. Soc. Am., 38, 661
- Ohman, Y., 1939, MNRAS, 99, 624
- Oloffson, H., Carlström, U., Eriksson, K., Gustafsson, B., Willson, L. A., 1990, Astron. Astrophys., 230, L13
- Omont, A., 1986, Astron. Astrophys., 164, 159
- Paczynski, B., 1970, Acta. Astron., 20, 47
- Paczynski, B., 1971, Acta. Astron., 21, 417
- Pascoli, G., Leclercq, J., Poulain, B., 1992, Publ. Astron. Soc. Pac., 104, 182
- Pedreros, M., 1989, Astron. J., 98, 2146
- Peimbert, M., Luridiana, V., Torres-Peimbert, S., 1995, Rev. Mexicana. Astron. Astrof., 31, 147
- Peimbert, M., 1978, IAU Symp., 76 Planetary Nebulae, ed Y Terzian (Dordrecht: Reidel), p215
- Peimbert, M., Torres-Peimbert, S., 1983, IAU Symp., 103 Planetary Nebulae, ed D R Flower (Dordrecht: Reidel), p233
- Perek, L., Kohoutek, L., 1967, Publ. House Czech. Acad. Sci., 1
- Phillips, J. P., 2000, Astron. J., 119, 342
- Phillips, J. P., Cuesta, L., 1998, Astron. Astrophys. Suppl. Ser., 133, 381
- Phillips, J. P., Cuesta, L., 1999, Astron. J., 118, 2919
- Phillips, J. P., Reay, N.K., Worswick, S. P., 1980, MNRAS., 193, 231
- Pickering, E. C., 1873, Amer. Acad. Arts Sci., 9, 1
- Pineau des Forêts, G., Flower, D. R., Aguillon, F., Sidis, V., Sizun, M., 2001, MNRAS, 323, L7
- Pottasch, S. R., 1984, Planetary Nebulae (Dordrecht: Reidel)
- Pottasch S.R., Baud B., Beintema D., Emerson, J., Harris, S., Habing, H. J., Houck, J., Jennings, R., Marsden, P., 1984, Astron. Astrophys., 138, 10
- Pottasch, S. R., 1981, Astron. Astrophys., 94, L13
- Pottasch, S. R., 1992, Astron. Astrophys. Rev., 4, 215
- Purcell, E. M., 1979, Astrophys. J., 231, 404
- Purton, C. R., Feldman, P. A., Marsh, K. A., 1975, Astrophys. J., 195, 479
- Purton, C. R., Feldman, P. A., Marsh, K. A., Allen, D. A., Wright, A. E., 1982, MNRAS, 198, 321
- Reay, N. K., Walton, N. A., Atherton, P.D., 1988, MNRAS, 232, 615
- Reipurth, B., 1987, Nature, 325, 787

- Renzini, A., 1981, Physical Processes in Red Giants, ed I Iben Jr. & A Renzini (Dordrecht: Reidel), p431
- Roddier, F., Roddier, C., Graves, J. E., Northcott, M. J., 1995, Astrophys. J., 443, 249
- Rodriguez,, L. F., Garcia-Barreto, J. A., Gomez, Y., 1985, Rev. Mexicana. Astron. Astrof., 11, 109
- Scarrott, S. M., 1991, Vistas Astron., 34, 163
- Scarrott, S. M., Scarrott, R. M. J., 1995, MNRAS, 277, 277
- Scarrott, R. M. J., Scarrott, S. M., Wolstencroft, R, D., 1993, MNRAS, 264, 740
- Scarrott, S. M., Warren-Smith, R. F., 1988, MNRAS, 232, 725
- Scarrott, S. M., Warren-Smith, R. F., Pallister, W. S., Axon, D. J., Bingham, R. G., 1983, MNRAS, 204, 1163
- Schild, H., 1995, Astron. Astrophys., 297, 246
- Schmidt, G. D., Cohen, M., 1981, Astrophys. J., 246, 444
- Schmidt-Voigt, M., Koppen, J., 1987, Astron. Astrophys., 174, 211
- Schwarz, H. E., Corradi, R. L. M., 1995, Astron. Astrophys., 293, 871
- Schwarz, H. E., Aspin, C., Corradi, Reipurth, B., 1997, Astron. Astrophys., 319,267
- Serkowski, K., Mathewson, D. L., Ford, V. L., 1975, Astrophys. J., 196, 261
- Shao, C. Y., Liller, W., 1968 IAU Symp., 34 Planetary Nebulae, ed D. E. Osterbrock, C R O'Dell (Dordrecht: Reidel), p320
- Shapley, H., 1930, Star Clusters (McGraw-Hill: New York), p230
- Shaw, R. A., Kaler, J. B., 1989, Astrophys. J. Suppl. Ser., 69, 495
- Shields, G. A., Aller, L. H., Keyes, C. D., Czyzak, S. J., 1981, Astrophys. J., 248, 569
- Shklovskii, I. S., 1956, Soviet Astron., 33, 222
- Shurcliff, W. A., 1962, Polarized Light, Production and Use (Harvard University Press: Cambridge, MA, USA)
- Smith, R. L., Rose, W. K., 1975, Astrophys. J., 176, 395
- Soker, N., 1997, Astrophys. J. Suppl. Ser., 112, 487
- Soker, N., 1994, MNRAS, 270, 774
- Soker, N., Livio, M., 1994, Astrophys. J., 421, 219
- Solf, J., 2000, Astron. Astrophys., 354, 674
- Somerville, W. B., Allen, R. G., Carnochan, D. J., He, L., McNally, D., Martin, P. G., Morgan, D. H., Nandy, K., Walsh, J. R., Whittet, D. C. B., Wilson, R., Wolff, M. J., 1994, Astrophys. J. Lett., 427, L47
- Stasinska, G., Szczerba, R., 1999, Astron. Astrophys., 352, 297
- Steffen, W., López, J. A., Astrophys. J., 508, 696
- Sternberg, A., Dalgarno, A., 1989, Astrophys. J., 338, 197
- Stockdale, D. P., 1996, Ph.D. Thesis, University of Durham
- Swings, J. P., Andrillat, Y., 1979, Astron. Astrophys., 74, 85

- Telesco, C. M., Harper, D. A., 1977, Astrophys. J., 211, 475
- Terzian, Y., Balick, B., Bignell, C., 1974, Astrophys. J., 188, 257
- Thronson, H. A., Latter, W. B., Black, J. H., Bally, J., Hacking, P., 1988 Publ. Astron. Soc. Pac., 100, 1446
- Tielens, A. G. G. M., 1993, IAU Symp. 155 Planetary Nebulae, ed R Weinberger, A Acker, (Dordrecht: Kluwer), p155
- Tifft, W. G., Conolly, L. P., Webb, D. F., 1972, MNRAS, 158, 47
- Tinbergen, J.,1996, Astronomical Polarimetry (Cambridge University Press: Cambridge, UK)
- Torres-Peimbert, S., Peimbert, M., 1977, Rev. Mex. Astron. Astrofis., 2, 181
- Trammell, S. R., Dinerstein, H. L., Goodrich, R. W., 1994, Astron. J., 108, 984
- Trammell, S. R., Goodrich, R. W., Dinerstein, H. L., 1995, Astrophys. J., 453, 761
- Tuchman, Y., Sack, N., Barkat, Z., 1979, Astrophys. J., 234, 217
- Van den Bergh, S., 1974, Astron. Astrophys., 32, 351
- Van der Hulst, H. C., 1957, Light Scattering by Small Particles (Wiley: New York)
- Van der Veen, W. E. C. J., Habing, H. J., 1988, Astron. Astrophys., 194, 125
- Vázquez, R., Torrelles, J. M., Rodriguez, L. F., Gomez, Y., López, J. A., Miranda, L. F., 1999, Astrophys. J., 515, 633
- Vassiliadis, E., Wood, P. R., 1993, Astrophys. J., 413, 641
- Vassiliadis, E., Wood, P. R., 1994, Astrophys. J. Suppl. Ser., 92, 125
- Vorontsov-Vel'Yaminov, B. A., 1961, Astronomicheskii Zhurnal, 38, 75
- Walker, H. J., Cohen M., 1988, Astron. J., 95, 1801
- Walker, H. J., Cohen, M., Volk, K., Wainscoat, R. J., Schwartz, D. E., 1989 Astron. J., 98, 2163
- Walsh, J. R., 1981, MNRAS, 194, 903
- Warren-Smith, R. F., 1979, Ph.D. Thesis, University of Durham
- Weaver, J., McCray, R., Castor, J., Shapiro, P., Moore, R., 1977, Astrophys. J., 218, 377
- Westerlund, B. E., Henize, K. G., 1967, Astrophys. J. Suppl. Ser., 14 154
- White, R. L., Becker, R. H., 1982, Astrophys. J., 262, 657
- Whittet, D. C. B., 1992, Dust in the Galactic Environment (IOP Publishing)
- Whittet, D. C. B., Martin, P. G., Hough, J. H., Rouse, M. F., Bailey, J. A., Axon, D. J., 1992, Astrophys. J., 386, 562
- Wickramasinghe, N. C., 1973, Light Scattering Functions for Small Particles with Applications in Astronomy (Hilger: London)
- Wilking, B. A., Lebofsky, M. J., Rieke, G. H., 1982, Astron. J., 87, 695
- Wolff, M. J., Code, A. D., Groth, E. J., 2000, Astron. J., 119, 302
- Woolf, N. J., Ney, E. P., 1969, Astrophys. J. Lett., 155, L181
- Wood, P. R., 1974, Astrophys. J., 190, 609
- Zhang, C. Y., 1995, Astrophys. J. Suppl. Ser., 98, 659

- Zhang, C. Y., Kwok, S., 1990, Astron. Astrophys., 237, 479
- Zuckerman, B., Dyck, H. M., 1986, Astrophys. J., 304, 394
- Zweigle, J., Neri, R., Bachiller, R., Bujarrabal, V., Grewing, M., 1997, Astron. Astrophys., 324, 624

ACKNOWLEDGEMENTS

Firstly I would like to thank my supervisors Prof. D. R. Flower, Dr. D. Stockdale, and the late Dr. S. M. Scarrott whose memory lives on. To them I am indebted for their patience, understanding, and much appreciated guidance. I am also indebted to Dr. P. W. Draper for his advice upon the many technical issues which have arisen during the course of my Ph.D. Many thanks also go out to my contemparies of the Durham Polarimetry group, particularly Michelle Felton and Stephen Bowlzer.

Special appreciation goes to PPARC for the provision of STARLINK software at the University of Durham, and for whom the possibility of pursuing a Ph.D. would have been impossible. Thanks also to the head of the Department of Physics, Prof. M. R. Pennington for the facilities provided in Durham.

Thanks go to Mr Alan Lotts, for whom I am indebted for his assistance and advice with all technical aspects of the computing facilities within the Department of Physics. Many thanks also to the administrative and technical staff of the McDonald Observatory, Texas and Sutherland Observatory, South Africa in ensuring that all observing went well.

Special gratitude goes out to my loving mother, father, and dear sister Jane without whom I would have never reached the end of my Ph.D. My memory also goes out to my grandfather whose spirit will always remain with me, pushing me onward.